GEORGIA INSTITUTE OF TECHNOLOGY
OFFICE OF CONTRACT ADMINISTRATION
SPONSORED PROJECT INITIATION

Date: 8/27/80

Project Title: CHARACTERIZATION OF HIGH TEMPERATURE VAPORS OF IMPORT TO COMBUSTION AND GASIFICATION IN THE ENERGY TECHNOLOGIES

Project No: G-33-661

Project Director: DR. JAMES L. GOLE

Sponsor: U.S. DEPARTMENT OF ENERGY; MORGANTOWN ENERGY TECHNOLOGY CENTER; P.O. BOX 880; MORGANTOWN, WV 26505

Agreement Period: From 3/1/80 Until 3/31/81 (CONTRACT PERIOD)

Type Agreement: CONTRACT NO. DE-AC21-80MC14615 AND MODIFICATION NO. 1

Amount: $74,749 G-33-661
4,653 G-33-321
$79,402 TOTAL

Reports Required: Notice of Energy R&D Project; Quarterly Technical Progress Reports; Contract Management Summary; Project Status Report; Topical Report; Final Technical Report

Sponsor Contact Person (s):

Technical Matters

TECHNICAL PROJECT OFFICER
KENT CASLETON
U.S. DEPARTMENT OF ENERGY
MORGANTOWN ENERGY TECHNOLOGY CENTER
P.O. BOX 880
MORGANTOWN, WV 26505

Contractual Matters
(thru OCA)

OFFICE OF NAVAL RESEARCH
RESIDENT REPRESENTATIVE
325 HINMAN RESEARCH BUILDING
GEORGIA INSTITUTE OF TECHNOLOGY
ATLANTA, GEORGIA 30332

ATTN: THOMAS A. BRYANT

Defense Priority Rating: NONE

Assigned to: CHEMISTRY (School/~~Laboratory~~)

COPIES TO:

- Project Director
- Division Chief (EES)
- School/Laboratory Director
- Dean/Director—EES
- Accounting Office
- Procurement Office
- Security Coordinator (OCA)
- ✓ Reports Coordinator (OCA)
- Library, Technical Reports Section
- EES Information Office
- EES Reports & Procedures
- Project File (OCA)
- Project Code (GTRI)
- Other C E Smith

GEORGIA INSTITUTE OF TECHNOLOGY
OFFICE OF CONTRACT ADMINISTRATION

SPONSORED PROJECT TERMINATION

Date: 8/31/81

Project Title: Characterization of High Temperature Vapors of Import To Combustion and Gasification in the Energy Technologies

Project No: G-33-661

Project Director: Dr. James L. Gole

Sponsor: U. S. Department of Energy; Morgantown Energy Technology Center; P. O. Box 880; Morgantown, W.V. 26505

Effective Termination Date: 3/31/81

Clearance of Accounting Charges: 3/31/81

Grant/Contract Closeout Actions Remaining:

- X Final Invoice and Closing Documents
- _ Final Fiscal Report
- X Final Report of Inventions
- X Govt. Property Inventory & Related Certificate
- _ Classified Material Certificate
- _ Other _____

XC - S. Smalley G+C Dmk 6/13/83

Assigned to: Chemistry (School/Laboratory)

COPIES TO:

Administrative Coordinator
Research Property Management
Accounting Office
Procurement Office
Research Security Services
Reports Coordinator (OCA)
Legal Services (OCA)
Library, Technical Reports
EES Research Public Relations (2)
~~Project File (OCA)~~
Other: _____

FINAL REPORT

March 1, 1980-March 1, 1981

TITLE OF CONTRACT: The Characterization of High Temperature Vapors of Import to Combustion and Gasification Processes in the Energy Technologies

PLACE OF WORK: Georgia Institute of Technology
Department of Chemistry
Atlanta, Georgia 30332

PRINCIPAL INVESTIGATOR: James L. Gole

SCOPE OF CURRENT EFFORTS

Low tolerance levels for certain species in process streams impose stronger requirements for reliable thermodynamic and kinetic data in order to predict low level species concentrations. In addition, there must be serious concern focused on whether or not these systems are best represented via equilibrium or non-equilibrium models. We have been concerned with the characterization of important processes in these inherently high temperature systems through application of chemiluminescent and laser fluorescent techniques to the determination of bond energies, spectroscopic constants, and rapid energy transfer processes. Our focus has been on the monohydroxides of sodium and potassium and the oxides and sulfides of select metals including SiO, SiS, Na_2O, and NaO. We have investigated and are continuing to investigate non-equilibrium routes for the formation of these compounds and have carried out some kinetic parameterization. In addition, we have been engaged in the study of rapid energy transfer routes among the electronic states of high temperature molecules. Thus far these studies have indicated that both V-E and E-E energy transfer can occur at rates which may approach 500 times

the calculated gas kinetic rate. These surprising results demonstrate that vibrationally and/or electronically excited high temperature molecules act as if they were "large" and "diffuse" entities capable of significant interaction at very long range. The rapid energy transfer is a general phenomenon and effects have been observed in several molecules including SiO and KOH. The observation of such rapid energy transfer has significant implications for the modeling of energy generating systems and the characterization of heat flow in these systems. The nature of the rapid energy transfer means that both kinetic reaction rate data and energy transfer data must be included in order to obtain a realistic modeling of an energy generating system.

Our research effort has been divided into four task areas which may be summarized as follows:

Task I: Studies on SiO including the characterization of the $Si-N_2O$, $M-N_2O$, and $Si-O_3$ reactions.

Task II: Studies on SiS including the characterization of dynamic constraints for the Si-OCS reaction and an investigation of the $Si-S_2$ reaction.

Task III: Production and characterization of KOH and NaOH. This work includes the extensive calibration of an optical multichannel analyzer for the analysis of the KOH emisssion spectrum and the ready use of this device at the Morgantown Energy Technology Center. This work has also included the determination of stringent lower bounds to the K-OH and Na-OH bond energies.

Task IV: Characterization of further systems commensurate with the mutual agreement of DOE Morgantown and the Principal Investigator.

This task has included:

i) A major preliminary effort has involved the construction of an appropriate apparatus for the study and

characterization of Na_2O using laser induced fluorescence spectroscopy. A significant component of spectra have been obtained using argon ion laser induced fluorescence. This work which is summarized elsewhere,[1,2] has lead to the tentative determination of ground state constants.

ii) Initial efforts have been made to generate spectra for the alkali monoxides and monosulfides NaO, NaS, KO, and KS. Preliminary spectra have been obtained under a variety of experimental conditions.

iii) The investigation of ultrafast energy transfer routes in high temperature molecules.

iv) In collaboration with the Morgantown Energy Technology Center, we have recently characterized the methane-fluorine combustion system.

In carrying out the effort outlined above, we have formulated and made available to the support research branch of the Morgantown Energy Technology Center (1) extensive computer programs for the calculation of molecular electronic spectra, (2) a users manual for the calibration and operation of an optical multichannel analyzer system, (3) extensive computer programs for the normal coordinates analysis of polyatomic molecules, and (4) detailed apparatus designs.

UNDER TASK I

(i) We have continued our investigations of the chemiluminescent emission from the "single collision" bimolecular metathesis $Si + N_2O \rightarrow SiO^* + N_2$. Recall that the experimental spectrum (see Figures 1-3, Final Report for July 1, 1979-March 1, 1980, henceforth referred to as R-1) consists of emission from the $b^3\Pi$, $a^3\Sigma^+$, and $A^1\Pi$ systems of SiO. Previous analysis of the $b^3\Pi$ system indicated a strongly non-equilibrium product distribution (based on spectral computer simulation--Figures 1, 4-R1). This work has now been extended to the $A^1\Pi$ system where appropriate

instrument calibrations have been completed and the analysis of the population distribution for the $A^1\Pi$ system is virtually complete. As noted previously (R1), an important result from the analysis of the $A^1\Pi$ and $b^3\Pi$ emission systems is that we have apparently studied the process

$$Si + N_2O \rightarrow SiO^* \ (a^3\Sigma^+, b^3\Pi, A^1\Pi) + N_2(v'' \geq 5) \qquad (1)$$

In other words, the reaction of silicon with N_2O is so fast that the N-N bond length is left virtually intact as an oxygen atom is ripped off from N_2O. This is a very surprising and intriguing result for these highly exothermic metatheses (see also discussion R1). Its consequence is to leave the nitrogen molecule in a state of high vibrational excitation. In response to the apparent observation of the process (1), two approaches toward elucidation have been taken: (1) Several experimental schemes have been developed in an attempt to find direct spectroscopic evidence for formation of vibrationally excited N_2 molecules resulting from the process (1). (2) Comparisons have been made with several other M-N_2O metatheses and the Ti-N_2O and Al-N_2O have been characterized more carefully.

Our results thus far indicate that similar effects are observed in all M-N_2O reactions and that this unusual energy balance and product partitioning may be characteristic of several fast processes occurring in high temperature systems. Among other factors this result has important implications for the understanding of energy partitioning in these systems. Word done thus far to elucidate vibrational excitation is summarized in Appendix A.

(ii) As noted previously (R-1), the Si-O_3 reaction is also characterized by intriguing dynamic constraints closely tied to spin conservation

in chemical reaction. It appears that we have observed chemiluminescent emission corresponding to the processes

$$Si(^3P) + O_3(^1A_1) \rightarrow SiO^*(A^1\Pi) + O_2(^3\Sigma_g, v'' \geq 0)$$

$$Si(^3P) + O_3(^1A_1) \rightarrow SiO^*(b^3\Pi) + O_2(^1\Sigma_g{}^+)$$

The chemiluminescent emission from the single collision silicon-ozone reaction is extremely complicated and overlapped. In order to aid in the interpretation of the single collision studies, we have carried out a multiple collision study at $P_{total} \approx 2$ torr (10 → 50 μ O_3, 2 torr ultrahigh purity argon). The resulting spectrum, shown as the lower scan in Figure 1, corresponds primarily to the $A^1\Pi$ system of SiO; however, our spectral calibration done for the Si-N_2O reaction (SiO^* emission from $A^1\Pi, b^3\Pi$) indicates that there are unusual intensity distributions at wavelengths shorter than λ = 3000 Å which cannot be attributed to the SiO $b^3\Pi - X^1\Sigma^+$ band system. We are currently involved in careful studies of the Si-O_3 reaction over the pressure range from single to multiple collision conditions (note indication of initial efforts in R-1). The results of this study thus far indicate the presence of rapid energy transfer routes characterizing the products of the silicon ozone reaction. In other words, the unusual product distribution which must lead to the anomalous intensity distribution at $\lambda \leq$ 3000 Å in the SiO spectrum is closely tied to energy transfer among SiO electronic states proceeding at rates at least comparable to those expected for gas kinetic processes. In order to carefully unravel the SiO systems, these very fast processes are being studied over a wide pressure range.

The parameterization required to obtain a good fit to the SiO spectrum in Figure 1 provides us with (1) considerable additional information on several levels of the ground and excited states of SiO, and (2) important information on rapid energy transfer routes in this molecule.

Finally, we should note that we are attempting to definitively establish the presence of $O_2(^1\Sigma_g^+) - O_2(^3\Sigma_g^-)$ emission in the Si-O_3 system (see discussion in R-1). Attempts to observe this emission have not yet been successful; however, a new red sensitive detection system which will be used to study the Si + O_3 and K_2 + H_2O_2 reactions has been delivered to the laboratory and we anticipate successful detection with this device.

Given the completion of the projects outlined in (i) and (ii) above (see also Appendix A), we anticipate that a lower bound to the SiO dissociation energy will be determined.

UNDER TASK II

(i) Under this task, we have already studied the Si-OCS reaction and evaluated a lower bound to the SiS dissociation energy (see R-1 pg. 5, 6 and reprints included with R-1). Further work involving Task II has now been carried out. The SiS $a^3\Sigma^+ - {}^1\Sigma^+$ band system characterizng the Si-OCS reaction has been analyzed using an appropriate computer simulation program written in our laboratory (see R-1, Figures 6, 7). The resultant SiS^* population distribution was found to be close to Boltzmann at 645 K (Figure 2) indicating surprising thermalization. This result seemed to indicate that a long-lived complex was formed in the OCS reaction with silicon. In an attempt to elucidate this process furhter, we have attempted to assess whether significant dynamic constraints are operative in the Si-OCS reaction. In order to do this, we have carried out a surprisal analysis. Here one

compares the observed experimental distributions found of the Si-OCS reaction and the relative rates for formation of product molecules in the populated levels of the $b^3\Sigma^+$ state with a "prior" distribution calculated on the basis of the completely statistical population of levels. In other words, the prior distribution assumes no dynamic constraints. In order to make this comparison we have derived the appropriate expressions for the determination of "prior rates for formation of excited ro-vibronic states." This derivation is given in Appendix B. The results of this analysis for the distribution shown in Figure 2 are given in Figure 3. In the Figure $k_{v'}$ corresponds to the relative rate constant for formation in a given vibrational level v' of the $b^3\Sigma^+$ state (open triangles), $f_{v'}$ corresponds to the fraction of energy in vibration (squares), and the open circles denote the surprisal defined as $-\ell n(k_{v'}/k^0_{v'})$ where $k^0_{v'}$ is calculated from the derivation in Appendix B. If a reaction proceeds with no dynamic constraints a horizontal line should be obtained from the surprisal. Figure 3 demonstrates that this is clearly not the case and that although a long-lived complex may be formed, there are further important factors strongly controlling this reaction.

(ii) A reasonably well defined dimeric sulfur source has been developed in the laboratory; however, the results obtained using this source add little to the knowledge obtained from the Si-OCS reaction.

UNDER TASK III

KOH is one of the most important constituents in the high stress environments characterizing energy generating systems. The first electronic emission spectrum for this molecule was obtained in our laboratory (see R-1). The spectrum which correlates closely with emission spectra observed for the KCl and KBr molecules most likely corresponds to a progression in the K-OH

stretch. Each of the major vibrational features also appears to be characterized by further vibrational fine structure which we tentatively attribute to the KOH bending motion.

We have been concerned with the optimization of an appropriate system involving the potassium-hydrogen peroxide (95%) flame so as to obtain much higher resolution spectra for KOH. Because there are problems in maintaining a stable potassium beam and signals are weak, we have of necessity determined that an optical multichannel analyzer represents the most logical device for characterizing the KOH spectrum. This device combines the best aspects of both electrooptical and film (plate) detection.

While calibration of the system at first appeared straightforward, several procedures were tried before a satisfactory calibration scheme could be augmented. We have generated an appropriate manual which outlines the rules for calibrating response characteristics and obtaining reliable spectra at the resolution needed. This manual is now in the hands of Dr. Kent Castleton at DOE Morgantown; a copy is also included in Appendix C.

In addition to our efforts with the multichannel analyzer system, we have engaged in further thrusts to obtain a stabilized KOH^* flame by producing the radical under a variety of flame conditions. The detailed results of these efforts are summarized in two manuscripts reproduced in Appendices D and E. Here we detail changes in the KOH spectrum as a function of experimental conditions such that a ready comparison with results obtained for the alkali halides allows the determination of a stringent lower bound for the KOH bond energy. As discussed in Appendices D and E, the determination of the KOH bond strength can be made from the KOH emission spectrum observed under "diffusion flame" conditions.

We have progressively improved diffusion flame spectra for KOH. This can be seen by comparing the spectra in Figure 9, Appendix D; Figure 4, Appendix E, and Figure 4 included with this report. The notable peak separations observed in the short wavelength onset of Figure 4 correspond closely with the fundamental vibrational frequency measured for KOH. The significance of this agreement is considered at length in Appendix E. From a KOH spectrum similar to that in Figure 4, we anticipate the ability to extract frequency separations for several levels of the ground electronic state of the KOH molecule. When combined with millimeter wave studies (see Appendix E) this data should allow a very effective mapping of the very important ground state parameters for KOH. For the purpose of KOH spectral analysis and for the study of Na_2O, a computer program is now in production in our laboratory. An initial program for computing vibrational structure has already been given to Dr. Castleton. We might note in passing that the calibration procedure developed in our laboratory has saved the Castleton group a minimum of six months' effort and represents the only long range calibration procedure available for the system at the present time.

We have also obtained weak "diffusion flame" spectra for NaOH from which a lower bound for the NaOH dissociation energy could be determined. For KOH, we find $D_o^\circ \geqslant 88.2$ kcal/mole; (for NaOH, $D_o^\circ \geqslant 75.2$ kcal/mole), notably higher than the currently accepted value. We anticipate that further improvements in current apparatus will lead to a higher stringent lqwer bound for the KOH dissociation energy as well as the determination of molecular constants for the ground state of KOH.

UNDER TASK IV

(i) We have developed an apparatus for the study of Na_2O. A preliminary version of this work has been published and can be found in Appendix F. Further

discussion can be found in Appendices D and E. Briefly, the following points are of interest:

(a) An apparatus for the controlled vaporization of Na_2O has been designed. This design is now in the hands of Dr. Castleton.

(b) A computer program for carrying out a normal coordinate analysis on the molecule has been written.

(c) A computer program for spectral analysis has been made available to Dr. Castleton.

(d) A significant component of spectra have been obtained using argon ion laser induced fluorescence.

(e) Molecular constants for the ground electronic state of Na_2O have been determined.

ii) We have obtained a preliminary emission spectrum for NaO (Figure 5) and anticipate further work on this molecule when the components for our red sensitive detection system become operational in the laboratory. The spectrum was obtained through use of the Na-N_2O system. Similar spectra have also been obtained for NaS (Na-OCS) and KO (K-NO_2).

iii) We have investigated ultrafast energy transfer routes in high temperature molecules. Effects have now been observed which indicate energy transfer that proceeds at rates which for certain levels approach 500 times the gas kinetic rates. Effects due to rapid energy transfer have now been observed in BO, SiO, KOH, ScO, and YO. Two papers on these effects have now been written up and reprints on ScO and on BO are enclosed (Appendix G) with this report. The work is summarized in the following abstracts.

(a) Nitrogen dioxide reacts with scandium to yield the $B^2\Sigma^+ - X^2\Sigma^+$ spectrum of ScO. This reaction has been characterized

from 10^{-5} to 1 torr in order to study relaxation and rapid intramolecular E-E transfer among ScO excited states. At the lowest pressures, a ground state metal atom interacts with a tenuous atmosphere of oxidant gas (beam-gas configuration). These "single collision" studies are extended in a controlled manner to higher pressure by entraining the metal atoms in argon and subsequently carrying out the oxidation of this mixture. At all pressures, the measured $B^2\Sigma^+$ vibrational populations follow a markedly non-Boltzmann distribution. At the lowest pressures, the formation of ScO $B^2\Sigma^+$ results directly from the reaction $Sc + NO_2 \rightarrow ScO^* + NO$. At higher pressures, the $B^2\Sigma^+$ state is also populated via rapid intramolecular energy transfer from long-lived, weakly emitting "reservoir" states via the sequence $Sc + NO_2 + Ar \rightarrow ScO(res) + NO + Ar$ and $ScO(res) + Ar \rightarrow ScO(B^2\Sigma^+) + Ar$. Spin orbit and Coriolis interactions in ScO connect rovibronic levels of $B^2\Sigma^+$ and low-lying $^4\Pi_r$ or $^2\Pi_i$ reservoir states resulting in the observation of substantial perturbations in $B^2\Sigma^+$. Collisional energy transfer is particularly efficient for the most strongly perturbed levels of the $B^2\Sigma^+$ state. This energy transfer is manifest by the appearance of "extra" band heads representing normally forbidden (small electronic transition moment or Franck-Condon factor) "reservoir state"-ground state transitions which become allowed because of a small admixture of $B^2\Sigma^+$ character. The relative intensities of the extra and "main" $B^2\Sigma^+ - X^2\Sigma^+$

transitions are strongly dependent on argon buffer gas pressure. A quantitative description of this dependence gives an estimate for the amount of mixing between the reservoir state and $B^2\Sigma^+$ and for the rate of energy transfer between these two states. *Collisional transfer to ScO $B^2\Sigma^+$ $v' = 3 - 9$ is found to proceed at rates which for certain levels approach 100 times gas kinetic.* The effects observed in ScO demonstrate that the excited states of this molecule interact in the presence of a collision partner as if they were large diffuse entities. These effects are not pathological. This behavior may have important implications for the modeling of energy systems as well as the ability to create population inversions requisite for the construction of visible chemical laser systems.

(b) Boron atoms react with oxygen (O_2) and nitrous oxide (N_2O) to yield the $A^2\Pi$ - $X^2\Sigma^+$ spectrum of BO. These reactions have been characterized from 10^{-5} to 10^{-3} torr and at P_{Total} ~1 torr in order to study relaxation and the rapid intramolecular V-E transfer $BO(X^2\Sigma^+, v'' = 17) + X \rightarrow BO(A^2\Pi_{1/2}, v' = 4) + X$ where X = O_2, N_2O, or a combination of these oxidants with argon. At the lowest pressures, a ground state boron atom interacts with a tenuous atmosphere of oxidant gas (beam-gas configuration). These "single collision" studies are extended in a controlled manner to higher pressure by entraining the metal atoms in argon and subsequently carrying out the oxidation of this mixture. At all pressures the measured $A^2\Pi$ vibrational populations

follow a markedly non-Boltzmann distribution. At pressures as low as 6×10^{-5} torr, the formation of BO $A^2\Pi_{1/2}$, $v' = 4$ results from both the direct reaction $B + RO \rightarrow BO^* + R$ and the collisional transfer $BO(X^2\Sigma^+) + RO \rightarrow BO(A^2\Pi) + RO$. The spin orbit interaction in BO connects rovibronic levels of $X^2\Sigma^+$ and $A^2\Pi_{1/2}$ facilitating a route for rapid intramolecular energy transfer. This energy transfer leads to the observation of sharp features in the neighborhood of the BO $A^2\Pi - X^2\Sigma^+$ (4,0) band which may be correlated with the $J' = 18.5 - 21.5$ perturbed rotational levels of $BO(A^2\Pi_{1/2})$. We characterize this phenomenon determining population distributions, rotational temperatures, and the temperature dependence (boron source) of the chemiluminescent emission. The effects observed in BO demonstrate that a highly vibrationally excited ground state species interacts in the presence of a collision partner with a cross section substantially in excess of that expected for "gas kinetic" interaction. This behavior may have important implications for the modeling of energy systems as well as the ability to create population inversions requisite for the construction of visible chemical laser systems.

iv) Research efforts on the methane-fluorine combustion system are presented in Appendix H. This work is summarized in the following abstract:

The chemiluminescent emission which results from excited state product formation upon the intimate mixing of CH_4 with F_2 is

shown to be dominated by visible emission from $CH^*(A^2\Delta\text{-}X^2\Pi)$, $C_2^*(A^3\Pi_g - X^3\Pi_u)$, $HCF^*(\tilde{A}^1A'' - \tilde{X}^1A')$ and vibrationally excited $HF^\dagger(X^1\Sigma^+)$. The corresponding reaction mixture $CD_4 + F_2$ produces the deutero analogs. This study represents the first observation of the HCF emission spectrum from a CH_4/F_2 flame. The observation of the HCF $\tilde{A}^1A'' - \tilde{X}^1A'$ emission spectrum and the corresponding DCF system allows the unequivocal assignment of these visible transitions to a progression dominated by the excited state bending mode. Transitions $(0, \upsilon_2', 0) \rightarrow (0, 0, 0)$, υ_2 = 1-5 for HCF and υ_2' = 2-6 for DCF are observed. An analysis of the spectra yields the electronic and vibrational parameters $T_o = 17274 \pm 6.8\ cm^{-1}$, $\omega_e = 1024 \pm 6.4\ cm^{-1}$, $\omega_e x_e = -7.7 \pm 1.2\ cm^{-1}$ for HCF and $T_o = 17281 \pm 8\ cm^{-1}$, $\omega_e = 787.5 \pm 4.4\ cm^{-1}$, $\omega_e x_e = -3.86 \pm 0.5\ cm^{-1}$ for DCF. Each vibrational transition shows resolved K-type subbands characteristic of a near-symmetric rotor. Although this structure is highly perturbed for the entire HCF system, a partial rotational analysis has been obtained for two bands in the DCF spectrum. The derived rotational parameters are also consistent with the observation of the excited state bending mode.

Principal Investigator

The Principal Investigator has devoted 40+% of his research time to the research efforts outlined here. This amounts to approximately 25 hours per week.

Personnel

Graduate students working on and supported in part by this project include Mr. Gary Green, Mr. Alfred Hanner, Ms. Beatriz Cardelino, Mr. Winfred Crumley, and Mr. Jeffrey Appling. Mr. Randall Childs is also participating in the computational aspects of this project. In addition, Dr. S. A. Pace is continuing his collaboration on several aspects of this research.

Public Relations

Seminars and invited papers describing DOE sponsored work were given at the following locations:

1.	179th National A.C.S. Meeting	3/26/80
2.	Armstrong State College	4/14/80
3.	Columbus Spectroscopy Symposium	6/15/80
4.	Gordon Conference on High Temperature Chemistry	8/08/80
5.	Aerodyne Research Incorporated	8/12/80
6.	The University of Iowa	10/29/80
7.	North Dakota State University	10/31/80
8.	Clemson University	11/13/80
9.	Furman University	11/14/80
10.	Electro-optics/Laser 80 Symposium	11/19/80
11.	State University of New York at Binghampton	11/21/80
12.	Morgantown Energy Technology Center	2/3/81

13.	The University of Pittsburgh	2/19/81
14.	Physics Department, Georgia Institute of Technology	2/25/81
15.	181st National A.C.S. Meeting	3/31/81
16.	Bell Telephone Laboratories	4/8/81
17.	Drexel University	4/9/81

Publications

1. "Single and Multiple Collision Chemiluminescent Studies of the Si-OCS and Ge-OCS Reactions--A Study of the SiS and GeS $a^3\Sigma^+ - X^1\Sigma^+$ and SiS $b^3\Pi - X^1\Sigma^+$ Intercombination Systems and the Nature of SiS Collisional Quenching," with G. J. Green, Chem. Phys. *46*, 67 (1980).

2. "A Study of the Methane-Fluorine Flame Including an Analysis of the $A^1A'' - X^1A^1$ Emission Spectrum of HCF," with R. I. Patel, G. W. Stewart, K. Castleton, and J. R. Lombardi, Chem. Phys. *52*, 461 (1980).

3. "Nonequilibrium Product Distributions Observed in the Multiple Collision Chemiluminescent Reaction of Sc with NO_2. Perturbations, Rapid Energy Transfer Routes and Evidence for a Low-Lying Reservoir State," with S. A. Pace, J. Chem. Phys. *73*, 836 (1980).

4. "Evidence for Ultrafast V-E Transfer in Boron Oxide (BO)," with A. Hanner, J. Chem. Phys. *73*, 5025 (1980).

5. "Laser Spectroscopy of Refractory Compounds," presented as an invited contribution to Electro-Optics Laser 80, Proceedings of the Electro-optics/Laser 80 Conference and Exhibition, pp. 127-140.

6. "The Characterization of High Temperature Vapors of Import to Combustion and Gasification Processes in the Energy Technologies," Proceedings of the Morgantown Energy Technology Center Meeting on High Temperature, High Pressure Particulate and Alkali Control in Coal Combustion Process Streams - Morgantown, West Virginia, 1981 (in press).

7. "Aspects of Sparsely Studied Gas Phase Chemistry of Import to the Energy Technologies," Optical Engineering (in press).

Publications in Preparation

1. "Observation of the KOH Emission Spectrum - A New Lower Bound to the KOH Dissociation Energy," with B. Cardelino (in preparation).

2. "The Characterization of the Single Collision Chemiluminescent Emission from the Si-N_2O and Si-O_3 Reactions and a Comparative Study of Spin Conservation Effects and Stripping Mechanisms in Metal Atom-N_2O Reactions," with G. J. Green and B. Cardelino (in preparation).

3. "Laser Induced Fluorescence Spectra of Li_2O and Na_2O," with Winfred Crumley.

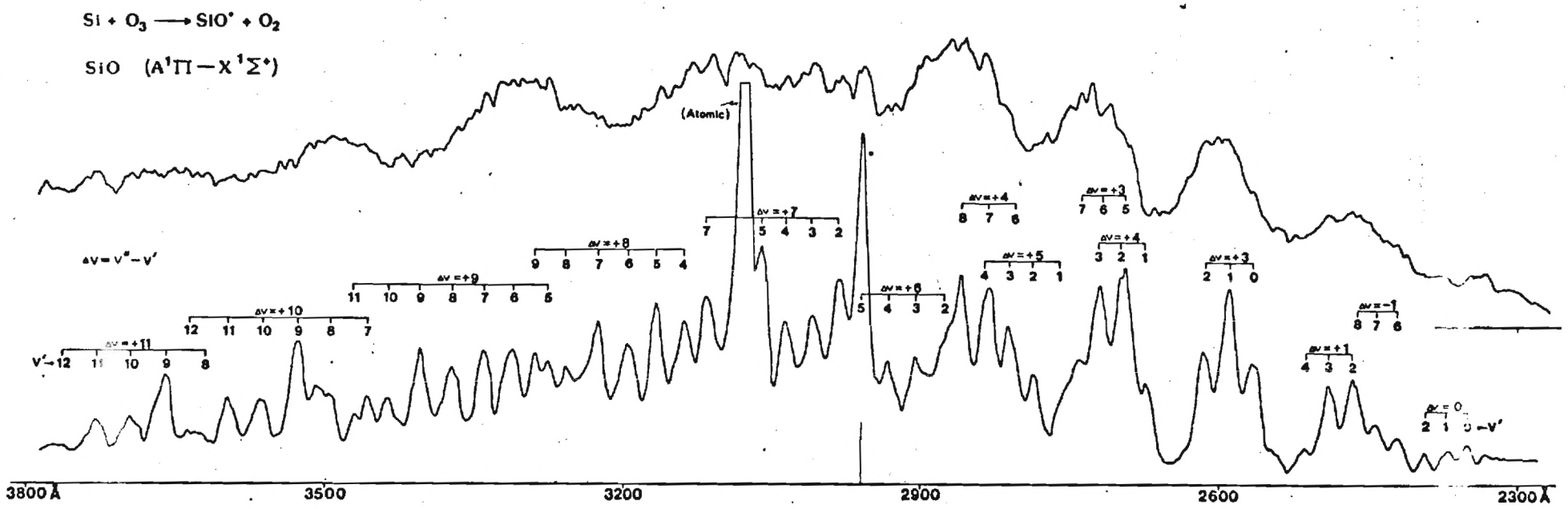
Si + O3 ⟶ SiO* + O2
SiO (A¹Π − X¹Σ⁺)
(Atomic)
Δv = v″ − v′
Δv = +11
Δv = +10
Δv = +9
Δv = +8
Δv = +7
Δv = +6
Δv = +5
Δv = +4
Δv = +3
Δv = +1
Δv = −1
Δv = 0
v′ → 12 11 10 9 8
12 11 10 9 8 7
11 10 9 8 7 6 5
9 8 7 6 5 4
7 5 4 3 2
5 4 3 2
4 3 2 1
3 2 1
2 1 0
8 7 6
7 6 5
4 3 2
2 1 0 ← v′
3800 Å
3500
3200
2900
2600
2300 Å

Figure 1

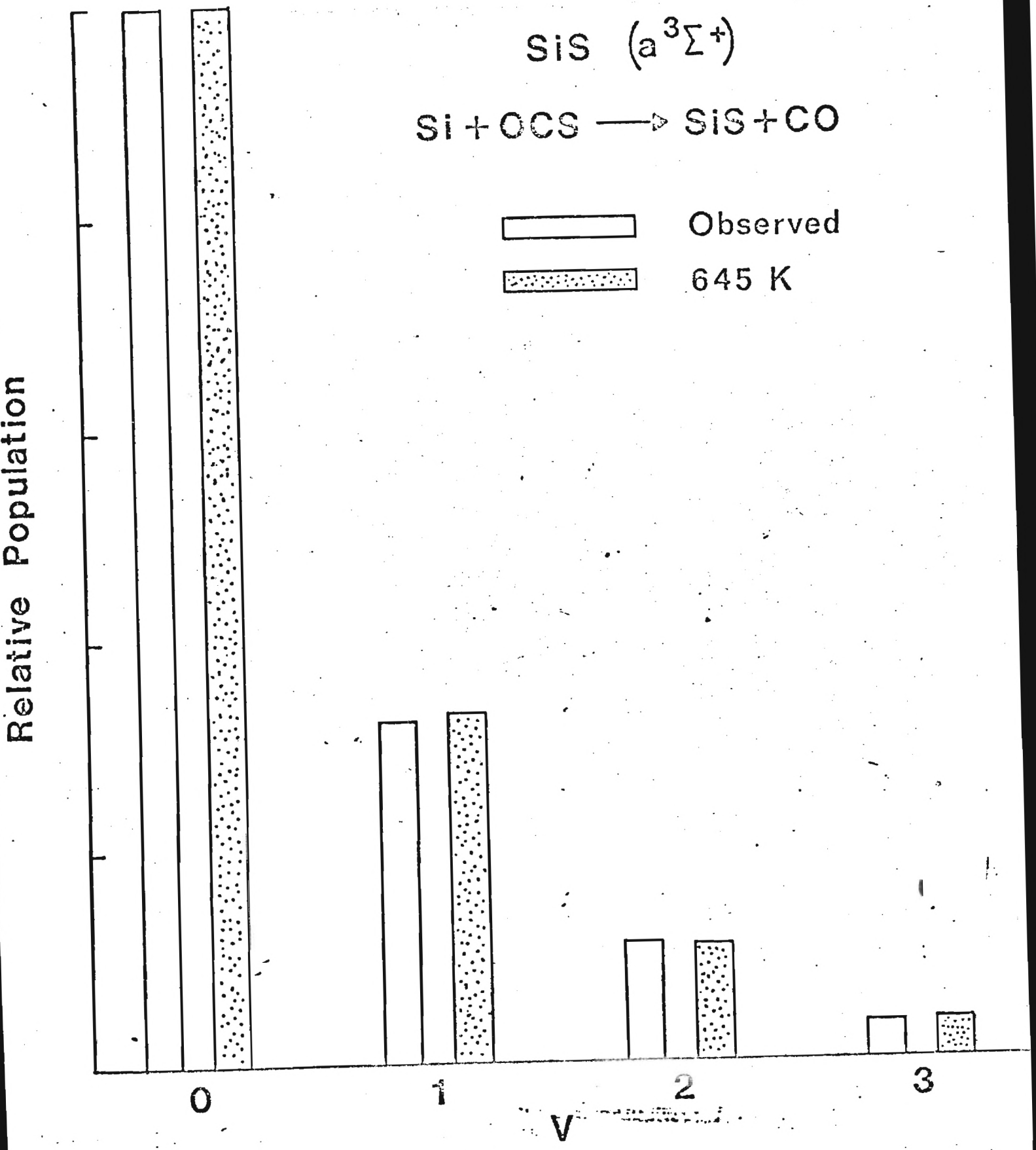
SiS $(a^3\Sigma^+)$
Si + OCS ⟶ SiS + CO
Observed
645 K
Relative Population
0
1
2
3
V

Figure 2

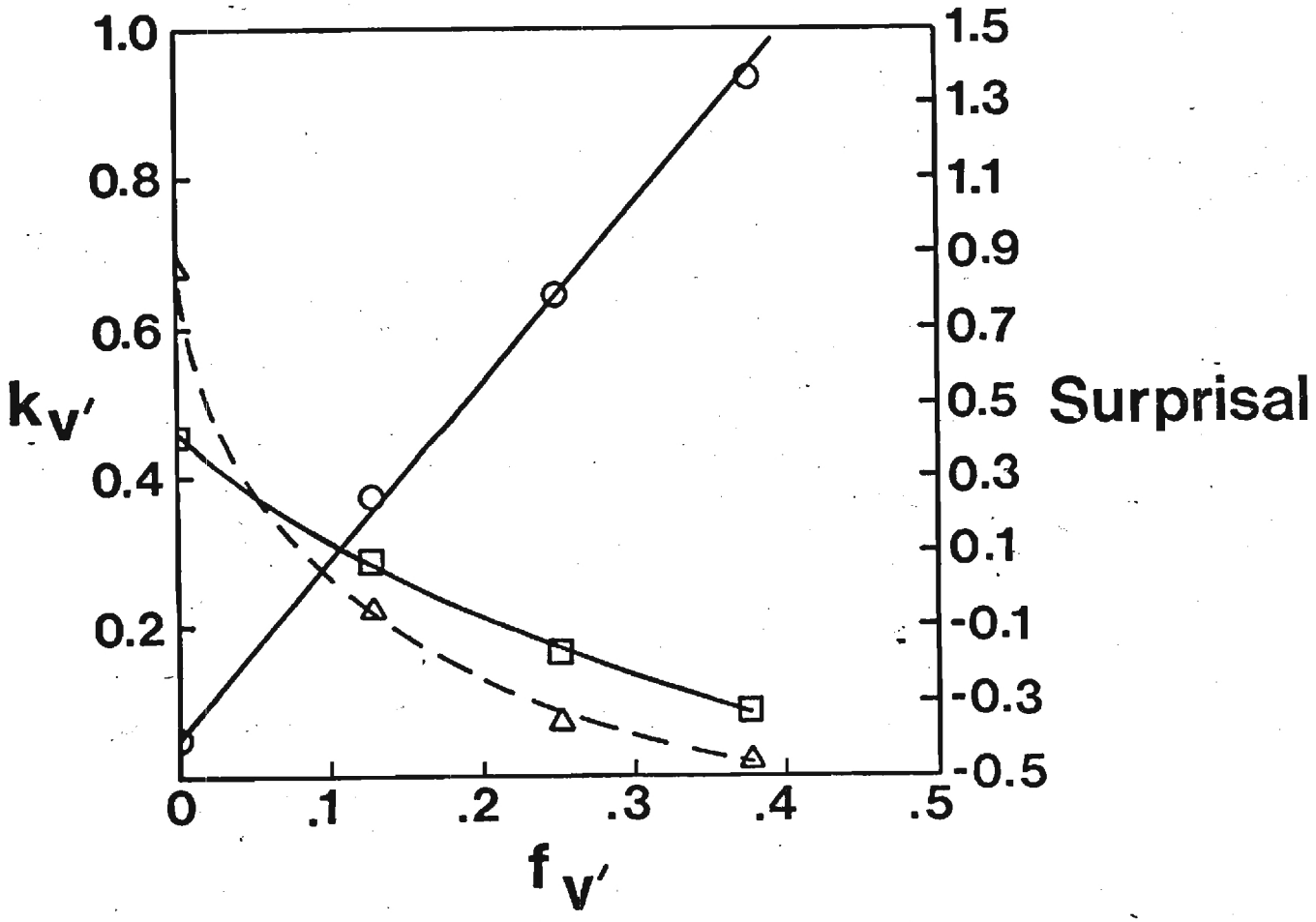
1.0
0.8
0.6
0.4
0.2
$k_{v'}$
0
.1
.2
.3
.4
.5
$f_{v'}$
1.5
1.3
1.1
0.9
0.7
0.5
0.3
0.1
-0.1
-0.3
-0.5
Surprisal

Figure 3

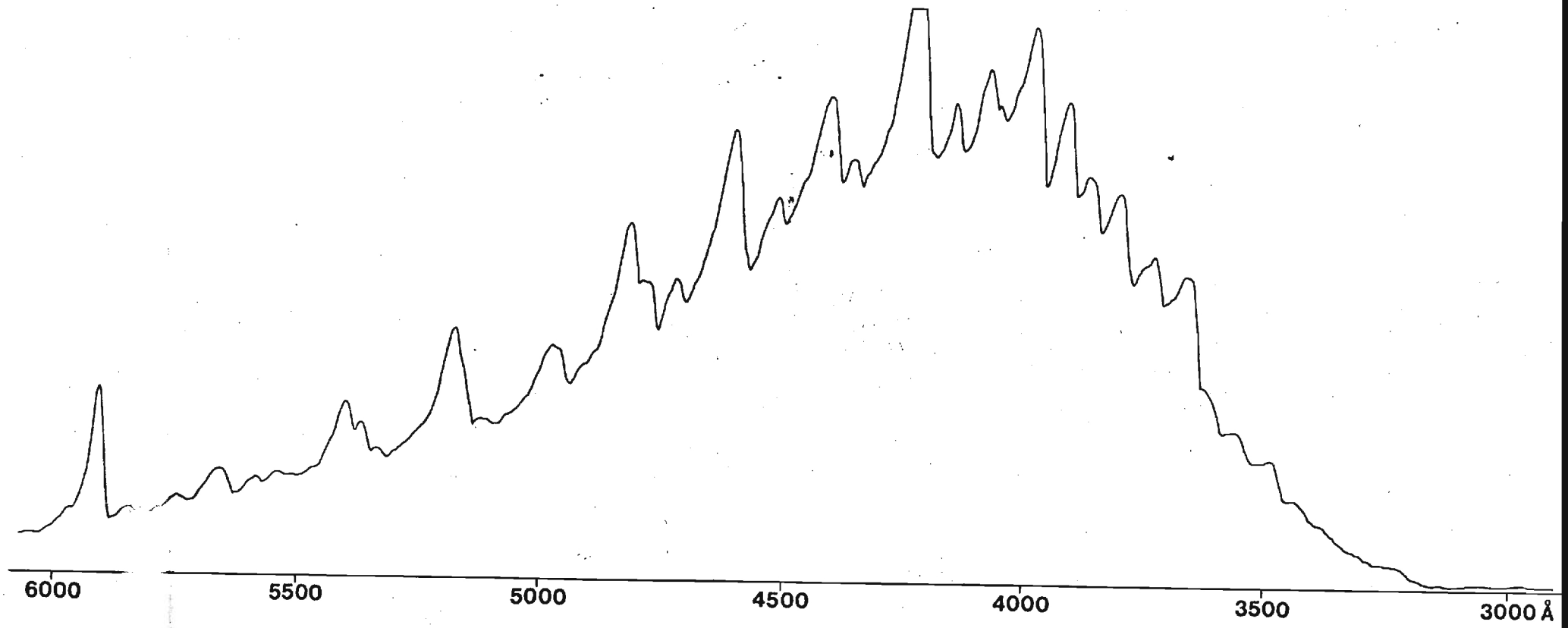

Figure 4

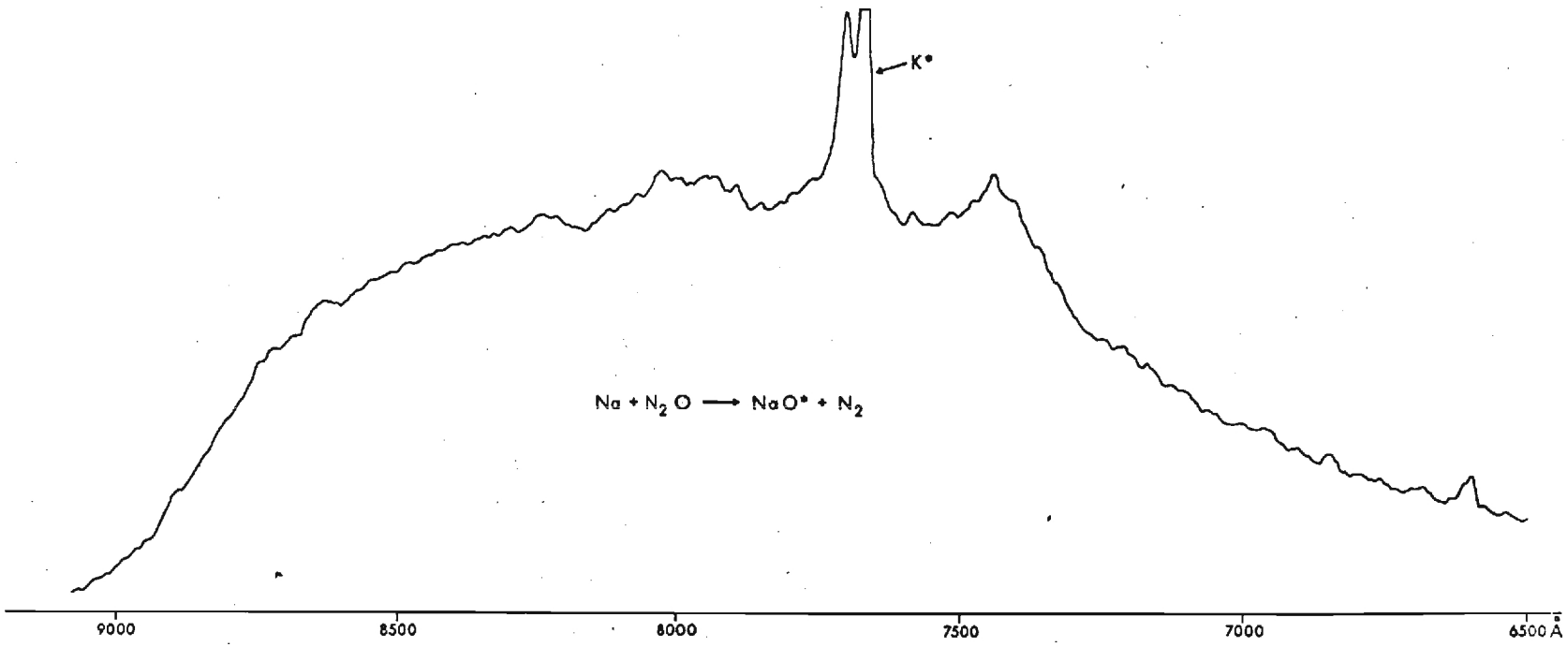

Figure 5

APPENDIX A

EXPERIMENTAL SCHEMES FOR DETECTION OF VIBRATIONALLY EXCITED N_2

APPENDIX A

Several experimental schemes have been developed in an attempt to find direct spectroscopic evidence for formation of vibrationally excited (ground electronic state) N_2 molecules formed as a result of the $Si + N_2O \rightarrow SiO^* + N_2$ reaction. The fundamental idea behind each experimental method is simply stated. The emission observed from vibrationally excited N_2 molecules formed in reaction and subsequently *externally* excited will be substantially different from the emission observed for externally excited N_2 molecules found in an equilibrium, or Boltzmann, distribution at room temperature. This is easily understood if we realize that for a particular ground state vibrational level population, different excited electronic state vibrational levels can be preferentially pumped according to the respective Franck-Condon factors governing the ground state-excited state transition. Emission from an upper electronic state to a lower electronic state is also governed by the respective Franck-Condon factors for the given (v',v'') transitions between these two states; thus, ultimately the emission bands observed will indicate in which initial vibrational levels the N_2 molecules are to be found.

1) MERCURY LAMP STUDIES

This first experimental arrangement employed a 200 W, high pressure mercury lamp (Oriel), whose output was focused through an optical quartz window onto a chemiluminescent flame at right angles to the viewing optics for a spectrometer/detection system. The mercury lamp output was passed through an aperture (slit) to minimize scattered light and to define the

region of the reaction zone which was irradiated. The lamp could be easily used in conjunction with either our single collision or multiple collision apparatuses. For more UV intensity, a deuterium or 1000 W xenon lamp could be substituted. Intense UV radiation was desired in order to gain access primarily to the Vegard-Kaplan ($A^3\Sigma_u^+ - X^1\Sigma_g^+$) system of N_2. Spectral regions in which we expected emission from N_2 have been scanned both in the first and second orders of our grating monochromator. Unfortunately, the intense $b^3\Pi - X^1\Sigma^+$ SiO^* emission also observed (as well as SiO^* $A^1\Pi - X^1\Sigma^+$ emission) has made definitive assignment of any N_2 emission features difficult.

2) ARGON ION LASER STUDIES

As an alternative means of optical excitation, the output from an Argon ion laser (Spectra Physics 171) can be directed and focused into the heart of the reaction zone, again at right angles to the spectrometer/detection system. Typically, 4-5 W continuous wave power at 4880 Å was used for this excitation scheme. Multi-photon absorption by the N_2 formed in the reaction should provide access to the lower-lying electronic states of N_2. The initial spectra taken do show extensive emission from 1600-3500 Å, none of which can as yet be positively assigned to specific N_2 emission bands. It was found, however, that most of the emission persisted even with the oxidant N_2O turned off. Residual gases found in the system (this technique has only been tried under multiple collision conditions, background pressure ~ 40 μ) or impurities in the Ar carrier gas may be the cause of much of the observed emission. Extension to single collision studies should eliminate this problem.

3) ELECTRIC FIELD STUDIES

Electrical excitation of species found in the reaction zone can be achieved through use of a +DC voltage with respect to ground at the reaction zone. To accomplish this, a helical nichrome wire grid was positioned on an annular boron nitride support (for electrical isolation from ground) positioned directly on the cooling jacket of the oven assembly in our multiple collision apparatus. The grid itself was placed directly above the crucible at the point where the oxidant jet array is situated, encircling the chemiluminescent flame region. Applied voltages from +25 to +200 VDC were maintained via a 3 KV/DC high voltage supply (Fluke 415B). Voltages were carefully regulated according to total system pressure (.05-1.0 torr) so as to maintain a stable discharge, yet avoid shorting the grid as a result of space charge accumulation. Observation of N_2 emission from the Second Positive ($C^3\Pi_u - B^3\Pi_g$) system has been made with this arrangement using room temperature N_2 alone, but efforts to make this same observation under the reaction conditions for the $Si + N_2O \rightarrow SiO^* + N_2$ reaction have been hampered due to extensive Ar emission (Ar being the carrier gas) and intense SiO^* emission. Slight modifications in this experimental arrangement may alleviate this problem.

4) ELECTRON BOMBARDMENT STUDIES

The possibility of observing not only N_2 emission, but also N_2^+ emission, was explored by means of electron bombardment ionization/excitation of N_2. An electron gun was constructed to achieve this ionization/-excitation and will be briefly described. The source of thermionically

emitted electrons in the gun is a helical filament of .010" tungsten/2% thorium wire, current to which is supplied through 12 gauge copper buss wires (~5A, 9VAC). The electrons are accelerated through a 1/4" circular aperture by applying +40 to 200 VDC to a thin copper annulus situated ~1" from the filament. The filament and accelerator are surrounded by a 3/4" ID graphite tube in order to prevent blackbody radiation from the filament from reaching the detection system and to spatially contain the emitted electrons for acceleration into the chemiluminescent flame region. The entire electron gun assembly is secured in a vertical position ~1-2" directly above the reaction zone in either our single collision or multiple collision apparatuses. To date, this technique has proven most fruitful in reproducible production of the Second Positive ($C^3\Pi_u - B^3\Pi_g$) system of N_2 over the pressure range 10^{-5}-1 torr. Many emission bands have yet to be identified, however, and may be due to N_2^+ emission. Again, when the N_2 emission detection was carried out during the reaction $Si + N_2O \rightarrow SiO^* + N_2$, the SiO^* emission predominated the spectral regions in which we expected N_2 emission. Further work will be carried out on this system.

It should be apparent that straightforward characterization of vibrationally excited N_2 is hampered by overlap with SiO^* emission in the Si-N_2O system. Therefore, in order to determine the effects which should be observed, we have chosen to look carefully at two other systems, Ti-N_2O and Al-N_2O. Both systems appear to display the characteristics inherent in the rapid stripping of an oxygen atom from N_2O and the subsequent formation of vibrationally excited N_2 as a product. They hold the added advantage that the metal oxide product spectral emission cuts of

at much longer wavelengths 3000 Å for TiO* (see Figure A1) and 7000 Å for weakly emitting AlO*. The results obtained thus far are promising and we expect to obtain more definitive information shortly.

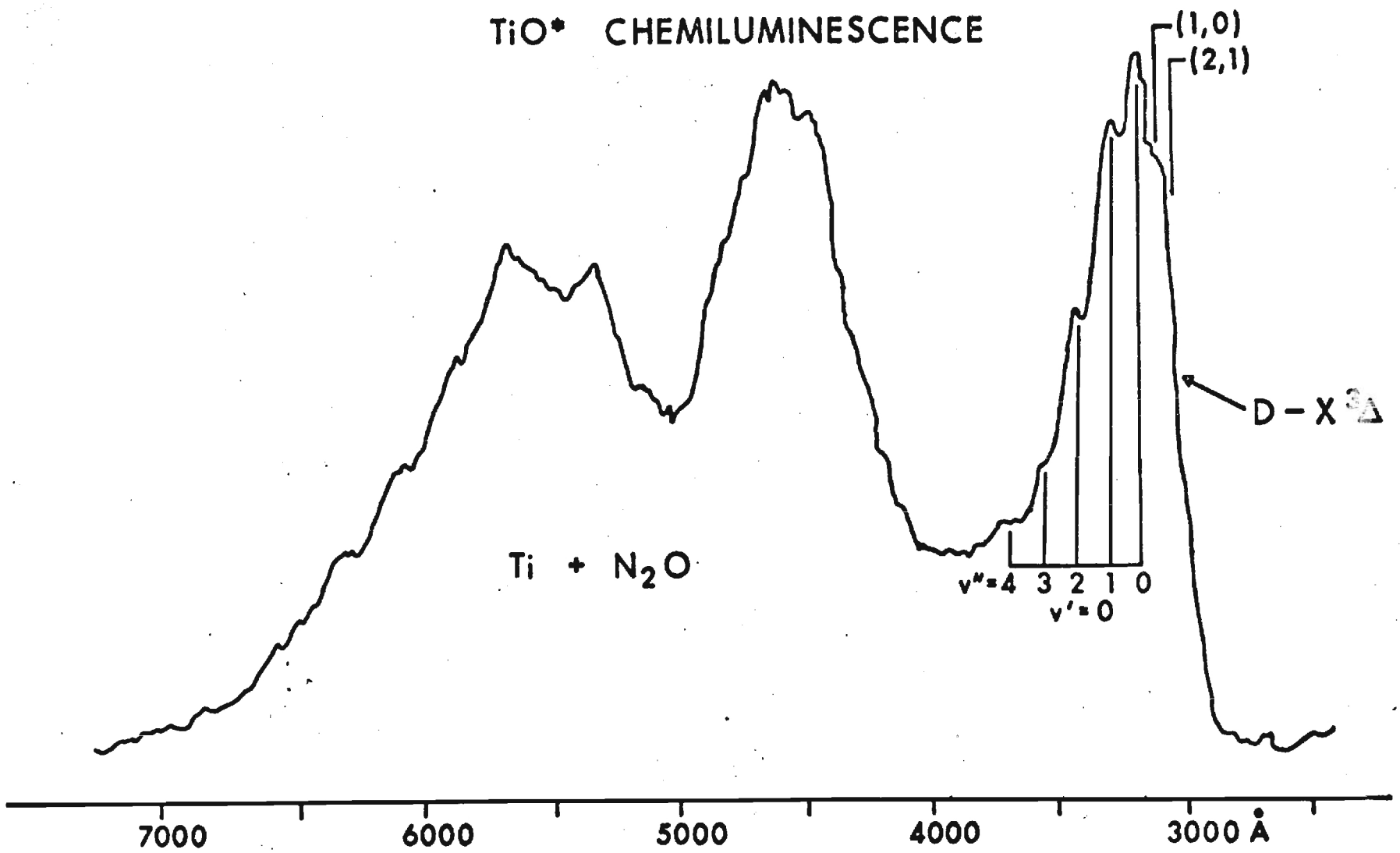
TiO* CHEMILUMINESCENCE
(1,0)
(2,1)
D – X $^3\Delta$
Ti + N_2O
v"=4 3 2 1 0
v'=0
7000
6000
5000
4000
3000 Å

Figure A-1

APPENDIX B

PRIOR RATES FOR FORMATION OF EXCITED ROVIBRONIC STATES

APPENDIX B

Derivations of the expressions from which one may calculate the density of states, and hence the detailed prior relative rate constants for formation of product molecules, have been given by Ben-Shaul, Levine, and Bernstein[1] for the atom-diatom (A+BC → AB+C) interaction. Although the expressions given are for formation of products in the electronic ground state, the consideration of excited electronic species (electronic excitation of a product (metal oxide) molecule is considered here) requires only minor alterations to these expressions. As suggested in Section IV-E, the electronic degeneracies and zero-point to zero-point endoergicities must be incorporated into the appropriate expressions as follows.

The conditional prior relative rate constant for formation of vibrational level v in electronic state n of AB is given by

$$P^{o}(v,n|E) = \rho(v,n,E)/\rho(E) \qquad (B1)$$

where $\rho(v,n,E)$ is the density of states with the product in vibrational state v and electronic state n, at a total (fixed) energy E. $\rho(E)$ is the total density of states. Equation (B1) may be rewritten as

$$P^{o}(v,n|E) = \sum_{J=0}^{J^{*}(v,n)} \rho(v,J,n,E)/\rho(E) \qquad (B2)$$

where $\rho(v,J,n,E)$ is the density of states with rotational quantum number J, and $J^*(v,n)$ is the maximum value of J which is allowed by conservation of energy. $J^*(v,n)$ is given by (vibrating rotor (VR) approximation)[1]

$$B_v J^*(J^*+1) = E-\Delta E_o-E_v \tag{B3}$$

where ΔE_o is the zero-point to zero-point endoergicity for the formation of electronic state n ($D_o^\circ(BC)-D_o^\circ(AB)+T_o(n)$), and E_v is the vibrational energy of the product molecule AB.

$\rho(v,J,n,E)$ is given by

$$\rho(v,J,n,E) = g(n)(2J+1)\rho_T(E_T) \tag{B4}$$

where g(n) is the degeneracy of the electronic state and $\rho_T(E_T)$ is the density of translational states with translational energy

$$E_T = E-\Delta E_o-E_v-E_R \tag{B5}$$

where E_R is the rotational energy of AB. Using the expression for $\rho_T(E_T)$ given by Ben-Shaul et al.,

$$\rho(v,J,n,E) = g(n)(2J+1)A_T(E-\Delta E_o-E_v-E_R)^{1/2} \tag{B6}$$

where

$$A_T = \frac{\mu^{3/2}}{2^{1/2}\pi^2\hbar^3} \tag{B7}$$

and μ is the reduced mass for the relative translational motion. Within each electronic state n,

$$P^{o}(v,n|E) \propto \sum_{J=0}^{J^*(v,n)} \rho(v,J,n,E) \qquad (B8)$$

Substituting eq. (B6) into (B8), assuming J is a continuous variable, and integrating over J,

$$P^{o}(v,n|E) \propto \frac{2g(n)A_T}{3B_{v,n}} (E-\Delta E_o-E_v)^{3/2} \qquad (B9)$$

where $B_{v,n}$ is the rotational constant for vibrational level v in electronic state n of AB. In the rigid-rotor-harmonic-oscillator approximation, $B_{v,n}=B_{e,n}$.

The prior relative rate for formation of electronic state n is given by

$$P^{o}(n|E) \propto \sum_{v=0}^{v^*(n)} P^{o}(v,n|E)$$

where $v^*(n)$ is the highest vibrational state which may be populated in the electronic state n.

For an atom-triatomic reaction, at least two additional degrees of freedom are introduced, and these must be incorporated into the density of states calculations in order to evaluate the prior rates. Since the chemiluminescence experiments described here indicate the formation of only one species

in an excited electronic state, the following derivation assumes that only reactions of the type

$$M+ABO \rightarrow MO+AB$$

occur, in which AB is formed in a manifold of ro-vibrational levels in its ground electronic state. The AB molecule will be treated using the rigid rotor-harmonic oscillator (RRHO) approximation.

The internal energy of the AB molecule

$$\varepsilon = E-\Delta E_o-E_T-E_R(MO)-E_v(MO) \quad . \tag{B11}$$

In a manner analogous to the atom-diatom case,

$$P^o(v,n|E) \propto \sum_{J=0}^{J^*} \rho(v,J,n,E) \quad . \tag{B12}$$

Now, because of the additional degrees of freedom,

$$\rho(v,J,n,E) = \sum_{\varepsilon=0}^{\varepsilon_{max}} \rho(v,J,n,E,\varepsilon) \tag{B13}$$

where ε_{max} is the maximum internal energy which may appear in the AB molecule. From conservation of energy

$$\varepsilon_{max} = E-\Delta E_o-E_v(MO)-E_R(MO) \tag{B14}$$

(i.e., $E_T=0$).

The incorporation of internal energy in the AB molecule into the density of states calculation yields

$$\rho(v,J,n,E,\varepsilon) = (2J+1)\rho_{I(AB)}(\varepsilon)\rho_T(E_T)g(n) \qquad (B15)$$

where $\rho_{I(AB)}(\varepsilon)$ is the density of internal states of the AB molecule with internal energy ε. In the RRHO approximation[1]

$$\rho_{I(AB)}(\varepsilon) = (\hbar\omega_e(AB)B_e(AB)^{-1}\varepsilon = A_I\varepsilon \qquad (B16)$$

where $\omega_e(AB)$ is the vibrational frequency and $B_e(AB)$ is the rotational constant for the ground electronic state of AB. Thus,

$$\rho(v,J,n,E,\varepsilon) = (2J+1)A_I\varepsilon(E-\Delta E_o-E_v(MO)-E_R(MO)-\varepsilon)^{1/2}g(n) \qquad (B17)$$

Replacing the sum in equation (B13) by an integral (i.e. assuming ε is continuous)

$$\rho(v,J,n,E) = \frac{(2J+1)4A_IA_T}{15}(E-\Delta E_o-E_v(MO)-E_R(MO))^{5/2}g(n) \qquad (B18)$$

Thus, from equation (B12),

$$P^o(v,n|E) \propto \sum_{J=0}^{J^*}\rho(v,J,n,E)$$

$$\approx g(n)\int_o^{J^*}\frac{4(2J+1)A_IA_T}{15}(E-\Delta E_o-E_v(MO)-E_R(MO)^{5/2}dJ. \qquad (B19)$$

Since $B_v^*(MO)(J^*(J^*+1)) = E-\Delta E_o-E_v(MO)$,

$$P^o(v,n|E) \propto \frac{g(n)8A_IA_T}{105B_v(MO)} (E-\Delta E_o-E_v(MO))^{7/2} . \qquad (B20)$$

Finally,

$$P^o(n|E) = \sum_{v=0}^{v^*(n)} P^o(v,n|E) .$$

A P P E N D I X C

REPRODUCIBILITY AND CALIBRATION OF

IDARSS TN 1710 SYSTEM

Reproducibility and Calibration of the IDARSS - TN1710 System.

B. Cardelino

October 1980

I. Reproducibility of the EDARSS - TN1710 system.

A. Channel number and wavelength correspondence.

The effect of changing the setup of the wavelength on the spectrometer was followed with the Hg peak at 5460.74 Å. See table 1. The difference of the channel number when the wavelength was setup coming from lower wavelengths or coming from higher wavelengths was found to be around 9 channels. 9 channels correspond to 1.8 Å.

The difference of the channel number on successive settings but always coming from lower wavelength was not higher than 3 channels (.6 Å)

The reproducibility of the channel numbers of 7 peaks of the Ne emission was done with unchanged λ, slit opening, gain, and exposure time. Table 2 shows changes in the channel numbers of 2 at most and unfrequent. When the conditions of gain and exposure time were improved (Tables 3 to 6) no more than a change of one unit was seen. 1 channel corresponds to .2 Å

B. Relative intensities

The uncertainty decreased when the gain and the exposure time were adjusted such that the response would be almost to the saturation limit. (Tables 3 to 6).

When different sets are compared (Table 7)

a) There is no set that seems to be much better

b) The total uncertainty seen was 6% for a relative small peak.

When two sets, ran under the same conditions but in different days, were compared (Tables 3 and 5) we obtained:

76.16	77.6	76.9	2%
12.84	12.0	12.4	7%
23.26	22.0	22.6	6%
95.04	103.0	99.0	8%
221.84	231.9	226.9	4%
207.96	210.3	209.1	6%

Presumably, changes in the settings of the λ, the gain, the exposure time, and other factors, may cause these big uncertainties. Table 9 shows a worse example.

The uncertainties increase with decreasing number of counts. Accordingly, if the number of scans is increased, the uncertainty is improved (in general).

When the spectra may be run at both high gain and exposure time, the uncertainty improves (Table 8).

Rules:

1. Set λ on SPEX and leave it unchanged. Do not turn on and off the spectrometer. Set it from lower wavelengths, slowly.
2. Adjust GAIN and EXPOSURE TIME to get almost saturation
3. Run several spectra.

   Probably: not more than .2Å uncertainties and less than 3% on the intensities.

4. If different sets of GAIN/EXPOSURE TIME values were used and several spectra were recorded, the highest standard deviation we obtained was 3.5%.

II. Calibration of the DARSS-TN1710 system.

A. Wavelengths.

First case $\lambda = 5400$. We selected 7 peaks. Assuming λ is at channel # 550 and that there are .2Å per channel, their wavelengths are estimated. The "American Institute of Physics Handbook" was used to assign the correct wavelength (air).

channel	λ estimated	λ table
67	5496 Å	5494.42 Å
310	5448	5448.51
384	5432	5433.65
545	5401	5400.56
828	5344	5343.28
840	5342	5341.09
894	5331	5330.28

An average value for Å per channel is obtained:

$$\frac{5494.42 - 5330.28}{894 - 67} = .1985 \text{ Å per channel}$$

Location of the λ is estimated: $\frac{.56 \text{ Å}}{.1985 \text{ Å/ch}} = 2.8 \text{ channels}$

$$545 + 3 = \boxed{548}$$

Range seen by DARSS: $67 \times .1985 = 13.30$Å $\quad 5494.42 + 13.30 = \underline{5507.7 \text{ Å}}$

$(1024 - 894) \times .1985 = 25.81$Å $\quad 5330.28 - 25.81 = \underline{5304.5 \text{ Å}}$

Second case $\lambda = 5500$. We selected 5 peaks.

channel	λ estimated	λ table
235	5562	5562.77
567	5496	5494.42
801	5449	5448.51
878	5434	5433.65
956	5418	5418.55

Average Å per channel : $\frac{5418.55 - 5562.77}{956 - 235} = .2000 \text{ Å/channel}$

λ location : $\frac{62 \text{ Å}}{.2 \text{ Å/ch}} = 310$ ch. $\quad 235 + 310 = \boxed{545}$

Range : $235 \times .2 = 47$ Å $\quad 5562.77 + 47 = 5609.77$ Å

$(1024 - 956) \times .2 = 13.6$ Å $\quad 5418.55 - 13.6 = 5404.95$ Å

The data are plotted in FIGURE 1.

The points were fitted into a line by least-square regression with the program shown in FIGURE 2. Results are in FIGURE 3.

Case 1. $.200 \pm .001$ Å per channel

$\lambda_1 = (5509.36 \pm .83) - .20 = 5509.16 \pm .83$

correlation = .9997786

Case 2. $.200 \pm .002$ Å per channel

$\lambda = (5609. \pm 1) - .20 = 5609. \pm 1.$

correlation = .999825

Estimate of the uncertainty using the least-square regression line:

For case 2, slope is $.200 \pm .002$.
The biggest distance we have between two peaks is 166:

$$(\text{peak } 567 - \text{peak } 235)/2 = 166$$

For this situation (supposing we want to know the wavelength corresponding to channel $235+166 = 401$) the uncertainty estimated would be:

$$\left[(567 \pm 1) - 401 \right] (.200 \pm .002) =$$
$$(166 \pm 1)(.200 \pm .002) =$$
$$(166 \pm .6\%)(.200 \pm 1\%) =$$
$$33.2 \pm 1.6\% = 33.2 \pm .5 \text{ Å}$$

Rules:

Choose not less than five known peaks distributed along the 200 Å region seen by the DARSS.
Correlate linearly the channels with the known wavelengths to get the # of Å per channel and its uncertainty.
Calculate the wavelength of any channel using the nearest known peak as a reference.
Considering the uncertainty in the channel of the known peak, the calculated wavelength will have an uncertainty of less than .5 Å.

B. Calibration of DARSS intensities:

Analysis of case 1. $\lambda_{547} = 5400.56$ .28 Å per channel

Peak Channels	λ expected	from Table 10	from Handbook (Figure 6)
29	5504	5508	5507.34
68	5496	5496	5494.41
96	5491	–	–
184	5473	–	–
216	5467	–	–
264	5457	5460	–
295	5451	5454	–
310	5448	–	5448.51
339	5442	5444	–
352	5440	–	–
385	5433	5435	5433.65
447	5420	–	5418.15
547	5400.56	5400	5400.56
682	5374	5374	5372.31
744	5361	–	5360.44
770	5356	–	5355.42
802	5350	–	5349.21
840	5342	5340	5341.09
895	5331	5330	5330.78

Notes: Peak channels from Table 11.

Analysis of case 2 $\lambda_{567} = 5494.42$ .2Å/channel

Peak channel	(table 12) Counts	λ expected	from table 10	Rel Int	from Handbook
32	5222	5601			
44	8299	5599	5600	8	
58	17593	5596	—		
99	8156	5588	5591	4	5589.38
136	3714	5580	5584	1	
184	29282	5571	5574	19	5576.05 ?
235	68833	5561	5564	30	5562.77
254	43071	5557	5560	32	5559.09
347	3968	5538	—		5538.64
358	5694	5536	—		
380	7034	5532	—		5533.68
425	8929	5523	5526	5	—
577	14722	5504	5508	12	5507.34
567	49806	5494.42	5496	47	5494.42
594	5160	5489.	—		—
677	4205	5472	—		—
708	4791	5466	—		—
756	6801	5457	5460	5	—
785	13254	5451	5454	13	—
801	11822	5448	—		5448.51
829	6326	5442	5444	7	—
845	4520	5439	—		—
879	18954	5432	5435	10	5433.65
943	8389	5419			5418.55

Comparison of the common peaks of cases 1 and 2.

	case 1		case 2			
~λ	channel	counts	channel	counts	adjusted	% diff
504	29	1284	517	14722	1669 1351	26.5
494	68	5647	567	49806	5647 4570	(21)
489	96	505	594	5160	585 473	15.7
472	184	329	677	4205	477 386	37 (16)
466	216	356	708	4791	543 440	42 (21)
457	265	593	756	6801	771 624	26.5
451	295	1128	785	13254	1503 1216	29.8
448	310	957	801	11822	1340 1085	33 (13)
442	339	641	829	6326	717 580	11 (10)
439	353	443	845	4520	512 415	14.7
432	385	1739	879	18954	2149 1739	21 -
419	443	970	943	8389	951 770	2 (23)

We will try to improve the comparison by developing a response curve for the DARSS.

DARSS response.

We decided to follow the response of the DARSS by following the number of counts it gives for a given peak, when the peak appears in different channels. We choose Ne emission peak at $\lambda = 5850 Å$.

From setting the spectrometer wavelength from 5745 to 5940Å we would cover the channels from 28 to 990.

We set: slit = 150 μm
gain = 4
ET = .03

and repeated measurements at any given spectrometer setting. The measurements showed a systematic asymptotic growth (Figure 7, A).

The effect of maximizing the exposure time was tried in order to get to the asymptote. This showed no improvement (Figure 7, B).

The effect of maximizing the gain was tried with no success (Figure 7, C).

The effect of subjecting the diode to a relatively long exposure of radiation was tried by scanning for different periods of time prior to the collection of the measurements. Figure 8 shows the curves for three different channels, after scanning previously 0, 2500, and 4096 times. These three values

correspond to 0, 1.25 min, and 2.05 min of exposure of the diodes with radiation.

> Rule:
> Subjecting the DARSS to radiation exposure prior to the collection of the measurements improves considerably the reproducibility on the intensities to less than 1.6% uncertainty.

A response curve was then done choosing a set of gain and exposure time exactly below saturation for the whole range of wavelengths.

GAIN = 4.
ET = .03026
SLIT = 150 μm
SCANNING = 20
PREVIOUS SCANNING = BETWEEN 2500 to 12300
or 1.25 min to 6.20 min.

Table 13 shows the values obtained. The standard deviation was calculated after reaching the asymptote.
A plot for the percent response is shown in Figure 9.

The biggest standard deviation we registered was 1.6%.

The response curve was not satisfactory, so two changes were tried.

1) Cooling system to the DARSS
2) Change of the setting of the DARSS focus.

1) The effect of changes of temperature on the DARSS were followed with the background radiation at a given channel.
After a long period in which the diode was radiated with the Ne lamp, the lamp was turned off.
With: λ at 5292.5
Gain = 3
ET = .55
Slit = 246 μm
Scans = 16

The following numbers were obtained:

→ 2787 2756 2748 2751 2748 2751 2745
2747 2745 2747 2747 2748 2746 2748
2751 2752 2753 2751 2756 2751 2752

showing first a decrease on the counts and then a stabilization around 2752.

Then the DARSS was covered (for any light leak) and we obtained:

→ 2750 2752 2758 2754 2755 2759 2763
2765 2767 2768 2765 2780

Showing the effect of warm up.

The flow of water was increased and the background value dropped steadily to around 1200.

2) Peak 5400 Å was set on channel 550. Then the focus adjustment was turned CCW until there was no response. The focus setting was then turned clockwise until a maximum response was obtained. That occurred when λ spex (5400.96) was at channel 551.

With the new adjustment another response curve was obtained. Table 14 contains the data. Figure 10 shows both calibration curves. The second one was followed with peak at 5400.96 Å. Points obtained following peaks at 5330.78 and 5341.09 are shown on the curve.

When the width of the 5400 peak was compared with the two different focus adjustments, we obtained

a) old adjustment: 96 channels to go from 293 to 295 relative intensities.
Slit = 200 μm

b) new adjustment: 56 channels to go from 289 to 295 relative intensities
Slit = 246 μm

Rule:
Focus adjustment should be done to maximize the response.
A calibration curve for the intensities should be done after the adjustment.
The adjustment:
1) makes the response curve more linear
2) improves the resolution

Using the calibration curve obtained after the DARSS focus adjustment, several peaks were followed. The standard deviation on their corrected intensities came out less than 4%. (Table 15). The % response for any given channel was obtained by interpolation using the program shown on Figure 4. Figure 5 has the input and output to the program.

Rule: The response is substantially affected by changes on the DARSS temperature.

Rule: the calibration curve is dependent on the energy region seen.

TABLE 1

LAMP = Hg λ = 5460 Å ET = .67 SLIT = 50 μm

SCANS = 1

PEAK FOLLOWED: 5460.74 Å

λ setup coming from higher wavelengths:		λ setup coming from lower wavelengths:	
gain = 1.	channel # = 555	gain = 1.	channel # = 545
2.	555	2.	546
3.	556	3.	548
1.	556	1.	547
3.	554	2.	547
		1.	546
		3.	548
		1.	545

TABLE 2

LAMP = Ne λ from lower wavelengths = 5400 Å slit = 200 μm

GAIN = 4.00 ET = .81 (under saturation)

SCANS = 40 BACKGROUND SUBSTRACTION = 39

DARSS λ REGION = 5500 - 5300 Å

channel	counts	relative	channel	counts	relative	channel	counts	relative		
68	4443	78.7	68	4461	79.9	68	4349	78.3		
311	779	13.8	309*	840	15.0	310*	833	15.0		
385	1342	23.8	385	1410	25.3	385	1390	25.0		
546	112972	2000.0	546	111681	2000.0	546	111042	2000.0		
829	5492	97.2	829	5473	98.0	829	5474	98.6		
840	12612	223.3	840	12547	224.7	840	12357	222.6		
894	11668	206.6	894	11427	204.6	894	11290	203.3		
68	4387	79.0	68	4321	78.9		78.96	Maxim Uncert.		2.03 %
310	846	15.2	310	836	15.3		14.86			10.09 %
385	1382	24.9	385	1381	25.2		24.84			6.04 %
546	111050	2000.0	546	109583	2000.0		97.62			2.15 %
829	5360	96.5	829	5356	97.8		222.50			1.80 %
840	12281	221.2	840	12091	220.7					
895*	11334	204.1	895	11151	203.5		204.42			1.61 %

TABLE 3

LAMP = Ne λ from lower wavelengths = 5400 Å slit = 200 μm

GAIN = 4.00 ET = 1.13 (almost to saturation)

SCANS = 40 BACKGROUND SUBSTRACTION = 4/0

DARSS λ REGION = 5500 – 5300 Å

68	6044	79.6	68	5545	75.9	68	5675	77.1
310	1223	16.1	311	949	13.0	311	922	12.5
385	1979	26.1	385	1705	23.3	385	1701	23.1
546	151840	2000.0	547	146046	2000.0	546*	147265	2000.0
829	7479	98.5	829	6924	94.8	829	7011	95.2
840	17116	225.4	840	16185	221.6	840	16390	222.6
895	15919	209.7	895	15189	208.0	895	15295	207.7
68	5647	76.4	68	5606	76.3	68	5471	75.1
310*	957	13.0	311*	947	12.9	310	931	12.8
385	1738	23.5	386*	1707	23.2	386	1689	23.2
547*	147195	2000.0	547	147027	2000.0	547	145716	2000.0
829	7042	95.3	829	6981	95.0	829	6915	94.9
840	16472	222.9	840	16285	221.5	840	16073	220.6
895	15478	209.5	895	15272	207.7	895	15076	206.9

76.16	2.6 %
12.84	3.9 %
23.26	1.7 %
–	–
95.04	.5 %
221.84	1.0 %
207.96	1.3 %

TABLE 4

LAMP = Ne λ from lower wavelengths = 5400 Å slit = 200 μm

GAIN = 7.00 ET = .65 (almost to saturation)

SANS = 40 BACKGROUND SUBSTRACTION = 40

DARES λ REGION = 5500 - 5300 Å

68	5922	77.0
311	1004	13.1
385	1796	23.4
546	153789	2000.0
829	7585	98.6
840	17751	230.8
895	16715	217.4

68	5823	76.1
311	967	12.6
385	1756	23.0
547	152993	2000.0
829	7527	98.4
840	17552	229.4
895	16547	216.3

68	5886	76.7
310	973	12.7
385	1782	23.2
547	153911	2000.0
829	7527	98.1
840	17523	228.4
895	16441	214.3

68	5839	75.9
311	992	12.9
385	1763	22.9
546	153831	2000.0
829	7554	98.2
840	17717	230.3
895	16473	214.2

68	5866	76.3
311	993	12.9
385	1766	23.0
547	153716	2000.0
829	7430	96.7
840	17542	228.2
895	16454	214.1

68	5876	76.1
311	979	12.7
386	1792	23.2
547	154432	2000.0
829	7593	98.3
840	17715	229.4
895	16610	215.1

	76.35	1.4%		
	12.82	3.9%		
	23.12	2.2%	229.42	1.1%
	98.05	1.9%	215.23	1.5%

TABLE 5

LAMP = Ne λ from lower wavelengths = 5700 Å slit = 200 μm

GAIN = 4.00 ET = 1.13 (almost to saturation)

SCANS = 40 BACKGROUND SUBSTRACTION = 40

DARSS λ REGION = 5500 - 5300 Å°

67	6000	77.2	67	5949	77.3	67	5985	77.1
309	879	11.3	310	931	12.1	309	936	12.1
384	1714	22.0	385	1656	21.5	384	1733	22.3
545	155465	2000.0	545	153927	2000.0	545	155291	2000.0
828	8002	102.9	828	7917	102.8	828	8046	103.6
840	17855	231.0	840	17949	233.2	840	18044	232.4
893	16312	209.8	893	16253	211.2	893	16380	211.0
67	6032	78.0	67	6042	78.4		77.6	1.0%
309	943	12.2	309	936	12.1		12.0	6.7%
384	1695	21.9	384	1737	22.5		22.0	4.5%
545	154591	2000.0	545	154114	2000		-	
828	7912	102.4	828	7944	103.1		103.0	1.2%
840	17827	230.6	840	17885	232.1		231.9	1.1%
893	16187	209.4	893	16186	210.1		210.3	.9%

TABLE 6

LAMP = Ne λ from lower wavelengths = 5400 Å slit = 200 μm

GAIN = 9.50 ET = 0.41 (almost to saturation)

SCANS = 40 BACKGROUND SUBSTRACTION = 40

67	5024	76.0	67	4964	74.9	68	4742	73.1
310	836	12.7	310	825	12.5	308	812	12.5
384	1505	22.8	384	1477	22.3	384	1444	22.3
545	132168	2000.	545	132486	2000.	545	129128	2000.
828	6949	105.2	828	6746	101.8	828	6576	101.4
840	15605	236.1	840	15416	232.7	840	15265	235.3
893	14137	213.9	894	14069	212.4	894	13910	214.4
67	4809	74.3	67	4877	74.7	74.6	4%	
310	826	12.8	310	851	13.0	12.7	4%	
384	1479	22.9	384	1472	22.5	22.6	2.7%	
546	129424	2000.	546	130641	2000.	-		
829	6489	100.3	829	6625	101.4	102.0	5%	
840	15056	232.7	840	14799	226.6	232.7	4.0%	
894	13736	212.3	894	14037	214.9	213.6	1.2%	

TABLE 7

Comparison of Tables 4, 5, and 6.

GAIN 4 ET 1.13			GAIN 7 ET .65			GAIN 9 ET .41		
67	77.6	1%	68	76.4	1%	67	74.6	4%
309	12.0	7%	311	12.8	4%	310	12.7	4%
384	22.0	5%	385	23.1	2%	384	22.6	3%
545	2000.		546	2000.		545	2000.	
828	103.0	1%	829	98.1	2%	828	102.0	5%
840	231.9	1%	840	229.4	1%	840	232.7	4%
893	210.3	1%	895	215.2	2%	894	213.6	1%

67	76.2	max. unc.	4%
310	12.5		6%
384	22.6		5%
545	2000.		–
828	101.0		5%
840	231.3		1%
894	213.0		2%

standard deviation for 310: $12.5 \pm .4$ so $12.5 \pm 3.5\%$.

TABLE 8

LAMP = Ne λ from lowest wavelengths = 5500 Å slit = 200 μm

GAIN = 9.50 ET = 10.01

SCANS = 40/40 in first two runs 20/20 in third.

	40/40		40/40		20/20	
58	17593	127.8	17794	129.3	8903	129.6
99	8156	59.2	8289	60.2	4094	59.6
184	29282	212.7	29289	212.8	14681	213.8
235	68833	500.	68810	500.	34340	500.
254	43071	312.9	43215	314.0	21423	311.9
425	8929	64.9	8832	64.2	4422	64.4
517	14722	106.9	14705	106.9	7382	107.5
567	49806	361.8	50076	363.9	24935	363.1
785	13254	96.2	13254	96.3	6624	96.4
801	11822	85.9	11821	85.9	5932	86.4
878	18954	137.7	19038	138.3	9451	137.6
943	8389	60.9	8368	60.8	4213	61.3

58	128.9	.4%
99	59.7	2%
184	213.1	1%
235	500.	—
254	312.9	1%
425	64.5	1%

517	107.1	1%
567	362.9	1%
785	96.3	.2%
801	86.1	1%
878	137.9	.4%
943	61.0	1%

TABLE 9

LAMP - Ne λ from lower wavelength = 5500Å slit = 200 μm

GAIN = 7.00 ET = 14.01 20/20 SCANS

58	8600	126.6	8565	126.7	9232	116.3	8729	114.8
99	4038	59.4	4019	59.4	3511	44.2	3756	49.4
84	14640	215.5	14462	213.9	16343	205.9	15983	210.2
235	33975	500.	33811	500.	39683	500.	38012	500.
354	21358	314.3	21139	312.6	24504	308.7	23469	308.7
25	4377	64.4	4377	64.7	4062	51.2	4269	56.2
77	7332	107.9	7334	108.5	7576	95.4	7564	99.5
67	24947	367.1	24665	364.7	28586	360.1	27531	362.1
95	6501	95.7	6428	95.1	6601	83.2	6514	85.7
91	5817	85.6	5764	85.2	5785	72.9	5911	77.8
78	9347	137.6	9314	137.7	9873	125.6	9871	129.8
43	4113	60.5	4140	61.2	3704	46.6	3864	50.8

← different days →

126.7	1%			115.6	1%		
59.4	0%			46.8	11%		
214.7	1%			208.1	2%		
313.5	1%			308.7	0%		
64.5	1%			53.7	9%		
98.2	1%			97.5	4%		
66.9	1%			361.1	.3%		
95.4	1%	137.7	.1%	84.5	3%	127.7	3%
85.4	1%	60.9	1%	75.4	7%	48.7	9%

TABLE 19. Data from Photo tube 4840

λ	Rel. Int.	λ	Rel. Int.	λ	Rel. Int.	λ	Rel. Int.
3914 Å	256	4715 Å	85	5299 Å	13	5820 Å	201
3948	1521	4753	109	5330	170	5850	50000
4044	1743	4770	89	5340	180	5872	63
4057	95	4790	6	5374	11	5882	3361
4159	1121	4837	15	5400	1094	5904	122
4180	1547	4867	5	5435	10	5908	76
4192	2026	4877	15	5444	7	5915	34
4201	1776	4889	20	5454	13	5944	5705
4250	203	4896	6	5460	5	5965	57
4260	3168	4958	18	5486	47	5975	1577
4267	258	4992	5	5508	12	5989	37
4272	402	5007	5	5526	5	6030	1584
4300	368	5030	17	5560	32	6074	3987
4334	3047	5038	63	5564	30	6086	5773
4346	1980	5050	5	5574	19	6130	235
4426	46	5060	18	~~5584~~	1	6143	7135
5012	210	5075	12	5591	4	6164	3025
5019	149	5082	37	5600	8	6217	2156
5025	152	5088	5	5610	18	6266	5172
5039	65	5118	73	5652	13	6302	1830
5056	32	5144	24	5657	46	6334	3615
5087	56	5152	27	5662	13	6380	5503
5097	49	5162	31	5683	6	6402	6043
4630	45	5190	61	5690	30	6506	4088
4659	37	5205	21	5720	24	6540	2297
4705	262	5211	15	5740	15	6600	3377
4710	207	5223	45	5748	85		
		5254	20	5764	374		
				5800	62		

TABLE II

GAIN = 1/100

ST = 1.13

TOTAL SCANS = 80

SPEX λ = 5400

SLIT = 200 μm

&f_L	0 12141		120 30067		2	0		
0.0	39	48	30	45	43	58	55	55
8.0	46	44	55	63	68	89	97	107
16.0	127	130	154	179	185	226	244	279
24.0	380	503	705	964	1189	1284	1200	985
32.0	776	631	537	478	416	379	345	330
40.0	345	330	324	330	368	376	368	376
48.0	403	407	418	435	471	507	508	571
56.0	623	685	762	848	972	1152	1476	2002
64.0	2820	3871	4812	5438	5647	5574	5209	4489
72.0	3539	2638	2032	1635	1439	1241	1066	906
80.0	792	708	636	617	604	585	561	537
88.0	505	455	426	428	447	470	487	496
96.0	505	476	466	437	374	348	317	305
104.0	290	301	272	292	258	263	260	269
112.0	267	270	259	243	250	236	193	200
120.0	162	173	172	165	156	154	161	170
128.0	168	184	194	199	197	175	180	172
136.0	156	159	149	145	162	134	141	146
144.0	143	129	126	126	144	130	136	126
152.0	135	122	122	121	135	119	142	121
160.0	128	126	135	141	135	125	142	136
168.0	154	132	147	132	142	136	141	164
176.0	180	187	222	268	296	304	323	322
184.0	329	286	253	211	214	169	184	168
192.0	154	158	156	146	167	161	170	169
200.0	177	186	196	179	183	190	178	185
208.0	200	208	215	265	285	318	324	349
216.0	356	335	307	301	275	245	208	215
224.0	202	163	173	174	202	160	193	203
232.0	224	174	183	173	163	183	200	206
240.0	204	174	210	186	172	187	206	206
248.0	193	242	252	247	229	244	297	283
256.0	286	326	313	322	355	407	479	535
264.0	575	593	591	541	487	429	390	343
272.0	314	299	259	260	295	294	265	260
280.0	306	282	262	284	299	309	304	338
288.0	370	445	528	713	918	1077	1128	1128
296.0	1086	980	832	655	513	446	384	365
304.0	410	440	507	648	819	906	957	951
312.0	938	877	770	624	464	392	333	330

320.0	309	302	314	297	275	277	297	289
328.0	285	288	302	317	333	392	472	554
336.0	614	629	637	641	634	584	513	442
344.0	411	380	357	331	332	320	366	400
352.0	442	433	429	421	388	343	314	266
360.0	262	248	235	234	235	239	234	243
368.0	272	255	272	293	303	312	333	345
376.0	365	364	403	474	606	862	1247	1564
384.0	1719	1739	1705	1601	1353	997	660	535
392.0	438	395	350	333	318	309	301	293
400.0	314	308	311	321	309	294	269	259
408.0	239	232	207	233	213	226	238	238
416.0	252	250	249	245	258	276	279	248
424.0	237	238	265	243	246	245	273	270
432.0	278	274	267	313	292	332	355	371
440.0	416	517	694	856	932	961	970	942
448.0	906	777	635	521	475	457	446	461
456.0	487	491	527	529	516	502	472	419
464.0	372	341	350	344	319	335	342	338
472.0	342	338	364	362	362	366	391	379
480.0	390	400	422	479	530	597	651	674
488.0	690	695	723	713	698	737	820	925
496.0	1045	1107	1193	1246	1292	1338	1307	1302
504.0	1296	1367	1419	1465	1539	1616	1683	1771
512.0	1891	1997	2117	2250	2368	2511	2717	2910
520.0	3125	3334	3588	3861	4203	4562	4970	5460
528.0	5987	6549	7217	7982	8892	9845	10974	12338
536.0	13886	15723	18216	21442	26652	37523	61254	97502
544.0	128170	143156	147790	147795	140706	119991	84606	51294
552.0	32456	23953	19656	16824	14603	12817	11312	10027
560.0	8979	8021	7234	6563	5935	5394	4918	4495
568.0	4115	3780	3469	3187	2950	2700	2560	2391
576.0	2269	2136	2045	1908	1779	1672	1587	1494
584.0	1378	1314	1231	1126	1069	1030	969	933
592.0	857	805	773	710	656	601	551	522
600.0	473	448	441	438	399	398	421	423
608.0	415	419	413	426	389	383	362	333
616.0	314	289	275	260	257	250	267	263
624.0	271	234	273	293	298	300	277	286
632.0	274	251	253	216	208	189	188	203
640.0	194	204	203	191	181	181	181	169
648.0	173	184	193	204	196	192	203	186
656.0	193	201	195	197	197	188	204	223
664.0	233	243	302	357	446	465	490	488
672.0	503	510	503	527	559	582	594	645
680.0	771	882	928	891	864	789	722	619
688.0	474	383	317	300	289	280	287	274
696.0	234	245	221	218	223	214	205	182
704.0	196	170	159	190	200	210	205	229
712.0	231	241	234	240	239	225	203	197
720.0	177	183	191	199	195	204	213	215

728.0	223	256	276	276	281	287	299	310
736.0	323	330	341	385	511	688	912	1071
744.0	1168	1155	1093	1004	845	648	456	338
752.0	310	311	294	297	303	305	313	305
760.0	286	272	314	352	438	487	481	541
768.0	569	594	605	556	518	447	352	306
776.0	307	280	266	270	272	271	260	255
784.0	253	263	262	275	322	326	310	345
792.0	386	387	397	486	593	698	757	776
800.0	795	804	765	720	641	593	601	609
808.0	607	632	655	691	741	755	823	877
816.0	959	1051	1152	1286	1413	1527	1635	1832
824.0	2168	2930	4231	5683	6738	7042	6935	6773
832.0	6913	6776	6462	6101	6709	8830	12116	14936
840.0	16472	16185	15249	14621	13807	10797	7260	4802
848.0	3504	2755	2294	2017	1797	1625	1483	1367
856.0	1279	1201	1129	1078	1024	973	918	883
864.0	852	835	824	835	840	835	833	853
872.0	875	898	887	941	965	1036	1125	1210
880.0	1282	1380	1506	1625	1770	1933	2179	2497
888.0	3052	4189	6211	9180	12192	14228	15277	15478
896.0	14870	13360	10886	7774	5176	3595	2714	2199
904.0	1866	1644	1490	1341	1200	1087	1055	1016
912.0	1052	1132	1276	1395	1388	1289	1274	1239
920.0	1172	987	818	657	569	459	449	420
928.0	406	355	343	311	330	283	283	273
936.0	269	247	232	243	224	215	221	205
944.0	189	207	188	190	159	178	178	173
952.0	190	170	159	171	196	201	220	241
960.0	233	272	287	295	286	284	261	248
968.0	225	210	216	208	204	209	212	224
976.0	228	225	231	217	214	188	166	158
984.0	162	157	158	156	154	140	144	174
992.0	178	168	150	150	170	166	181	185
1000.0	174	202	192	188	162	174	171	147
1008.0	149	170	172	178	169	169	191	202
1016.0	218	238	301	380	453	1048	569	3	0

TABLE 12

SAX λ = 5300

GAIN = 9.5

SCANS #= 80 ET= 10.01026

0	12142	120	50004	2	0			
0.0	222	215	213	214	226	229	241	228
8.0	235	251	301	349	466	573	651	701
16.0	735	829	929	999	1109	1172	1324	1498
24.0	1779	2150	2735	3463	4191	4769	5120	5249
32.0	5222	5049	4868	4761	4782	4866	5168	5668
40.0	6365	7052	7741	8157	8299	8015	7573	7042
48.0	6650	6443	6603	7080	7882	9247	11408	13952
56.0	16213	17473	17593	16952	15220	12636	9667	7320
64.0	5789	4874	4270	3890	3535	3303	3124	2981
72.0	2855	2738	2669	2615	2547	2537	2457	2499
80.0	2425	2446	2367	2375	2362	2444	2452	2469
88.0	2521	2608	2715	2943	3238	3772	4381	5256
96.0	6327	7362	7978	8156	7914	7422	6644	5673
104.0	4546	3597	2947	2638	2457	2340	2252	2148
112.0	2101	2051	2003	1988	1940	1955	1916	1895
120.0	1868	1903	1925	1906	1913	1932	1954	1988
128.0	2045	2170	2422	2790	3176	3479	3633	3713
136.0	3714	3592	3320	2932	2605	2374	2208	2103
144.0	2041	2029	2004	1969	1949	1945	1930	1938
152.0	1959	1987	2011	2029	2081	2165	2240	2339
160.0	2472	2647	2887	3096	3306	3431	3563	3658
168.0	3751	3798	3919	4099	4313	4603	5034	5532
176.0	6263	7383	9438	13205	18603	23965	27431	28896
184.0	29282	28459	26487	22404	17001	12076	9093	7562
192.0	6903	6512	6318	6162	6024	5917	5827	5671
200.0	5520	5428	5305	5161	5005	4881	4790	4769
208.0	4764	4749	4765	4821	4920	5032	5222	5425
216.0	5676	5959	6320	6712	7152	7659	8271	8956
224.0	9817	10783	12034	13730	16503	21521	30670	43822
232.0	56364	64333	68193	66833	66912	61074	50397	36857
240.0	26124	19688	16541	15052	14531	14684	15671	17635
248.0	20147	22417	24697	28385	34193	40085	43071	42687
256.0	41034	38865	35687	30422	22902	16196	12120	9997
264.0	8760	7896	7174	6595	6138	5798	5511	5220
272.0	5002	4841	4744	4644	4523	4416	4349	4327
280.0	4214	4167	4211	4359	4413	4340	4168	3983
288.0	3816	3620	3316	3042	2812	2626	2543	2489
296.0	2401	2337	2217	2127	2051	2042	2064	2100
304.0	2098	2082	2021	1990	1939	1948	1938	1946

312.0	1965	1990	1994	1989	1936	1923	1934	1943
320.0	1955	1942	1971	1998	1987	1944	1938	2008
328.0	2055	2058	2057	2085	2116	2146	2134	2181
336.0	2216	2245	2275	2385	2514	2741	3073	3485
344.0	3725	3864	3948	3969	3859	3640	3334	3179
352.0	3242	3665	4407	5158	5531	5701	5694	5586
360.0	5191	4475	3646	3159	2913	2849	2823	2845
368.0	2872	2927	3084	3211	3305	3551	3989	4607
376.0	5163	5597	6042	6625	7034	6937	6442	5869
384.0	5412	4857	4098	3432	2962	2769	2661	2649
392.0	2610	2573	2547	2498	2452	2459	2478	2557
400.0	2661	2815	3096	3429	3635	3736	3701	3656
408.0	3499	3266	2987	2824	2785	2824	2878	2937
416.0	2999	3119	3266	3527	4061	5237	6807	8058
424.0	8680	8929	8840	8508	7552	6073	4668	3840
432.0	3422	3211	3061	2954	2804	2692	2587	2549
440.0	2494	2514	2519	2538	2571	2538	2495	2495
448.0	2480	2443	2400	2391	2356	2366	2368	2404
456.0	2400	2330	2314	2285	2273	2227	2148	2111
464.0	2087	2100	2117	2152	2157	2147	2123	2093
472.0	2051	2052	2035	2023	2026	2032	1996	1976
480.0	1958	1981	1979	2035	2111	2211	2288	2377
488.0	2472	2584	2681	2743	2769	2764	2757	2734
496.0	2733	2729	2755	2827	2854	2970	3044	3160
504.0	3266	3407	3601	3866	4161	4473	4835	5359
512.0	6417	8496	11295	13547	14477	14722	14602	13979
520.0	12228	9469	7074	5645	4914	4526	4224	4044
528.0	3884	3736	3592	3458	3293	3150	3102	3073
536.0	3014	3074	3159	3245	3255	3365	3485	3610
544.0	3708	3827	3919	4049	4178	4323	4440	4620
552.0	4884	5194	5526	5957	6379	7034	7779	8811
560.0	10249	12931	18439	28196	38995	46176	49175	49806
568.0	48556	44809	37032	27266	19899	16004	14035	12782
576.0	11520	9938	8269	7166	6541	6200	5992	5836
584.0	5625	5389	5202	5005	4783	4568	4501	4710
592.0	4993	5142	5160	5120	5035	4860	4503	4027
600.0	3629	3379	3236	3219	3189	3168	3140	3179
608.0	3257	3356	3352	3310	3208	3102	2940	2757
616.0	2498	2318	2234	2183	2095	2042	2051	2079
624.0	2138	2255	2304	2342	2330	2335	2285	2158
632.0	2016	1948	1894	1855	1817	1769	1719	1753
640.0	1730	1720	1721	1730	1710	1681	1646	1675
648.0	1703	1645	1606	1598	1616	1654	1642	1673
656.0	1724	1751	1715	1774	1844	1863	1860	1819
664.0	1837	1896	1879	1885	1928	2000	2091	2342
672.0	2771	3360	3801	4085	4152	4205	4051	3689
680.0	3148	2688	2431	2326	2271	2205	2167	2162
688.0	2143	2100	2102	2183	2257	2371	2431	2516
696.0	2567	2608	2586	2606	2660	2781	3005	3400
704.0	3865	4290	4508	4660	4791	4751	4499	4065
712.0	3638	3341	3140	2901	2758	2710	2742	2805

720.0	2750	2537	2408	2132	2301	2367	2548	2499
728.0	2323	2261	2268	2251	2261	2290	2257	2230
736.0	2250	2297	2314	2351	2447	2598	2731	2809
744.0	2887	2952	3020	3113	3171	3368	3689	4246
752.0	4966	5776	6407	6783	6801	6437	5867	5191
760.0	4420	3863	3610	3584	3596	3512	2999	2525
768.0	2570	2633	2766	2885	2989	3181	3313	3343
776.0	3589	3798	4019	4540	5736	7745	10031	11804
784.0	12833	13254	13158	12666	11159	9196	7007	5659
792.0	5059	4877	4955	5322	6198	7852	9776	11094
800.0	11646	11822	11525	10873	9564	7781	6011	4922
808.0	4372	4066	3842	3649	3454	3328	3265	3249
816.0	3237	3230	3240	3278	3349	3472	3667	3987
824.0	4467	5033	5435	5965	6304	6326	6133	5627
832.0	5212	4771	4507	4324	4000	3700	3440	3341
840.0	3434	3634	3827	4049	4440	4520	4355	4115
848.0	3789	3394	3017	2746	2607	2549	2529	2540
856.0	2585	2596	2631	2605	2645	2734	2893	3011
864.0	3130	3197	3324	3477	3715	4005	4368	4960
872.0	6190	8367	11540	14889	17207	18345	18954	18515
880.0	16971	14144	10770	7805	5795	4763	4206	3868
888.0	3647	3466	3339	3243	3174	3169	3144	3089
896.0	3047	3005	2932	2810	2644	2560	2482	2457
904.0	2482	2470	2497	2462	2449	2402	2382	2377
912.0	2431	2465	2479	2439	2373	2275	2256	2266
920.0	2305	2310	2274	2293	2345	2359	2374	2386
928.0	2446	2465	2505	2580	2712	2826	3002	3318
936.0	3871	4699	5887	7017	7708	8143	8302	8389
944.0	8162	7494	6421	5464	4815	4473	4302	4332
952.0	4445	4606	4706	4813	4866	4779	4532	4213
960.0	3886	3605	3407	3304	3184	3108	3045	3091
968.0	3188	3303	3357	3382	3478	3591	3715	3872
976.0	4098	4280	4531	4847	5324	5841	6379	7041
984.0	7459	7963	8380	8461	8906	9038	9121	9366
992.0	10006	10844	11512	12204	12763	13232	13499	13719
1000.0	13804	13964	14299	14890	15513	16279	17148	18023
1008.0	19055	20176	21356	22746	24221	25887	27658	29458
1016.0	31357	33473	35548	37532	39458	2	3	0

TABLE 13

Channel	counts	%	channel	counts	%
29	78119±112	97.8±.1	633	65142±498	81.5±.6
38	78801±68	100.00±.09	659	61911±304	77.5±.4
45	78461±44	98.20±.06	683	64287±371	80.5±.5
53	77525±369	97.0±.5	733	59638±15	74.64±.02
63	76019±27	95.141±.003	784	57344±61	71.77±.08
86	73717±93	92.3±.1	810	57857±63	72.41±.08
110	71759±79	89.8±.1	836	51514±88	65.25±.86
135	71385±24	89.34±.03	866	53390±326	66.82±.4
158	69176±164	86.6±.2	887	52559±379	65.8±.5
188	67127±31	84.01±.04	940	49958±813	62.5±1.0
215	67377±225	84.3±.3	990	44928±452	56.2±.6
240	68248±40	85.40±.05			
267	68999±198	86.4±.2			
291	70132±247	87.8±.3			
315	69598±523	87.1±.6			
341	68084±49	85.20±.06			
366	69195±523	86.6±.7			
390	69788±713	87.3±.9			
413	69500±417	87.0±.5			
438	68875±83	87.5±.1			
487	68188±74	85.34±.09			
535	66291±30	82.97±.04			
561	66150±404	82.8±.6			
584	60148±101	75.3±.1			
610	65437±72	81.90±.09			

TABLE 14

SLIT = 246 μm
GAIN = 3.
ET = .39
SCANS = 16/16
COOLING.

channel #	counts	% Response
29	47850	75.61
31	61829	97.69
32	63288	100.
34	61774	97.61
40	60207	95.13
51	57290	90.52
59	54579	86.14
73	50213	79.34
83	48355	76.40
97	46577	73.60
121	43737	69.11
146	42657	67.40
172	41816	66.07
199	42304	66.84
225	43065	68.05
249	42282	66.81
275	44743	70.70
301	41919	66.24
325	45813	72.39
350	46737	73.85
375	48031	75.89
399	47639	75.27
424	48082	75.97
450	48319	76.35
475	47641	75.28
498	47185	74.57
522	47236	74.64
546	47082	74.39
571	46157	72.93
596	44238	69.96
619	48120	74.45
644	47332	74.79
668	48437	76.53
692	48117	76.01
717	48382	76.03
742	48382	76.04
766	48208	76.75
792	48857	76.84
818	47895	75.84
844	47620	75.24
870	47712	75.39
895	46800	73.95
922	46149	72.92
949	45650	72.13
975	44613	70.49
998	44125	69.72

TABLE 15

PEAK: 5452 Å

channel	counts	% response	adjusted counts	
43	695	93.87	740	
192	497	66.64	746	
346	547	73.62	743	756.8 ± 26.2
492	562	74.76	752	3.5%
636	600	74.68	803	

PEAK: 5421 Å

46	639	92.62	690	
194	438	66.70	657	
348	497	73.73	674	674.7 ± 12.8
484	512	74.69	686	1.9%
640	507	74.74	678	
788	522	78.76	663	

PEAK: 5410 Å

98	474	73.41	646	
252	430	67.26	639	
406	533	75.47	706	670.3 ± 24.4
550	503	74.16	678	3.6%
696	527	77.68	678	
846	508	75.25	675	

PEAK : 5372Å

162	365	66.58	548
288	394	68.47	575
446	431	76.29	565
585	422	71.27	592
730	453	78.04	580
882	421	74.70	564

570.7 ± 15.2

2.7%

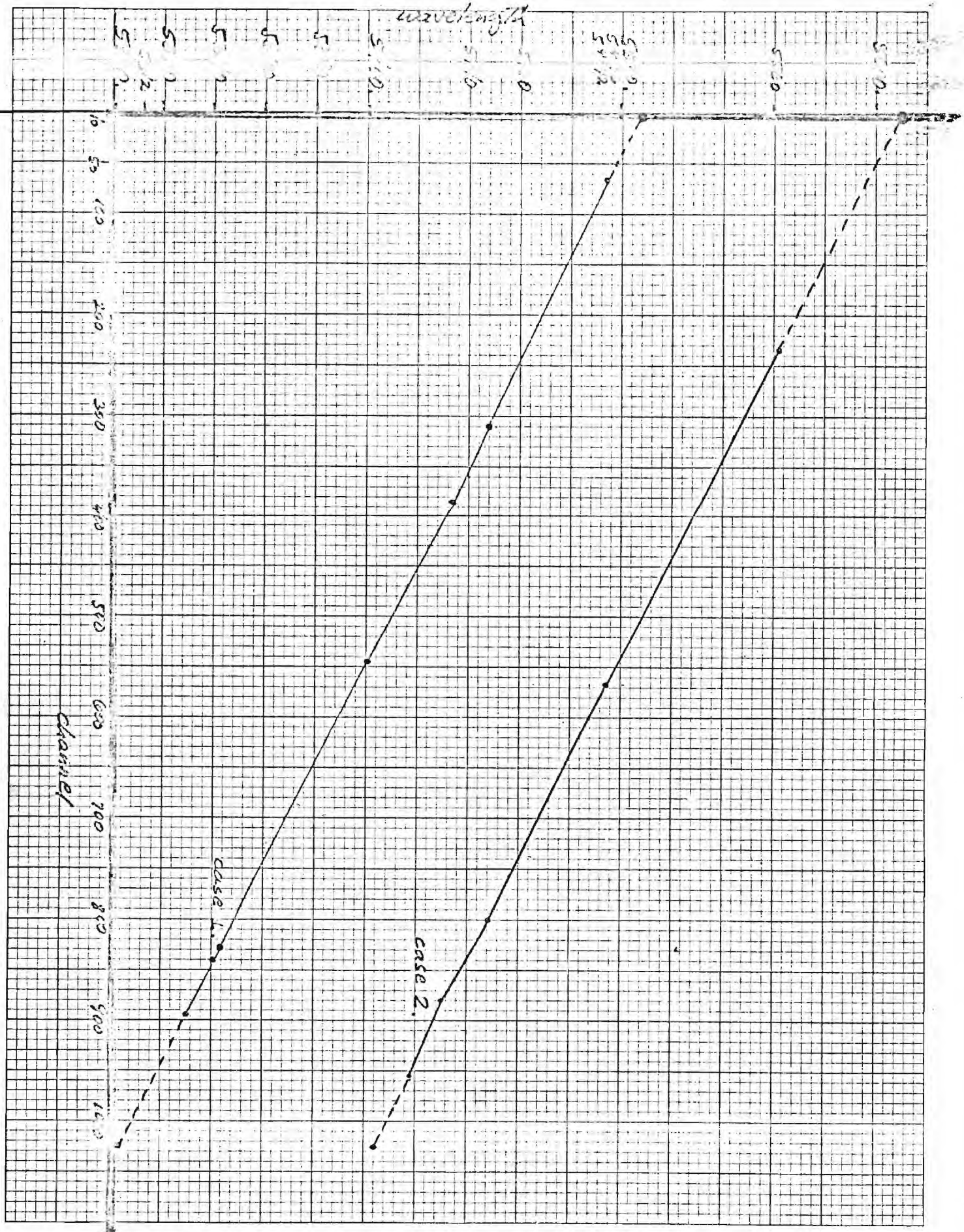

CITADEL® NO. 640 - SCIENCE - 5 SQUARES TO CENTIMETER

FIGURE 1

Figure 2.

```
      PROGRAM LEAST(INPUT,TAPE5=INPUT,OUTPUT,TAPE8=OUTPUT)
      DIMENSION X(20),Y(20)
      READ(5,7)N
    7 FORMAT(I2)
      DO 10 I=1,N
      READ(5,*)X(I),Y(I)
   10 CONTINUE
      DO 15 I=1,N
      WRITE(8,3) X(I),Y(I)
    3 FORMAT(1X,2F14.7)
   15 CONTINUE
A.B:  XAVER=0.
      YAVER=0.
      SXY=0.
      SXX=0.
      SYY=0.
      DO 20 I=1,N
      XAVER=XAVER+X(I)
      YAVER=YAVER+Y(I)
      SXY=SXY+X(I)*Y(I)
      SXX=SXX+X(I)*X(I)
      SYY=SYY+Y(I)*Y(I)
   20 CONTINUE
      XAVER=XAVER/N
      YAVER=YAVER/N
      SXY=SXY-N*XAVER*YAVER
      SXX=SXX-N*XAVER*XAVER
      SYY=SYY-N*YAVER*YAVER
      A=SXY/SXX
      B=YAVER-A*XAVER
      VARA=(SXX*SYY-SXY*SXY)/(SXX*SXX*(N-2))
      VARB=VARA*((SXX/N)+XAVER*XAVER)
      SDEVA=SQRT(VARA)
      SDEVB=SQRT(VARB)
      COR=SXY*SXY/(SXX*SYY)
      WRITE(8,4)
    4 FORMAT(3X,*SLOPE*9X*INTERCEPT*5X*ST. DEV. SLOPE*2X*
     1ST. DEV. INT. *3X*CORRELATION*)
      WRITE(8,5)A,B,SDEVA,SDEVB,COR
    5 FORMAT(5F14.7)
      STOP
      END
```

FIGURE 3.

Case 1.

67.0000000	5494.4200000
310.0000000	5448.5100000
384.0000000	5433.6500000
545.0000000	5400.5600000
828.0000000	5343.2800000
840.0000000	5341.0900000
894.0000000	5330.2800000

SLOPE	INTERCEPT	ST. DEV. SLOPE	ST. DEV. INT.	CORRELATION
-.2000365	5509.3616099	.0013313	.8322372	.9997786

case 2.

235.0000000	5562.7700000
567.0000000	5494.4200000
801.0000000	5448.5100000
878.0000000	5433.6500000
956.0000000	5418.5500000

SLOPE	INTERCEPT	ST. DEV. SLOPE	ST. DEV. INT.	CORRELATION
-.1999710	5609.0400567	.0016185	1.1900241	.9998035

FIGURE 4

```
/OLD,INTERP
/LNH
      PROGRAM INTERP(INPUT,OUTPUT,TAPE5=INPUT,TAPE6=OUTPUT)
      DIMENSION X(100),Y(100),D(25)
      READ(5,101)N,NN
  101 FORMAT(I2,1X,I2)
      DO 333 I=1,NN
      READ(5,*)D(I)
  333 CONTINUE
      DO 100 I=1,N
      READ(5,*)X(I),Y(I)
  100 CONTINUE
      DO 444 I=1,NN
      XX=D(I)
      DO 30 K=1,N
      IF(XX-X(K))10,20,30
   30 CONTINUE
   20 YY=Y(K)
      WRITE(6,103)XX,YY
  103 FORMAT(*CHANNEL,EXACT Y*,3X,F7.2,3X,E12.5)
      GO TO 444
   10 A=(Y(K)-Y(K-1))/(X(K)-X(K-1))
      B=XX-X(K-1)
      C=B*A
      YY=Y(K-1)+C
      WRITE(6,106)XX,YY
  106 FORMAT(*CHANNEL,INTERPOLATED Y*,3X,F7.2,3X,E12.5)
  444 CONTINUE
      STOP
      END
/
```

FIGURE 5

INPUT:

```
/OLD, DARSSD
/LNH
46 23
43.  192.  346.  492.  636.  46.  194.  348.  494.  640.  788.
98.  252.  406.  550.  696.  846.  162.  288.  446.  585.  730.  882.
 29.   75.61   31.   97.69   32.  100.00   34.   97.61   40.   95.13   51.   90.52
 59.   86.14   73.   79.34   83.   76.40   97.   73.60  121.   69.11  146.   67.40
172.   66.07  199.   66.84  225.   68.05  249.   66.81  275.   70.70  301.   66.24
325.   72.39  350.   73.85  375.   75.89  399.   75.27  424.   75.97  450.   76.35
475.   75.28  498.   74.57  522.   74.64  546.   74.39  571.   72.93  596.   69.96
619.   74.45  644.   74.79  668.   76.53  692.   77.61  717.   78.03  742.   78.04
766.   77.75  792.   78.94  818.   75.84  844.   75.24  870.   75.39  895.   73.95
922.   72.92  949.   72.13  975.   70.49  998.   69.72
```

first line: # of data points, # of unknowns

second line - unknown values

following lines - data points (channel - response %)

OUTPUT:

```
/COMINT, TAPES, OUTPUT
CHANNEL, INTERPOLATED Y      43.00      .93873E+02
CHANNEL, INTERPOLATED Y     192.00      .66640E+02
CHANNEL, INTERPOLATED Y     346.00      .73616E+02
CHANNEL, INTERPOLATED Y     492.00      .74755E+02
CHANNEL, INTERPOLATED Y     636.00      .74681E+02
CHANNEL, INTERPOLATED Y      46.00      .92615E+02
CHANNEL, INTERPOLATED Y     194.00      .66697E+02
CHANNEL, INTERPOLATED Y     348.00      .73733E+02
CHANNEL, INTERPOLATED Y     494.00      .74693E+02
CHANNEL, INTERPOLATED Y     640.00      .74736E+02
CHANNEL, INTERPOLATED Y     788.00      .78757E+02
CHANNEL, INTERPOLATED Y      98.00      .72413E+02
CHANNEL, INTERPOLATED Y     252.00      .67259E+02
CHANNEL, INTERPOLATED Y     406.00      .75466E+02
CHANNEL, INTERPOLATED Y     550.00      .74156E+02
CHANNEL, INTERPOLATED Y     696.00      .77677E+02
CHANNEL, INTERPOLATED Y     846.00      .75252E+02
CHANNEL, INTERPOLATED Y     162.00      .66582E+02
CHANNEL, INTERPOLATED Y     288.00      .68470E+02
CHANNEL, INTERPOLATED Y     446.00      .76292E+02
CHANNEL, INTERPOLATED Y     585.00      .71267E+02
CHANNEL, INTERPOLATED Y     730.00      .78035E+02
CHANNEL, INTERPOLATED Y     882.00      .74699E+02
      .184 CP SECONDS EXECUTION TIME.
```

NEON (Continued)

Wave length	Arc	Discharge tube	Wave length	Arc	Discharge tube	Wave length	Arc	Discharge tube
I 4819.76	..	150	I 5101.33	..	35	I 5811.42	..	300
I 4819.94	..	70	5103.13	..	150	I 5816.61	..	50
I 4821.92	..	300	I 5103.22	..	150	I 5820.15	..	500
I 4823.17	..	100	I 5203.89	..	150	I 5828.91	..	75
I 4823.37	..	50	I 5208.96	..	70	I 5852.49	..	2000
I 4825.53	..	50	I 5210.57	..	50	I 5868.42	..	75
I 4827.31	..	1000	I 5214.31	..	35	I 5872.15	..	75
I 4827.59	..	300	I 5222.35	..	50	5872.53	..	35
I 4837.31	..	500	I 5234.03	..	50	I 5881.89	..	1000
I 4842.94	..	50	I 5273.01	..	40	I 5902.46	..	50
I 4849.53	..	30	I 5280.07	..	50	I 5906.43	..	50
I 4851.50	..	60	I 5298.19	..	150	I 5913.63	..	250
I 4852.65	..	100	I 5304.76	..	70	I 5918.91	..	250
I 4863.08	..	100	I 5314.78	..	30	I 5922.71	..	25
I 4864.35	..	30	I 5316.81	..	25	I 5931.48	..	75
I 4865.50	..	100	I 5320.30	..	75	I 5939.32	..	50
I 4866.48	..	80	I 5320.78	..	600	I 5944.83	..	500
I 4867.01	..	70	I 5333.32	..	50	I 5961.63	..	70
I 4868.27	..	70	I 5341.09	..	1000	I 5965.47	..	500
I 4881.91	..	1000	I 5343.28	..	600	I 5966.17	..	35
I 4885.08	..	100	I 5349.21	..	150	I 5974.63	..	500
I 4892.09	..	500	I 5355.18	..	150	I 5975.53	..	600
I 4897.92	..	70	I 5365.42	..	150	I 5987.91	..	150
I 4899.01	..	50	I 5369.01	..	150	I 5991.67	..	75
I 4928.23	..	70	I 5369.41	..	35	I 6030.05	..	100
I 4930.94	..	50	I 5370.25	..	25	I 6029.99	..	1000
I 4933.01	..	100	I 5370.29	..	25	I 6046.16	..	50
I 4941.99	..	100	I 5372.31	..	75	I 6064.55	..	50
I 4955.38	..	150	I 5374.97	..	50	I 6074.34	..	1000
I 4957.03	..	1000	I 5383.26	..	25	I 6096.16	..	300
I 4957.12	..	150	I 5400.56	..	2000*	I 6128.45	..	100
I 4973.54	..	100	I 5412.65	..	250	I 6132.51	..	100
I 4974.76	..	50	I 5418.55	..	150	I 6143.06	..	1000
I 4991.93	..	1501	I 5420.15	..	50	I 6156.39	..	100
I 5005.16	..	500	I 5433.65	..	250	6151.09	..	70 w
I 5015.53	..	50	I 5448.53	..	150	I 5156.14	..	50
I 5011.90	..	25	I 5450.41	..	50	I 6163.59	..	1000
I 5022.87	..	25	I 5507.34	..	25	I 6171.89	..	70
I 5031.35	..	250	I 5533.08	..	75	I 6175.29	..	50
I 5035.90	..	35	I 5538.61	..	50	I 6182.15	..	150
I 5037.75	..	500	I 5539.09	..	35	I 6189.08	..	70
I 5052.93	..	25	I 5562.11	..	150	I 6193.08	..	50
I 5074.20	..	35	I 5562.77	..	500	I 6205.79	..	100
I 5076.55	..	35	I 5563.05	..	75	I 6213.88	..	150
I 5080.35	..	150	I 5576.05	..	35	I 6217.28	..	1000
I 5083.97	..	25	I 5580.38	..	50	I 6225.74	..	50
I 5090.04	..	25	I 5652.57	..	75	I 6216.73	..	100
I 5104.70	..	35	I 5656.03	..	75	I 6258.80	..	100
I 5113.67	..	75	I 5656.66	..	500	I 6266.49	..	1000
I 5116.50	..	150	I 5662.35	..	75	I 6273.01	..	70
I 5117.01	..	35	I 5681.65	..	25	I 6276.04	..	50
I 5120.51	..	25	I 5680.82	..	150	I 6293.77	..	100
I 5122.76	..	150	I 5715.31	..	35	I 6303.78	..	100
I 5122.34	..	150	I 5718.36	..	150	I 6313.69	..	150
I 5141.94	..	500	I 5719.22	..	500	I 6328.17	..	300
I 5145.01	..	500	I 5719.53	..	75	I 6330.99	..	150
I 5145.12	..	35	I 5718.30	..	500	I 6334.43	..	1000
I 5150.08	..	35	I 5748.65	..	70	I 6351.87	..	100
I 5151.69	..	75	I 5760.58	..	70	I 6365.01	..	100
I 5154 12	..	50	I 5764.42	..	700	I 6382.99	..	1000
I 5158.66	..	50	I 5770.31	..	60	I 6101.08	..	100
I 6158.89	..	50	I 5804.10	..	75	I 6402 25	..	2000
I 5188.61	..	150	I 5801.45	..	300	I 6109.75	..	150

NEON (Continued)

Wave length	Arc	Discharge tube	Wave length	Arc	Discharge tube	Wave length	Arc	Discharge tube
I 6121.71	..	100	I 8139.63	..	60	I 8780.62	..	1000
I 6144.72	..	150	I 8156.11	..	300	I 8782.01	..	50
I 6506.53	..	1000	I 8218.70	..	30	I 8783.75	..	1000
I 6532.88	..	100	I 8250.38	..	150	I 8792.53	..	30
I 6598.95	..	1000	I 8266.08	..	200	I 8830.92	..	50
I 6602.91	..	100	I 8267.11	..	80	I 8853.87	..	700
I 6652.09	..	150	I 8300.53	..	600	I 8865.33	..	100
I 6666.59	..	100	I 8301.51	..	150	I 8867.76	..	500
I 6678.28	..	500	I 8365.75	..	150	I 8919.59	..	300
I 6717.04	..	70	I 8376.41	..	200	I 8988.58	..	200
I 6738.96	..	70	I 8377 61	..	800	I 9148.68	..	600
I 6929.47	..	1000	I 8417.18	..	100	I 9201.76	..	600
I 7021.05	..	500	I 8418.43	..	400	I 9220.05	..	150
I 7032.41	..	1000	I 8463.37	..	150	I 9221.69	..	200
I 7051.29	..	70	I 8483.45	..	80	I 9228.67	..	200
I 7059.11	..	200	I 8495.36	..	500	I 9275.53	..	100
7138.70	..	40	I 8514.70	..	60	I 9300.85	..	600
I 7173.04	..	1000	I 8571.36	..	100	I 9310.58	..	150
I 7245.16	..	1000	I 8592.91	..	60	I 9413.98	..	300
I 7301.82	..	30	I 8591.26	..	400	I 9326.52	..	600
I 7438.90	..	300	I 8634.65	..	600	I 9373.28	..	200
I 7472 42	..	50	I 8635.31	..	50	I 9425.38	..	500
I 7488.87	..	500	I 8647.05	..	300	I 9432.92	..	40
I 7535.77	..	300	I 8651.38	..	2000	I 9459 21	..	300
I 7544.05	..	100	I 8651.51	..	100	I 9486.68	..	500
I 7629.09	..	30	I 8679.19	..	500	I 9534.17	..	500
I 7927.13	..	40	I 8681.92	..	500	I 9547.10	..	300
I 7937.01	..	70	I 8701.15	..	200	I 9655.42	..	1000
I 7943.18	..	200	I 8771.79	..	100	I 9900.58	..	40
I 8082.46	..	200	I 8778.75	..	150	I 9902.31	..	30
I 8118.56	..	100						

(Neptunium)* NICKEL

Wave length	Arc	Spark	Wave length	Arc	Spark	Wave length	Arc	Spark
II 2001.29	..	30	II 2125.90	4	25	II 2278.77	12	25
II 2019.01	2	30	II 2126.80	2	25 w	II 2287.03	100	500
II 2020.97	..	30	II 2128.57	5	30	II 2302.99	10 s	35
II 2029.19	..	25	II 2161.23	10	30	I 2310.96	50 r	10 s
II 2032.30	2	25	II 2165.56	20	40 r	I 2312.51	30 W	6
II 2053.29	3	25	II 2171.67	12	30	II 2316.01	15	25 W
II 2054.32	..	25	II 2175.16	15	25	I 2317.16	30 r	12
II 2066.41	2	25	II 2180.17	4	40	I 2320.03	30 r	51
II 2080.85	3	35	II 2185.50	4	30	I 2325.79	30 r	9
I 2082.86	25	2	II 2188.05	4	25	II 2336.58	..	150
II 2084.86	..	25	II 2191.11	10	30	II 2356.68	..	30
I 2088.98	30 d	..	II 2200.70	20	30 n	II 2375.12	10	30
II 2090.10	3	25	II 2216.17	20	40 wn	II 2387.76	6	30
I 2095.73	25	2	II 2220.10	10	25	I 2301.81	40 r	10
II 2097.10	4	35	II 2222.91	15	25 w	II 2305.17	..	80
II 2103.38	..	25	II 2221 87	15	25	II 2413.05	..	50
II 2107.96	2	45	I 2214.53	40	..	II 2416.14	40	250 n
II 2111.72	25	9	II 2253.86	100	300	I 2123.33	25	4
II 2113.51	3	45	I 2259.57	300 w	..	II 2133 57	..	50
2124.31	30	..	II 2261.16	150	460	I 2431 41	40 w	..
I 2127 81	25	3	II 2270.21	100	400	2436.67	30 l	20
II 2125.11	4	25	II 2277.28	5	25	II 2437.89	40 w	200

*See end of Section II.

FIGURE 6

10 UNITS/DIVISION

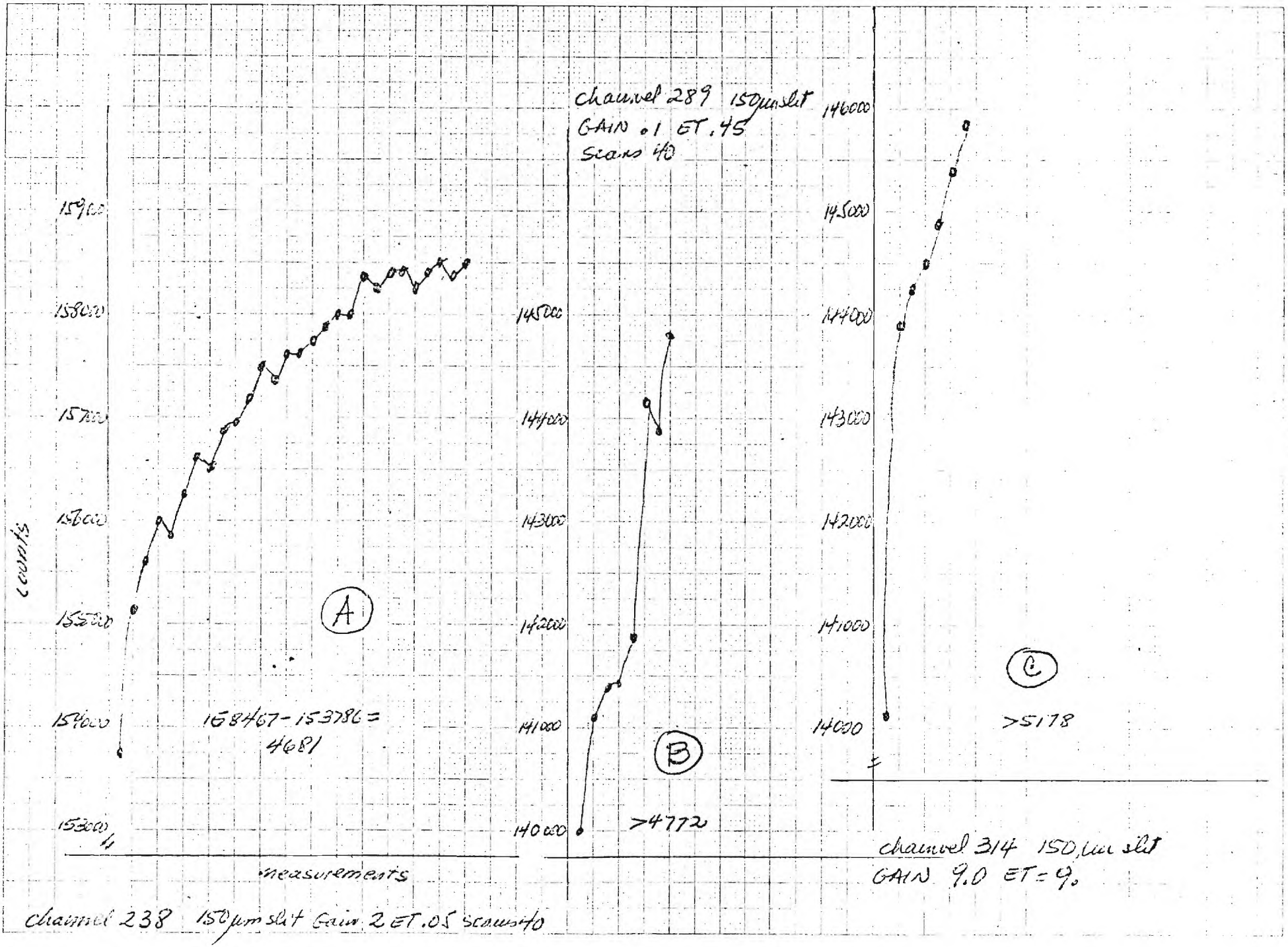

FIGURE 7

FIGURE 8

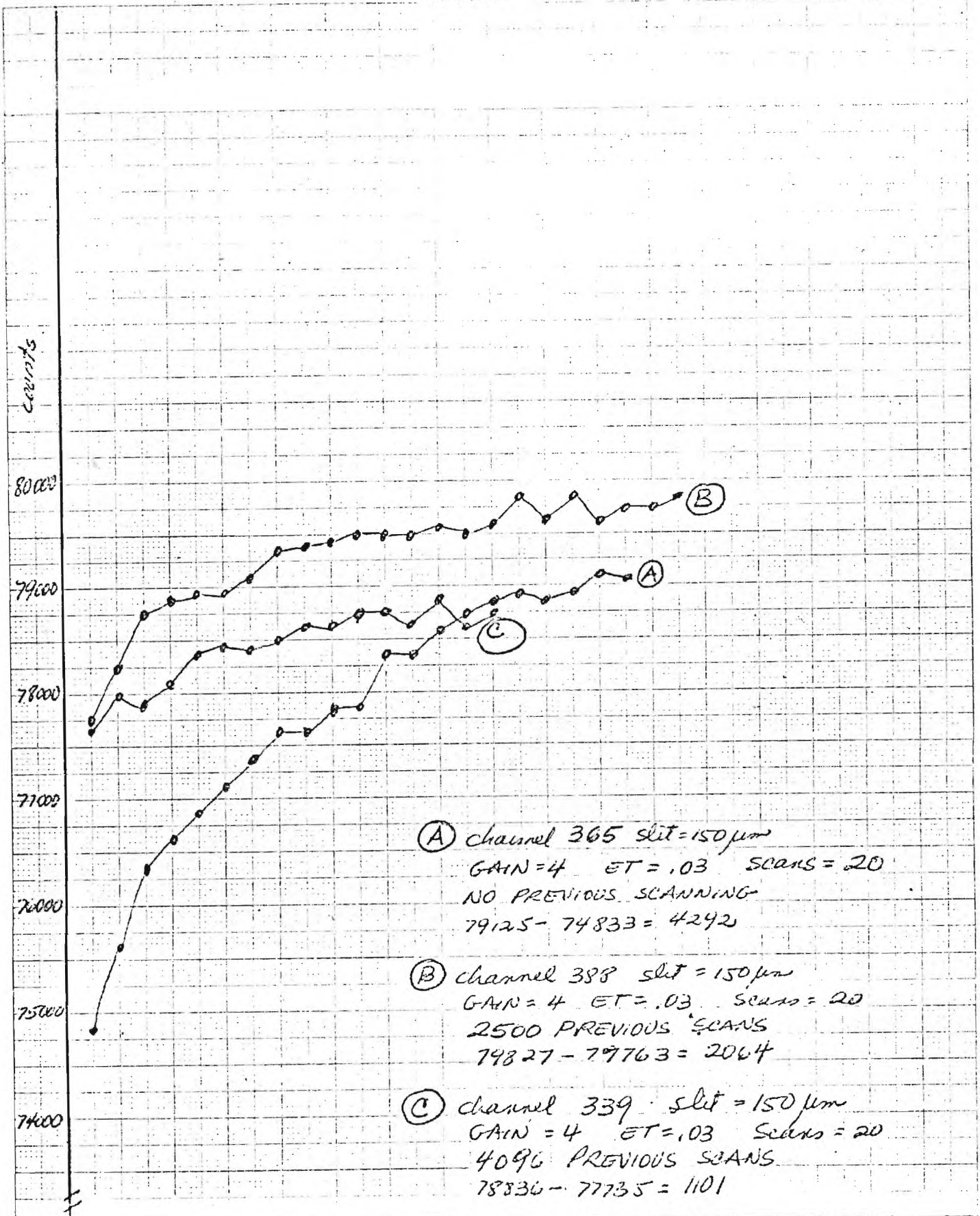

(A) channel 365 slit = 150 μm
GAIN = 4 ET = .03 scans = 20
NO PREVIOUS SCANNING
79125 - 74833 = 4292

(B) channel 388 slit = 150 μm
GAIN = 4 ET = .03 Scans = 20
2500 PREVIOUS SCANS
74827 - 79763 = 2064

(C) channel 339 slit = 150 μm
GAIN = 4 ET = .03 Scans = 20
4096 PREVIOUS SCANS
78836 - 77735 = 1101

measurements

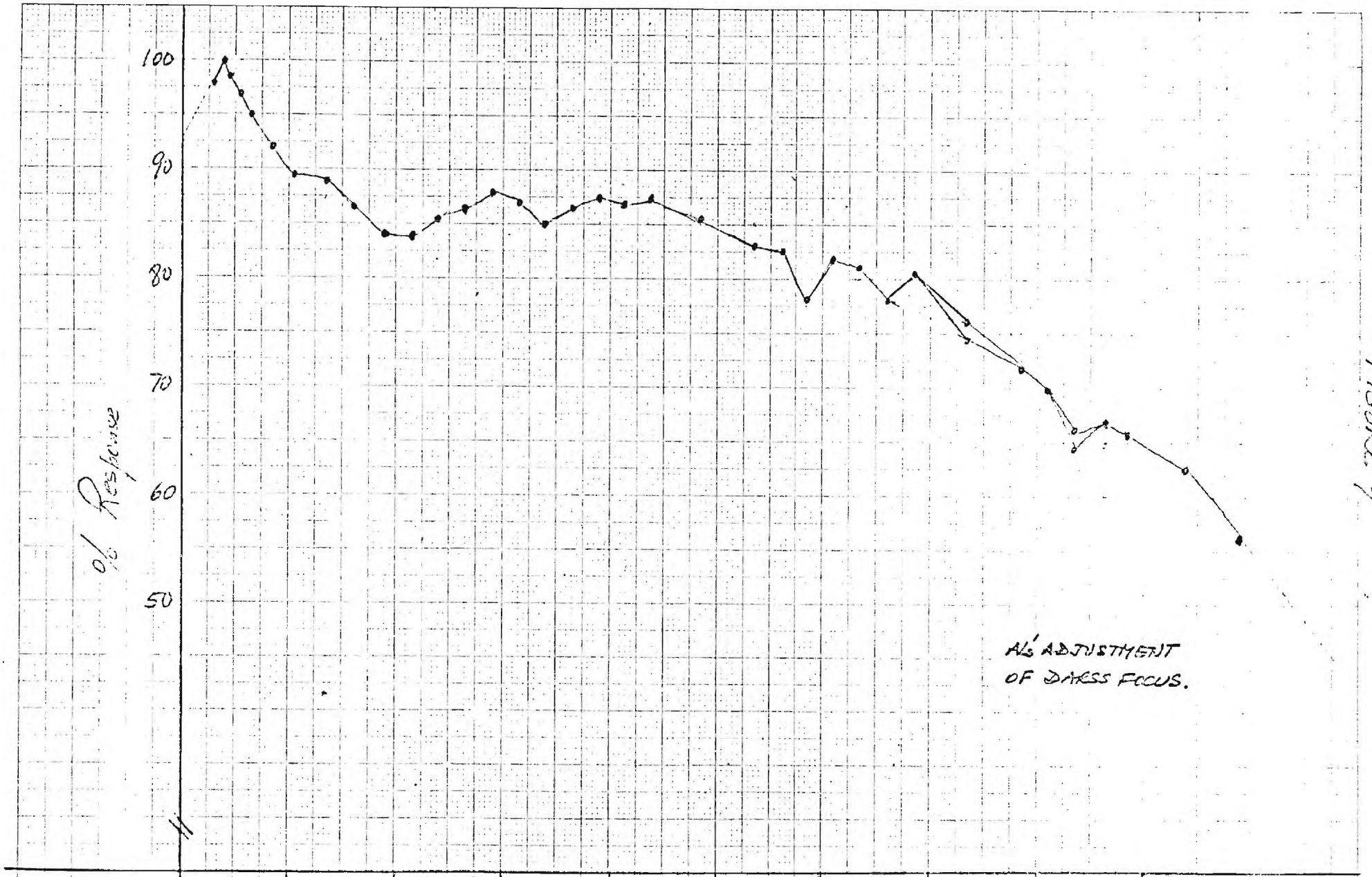
100
90
80
70
60
50
% Response
100
200
300
400
500
600
700
800
900
1000
Al ADJUSTMENT OF DARKS FOCUS.
followed with Ne peak λ = 5850 slit = 150 μm GAIN = 4 CT = .026 Scans = 20 Background = 20 Previous Scans = 1260-1288

Figure 9

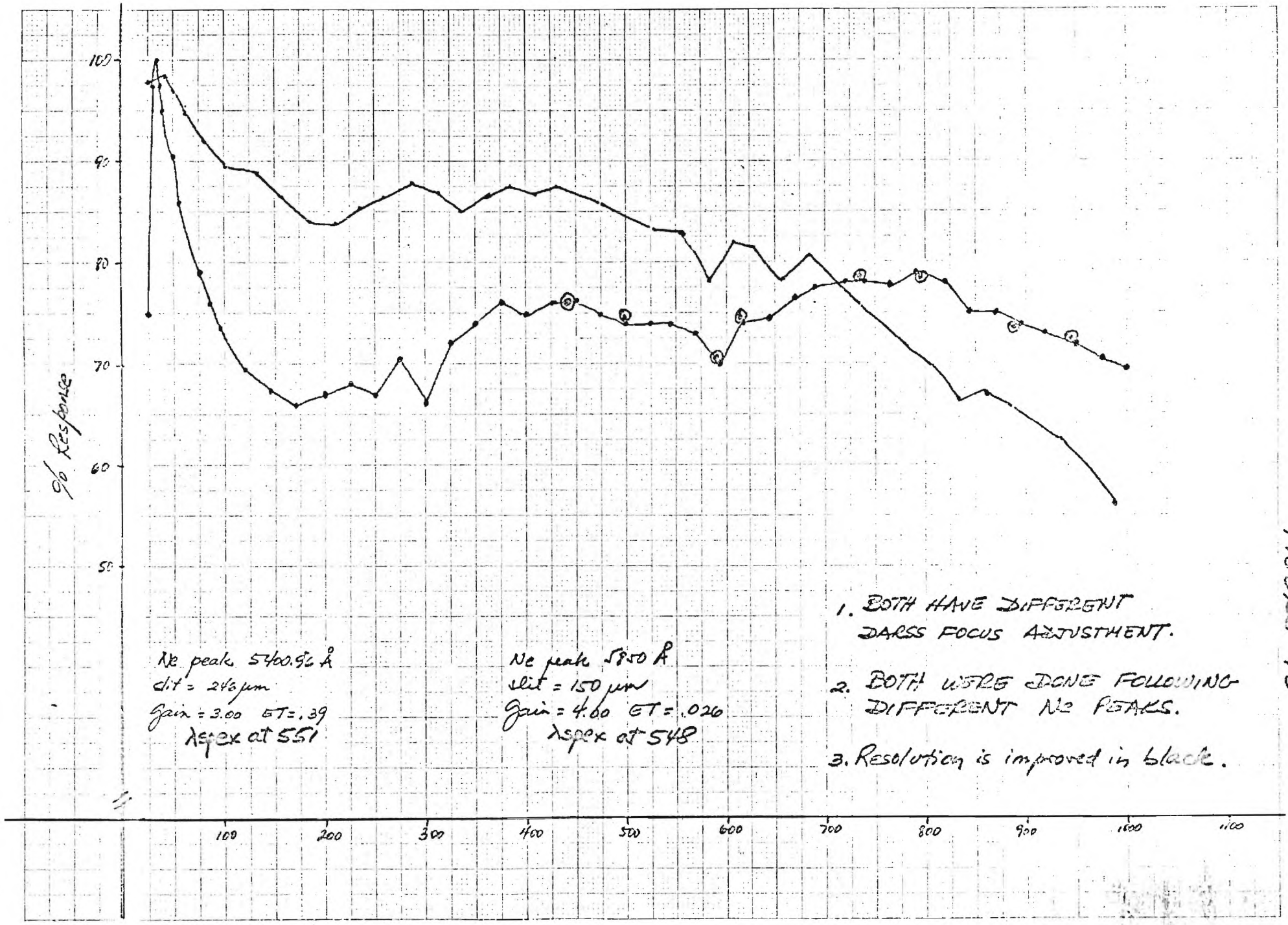
100
90
80
70
60
50
% Response
100
200
300
400
500
600
700
800
900
1000
1100
Ne peak 5400.9 Å
slit = 24 μm
Gain = 3.00 ET = .39
λspex at 551
Ne peak 5850 Å
slit = 150 μm
Gain = 4.00 ET = .026
λspex at 548
1. BOTH HAVE DIFFERENT GRASS FOCUS ADJUSTMENT.
2. BOTH WERE DONE FOLLOWING DIFFERENT Ne PEAKS.
3. Resolution is improved in black.

FIGURE 10

HEWLETT-PACKARD/MOSELEY DIVISION
9270-1025
FOR USE ON AUTOGRAF RECORDERS
10 UNITS/DIVISION

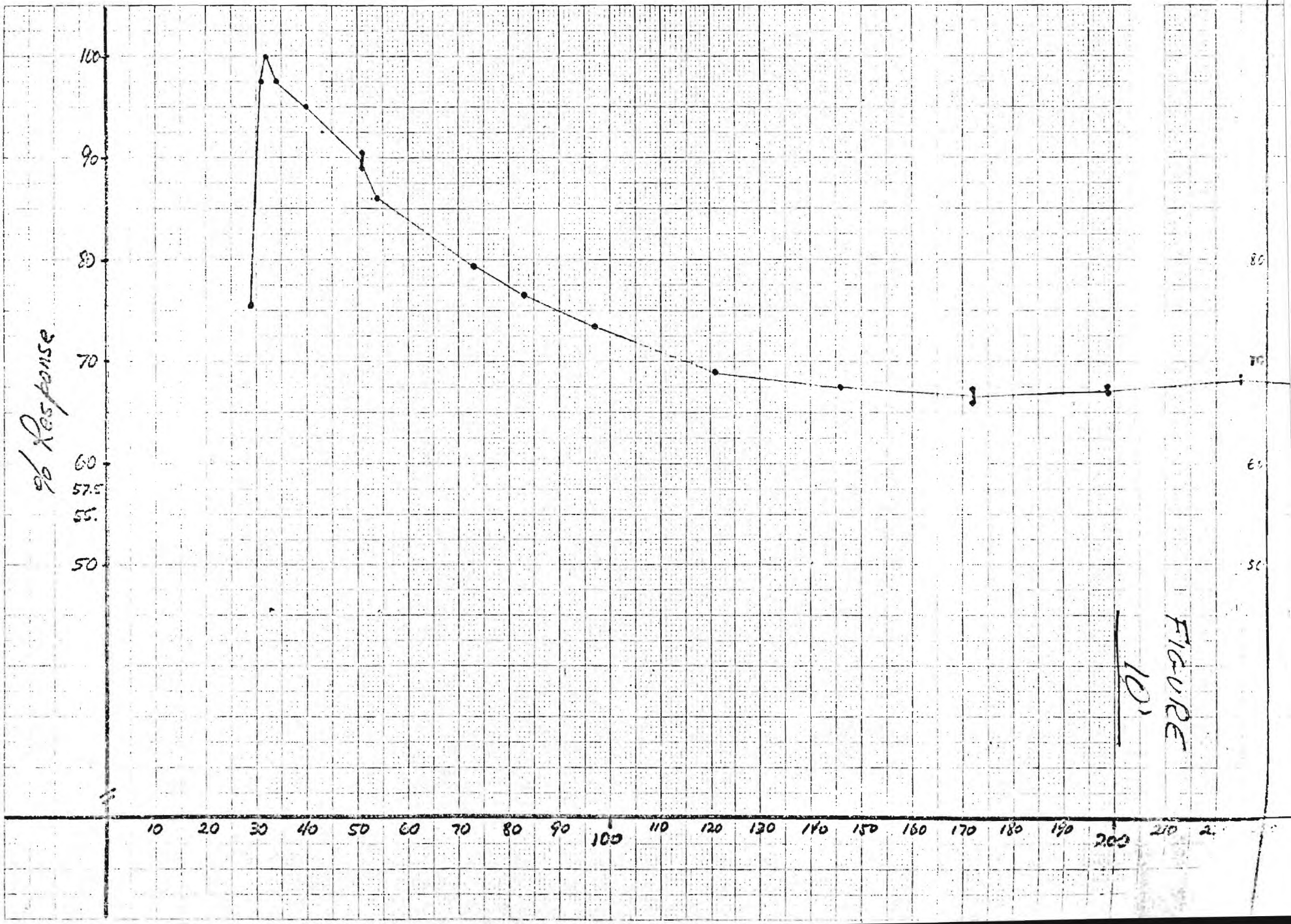

FIGURE 10

HEWLETT-PACKARD/MOSELEY DIVISION
9270-1023
FOR USE ON AUTOGRAF RECORDERS
10 UNITS/DIVISION

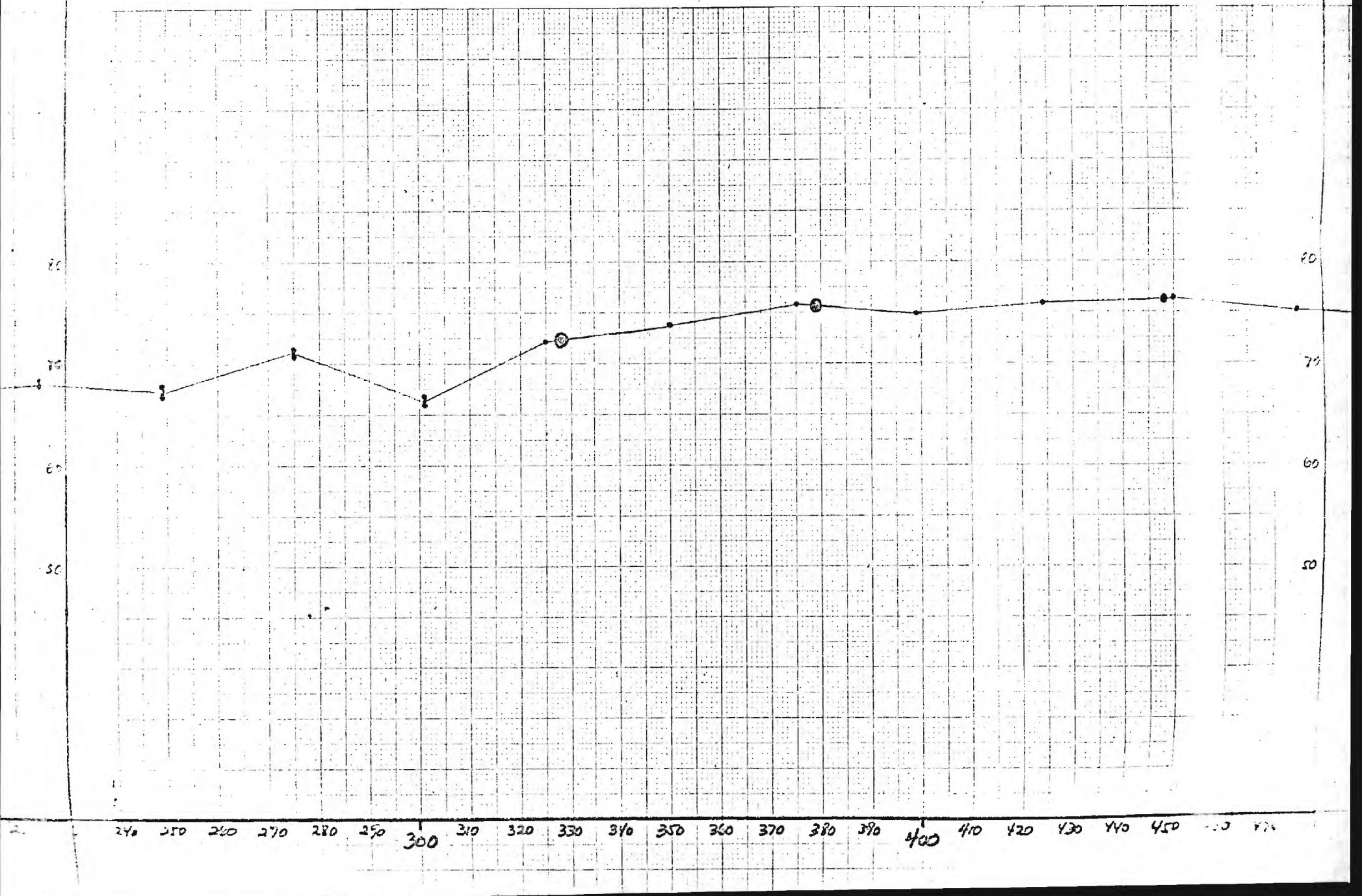

HEWLETT-PACKARD/MOSELEY DIVISION
9270-1023
FOR USE ON AUTOGRAF RECORDERS
10 UNITS/DIVISION

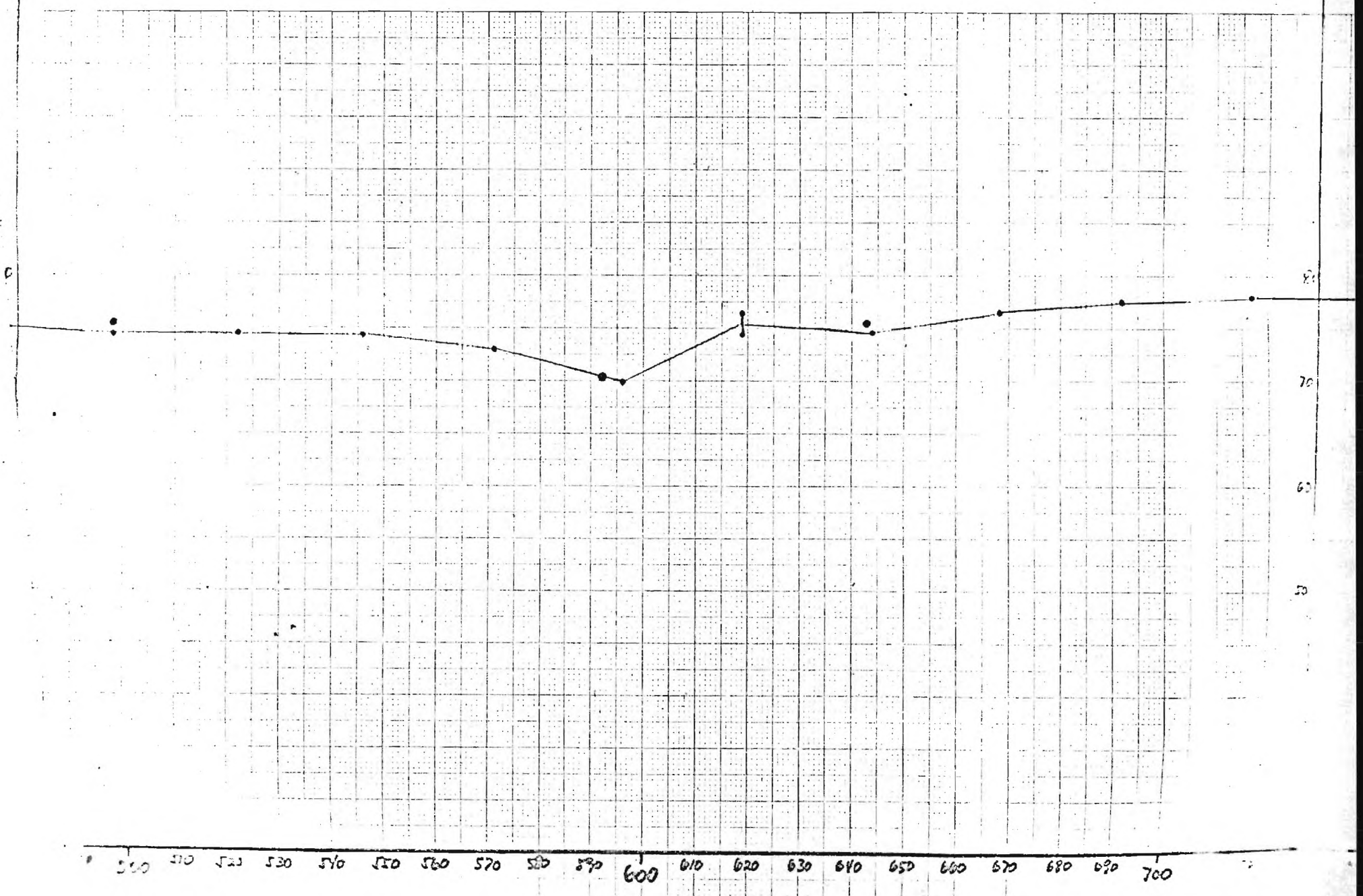

HEWLETT-PACKARD/MOSELEY DIVISION
9270-1023
FOR USE ON AUTOGRAF RECORDERS
10 UNITS/DIVISION

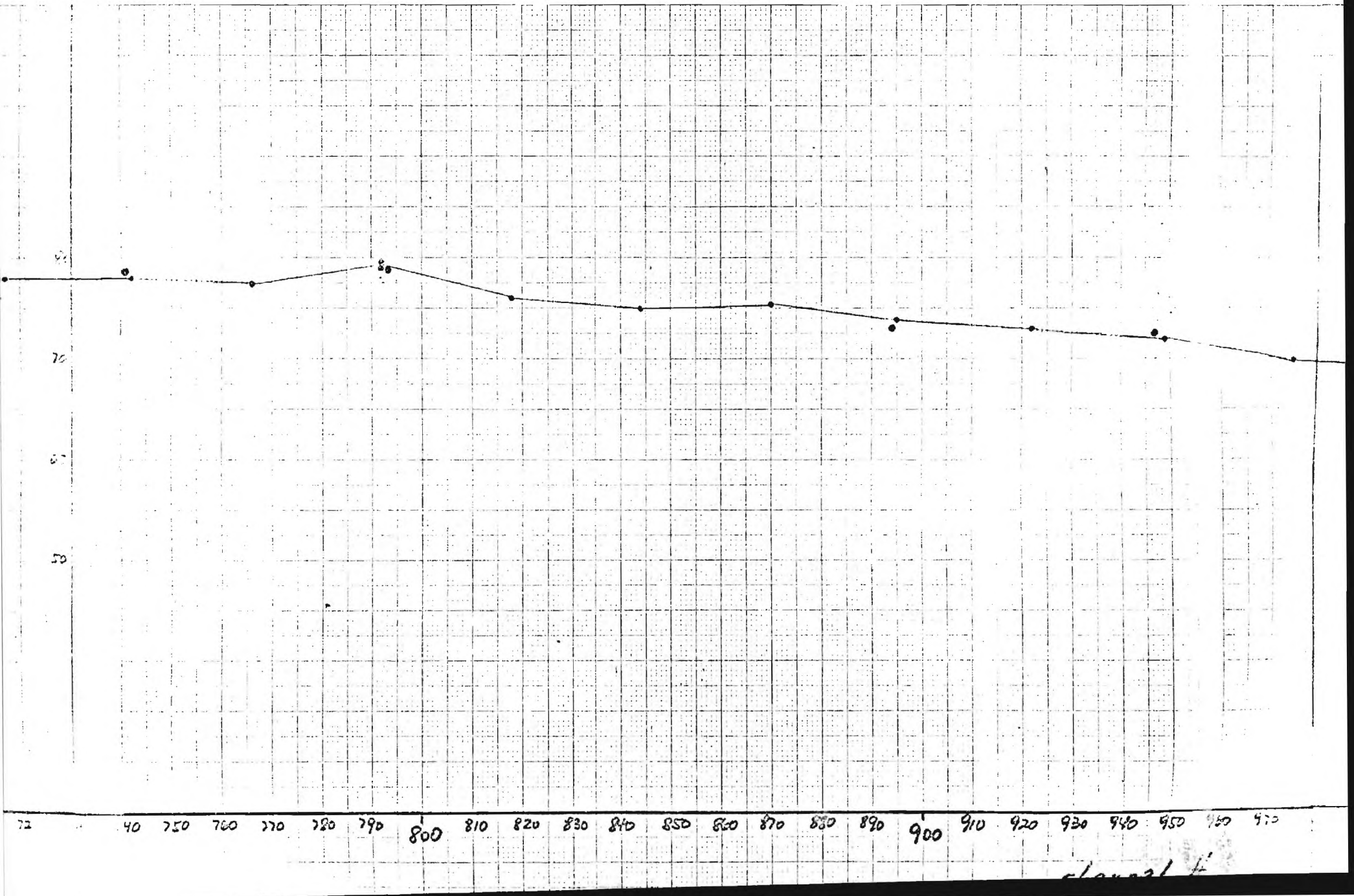

A P P E N D I X D

THE CHARACTERIZATION OF HIGH TEMPERATURE VAPORS OF IMPORT TO COMBUSTION AND GASIFICATION PROCESSES IN THE ENERGY TECHNOLOGIES

(Proceedings of the U.S. Department of Energy Contractor's Meeting, Morgantown, West Virginia, February 1981)

THE CHARACTERIZATION OF HIGH TEMPERATURE VAPORS OF IMPORT TO COMBUSTION AND GASIFICATION PROCESSES IN THE ENERGY TECHNOLOGIES

James L. Gole
Department of Chemistry
Georgia Institute of Technology
Atlanta, Georgia

Research efforts are outlined whose focus is the characterization of compounds of import to the energy technologies. The reactions of potassium and sodium with hydrogen peroxide have been used to excite chemiluminescence from KOH and NaOH. The study of this chemiluminescence over a wide variety of experimental conditions leads to the direct determination of stringent lower bounds for the K-OH and Na-OH bond energies. For KOH, we find $D_o^\circ \geq 85.2$ kcal/mole; for NaOH, $D_o^\circ \geq 75.2$ kcal/mole. The present results lead to an estimated K-OH bond strength of 88±2 kcal/mole, notably higher than the currently accepted value. The characterization of Na_2O via laser spectroscopy is summarized and molecular constants for this molecule are presented. Preliminary studies of the bonding and spectra of the alkali monoxides are presented. Recent studies of ultrafast energy transfer in a variety of high temperature molecules are also outlined.

Introduction

Low tolerance levels for certain species in process streams impose stronger requirements for reliable thermodynamic and kinetic data in order to predict low level species concentrations. In addition, there must be serious concern focused on whether or not these systems are best represented via equilibrium or non-equilibrium models. We have been concerned with the characterization of important processes in these inherently high temperature systems through application of chemiluminescent and laser fluorescent techniques to the determination of bond energies, spectroscopic constants, and ultrafast energy transfer routes. The evaluation of spectroscopic data leads to the determination of important molecular constants which can be used for the statistical mechanical evaluation of heat capacities, entropies and free energies, all of which are important to the understanding of energy related combustion and gasification environments. The compounds of interest are formed through a variety of in-situ synthetic metatheses over a wide range of temperature and pressure. The current studies also provide information useful for the characterization of non-equilibrium combustion phenomena and for the evaluation of kinetically dominated product formation routes.

Major Research Thrusts

In order to attack the topics outlined in our introductory remarks, our research effort has taken on five main thrusts:

(1) The primary emphasis in our research effort has involved the formation and analysis of alkali and alkaline earth monohydroxide electronic emission spectra in order to determine bond dissociation energies, evaluate molecular constants for use in thermodynamic models, and characterize spectral regions useful for the monitoring of reaction kinetics. Efforts thus far have focused on NaOH, KOH, and CaOH and the generation of excited electronic states for these species using chemiluminescent techniques.

(2) A major effort has involved the generation of spectra for the alkali oxides and sulfides using both chemiluminescent (NaO, NaS, KO, KS) and laser fluorescent (Na_2O) techniques.

(3) In carrying out chemiluminescent studies across a wide pressure range (10^{-6}-10^{2} torr)[1-4], we have observed and characterized ultrafast intramolecular energy transfer routes among the electronically and vibrationally excited states of several high temperature molecules. Thus far, these studies have indicated that energy transfer can occur at rates which may approach 1000 times the calculated gas kinetic rates. These surprising results demonstrate that vibrationally and/or electronically excited high temperature molecules act as if they were "large" or "diffuse" entities capable of strong interaction at very long range. This rapid energy transfer is a general phenomenon and effects have been observed in several molecules including SiO and KOH. The observation of such rapid energy transfer may have significant implications for the modeling of energy generating systems and the characterization of heat flow in these systems.

(4) We have been engaged in several studies to produce and characacterize spectra for both SiS[5] and SiO. Much of this effort has involved the determination of the SiS and SiO bond energies and the further interpretation of their spectroscopy so as to provide additional data for inclusion in the calculation of thermodynamic properties.

(5) In collaboration with the Morgantown Energy Technology Center, we have recently characterized the methane-fluorine combustion system.

In the present discussion we will focus on those efforts geared toward the characterization of alkali metal compounds, specifically KOH, NaOH, Na_2O, and NaO. Reference will also be made to other alkali hydroxides and oxides as well as the alkali halides.

Apparatus for Chemiluminescent Studies

In order to produce and study the emission spectra of alkali compounds, several devices for producing chemiluminescent spectra have been employed. In Figure 1, we depict a device which is used at very low pressures. The specific nature of the components in this device has been discussed elsewhere[6]. Briefly, a metal beam formed in the oven chamber effuses through a small orifice into a reaction chamber filled with a tenuous atmosphere (10^{-4}-10^{-6} torr) of oxidant gas. Reactions which yield light occur and they are monitored through the spectrometer window using an electrooptical detection system[6,7]. Because most excited electronic states have radiative lifetimes in the range 10^{-6} to 10^{-8} seconds, chemiluminescent species formed in the reaction chamber will emit light long before they undergo subsequent collision (collision frequency at 10^{-4} torr $\sim 10^{3}$ second) Hence, we refer to these processes as "single collision". The criteria for observing chemiluminescent emission is outlined in Figure 2 and discussed in more detail elsewhere[6]. Briefly, the heat of reaction for the process of interest must exceed the excitation required to populate an excited electronic product state. In Figure 2, we consider the formation of a metal oxide and note that those metal oxide excited states on which we focus must fall below the imaginary energy line depicted in the Figure. To first order, we must be concerned with the difference in the metal oxide and oxidant bond energies. If this difference corresponds to a reaction exothermicity sufficient to populate an excited electronic product state, we determine the highest quantum level populated in this state. This determination yields a lower bound to the heat of reaction and with careful temperature and pressure calibration can be used in a thermochemical cycle to determine a lower bound for the dissociation energy of the emitting product.

Those chemiluminescent spectra observed under single collision conditions can be quite complicated due to the significant non-equilibrium population of internal levels. Rotational and vibrational temperatures, where defined, may approach 30,000K. In order to simplify these spectra through controlled relaxation of internal modes, the device depicted in Figure 3 has been employed. Using this device, we extend single collision chemiluminescent studies to multiple collision conditions promoting primarily rotational relaxation and, in several cases, also minimal vibrational relaxation. The

oven system depicted in Figure 3 is placed in a chamber and operated at pressures ranging from 10^{-2} to 10^{2} torr. Again the precise nature of the oven components is discussed elsewhere[1-5]. Briefly, metal atoms generated in the central and highly insulated crucible are entrained in a carrier gas (note arrows) in the region above the crucible. They are then carried to the oxidant zone where the subsequent metal + carrier mixture is oxidized forming a flame. The small arrows below the flame in the Figure denote the position of the jets used for oxidant flow. Using this system, one is able to carry out a much more straightforward evaluation of molecular constants from the spectra that are generated. In addition this multiple collision device can be used to characterize rapid intramolecular energy transfer[1-4]. Here again, the population of excited electronic states and the observed spectra are determined overwhelmingly by the reaction exothermicity. The extension of "single collision" chemiluminescent studies to multiple collision conditions serves primarily to simplify and clean-up the spectrum. Through careful application of the entraining technique, we lose little of the spectral information garnered under "single collision" conditions and add the additional dimension of studying energy transfer processes.

A device which has also proven of great use in the characterization of spectra for the alkali halides and hydroxides is shown in Figure 4. Here one takes advantage of what is commonly referred to as a diffusion flame technique. Sodium or potassium is placed in the nipple (K in Figure 4) of a large glass bulb. This bulb is then sealed and heated to a temperature such that a significant concentration of alkali vapor exists. The appropriate oxidant is passed through the inlet I and a flame is generated at the cross hatched region F. This emission is observed through a window at W which is protected from alkali deposition using an argon flow at A. Further details of this device can be found elsewhere[8].

Thermochemistry and Spectroscopy of the Alkali Halides and Hydroxides

In Table I, we present thermochemical data on the fluorides, chlorides, and hydroxides of potassium, sodium and rubidium. Comparisons will be made between these species because (1) they are valence isoelectronic and (2) their observed emission spectra are expected to be similar.

It appears that the major characterization of any of the metal hydroxides has been through flame studies. Table II summarizes the nature of this situation and clearly indicates that in the vast majority of cases, indirect evidence is obtained for the hydroxide. Indeed; the presence of the hydroxides has been inferred from the optical spectroscopic study of free atom depletion. With the exception of the mass spectrometric value for KOH, the hydroxide data in Table I is obtained directly from 2nd law plots in H_2-O_2-CO flames. Difficulties in studying the mass spectra of alkali hydroxides stem from their tendancy to form dimeric species upon vaporization[9]. In addition, it should be noted that lithium forms a very stable binary oxide[10]. The bond energies determined for KOH via flame and mass spectrometric studies are in reasonable but not spectacular agreement.

It is generally felt that the nature of bonding in alkali hydroxides should be intermediate to that in the fluorides and chlorides. With this

in mind, the trends in Table I, would seem to indicate the possibility of a bond strength higher than the mass spectrometric value. This is significant since the flame studies do indicate a higher value for the bond energy.

We have been concerned with the direct characterization of potassium and sodium hydroxide through observation of "single" and "multiple" collision chemiluminescent spectra. The first observed electronic emission spectrum for KOH has now been obtained in our laboratory. This spectrum, a fast scan of which is shown in Figure 5, correlates closely with expectations based upon the observed emission spectrum for KCl. The hydroxide spectrum was obtained by reacting potassium with 95% hydrogen peroxide. The process which yields chemiluminescence is believed to correspond to the four center reaction

$$K_2 + HO\text{-}OH \longrightarrow KOH^* + KOH \qquad (1)$$

where KOH* denotes electronically excited KOH. This process is very much analogous to a process producing excited states of the alkali halides which, for alkali-chlorine reaction, is

$$M_2 + Cl_2 \longrightarrow MCl^* + MCl \qquad (2)$$

where M is potassium, rubidium, or cesium.

The close analogy which the potassium hydroxide spectrum bears to that of KCl leads to important comparisons between the two molecules and, in the final analysis, to a direct determination of the K-OH bond strength. In Figure 6, we depict emission spectra obtained for KCl, RbCl, and CsCl under single collision conditions (Apparatus Figure 1). The nature of the potential curves which give rise to the spectra in Figure 6 is depicted in Figure 7. Although drawn for KBr, the general features are similar for all the alkali halides. The alkali halides are characterized by a relatively stable ionic ground state and a grouping of several very shallow or repulsive excited states. The emission which one observes corresponds to a transition from one of these shallow or repulsive states to levels of the ground electronic state, the spectrum corresponding to a long progression in the vibrational levels of the ground electronic (ionic) state. The very shallow nature of the excited state potential has important consequences. One finds that the KCl spectrum changes drastically with the form of excitation and the experimental technique used to produce the emission system. The "single collision" spectrum in Figure 6 onsets at 4180Å (68.4 kcal/mole). A very similar spectrum is obtained when potassium dimers are entrained in argon and this mixture oxidized in the multiple collision device shown in Figure 2. A drastic change occurs when the reaction (2) is studied in a diffusion flame environment. Here the onset of the KCl spectrum is at 2866Å[11] some 1300Å to blue of the single and mutiple collision spectrum. This large change signals an important

characteristic of the alkali halide excited state potential. Whereas emission spectra involving strongly bound excited states are not drastically altered by the nature of a changing effective potential due to rotation, the shape and nature of shallow or repulsive states can be drastically altered by rotational excitation. This is exemplified for KI in Figure 8[12]. Here effective potential curves are constructed as a function of the rotational quantum number J and the relation

$$V_{effective}(J) = V_{rotationless} + \hbar^2 \frac{J(J+1)}{2\mu R^2} \qquad (3)$$

It should be noted that there is a substantial change in the minima for the effective potentials as a function of increasing rotational excitation and hence the quantum number J. The high J potentials correspond to the single and multiple collision spectra onsetting at 4180Å[11]; the low J potentials correspond to the diffusion flame emission system onsetting at 2866Å[11]. As a result of this shift in the excited state potential one observes emission to differing sets of ground state levels. In the diffusion flame experiments emission is observed to much lower regions of the ground state potential and hence the spectra onset much further to the blue[11].

The change in the emission spectra for the alkali halides as a function of experimental conditions may also be manifest in the alkali hydroxides. One anticipates that the potential function describing the K-OH stretch will be similar to that for KCl. If the potential curves for the excited states of K-OH are similar to those for KCl, they should be shallow and the KOH emission spectrum which results from reaction (1) should change significantly with excitation technique. This is observed, although the effect is not as pronounced as that in KCl. The single and multiple collision (argon entrainment - Figure 5) spectra for KOH onset at 3840Å whereas the spectrum obtained in a diffusion flame (Figure 9) onsets at 3360Å. This significant change signals the observation of a shallow "effective" potential for the K-OH normal mode[13].

The KCl and KOH spectra correspond to emission from shallow effective potentials close to the dissociation asympotote (Figure 7 and 8) of the ground electronic state. Given that we have strong evidence for these shallow effective potentials, we can use the onset of spectral emission to estimate the dissociation energy for the K-Cl and K-OH bonds. Because the diffusion-flame results must correspond to emission to lower levels of the ground state potential, this onset is chosen to give the best estimate of the bond dissociation energy. For K-Cl, the onset at 2866Å corresponds to 99.8 kcal/mole. This should be compared to the value in Table I D_0° (K-Cl) = 102.6±2 kcal/mole. It should be apparent that we are able to estimate a good lower bound to the K-Cl dissociation energy from the energy corresponding to the onset of the K-Cl diffusion flame spectrum. The onset of the KOH diffusion flame spectrum at 3360Å yields a lower bound of 85 kcal/mole for the K-OH bond energy[14]. A similar analysis of the sodium-hydrogen peroxide diffusion flame yields a lower bound of 75.2 kcal/mole corresponding to an onset at 3800Å.

The results which we have obtained for KOH and NaOH are significant for several reasons. They represent the first direct measurements of the bond energies for these species. The lower bound deduced for the K-OH bond strength indicates that the correct dissociation energy is on the order of 88±2 kcal/mole. This value considerably exceeds that obtained in the only mass spectrometric study of the manomer quoted in Table I. This much higher value for the KOH bond energy is consistent with the bounds estimated from metal atom flame depletion studies. An 8 kcal increase in the KOH bond strength has significant implications for the stability and effect of this compound in energy generating systems. The lower bound determined for the NaOH dissociation energy is consistent with the value 79±2 kcal/mole obtained in metal atom depletion studies.

It is anticipated that further studies of the K_2-H_2O_2 diffusion flame system will improve the lower bound currently obtained for the K-OH dissociation energy. It should be noted that the current result is not inconsistent with the recent findings of Wormhoudt and Kolb[15]. These authors observe unusually high KOH concentrations in their studies of coal fired MHD plasmas. Also recent theoretical calculations by England[16] indicate the possibility of a higher K-OH bond energy.

In addition to a refinement of the K-OH bond energy, the K_2-H_2O_2 diffusion flame spectrum will be used to provide structural information which can serve to map the ground state potential. The structural parameters (molecular constants) obtained will be of use in the calculation of thermodynamic properties for KOH. These studies are currently underway in our laboratory.

Laser Spectroscopy of Na_2O

In order to efficiently excite fluorescence from Na_2O we have constructed the device depicted in Figure 10. Figures 10(a) and 10(b) indicate the overall layout of the cell used in these experiments. Figure 10(c) indicates the window design which is frequently necessary when working with refractory species, the gas flow system being designed to provide a uniform circulation of gas over the windows. In order to carefully control the vaporization of Na_2O in a very localized region, the device depicted in Figures 10(d) and 10(e) is used. It consists of a crucible which is suspended on a 1/8" stainless steel tube such that once the overall device is connected to the cell sidearm, the crucible is centrally located to the viewing port. The positioning control whose diameter is the same as the window shown in Figure 10(c) is held in place in precisely the same fashion as the window. When connected to the overall cell, the crucible holder is rotated 90° with respect to its depiction in the Figure. When the cell is in operation, a laser beam traverses the path indicated in Figures 10(b) and 10(d). Na_2O is directly vaporized through a thin slit into the path of the laser beam. The slit and the laser beam are parallel and the laser induced fluorescence is viewed at 90°[17].

Using the cell described above and various pumping schemes, we have carried out experiments at both 100 μ (primarily background argon) and 10^{-6} torr. This range of background pressure allows us not only to do spectroscopy but also to observe quenching effects which appear to be quite

significant for Na_2O. Thus far, experiments have been conducted primarily with an argon ion laser; however, some excitation has been accomplished with a rhodamine dye laser. Examples of the spectra tentatively assigned to Na_2O are shown in Figure 11. They correspond to excitation at 5145 and 4880Å. It appears that we can excite laser induced fluorescence with several of the available argon ion laser lines (4579, 4765, 4880, 4965, 5017, 5145Å) and that the fluorescence spectra can be interconnected (significant overlap) in a rather substantial Deslanders Table. Much of our analysis of the observed spectra has depended on relating our Na_2O studies to available information on Li_2O. These data come primarily from matrix isolation spectroscopy[18] and recent quantum chemical calculations[19]. Briefly, the data has been used to (1) attempt to estimate the normal frequencies of vibration for Na_2O based on a reasonable extrapolation from Li_2O and (2) determine the most likely electronic transition which should be excited in the visible using an argon ion laser.

Using a notation common to several quantum chemical descriptions of linear $D_{\infty h}$ Li_2O, the valence orbital configuration for the ground state is

$$\ldots(3\sigma_g)^2(2\sigma_u)^2(1\pi_u)^4 \qquad {}^1\Sigma_g^+ \qquad (4)$$

where the valence orbitals are constructed primarily from 2s and 2p electrons on lithium and oxygen. The lowest Li_2O excited states correspond to the promoted configurations

$$\ldots(3\sigma_g)^2(2\sigma_u)^2(1\pi_u)^3(4\sigma_g)^1 \qquad {}^{1,3}\Pi_u \qquad (5)$$

$$\ldots(3\sigma_g)^2(2\sigma_u)^2(1\pi_u)^3(3\sigma_u)^1 \qquad {}^{1,3}\Pi_g \qquad (6)$$

and Grow and Pitzer[19b] have shown that these states are very low lying ($\Delta E_{excitation} \leq 1.3$ eV); therefore it is unlikely that even the strongly allowed ${}^1\pi_u - {}^1\Sigma_g^+$ transition corresponds to the fluorescence observed upon single photon pumping with an argon ion laser. A further promotion which will result in a strongly allowed transition, most likely in the visible region, leads to the configuration

$$\ldots(3\sigma_g)^2(2\sigma_u)^1(1\pi_u)^4(4\sigma_g)^1 \qquad {}^{1,3}\Sigma_u^+ \qquad (7)$$

We anticipate that the visible transition in Na_2O which is pumped by the argon ion laser corresponds to a $^1\Sigma_u^+ \leftarrow {}^1\Sigma_g^+$ excitation involving the analog of configurations (1) and (4). In pumping this transition one removes an electron from an orbital which is both Na-O and Na-Na antibonding and promotes this electron to an orbital which is both Na-O and Na-Na bonding. Hence, we expect that both the excited state stretching and bending frequencies should exceed that of the ground electronic state of Na_2O.

The ground state frequencies for Li_2O are (matrix isolation spectroscopy) $\nu_1 \approx 760$ cm^{-1}, $\nu_2 \approx 112$ cm^{-1}, and $\nu_3 \approx 990$ cm^{-1}. Formulating a normal coordinate analysis based on the Li_2O measurements, we estimate a vibrational frequency of between 540 and 585 cm^{-1} for the symmetric stretch (ν_1) and 74 cm^{-1} for the bending mode of Na_2O. This is not unreasonable when comparisons are made with NaO where the vibrational frequency appears to be ~526 cm^{-1} (recall that Na_2O appears to be a linear molecule).

Although absolute quantum level numberings have not been assigned[20], our extensive Deslandres Tables for the pumped transitions indicate an upper state vibrational frequency of ~650 cm^{-1} and a lower state (ground state) frequency of ~550 cm^{-1} consistent with the predictions outlined above. In addition, a closer view (Figure 12) of a region of the 5145Å spectrum in Figure 2 reveals what appear to be ~70 cm^{-1} separations expected for ground state bending mode of Na_2O. Tentatively, it appears that the spectra correspond to progressions in the symmetric stretching and bending modes of the ground and excited state in a $^1\Sigma_u^+ \leftarrow {}^1\Sigma_g^+$ transition.

These studies not only provide information which is extremely useful for the understanding of fundamental dynamic processes such as the reaction of sodium dimers and oxygen atoms but also they establish a foothold for analyzing kinetic processes in which Na_2O plays a significant role. Because Na_2O represents an important constituent in energy generating systems, we desire a means to carefully monitor its behavior. It should also be noted that in addition to their use for the characterization of reaction kinetics, the current studies allow the independent determination of thermodynamic parameters which are extremely useful in the modeling of energy systems. Before the advent of the laser, the study of these elevated temperature free radicals rested primarily within the province of the matrix isolation spectroscopist. The versatility introduced with the laser should allow the future comparison of molecular behavior in gas phase and matrix environments.

Bonding and Spectra of the Alkali Monoxides

There have been relatively few spectroscopic or thermodynamic studies of the alkali oxides. Based on the results of molecular beam studies (alkali metals + NO_2), Herm and Hershbach[21] have estimated the MO bond dissociation energies as follows: LiO (82±4), NaO (67±3), KO (71±3), RbO (68±3), and CsO (70±3 kcal/mole). The value for NaO is in fair but not spectacular agreement with the value of 60.3±4 kcal/mole deduced by Murad and Hilderbrand[22] using mass spectroscopy. Fundamental frequencies for LiO (750 cm^{-1})[18], KO (384)[23], and CsO (314)[23] have been measured using matrix isolation spectroscopy; however, the corresponding infrared absorptions in NaO and RbO have not yet been observed.

Evidence has been obtained for a change in the orbital makeup and symmetry of the ground electronic state upon traversing the series Li...CsO. The electronic ground state of LiO is $^2\Pi$. Freund et al.[24] have obtained very detailed spectra which demonstrate that this molecule is well represented by a crystal field model based on $Li^{\oplus}O^{\ominus}$. This model is in accord with ab initio calculations[25].

Reactive scattering experiments[21] have indicated that NaO also has a $^2\Pi$ ground state whereas the ground state of CsO is of $^2\Sigma$ symmetry. Most recently ESR-matrix experiments[26] have also demonstrated that RbO and CsO have $^2\Sigma$ ground states whereas the ground states of LiO, NaO and KO are probably $^2\Pi$. The observation of a $^2\Sigma^+$ ground state conflicts with the simple ionic model in which the electron donated by the alkali atom enters the $2p\sigma$ oxygen orbital along the internuclear axis, leaving a hole in the 2π orbital and resulting in a $^2\Pi$ state ($\sigma^2\pi^3$ molecular orbital configuration). An explanation for the observed trends can be obtained by evoking the concept of "inner shell bonding" in which one considers the mixing of filled (n-1)p alkali orbitals with the 2p oxygen orbitals. Figure 13 contrasts the molecular orbital scheme for NaO based on the alkali valence orbitals with the adjusted intershell orbital scheme for CsO[26,27]. The alkali monoxides are highly ionic molecules, $M^{\oplus}O^{\ominus}$, in both schemes but the latter gives a $^2\Sigma$ ground state ($...\pi^4\sigma$). The change from the valence to the inner shell scheme is governed by the location of the (n-1)p orbitals of M^+. These orbitals lie far below the 2p orbitals of O^- for Li or Na but become comparable in energy for Rb or Cs.

The significance of the orbital scheme discussed above can best be understood if we focus on the calculated ab-initio curves for LiO (Figure 14). It is apparent that the ground $X^2\Pi$ and low lying $A^2\Sigma^+$ states are separated by less than 2300 cm^{-1}. This energy increment will decrease for the sodium and potassium oxides. For RbO the $A^2\Pi_i$ state is separated by less than 3800 cm^{-1} from the ground $X^2\Sigma^+$ state[26].

We have obtained a preliminary chemiluminescent spectra for NaO using the chemiluminescent reaction

$$Na + N_2O \longrightarrow NaO^* + N_2$$

This spectrum is depicted in Figure 15. It would appear to correspond to emission between high vibrational levels of the $A^2\Sigma^+$ state and low vibrational levels of $X^2\pi$. The spectral cutoff at long wavelength is due to a rapid decrease in system detection efficiency. Similar spectra have now been observed for KO and NaS. Further investigations of these systems are planned when a red detection system has been assembled in our laboratory.

References

1. D. M. Lindsay and J. L. Gole, J. Chem. Phys. 66, 3886 (1977).

2. M. J. Sayers and J. L. Gole, J. Chem. Phys. 67, 5442 (1977).

3. J. L. Gole and S. A. Pace, J. Chem. Phys. 73, 836 (1980).

4. A. W. Hanner and J. L. Gole, J. Chem. Phys. 73, 5025 (1980).

5. G. J. Green and J. L. Gole, Chem. Phys. 46, 67 (1980).

6. J. L. Gole, Ann. Rev. Phys. Chem. 27, 525 (1976).

7. C. L. Chalek and J. L. Gole, J. Chem. Phys. 65, 2845 (1976); Chem. Phys. 19, 59 (1977) and see also reference 5 and references therein.

8. A. Tewarson, "Studies of Chemiluminescent Emission in Selected Low-Pressure Diffusion Flames", Ph.D. Thesis, Penn State University, 1969.

9. See for example, J. W. Hastie, "High Temperature Vapors, Sciences, and Technology", Academic Press, New York, 1975.

10. See for example, Cotton and Wilkinson, "Advanced Inorganic Chemistry", Third Edition, Interscience, New York, 1972.

11. See reference 8 and note also R. C. Oldenborg, J. L. Gole and R. N. Zare, J. Chem. Phys. 60, 4032 (1974). The longwavelength limit of the diffusion flame spectrum is 4654Å vs. 5708Å for the single collision spectrum. Hence the entire KCl spectrum is shifted to the blue ~1200Å when experimental conditions are changed from the single collision to the diffusion flame environment.

12. Taken from Oldenborg et. al. reference 11. Based on the study by K. J. Kaufmann, J. L. Kinsey, H. B. Palmer and A. Tewarson, J. Chem. Phys. 60, 4023 (1974).

13. Of course it is not completely correct to speak of an isolated K-O stretch in the KOH molecule. In reality there will be some coupling with the O-H stretch and the bending mode of the triatomic.

14. This is a stringent lower bound and more refined diffusion flame studies should yield an even higher value. Based upon the probable dissociation products for the ground and excited states of KOH, it is likely that the upper excited state potential may be significantly bound with respect to the dissociation assymptote of the ground electronic state. The much smaller change in the diffusion flame vs. single collision spectrum for KOH versus that for KCl indicates that this is probably the case. We anticipate that the emitting excited state of KOH may be bound by as much as 10 kcal/mole relative to the dissociation assymptote of the ground state.

15. J. Wormhoudt and C. E. Kolb, "Mass Spectrometric Determination of Negative and Positive Ion Concentrations in Coal-Fired MHD Plasmas", 10th Materials Research Symposium, NBS Special Publication 561, Volume 2.

16. W. B. England, J. Chem. Phys. 68, 4896 (1978).

17. It should be noted that extensive baffling is used in the system to avoid problems with scattered laser light.

18. a. R. C. Spiker, Jr. and Lester Andrews, J. Chem. Phys. 58, 702 (1973).
b. D. White, K. S. Seshardri, D. F. Dever, D. E. Mann and M. J. Linevsky, J. Chem. Phys. 39, 2463 (1963).
c. K. S. Seshardri, D. White, and D. E. Mann, J. Chem. Phys. 45, 4697 (1966).

19. a. R. J. Buenker and S. D. Peyerimhoff, J. Chem. Phys. 45, 3682 (1966).
b. D. T. Grow and R. M. Pitzer, J. Chem. Phys. 67, 4019 (1977).
c. E. L. Wagner, Theoret. Chim. Acta 32, 310 (1974).
d. T. K. Lin and D. D. Ebbing, Int. J. Quant. Chem. 6, 297 (1972).

20. The notation in Figure 1 is designed to give a relative numbering. Because v' and v", the absolute quantum numbers for the upper and lower states are not known, we use the notation v' + n', v" + n" where the indices in the figure denote the values of n' and n". In this case it is likely that the value of v" will exceed that for the level from which laser pumping occurs.

21. R. R. Herm and D. R. Herschbach, J. Chem. Phys. 52, 5783 (1970).

22. D. L. Hildenbrand and E. Murad, J. Chem. Phys. 53, 3403 (1970).

23. R. C. Spikers and L. Andrews, J. Chem. Phys. 58, 713 (1973).

24. J. M. Fruend, E. Herbst, R. P. Mariella, Jr. and W. Klemperer, J. Chem. Phys. 56, 1467 (1972).

25. M. Yoshimine, J. Chem. Phys. 57, 1108 (1972); B. Liu and M. Yoshimine, J. Chem. Phys. 60, 1427 (1974).

26. D. M. Lindsay, D. R. Herschbach and A. L. Kwiram, Mol. Phys. 32, 1199 (1976).

27. J. R. Morton and W. E. Falconer, J. Chem. Phys. 39, 427 (1963); W. E. Falconer, J. R. Morton and A. G. Streng, ibid 41, 902 (1964); R. C. Eachus and M. C. R. Symons, J. Chem. Soc. A304 (1971).

Figure Captions

Figure 1: Schematic of apparatus for the study of "single collision" chemiluminescent reactions.

Figure 2: Energy conservation in a "single collision" chemiluminescent reaction.

Figure 3: Schematic of burner system used for the study of multiple collision chemiluminescent spectra. See text for discussion.

Figure 4: Sketch of apparatus used for studying low-pressure chemiluminescent diffusion flames of alkali metal vapors burning in halogens and hydrogen peroxide. See text for discussion.

Figure 5: Chemiluminescent spectrum obtained for KOH* formed via the reaction of potassium dimers and 95% hydrogen peroxide. See text for discussion.

Figure 6: Chemiluminescent spectra of (a) KCl, (b) RbCl, (c) CsCl, with a resolution of 5Å or better. Also present in each trace are atomic (alkali) lines, some of which are off scale. (taken from reference 11.) See text for discussion.

Figure 7: Potential energy curves for an alkali halide molecule (drawn for KBr) showing the "zeroth order crossing" of the ionic and covalent states.

Figure 8: Effective excited state potential curves for KI constructed from the rotationless potential of Kauffman, Kinsey, Palmer, and Tewarson (reference 12) assuming a dissociation asymptote of 27000 cm^{-1} (see reference 11).

Figure 9: Chemiluminescent spectrum obtained for KOH* formed in a diffusion flame environment. See text for discussion.

Figure 10: Schematic diagram of apparatus for laser fluorescence studies of Na_2O.

Figure 11: Laser induced photoluminescence spectra of Na_2O taken at a resolution of 1Å and using the 5145 and 4880Å argon ion laser lines for excitation. See text for discussion.

Figure 12: Close-up of laser induced photoluminescence spectrum of Na_2O taken at a resolution of 0.5Å and using the 5145Å argon ion laser lines for excitation. See text for discussion.

Figure 13: Molecular orbital scheme for the alkali monoxides. See text for discussion.

Figure 14: Potential curves for extensive CI calculations on the $X^2\Pi$ and $A^2\Sigma^+$ of LiO.

Figure 15: Chemiluminescent spectrum tentatively attributed to NaO* formed in the reaction $Na+N_2O \rightarrow NaO^*+N_2$.

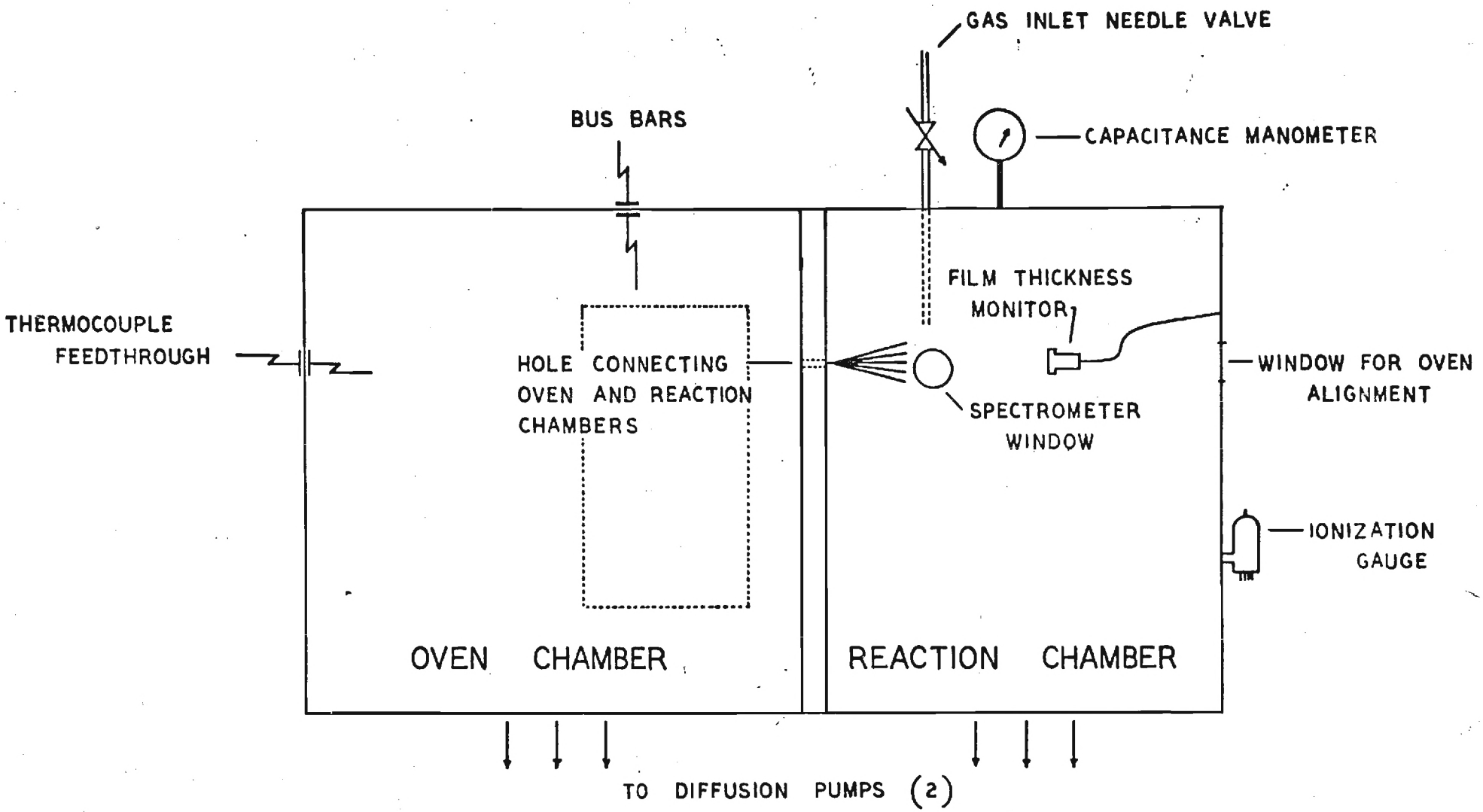
GAS INLET NEEDLE VALVE
BUS BARS
CAPACITANCE MANOMETER
FILM THICKNESS MONITOR
THERMOCOUPLE FEEDTHROUGH
HOLE CONNECTING OVEN AND REACTION CHAMBERS
WINDOW FOR OVEN ALIGNMENT
SPECTROMETER WINDOW
IONIZATION GAUGE
OVEN CHAMBER
REACTION CHAMBER
TO DIFFUSION PUMPS (2)

Figure 1

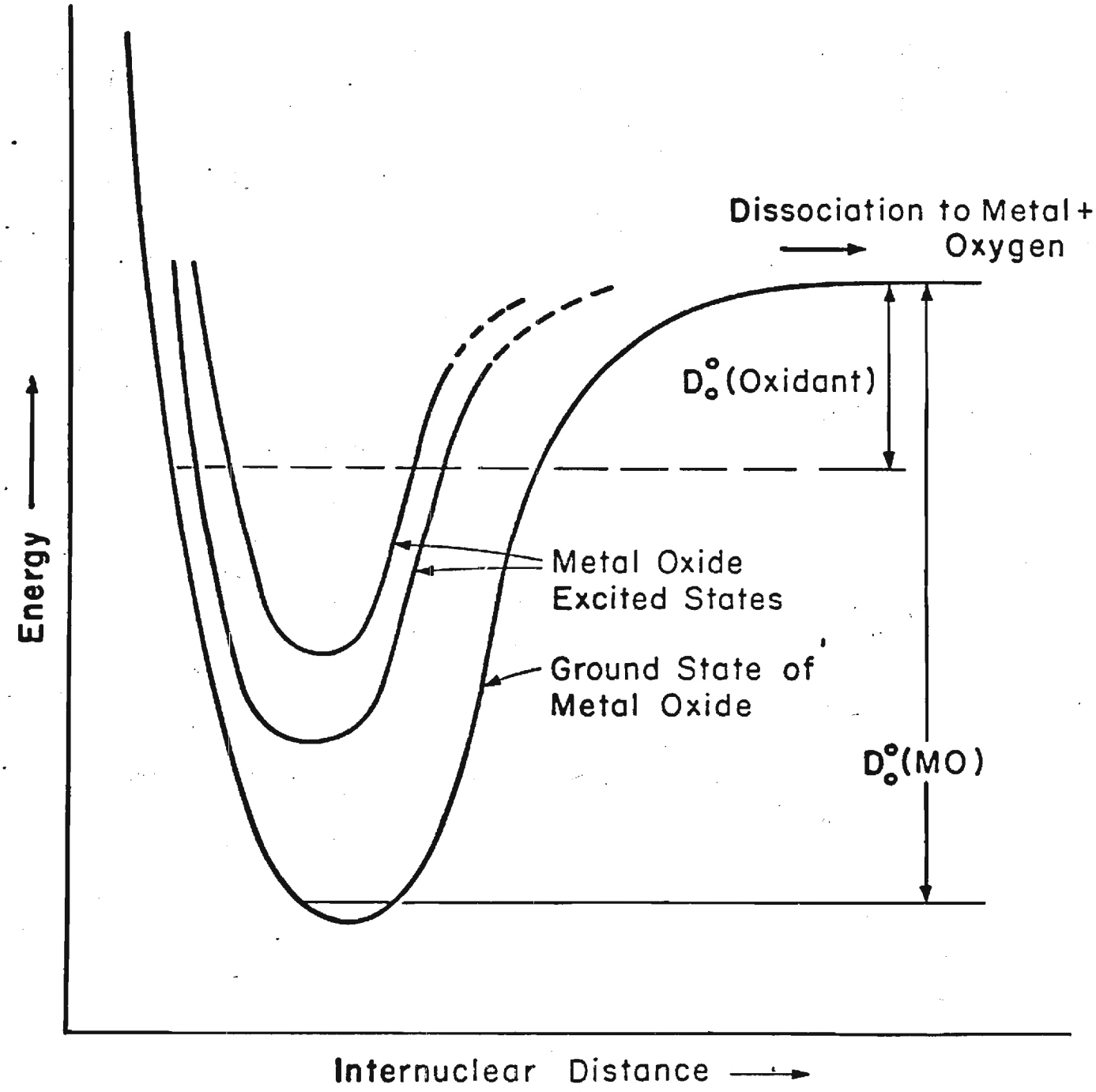
Dissociation to Metal + Oxygen
D_o°(Oxidant)
Energy
Metal Oxide Excited States
Ground State of Metal Oxide
D_o°(MO)
Internuclear Distance

Figure 2

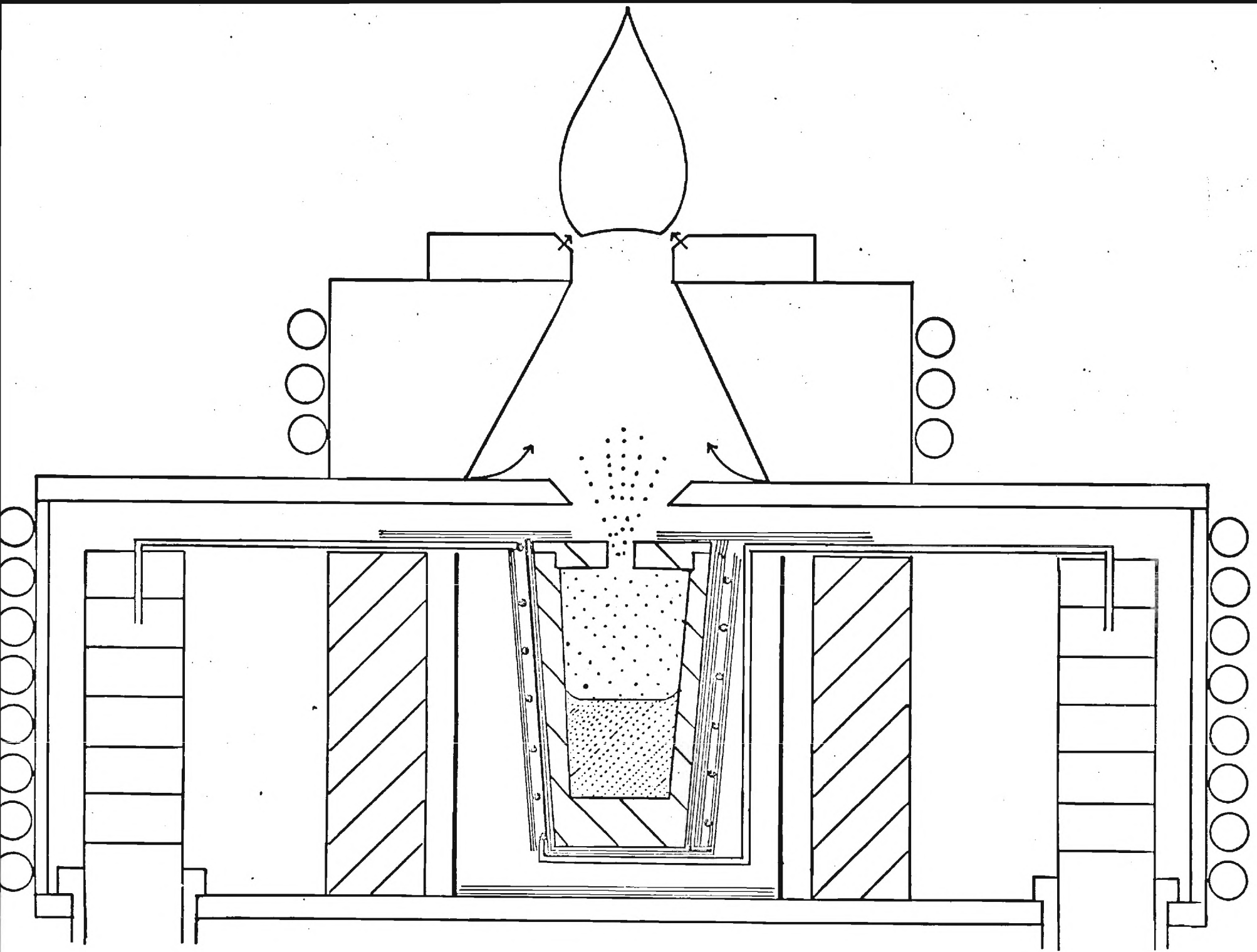

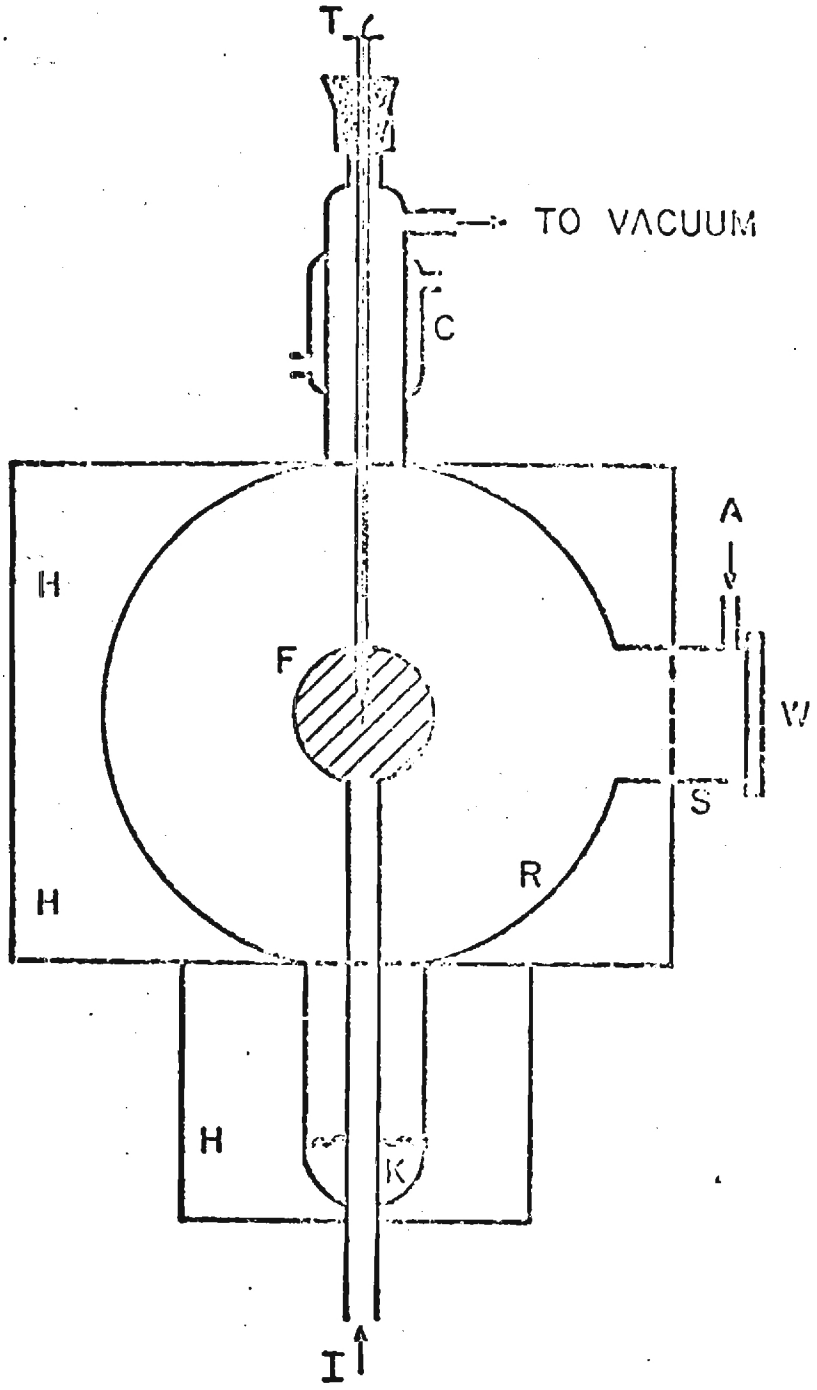

Figure 4

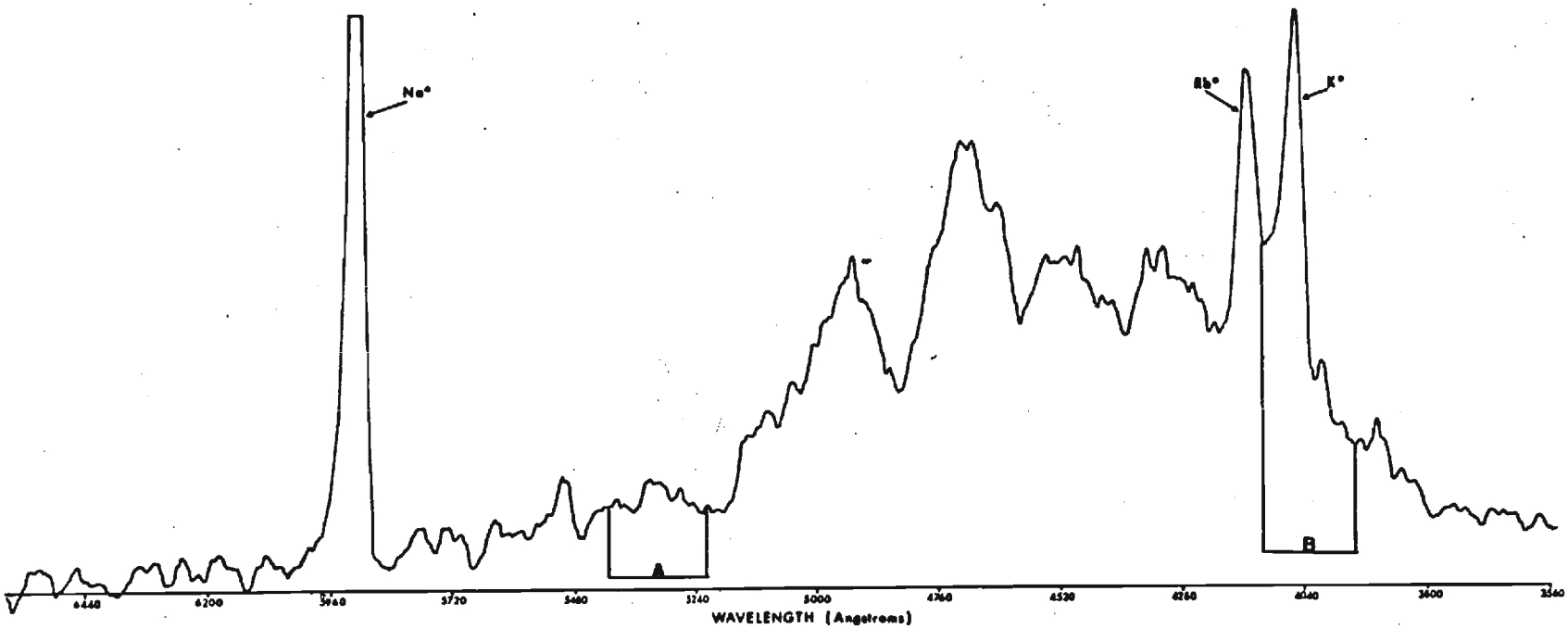
Na°
Rb°
K°
A
B
6440
6200
5960
5720
5480
5240
5000
4760
4520
4280
4040
3800
3560
WAVELENGTH (Angstroms)

Figure 5

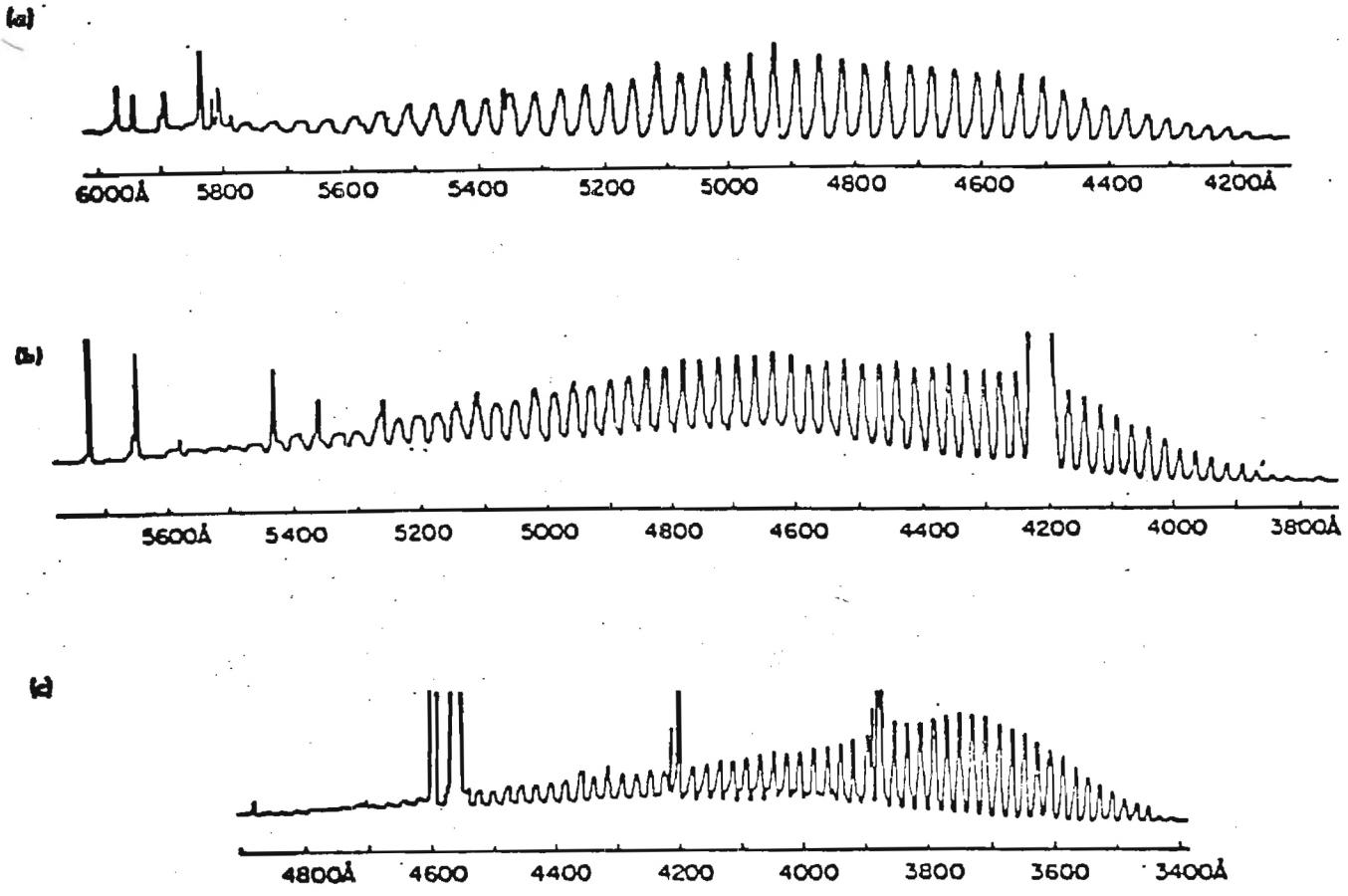
(a)
6000Å 5800 5600 5400 5200 5000 4800 4600 4400 4200Å
(b)
5600Å 5400 5200 5000 4800 4600 4400 4200 4000 3800Å
(c)
4800Å 4600 4400 4200 4000 3800 3600 3400Å

Figure 6

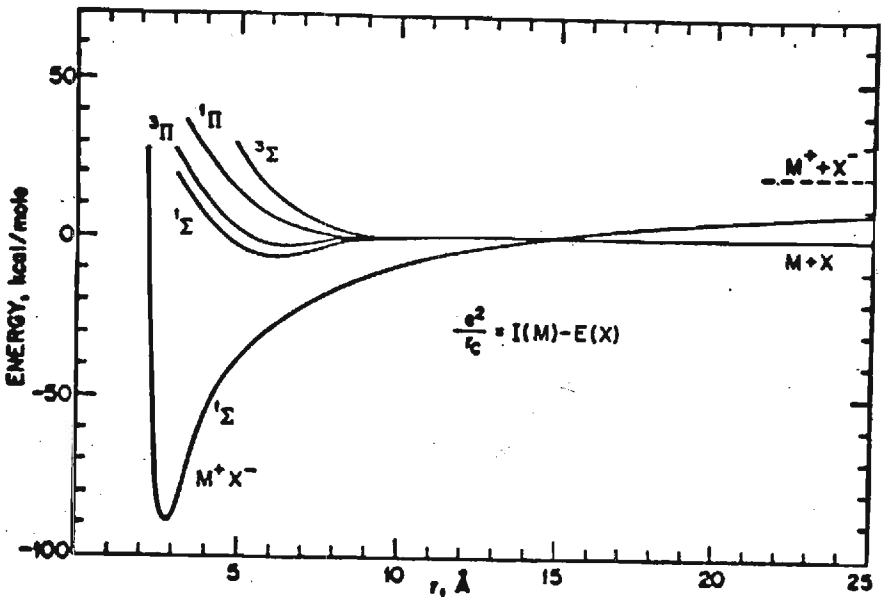
50
0
-50
-100
ENERGY, kcal/mole
5
10
15
20
25
r, Å
$^3\Pi$
$^1\Pi$
$^3\Sigma$
$^1\Sigma$
M^+X^-
M+X
$\frac{e^2}{r_c} = I(M)-E(X)$
$^1\Sigma$
M^+X^-

Figure 7

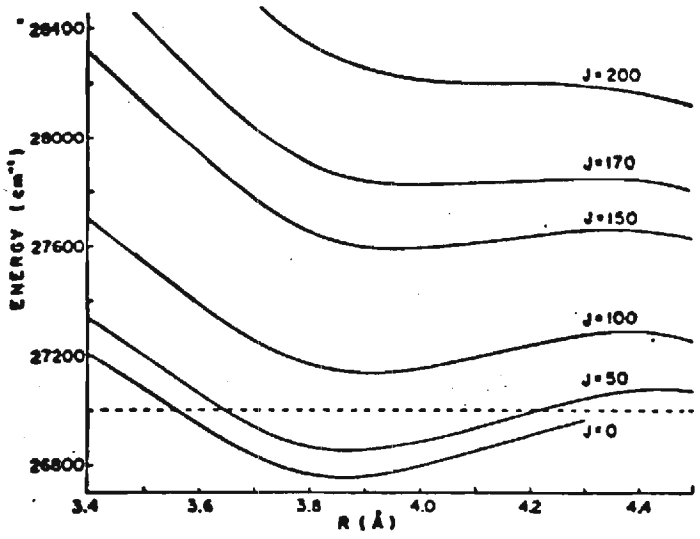
28400
28000
27600
27200
26800
ENERGY (cm⁻¹)
3.4
3.6
3.8
4.0
4.2
4.4
R (Å)
J=200
J=170
J=150
J=100
J=50
J=0

Figure 8

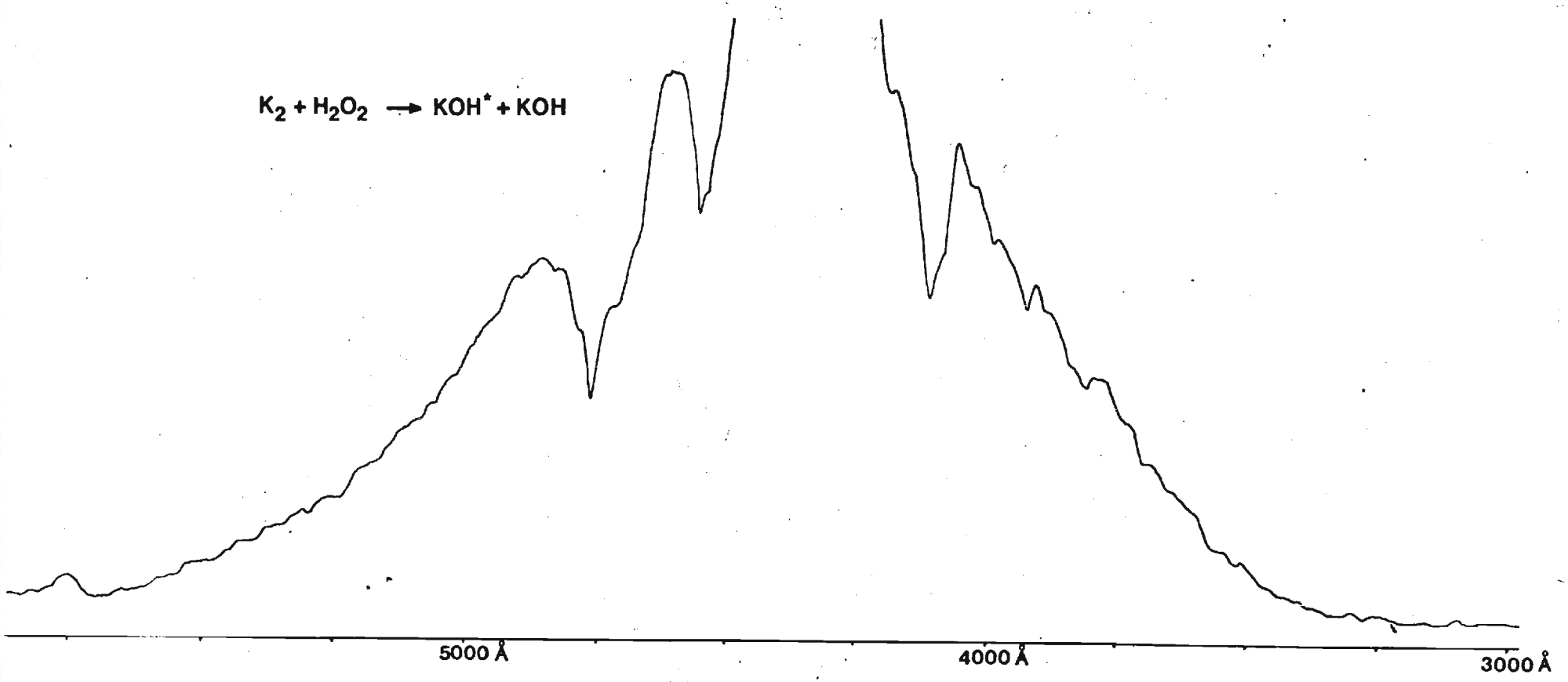

Figure 9

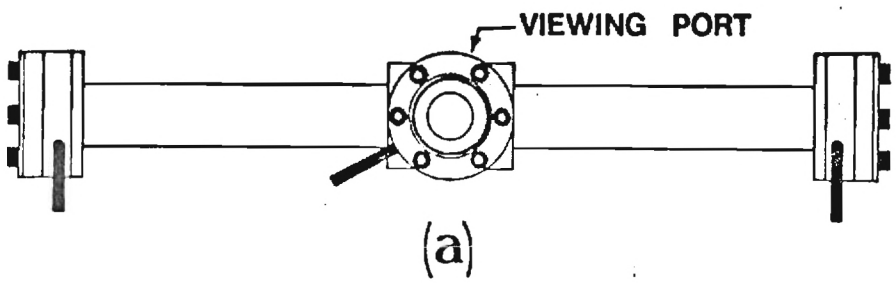

(a)

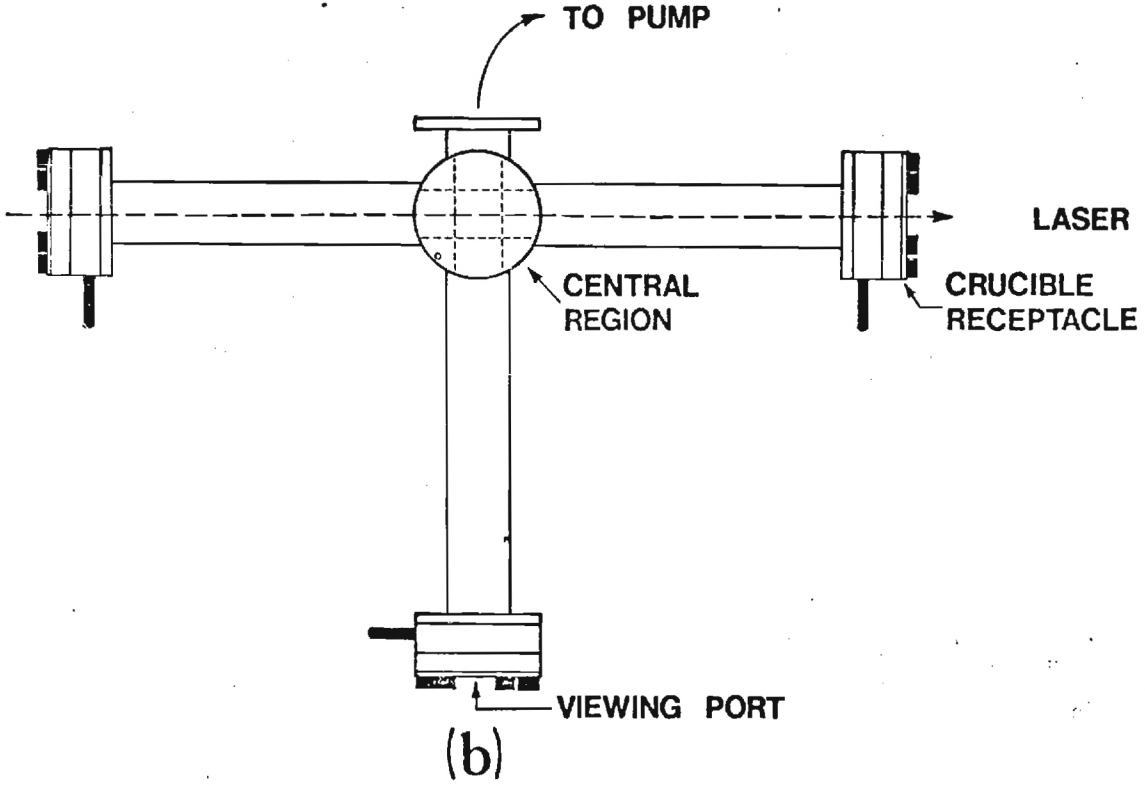

(b)

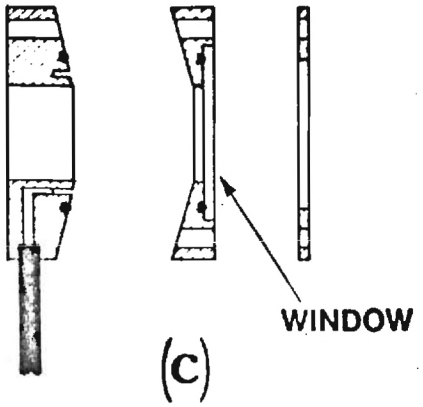

(c)

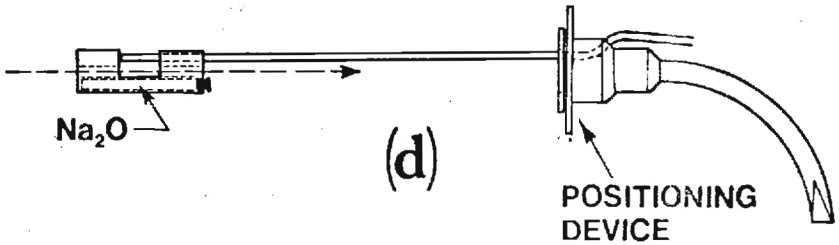

(d)

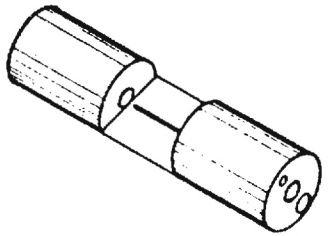

(e)

Figure 10

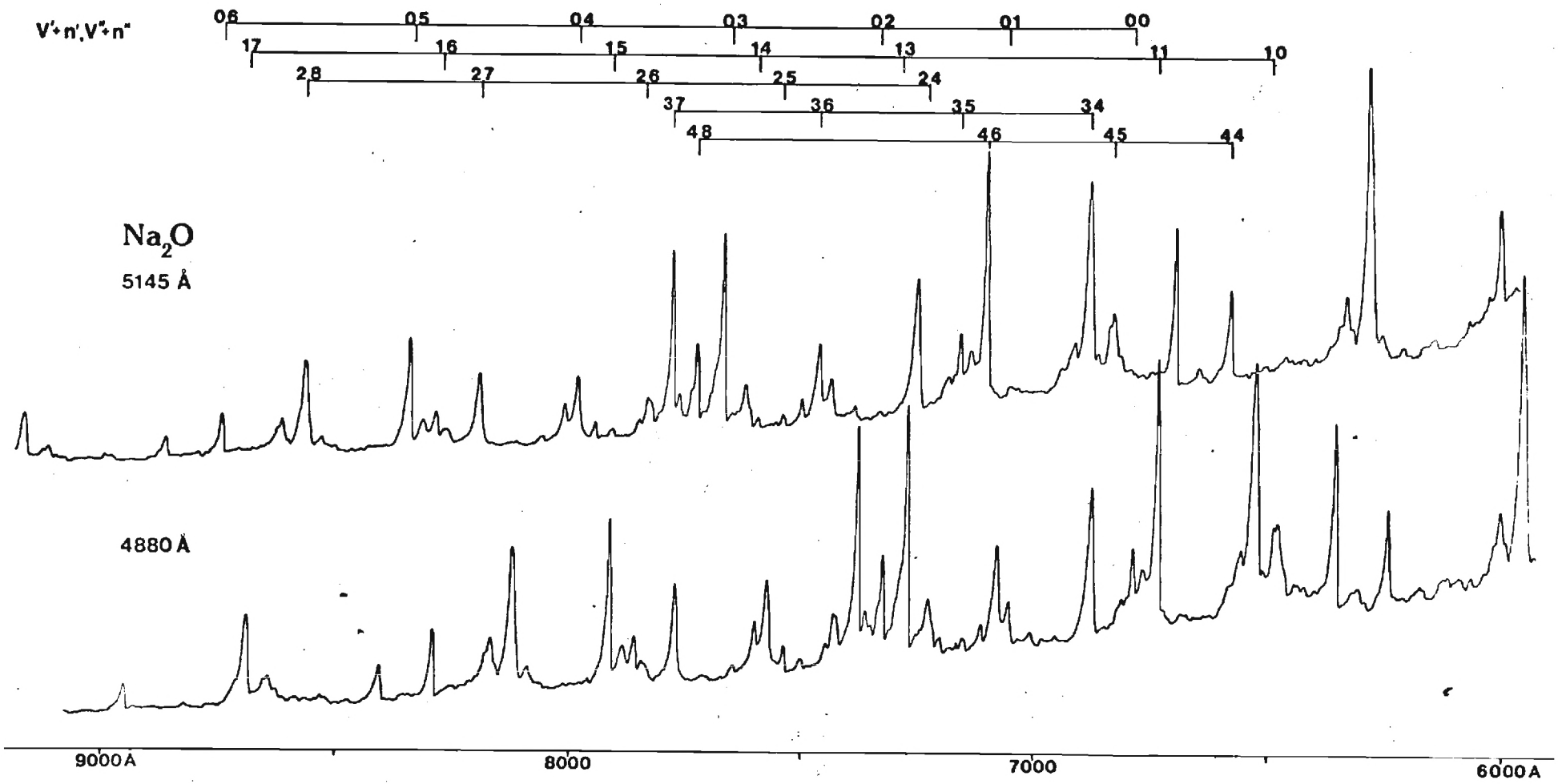
V'+n',V"+n"
06
05
04
03
02
01
00
17
16
15
14
13
11
10
28
27
26
25
24
37
36
35
34
48
46
45
44
Na_2O
5145 Å
4880 Å
9000 Å
8000
7000
6000 Å

Figure 11

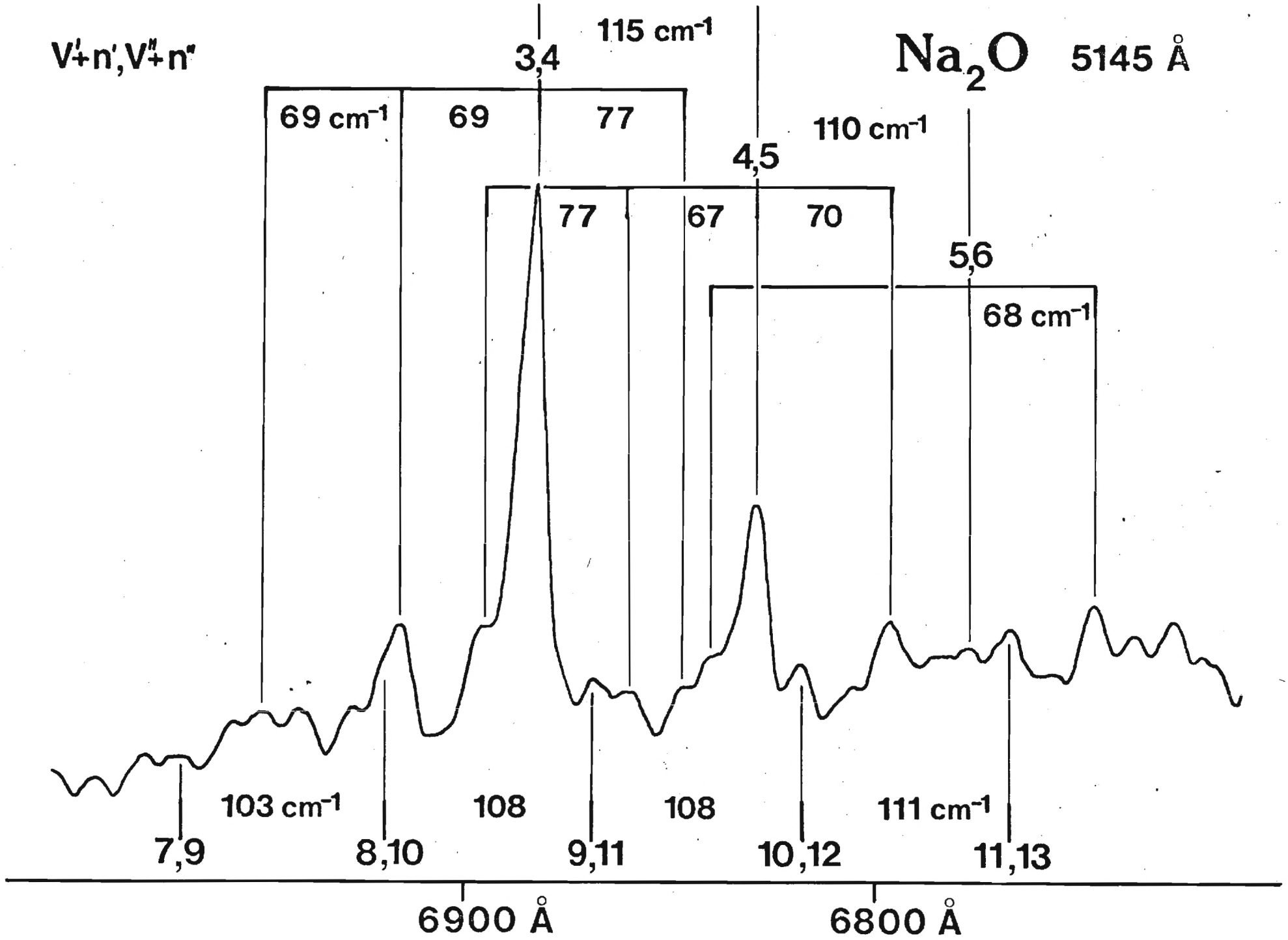
V'+n',V''+n''
115 cm-1
3,4
Na2O 5145 Å
69 cm-1
69
77
110 cm-1
4,5
77
67
70
5,6
68 cm-1
103 cm-1
108
108
111 cm-1
7,9
8,10
9,11
10,12
11,13
6900 Å
6800 Å

Figure 12

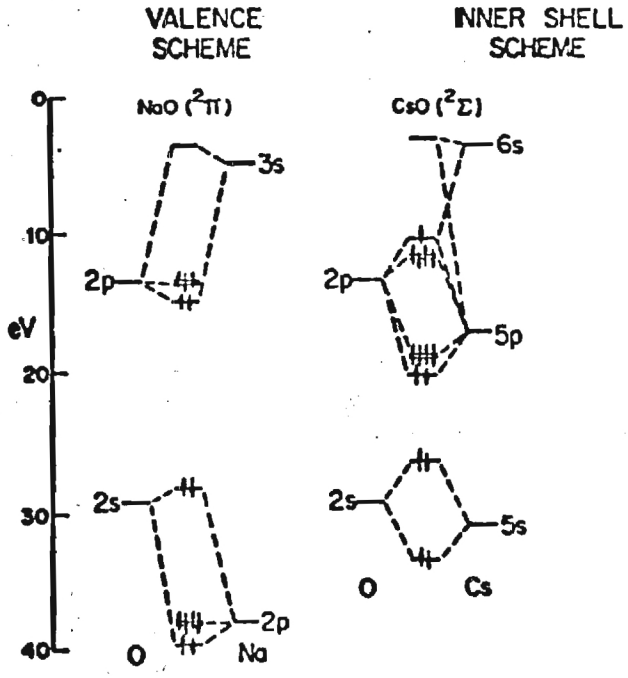
VALENCE SCHEME
INNER SHELL SCHEME
NaO ($^2\Pi$)
CsO ($^2\Sigma$)
0
10
20
30
40
eV
3s
2p
2s
2p
O
Na
6s
2p
5p
2s
5s
O
Cs

Figure 13

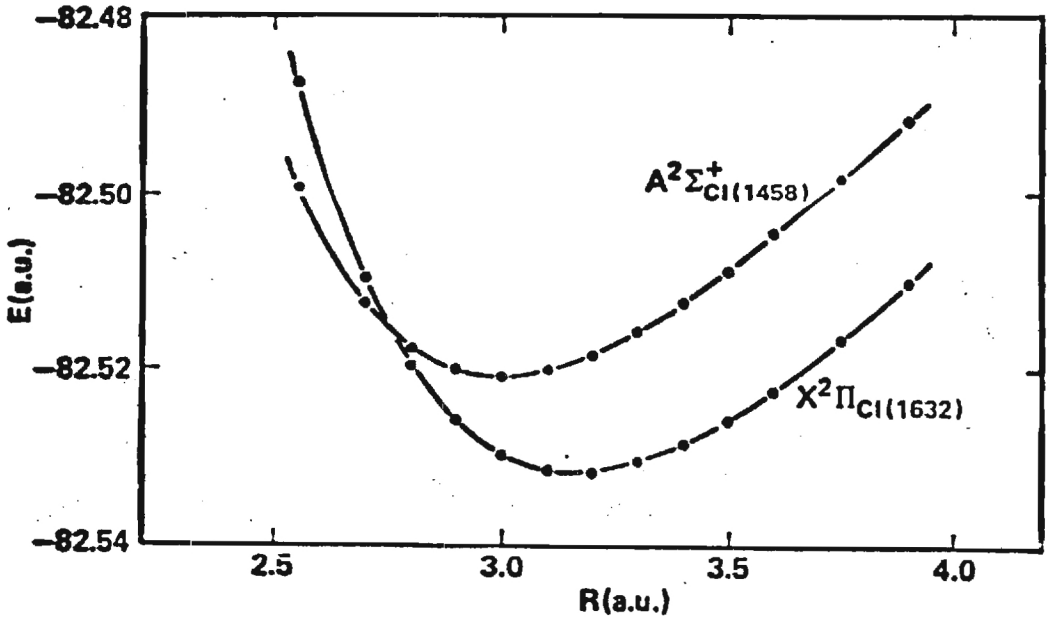
-82.48
-82.50
-82.52
-82.54
E(a.u.)
2.5
3.0
3.5
4.0
R(a.u.)
$A^2\Sigma^+_{CI(1458)}$
$X^2\Pi_{CI(1632)}$

Figure 14

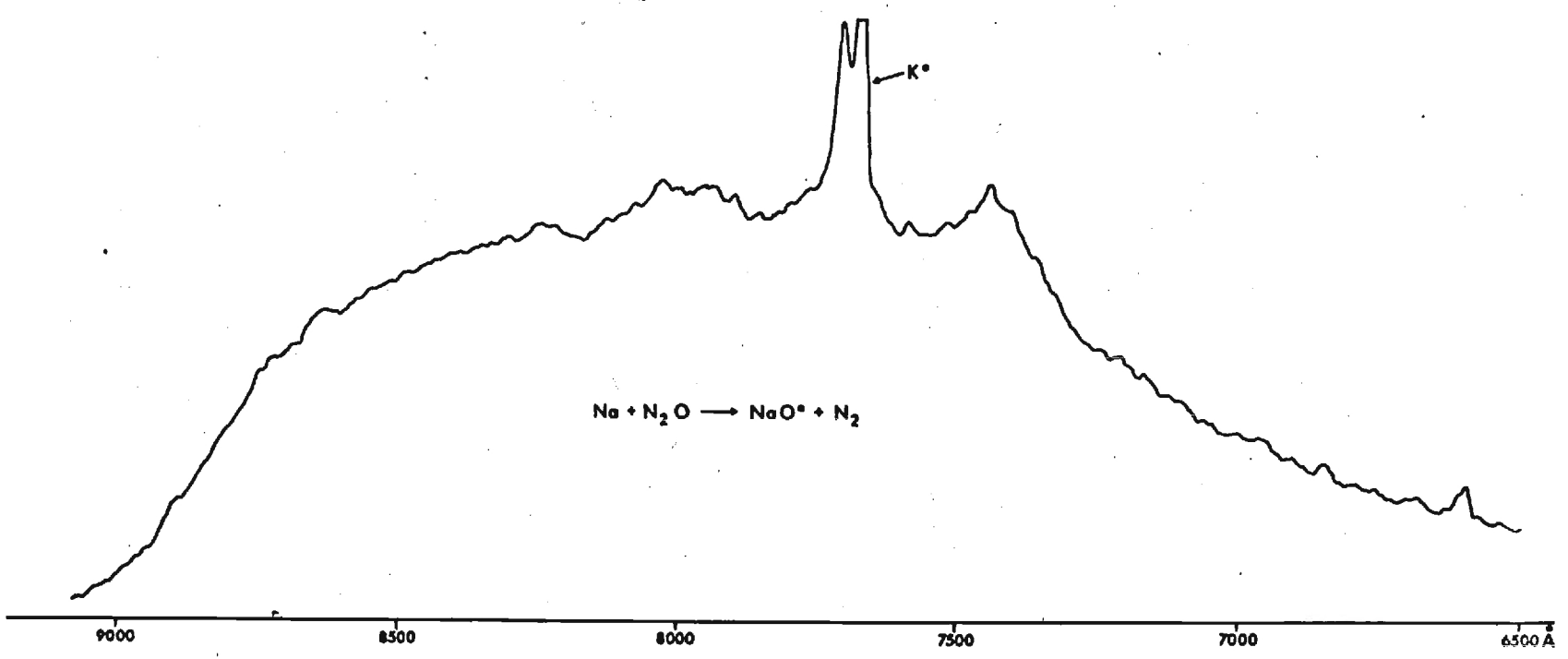

Figure 15

TABLE 1

	$D_0^0(M-X)$	
KF	117[a]	THERMOCHEMICAL
KCl	102.6±2[b]	THERMOCHEMICAL AND PHOTOFRAGMENT
KOH	84±2.5[c]	H_2-O_2-CO_2 FLAMES 2nd LAW DETERMINATION
	80±3[d]	MASS SPECTROMETRY
NaF	123[e]	NaOH 79±2[c] (FLAME--2nd LAW)
NaCl	97.6±2[b]	
RbF	115[f]	RbOH 86±3[c] (FLAME--2nd LAW)
RbCl	101.3±2[b]	

a. E. M. Bulewicz, C. G. James, T. M. Sugden, Trans. Faraday Soc. 37, 921 (1961); A. G. Gaydon, "Dissociation Energies and Spectra of Diatomic Molecules", 3rd Edition, Chapman and Hall, 1968.

b. T-M. R. Su and S. J. Riley, J. Chem. Phys. 72, 6632 (1980).

c. R. Kelly and P. J. Padley, Trans. Faraday Society, 67, 740 (1971).

d. L. N. Gorokhov, A. V. Gusarov and I. G. Panchenkov, Russ. J. Phys. Chem. 44, 150 (1970).

e. See reference a.

f. See reference a and A. D. Caunt and R. F. Barrow, Nature, 164, 753 (1949).

TABLE 2

Species	Nature of the Detection Method and Comments
AlOH	Mass spectrometric analysis of lean H_2-O_2 flames containing aluminum.[a] Controversial results.
Alkali Hydroxides	
LiOH	Inferred from optical spectroscopic study of free atom depletion in H_2-O_2-N_2 [b] and H_2-O_2-CO_2 [c] flames.
NaOH	Inferred from optical spectroscopic study of free atom depletion in H_2-O_2-N_2 [b] and H_2-O_2-CO_2 [c] flames.
KOH	Inferred from optical spectroscopic study of free atom depletion in H_2-O_2-N_2 [b] and H_2-O_2-CO_2 [c] flames.
RbOH	Inferred from optical spectroscopic study of free atom depletion in H_2-O_2-N_2 [b] and H_2-O_2-CO_2 [c] flames.
CsOH	Inferred from optical spectroscopic study of free atom depletion in H_2-O_2-N_2 [b] and H_2-O_2-CO_2 [c] flames.
Alkaline Earth Hydroxides	
CaOH	Molecular emission observed in post-flame gases of H_2-O_2-N_2 flames.[d] Presence also inferred from optical spectroscopic study of free atom depletion[e] -dissociation energy from depletion studies.[e] Also observed in acetylene-air or O_2 flames.[f]
SrOH	Molecular emission observed in acetylene-air flames.[d,f] Presence also inferred from optical spectroscopic study of free atom depletion-dissociation energy from depletion studies.[e]
BaOH	Emission in post-flame gases of H_2-O_2-N_2 flames.[d,e] Presence also inferred from spectroscopic study of free atom depletion-dissociation energy from depletion studies[e] and mass spectrometry.[g]
CuOH	Some emission band spectra observed in acetylene-air flame.[f,h]
FeOH	Emission band spectra observed in acetylene-air, H_2-O_2-N_2 and low pressure lean flames.[i] Presence also inferred from optical spectroscopic study of free atom depletion.[j]
MnOH	Emission band spectra observed in acetylene-air post-flame gases.[d,k]
InOH	Presence inferred from optical spectroscopic study of free atom depletion.[c,l]

TABLE 2 (continued)

Species	Nature of the Detection Method and Comments
GaOH	Presence inferred from optical spectroscopic study of free atom depletion.[c,l,m]

[a] M. Farber, R.D. Srivastava, M.A. Frisch and S.P. Harris, Faraday Symposium 8, High Temperature Studies in Chemistry, London, 1973.

[b] D.E. Jensen and P.J. Padley, Trans. Faraday Society 62, 2132 (1966).

[c] R. Kelly and P.J. Padley, Trans. Faraday Society 67, 740 (1971).

[d] R.W. Reid and T.M. Sugden, Disc. Faraday Soc. 33, 213 (1962); L.V. Gurvich, V.G. Ryabova and A.N. Khitrov, in "High Temperature Studies in Chemistry", Faraday Symp. No. 8, Paper 8, Chem. Soc. London (1973); J. Van der Hurk, J. Hollander and C.T.J. Alkemade, J. Quant. Spectrosc. Radiat. Transf. 13, 273 (1973).

[e] D.H. Cotton and D.R. Jenkins, Trans. Faraday Society 64, 2988 (1968).

[f] Cited in "Flame Spectroscopy" by R. Maurodiveanu and H. Boiteux, Wiley, New York (1965).

[g] F.E. Stafford and J. Berkowitz, J. Chem. Phys. 40, 2963 (1964).

[h] L.M. Bulewicz and T.M. Sugden, Trans. Faraday Society 52, 1481 (1956).

[i] M.J. Linevsky, Metal Oxide Studies; Iron Oxidation. Tech. Rep. RADC-TR-71-259.

[j] D.E. Jensen and G.A. Jones, J. Chem. Soc. Faraday Trans. I 69, 1448 (1973).

[k] P.J. Padley and T.M. Sugden, Trans. Faraday Society 55, 2054 (1959).

[l] E.M. Bulewicz and T.M. Sugden, Trans. Faraday Society 54, 830 (1958); 54, 1855 (1958).

[m] L.V. Gurvich and V.G. Ryabova, High Temp. USSR 2, 486 (1964).

A P P E N D I X E

"ASPECTS OF SPARSELY STUDIED GAS PHASE CHEMISTRY OF IMPORT TO THE ENERGY TECHNOLOGIES"

(Optical Engineering, in press)

"ASPECTS OF SPARSELY STUDIED GAS PHASE CHEMISTRY OF IMPORT TO THE ENERGY TECHNOLOGIES"

James L. Gole

Department of Chemistry
Georgia Institute of Technology
Atlanta, Georgia 30332

ABSTRACT

There is considerable interest in the need to improve the operation of systems which can potentially serve as alternate energy sources. Entailed in this effort is the desire to understand the vapor phase chemistry and compounds which may enter as by-products of the system under consideration. These compounds may have deleterious effects on the gas phase chemistry or play an important role through high temperature gas-solid corrosion kinetics. Here we outline the nature of the problem and focus on a subset of these molecules, the metal hydroxides and the alkali oxides and sulfides. A critical analysis of the data base is presented and new experiments are outlined which encompass the investigation of thermochemistry and the evaluation of molecular parameters through the study of visible, infrared, microwave and E.S.R. spectroscopy. Recent chemiluminescent experiments which lead to the evaluation of a new stringent lower-bound for the K-OH band energy are summarized. This stringent lower bound (88.2 kcal/mole) correlates within the quoted error bounds with the absolute upper bound of previous experimental determinations. Preliminary laser fluorescence studies on Na_2O are reported and the possible influence of "ultrafast" energy transfer (E-$\bar{E}$ and V-E transfer among the excited states of high temperature molecules) on the behavior of energy generating systems is noted.

INTRODUCTION

Recently, substantial interest has focused on the development of systems and technologies which can serve to avert projected energy shortages through the use of alternate fuel sources. This need has heightened the necessity for improving and optimizing the efficient use of energy systems which are, at present, typically no more than 40% efficient.

For practically all viable energy conversion systems, the common optimization parameter is the temperature. Generally the higher the temperature, the greater the efficiency for converting a source of energy to useful work. This, of course, is a direct consequence of the Carnot efficiency relation, usually expressed as

$$E_{max} = (T_{source} - T_{sink})/T_{source}$$

where E_{max} is the maximum efficiency attainable for a given source and sink temperature. Based strictly on the efficiency criterion, it is apparent that a high source temperature is desirable for energy conversion systems.

Suitable high source temperatures are definitely attainable. In coal or oil combustors or in nuclear fission fuel elements, where temperatures in excess of 2000° C are readily achieved, basic system operation problems lie in the containment of these high temperature reactive fuel systems and of the working fluid used to transfer the heat to an energy conversion unit. While this is essentially a materials problem involving, in large part, mechanical or solid state chemical phenomena, some of the materials problems arise from high temperature gas-solid

corrosion reactions and vapor phase phenomena which may enter as by-products of the system under consideration (impurities such as the alkali metals, sulfur, water vapor, etc.) or because of the introduction of seed materials (K_2SO_4 or K_2CO_3 in MHD applications) into the flow.

In this discussion, we will be concerned with a subset of these molecules which play an important role in high temperature vapor processes in the present technology or may be important in anticipated future developments. Unfortunately, data on these species is sparse and much work needs to be done. It is quite apparent that very stringent tolerance levels for certain species in process streams impose stronger requirements for reliable thermodynamic and kinetic data in order to predict the effects due to low level species concentrations. In addition, there must be serious concern focused on whether or not these systems are best represented via equilibrium or non-equilibrium models. The characterization of molecules in these systems requires the determination of bond energies and spectroscopic constants and may well require the elucidation of ultrafast intra- and intermolecular energy transfer.[1] The evaluation of spectroscopic data leads to the determination of important molecular constants which can be used for the statistical mechanical evaluation of heat capacities, entropies and free energies, all of which are important to the understanding of energy related combustion and gasification environments. In addition, the determination of the optical signature for those molecules of interest provides information useful for the characterization of non-equilibrium combustion phenomena and for the evaluation of kinetically dominated product formation routes. In order to focus on those areas where limited data needs considerable augmentation, we will first outline the nature of certain specific systems.

NATURE OF THE PROBLEM

Considerable effort will be required to attain basic parameters for molecules playing an important role in energy generating devices whose goal is the utilization of fossil fuel gasification and liquification. An important subset of these systems includes combustion powered magneto-hydrodynamics (MHD). Because MHD attempts to make a more varied use of the combustion environment, we focus on the nature of MHD power generation; however, excluding the use of seed materials, all high temperature combustion systems (coal gasification, vapor phase processes associated with gas turbines, etc.) appear to be plagued by a similar group of deleterious high temperature vapor phase constituents.

"MHD"

The generation of electrical energy using combustion powered magneto-hydrodynamic (MHD) systems has been the subject of considerable research effort in the past decade. In an MHD system one creates an electrically conducting "fluid" which, when passed through a magnetic field, develops an induced electric field across this fluid, along which a current can flow.[2] A direct electric current can pass along the induced field to electrodes which may be connected to an external load. The typical MHD generator is usually comprised of a sequentially connected combustion chamber, a super-sonic expansion nozzle, and a gas flow channel commonly referred to as a diffuser. Because the hot post-combustion materials normally have an insufficient free electron concentration to be good current carriers, thermally ionizable seed materials such as K_2CO_3 and K_2SO_4 are generally added to the flow.[3]

Recent evaluations[4] of the status of MHD devices as viable and competitive power systems indicate that the problems of maintaining gas

conductivity, seed recovery (98% recovery rate for economical operation) and of inhibiting channel materials degradation (prevention of corrosion of channel walls through coal slag-electrode and slag-insulator interactions) remain largely unsolved.

In order to successfully model, and hence optimize, the design and operation of an MHD unit, it is essential to provide a rigorous accounting of the gas chemistry, particularly within the diffuser. Despite considerable effort in this direction, it does not appear that satisfactory predictions of the electrical conductivity associated with a seeded coal combustion gas are currently within the grasp of the technology. It is extremely difficult to determine species concentrations in these complex high temperature systems even if it is assumed that the gases are in thermodynamic equilibrium.

If equilibrium is assumed in the MHD channel, one can, from a knowledge of all the species present and their thermodynamic functions, calculate steady-state free electron concentrations for a variety of composition, temperature and pressure conditions. Unfortunately, these calculations are based on primary thermochemical input data which is very uncertain for some of the species (see below). In addition, these thermochemical evaluations rely heavily on a correct choice of species, a factor which is again uncertain.

"Approximate Species Concentrations"

Based upon currently available thermochemical data, it can be calculated (determination of species concentrations) that approximately half the potassium seed is present in the form of essentially unionizable KOH and is therefore unavailable as an electron source. At temperatures in excess of 2600 K in a slightly lean coal/air combustion system at 3 atm pressure, the major potassium-containing species are calculated to be KOH,

K, KO and K^+.[5] Other significant vapor species include SiO_2, FeO, OH, SO_2 and NO in addition to the major combustion gas components N_2, H_2O, CO_2 and CO. The primary slag or fly ash components include SiO_2, Al_2O_3, Fe_3O_4, TiO_2, MgO, CaO, Na_2O and K_2O; however, evidence now exists that the negative ions of PO_2, FeO_2, and AlO_2 are potentially important since all of these species have high electron affinities. The presence of these impurities has important implications for cation formation and electron behavior in the MHD channel. Typical slag concentrations in a coal-fired system, while only on the order of 0.1%, can result in as much as 19% loss in electrical conductivity.[6]

The species we have mentioned and their possible precursors are not well characterized. The combined uncertainties in the heats of formation and molecular constants used in computing partition functions for KOH (JANAF)[7] cause the concentration ratio of K to KOH to be uncertain by at least an order of magnitude. Because of this uncertainty, it is not possible to make a reasonable judgment as to whether the concentration of KOH is sufficiently high to require restrictions on the amount of hydrogen present in the fuel. Clearly, the successful thermodynamic modeling of MHD gas chemistry requires better basic data than are presently available.

"Electron Transfer Cross Sections"

Given that the equilibrium assumption is valid, we can define a steady state electron concentration in the MHD channel. Electron mobility is then determined from momentum transfer cross sections between electrons and other species. The momentum cross sections can be obtained from electron-molecule collision cross sections. These 'cross section' data are not known and can only be estimated very approximately. What can be said definitely is that the most polar species such as H_2O and KOH

should have the highest cross sections. Indeed, the dipole moment of KOH is estimated to be 8 Debye.[6] In systems where calcium and magnesium impurities are found, it would seem that CaOH and MgOH should be carefully considered. KOH, CaOH and MgOH are, at present, sparsely characterized.

"Metal Hydroxides and the Hydrogen Fuel Economy"

Because of its close tie to those materials used to seed the MHD generator, KOH may well represent the most important hydroxide species in the MHD channel; however, the specific effect of the water vapor component of combustion gases on the channel components of any system (fossil fuel only or MHD) has not been considered carefully. It appears that volatile hydroxides of a number of species could be formed under typical operating conditions.

The importance of metal hydroxide characterization increases markedly when one considers that many of the existing materials and seed recovery problems are derived from the presence of combustion impurities, particularly coal slag. Because future prospects for a hydrogen fuel economy may provide a source of clean fuel for MHD and other combustion systems, experimental and theoretical evaluations of an H_2-O_2 MHD generator have been underway.[10] A cost analysis indicates the H_2 fuel system to be comparable with other fuels, the reduced materials problems and low pollution produced making this an attractive alternative. There is one possible major drawback. The presence of a large H_2O concentration may prove to be detrimental if the high temperature materials are susceptible to the formation of hydroxide vapor species. In this light, it would seem that current and future possibilities for energy conversion will require a good hydroxide data base. At the very least this data base should include thermodynamic heats of formation and molecular constants on the hydroxides of sodium, iron,

silicon, vanadium, calcium, and magnesium.

"The Alkali Problem and Sulfur Chemistry"

The nature of coal-fired systems in general and the MHD channel in particular is such that "alkali cleanup"[11] represents the most significant problem which must be addressed. While thermodynamic calculations indicate the importance of the alkali oxides (especially KO in the MHD channel), sulfur is also a significant impurity in coal-fired systems. Therefore, it is necessary to consider the nature of sulfur compounds and their relation to the only partially solved fuel corrosion problem. In focusing on turbine blade corrosion, the alkali sulfur salts are among the most important compounds which must be characterized. For example, in a combustion powered turbine system operating over a sea or ocean, sulfur may come in contact with sodium or potassium and one must assess the nature of alkali-sulfur compounds which are formed.

Such data is also of importance for the characterization of most coal and heavy fuel fired turbine generators.[12] Indeed, a great deal of effort is now focusing on fireside corrosion where one must consider the interactions of those alkali salts which plate out on boiler tubes.[12] With this strong interest it is amazing to note that the data on sodium and potassium sulfur compounds (NaS, KS, Na_2S, K_2S and higher sulfides) is miniscule. Information on molecular stabilities (heats of formation) and molecular constants must be obtained.

"The Equilibrium Assumption"

Our discussion thus far has been closely tied to the validity of the equilibrium assumption, and the problems of obtaining thermochemical and collision cross section data if this assumption is valid. However,

one of the troublesome factors in the modeling of coal and heavy fuel fired systems appears to be a complex gas mixture which may not correspond to an equilibrium composition. The correct modeling may require the use of kinetic parameterization and the rates for product formation. Similarly, electron producing ionization kinetics may also be an important factor in determining MHD conductivity.

In this connection one need only note the complex ion chemistry that results between metal additives and electrons in atmospheric laboratory flames. Indeed, the presence of excess concentrations of charged species in the reaction zone of hydrocarbon-containing flames has led to the suggestion of a non-equilibrium low pressure ($\sim$0.1 atm) MHD generator.[13] It is anticipated that the use of low gas pressures should allow the excess radical and ion concentrations generated by the combustion process to be maintained in the diffuser itself. Calculations show that, under these conditions, a 1500 K flame would give an ion yield equivalent to that of an equilibrium system at 2500 K.[13]

The possibilities noted here point strongly to the importance of considering controlled non-equilibrium environments and species formation in the modeling of the behavior of energy generating systems. It may be inappropriate to model these systems using only free energy minimization schemes. Product formation rates and ultrafast energy transfer may play a much more significant role than thermodynamics. In any case, the parameterization of those gas phase molecules known to be present in these systems is of paramount importance to the successful application of any reliable approach to modeling.

"THE NATURE OF THE DATA BASE"

In the following sections, we will outline and assess the nature of available data on several of the molecules whose importance has been considered in the previous section. Our emphasis will be on the metal hydroxides and the alkali oxides and sulfides. Our purpose will be to evaluate critically the data base and to suggest where further experimentation is needed.

METAL HYDROXIDES

"Water Vapor-Solid Reactions with Hydroxide Vapor Products"

While there have been several recent reviews[14] outlining evidence for vapor phase hydroxide formation, much of the evidence for hydroxide species is of an indirect and sometimes ambiguous nature. In a gas-solid system, the enhanced rate of transport for a given oxide in the presence of water vapor is usually taken to indicate formation of a volatile hydroxide species. Through systematic variation of gas composition and temperature one attempts to infer a formula for the transport species. In order to determine and extrapolate the pressure dependence of transport and deposition processes, it is important to clarify the exact identity of the hydroxides involved.[15] Thus far very few verifications of species identity have been made. Here thermodynamic and spectroscopic data can be of great importance. Only the hydroxides of the alkali metals, barium and aluminum appear to have been characterized by both mass and optical spectroscopy, and, in many cases, this optical spectroscopy is of an indirect nature (Table I). Our discussion will focus on the monohydroxides. Here compounds of the alkali's, BeOH, CaOH, BaOH, and AlOH are thought to be important in water vapor-solid interactions.[14]

"Thermochemistry"

It appears that the major thermodynamic characterization of the metal hydroxides has been through flame studies. Table I summarizes those monohydroxides identified in flames while Table II indicates currently accepted bond dissociation energies for the monohydroxides. For the most part, molecular emission has been excited in post flame gases and in many of the studies noted in Tables I and II, only indirect evidence is obtained for the hydroxide. Only recently (see below) has molecular emission from NaOH and KOH been excited in a "chemiluminescent" reaction.[16] Molecular emission tentatively attributed to CaOH* has also been observed in calcium oxidation flames[17] and some laser fluorescence studies of this alkaline earth hydroxide have also appeared.[18]

From Table II, it is clear that only two compounds have been characterized mass spectrometrically. Studies of the Group IIA hydroxides at elevated temperature are precluded for all but the barium compounds[19] because of a very high propensity for disproportionation to the oxides and resulting loss of water. Difficulties encountered in studying the alkali hydroxides may well stem from the tendency to form dimeric species upon vaporization. We should also note that lithium tends to form a very stable binary oxide. The bond energies determined for KOH[20-21] and BaOH[19,22] via flame and mass spectrometric studies are in reasonable but not spectacular agreement.

"Molecular Parameterization - The Alkali Hydroxides"

With the exception of the alkali metal compounds, molecular parameterization is virtually non-existent for the hydroxides. Abramowitz and coworkers[23-24] have obtained infrared spectra for matrix isolated NaOH, RbOH, and CsOH and their deuterated analogs. Belyaeva et. al.[25] have studied the infrared spectra of matrix isolated KOH. The data from these groups is summarized in Table III and corresponds to the assignment of ν_1, the MO stretching mode and ν_2, the bending mode. Extensive microwave and millimeter wave studies have now yielded significant parameterization for the ground states of NaOH, KOH, RbOH, and CsOH,[26-31] and rotational constants have been obtained for several excited vibrational levels.

As we have noted, KOH is one of the most important constituents in the high stress environments characterizing energy generating systems. While ground state rotational parameters have been determined for KOH and KOD, vibrational frequencies are still estimated for higher vibrational levels.[32] Although matrix data is available on the fundamental vibrations, no gas phase measurements have been made and no anharmonicities are known for any of the alkali hydroxides. There is hope, however, that recent chemiluminescent studies[16] can be correlated with the millimeter wave data to provide an extensive mapping of the vibrational structure of the ground electronic state. These studies have already provided a stringent lower bound for the KOH dissociation energy (88.2 kcal/mole) significantly higher than that indicated in the Janaf tables (85.4). Because of its potential for the parameterization of KOH and the alkali hydroxides in general, we feal that a summary of the present status of this work is appropriate. In this regard, it is instructive to compare the alkali halides and hydroxides.

In Table IV, we present thermochemical data on the fluorides, chlorides,

and hydroxides of potassium, sodium and rubidium. Comparisons will be made between these species because (1) they are valence isoelectronic and (2) their observed emission spectra are expected to be similar.

It is generally felt that the nature of the bonding in the alkali hydroxides should be intermediate to that in the fluorides and chlorides. With this in mind, the trends in Table IV would seem to indicate the possibility of a bond strength higher than the mass spectrometric value. This is significant since the flame studies do indicate a higher value for the bond energy. JANAF now recommends 85.4 kcal/mole in close agreement with the flame studies.

Cardelino et. al.[16] have obtained a KOH* chemiluminescent spectrum under a variety of conditions. The observed emission for KOH correlates closely with expectations based on the known chemiluminescent emission for KCl. In order to understand the nature of the KOH emission spectrum, it is instructive to consider spectra for the alkali halides.

Alkali halide spectra have been obtained in three distinct experimental environments.[33] They have been observed under "single collision" conditions where alkali dimers and halogen molecules react in a four-center process

$$M_2 + X_2 \rightarrow MX^* + MX \qquad (1)$$

the resulting MX* product emitting a photon before undergoing subsequent collision.[34] These studies have been extended to "multiple collision" conditions by entraining the alkali dimers in argon and subsequently oxidizing this mixture.[35] A much more effective collisional environment consists of a "diffusion flame" device where oxidant is passed through a nozzle into a bulb containing several torr of alkali vapor and one to twenty torr of argon.

In Figure 1, we depict emission spectra obtained for KCl, RbCl, and CsCl under single collision conditions. The nature of the potential curves which give rise to the spectra in Figure 1 is depicted in Figure 2. Although drawn for KBr, the general features are similar for all the alkali halides. The alkali halides are characterized by a relatively stable ionic ground state and a grouping of several very shallow or repulsive excited states. The emission which one observes corresponds to a transition from one of the shallow or repulsive states to levels of the ground electronic state, the spectrum corresponding to a long progression in the vibrational levels of the ground electronic (ionic) state. The very shallow nature of the excited state potential has important consequences. One finds that the KCl spectrum changes drastically with the form of excitation and the experimental technique used to produce the emission system. The "single collision" spectrum in Figure 1 onsets at 4180Å (68.4 kcal/mole). A very similar spectrum is obtained when potassium dimers are entrained in argon and this mixture oxidized in a multiple collision device. A drastic change occurs when the reaction (1) is studied in a diffusion flame environment. Here the onset of the KCl spectrum is at 2866Å[36] some 1300Å to blue of the single and multiple collision spectrum. This large change signals an important characteristic of the alkali halide excited state potential. Whereas emission spectra involving strongly bound excited states are not drastically altered by the nature of a changing effective potential due to rotation, the shape and nature of shallow or repulsive states can be drastically altered by rotational excitation. This is exemplified for KI in Figure 3.[37] Here effective potential curves are constructed as a function of the rotational quantum number J and the relation

$$V_{effective}(J) = V_{rotationless} + \hbar^2 \left(\frac{J(J+1)}{2\mu R^2}\right) \qquad (2)$$

It should be noted that there is a substantial change in the minima for the effective potentials as a function of increasing rotational excitation and hence the quantum number J. The high J potentials correspond to the single and multiple collision spectra onsetting at 4180Å;[36] the low J potentials correspond to the diffusion flame emission system onsetting at 2866Å.[36] As a result of this shift in the excited state potential one observes emission to differing sets of ground state levels. In the diffusion flame experiments emission is observed to much lower regions of the ground state potential and hence the spectra onsets much further to the blue.[36]

The spectrum for potassium hydroxide has been obtained by Cardelino et. al.[16] upon reacting potassium with hydrogen peroxide (90+%). The process which yields chemiluminescence is believed to correspond to the four center reaction

$$K_2 + HO - OH \rightarrow KOH^* + KOH \qquad (3)$$

where KOH* denotes electronically excited KOH. The close analogy which the potassium hydroxide spectrum bears to that of KCl leads to comparisons between the two molecules which, in the final analysis, involve a direct determination of the K-OH bond energy.

The change in the emission spectra for the alkali halides as a function of experimental conditions may also be manifest in the alkali hydroxides. One anticipates that the potential function describing the K-OH stretch will be similar to that for KCl. If the potential curves for the excited states of K-OH are similar to those for KCl, they should be shallow and the KOH emission spectrum which results from reaction (3) should change significantly with excitation technique. This is observed, although the effect is not as pronounced as that in KCl. Single

and multiple collision spectra for KOH onset at 3840Å whereas the spectrum obtained in a diffusion flame (Figure 4) onsets at 3240Å. This significant change signals the observation of a shallow "effective" potential for the K-OH normal mode.[38]

The KCl and KOH spectra correspond to emission from shallow effective potentials close to the dissociation asmptote (Figure 2 and 3) of the ground electronic state. Given that we have strong evidence for these shallow effective potentials, we can use the onset of spectral emission to estimate the dissociation energy for the K-Cl and K-OH bonds. Because the diffusion-flame results must correspond to emission to lower levels of the ground state potential, this onset is chosen to give the best estimate of the bond dissociation energy. For K-Cl, the onset at 2866Å corresponds to 99.8 kcal/mole. This should be compared to the value in Table IV: D_o°(K-Cl) = 102.6±2 kcal/mole. It should be apparent that we are able to estimate a good lower bound to the K-Cl dissociation energy from the energy corresponding to the onset of the K-Cl diffusion flame spectrum. The onset of the KOH diffusion flame spectrum at 3240Å yields a lower bound of 88.2 kcal/mole for the K-OH bond energy.[39]

The result obtained by Cardelino et. al.[16] is significant for several reasons. It represents the first direct measurement of the bond energy for this species. The lower bound deduced for the K-OH bond strength indicates that the correct dissociation energy is on the order of 90±2 kcal/mole. This value considerably exceeds that obtained in the only mass spectrometric study of the monomer quoted in Table IV. The much higher value for the KOH bond energy is more consistent with the bounds estimated from metal atom flame depletion studies, but does indicate a slightly higher value.[39] A several kilocalorie increase in the KOH bond strength has significant implications for the stability and effect of this compound in energy generating systems.[40]

It is anticipated that further studies of the K_2-H_2O_2 diffusion flame system will improve the lower bound currently quoted for the K-OH bond-energy. It should be noted that the present result is not inconsistent with the recent findings of Wormhoudt and Kolb.[41] These authors observe unusually high KOH concentrations in their studies of coal fired MHD plasmas. Also, recent theoretical calculations by England[42] indicate the possibility of a higher K-OH bond energy.

In addition to a refinement of the K-OH bond energy, higher resolution spectra of the K_2-H_2O_2 diffusion flame should provide very useful information on the vibrational structure of the ground state normal mode "hot" bands. With reasonable luck, it should be possible to correlate these studies with the millimeter wave results mentioned earlier. The structural parameters (molecular constants) obtained will be of use in the calculation of thermodynamic properties for KOH.

"The Alkaline Earth Hydroxides"

To date, there is very little molecular parameterization on the alkaline earth hydroxides. Brom and Weltner have obtained ESR spectra for BeOH[43] and MgOH.[44] Weeks et. al.[45] have studied laser excited molecular fluorescence from CaOH and SrOH in an air-acetylene flame, proposing a preliminary energy level diagram for CaOH. These authors also comment on apparent earlier observations of CaOH and SrOH in both absorption [46] and fluorescence.[47] More recently Haraguchi et. al.[48] have excited laser fluorescence from BaOH again indicating the nature of previous absorption[49] and emission[50] studies and presenting a preliminary energy level diagram.

Using the chemiluminescent emission from the Ca-H_2O_2 reaction, Hanner et. al.[51] have succeeded in obtaining "single collision" emission from CaOH, determining a preliminary CaOH bond energy of 102.8 kcals/mole. This result is in good agreement with the flame studies of Cotton and Jenkins[52] and Kalff and Alkemade.[53] These studies will be extended to consider strontium and barium reactions allowing the determination of lower bounds for the alkaline earth hydroxide bond energies. It should be noted that the calcium and strontium compounds do not appear to be accessible to mass spectrometry.

The sparse nature of the data on the alkaline earth hydroxides definitely leaves a very fruitful and potentially significant area for study.

"Other Metal Hydroxides"

There is no doubt that experimental techniques developed for the alkali and alkaline earth hydroxides will soon be extended to other important metal hydroxides. Of particular note should be the hydroxides of vanadium, silicon, and iron. These species will weigh heavily in future technological developments.

"BONDING AND SPECTRA OF THE ALKALI MONOXIDES AND MONOSULFIDES"

A. Bonding in the Diatomic Metal Oxides and Sulfides

There have been relatively few spectroscopic or thermodynamic studies of the alkali oxides. Based on the results of molecular beam experiments (alkali metals + NO_2), Herm and Hershbach[54] have estimated the MO bond dissociation energies as follows: LiO (82±4), NaO (67±3), KO (71±3), RbO (68±3), and CsO (70±3 kcal/mole). The

value for NaO is in fair but not spectacular agreement with the value of 60.3±4 kcal/mole deduced by Murad and Hildenbrand[55] using mass spectroscopy. Fundamental frequencies for LiO (750 cm^{-1}),[56] KO (384),[57] and CsO (314)[57] have been measured using matrix isolation spectroscopy; however, the corresponding infrared absorptions in NaO and RbO have not yet been observed.

Evidence has been obtained for a change in the orbital makeup and symmetry of the ground electronic state upon traversing the series LiO...CsO. The electronic ground state of LiO is $^2\Pi$. Freund et. al.[58] have obtained very detailed spectra which demonstrate that this molecule is well represented by a crystal field model based on $Li^{\oplus}\,O^{\ominus}$. This model is in accord with ab initio calculations.[59]

Reactive scattering experiments[54] have indicated that NaO also has a $^2\Pi$ ground state whereas the ground state of CsO is of $^2\Sigma$ symmetry. Most recently ESR-matrix experiments[60] have also demonstrated that RbO and CsO have $^2\Sigma$ ground states whereas the ground states of LiO, NaO and KO are probably $^2\Pi$. A recent theoretical calculation[61] is in slight conflict with this conclusion indicating that the ground state of KO is $^2\Sigma^+$.

The observation of a $^2\Sigma^+$ ground state conflicts with the simple ionic model in which the electron donated by the alkali atom enters the $2p\sigma$ oxygen orbital along the internuclear axis, leaving a hole in the 2π orbital and resulting in a $^2\Pi$ state ($\sigma^2\pi^3$ molecular orbital configuration). An explanation for the observed trends can be obtained by evoking the concept of "inner shell bonding" in which one considers the mixing of filled $(n-1)p$ alkali orbitals with the 2p oxygen orbitals.

Figure 5 contrasts the molecular orbital scheme for NaO based on the alkali valence orbitals with the adjusted intershell orbital scheme for CsO.[60,61] The alkali monoxides are highly ionic molecules, $M^{\oplus}O^{\ominus}$, in both schemes but the latter gives a $^2\Sigma$ ground state ($...\pi^4\sigma$). The change from the valence to the inner shell scheme is governed by the location of the (n-1)p orbitals of M^+. These orbitals lie far below the 2p orbitals of O^- for Li or Na but become comparable in energy for Rb or Cs.

The significance of the orbital scheme discussed above can best be understood if we focus on the calculated ab-initio curves for LiO (Figure 6). It is apparent that the ground $X^2\Pi$ and low lying $A^2\Sigma^+$ states are separated by less than 2300 cm^{-1}. This energy increment will decrease for the sodium and potassium oxides. For RbO, the $A^2\Pi_i$ state is separated by less than 3800 cm^{-1} from the ground $X^2\Sigma^+$ state.[60]

While the sulfides are expected to display similar bonding trends, it may well be that the possibility of "inner shell bonding" decreases because of the small binding energy for the 3p electron on sulfur. Therefore, the ground states of LiS, NaS and KS are expected to be $^2\Pi$ and the ground state of RbS may be $^2\Pi$ with a very low lying $^2\Sigma$ state. To date, no information is available on the alkali sulfides; however, the metal sulfide bond energies are expected to be somewhat lower than the corresponding oxides.

As should be apparent from the previous discussion, data which will prove of use for the future assessment of metal oxide and sulfide interactions is virtually unavailable. The characterization of these species will not represent a trivial problem. Experimental difficulties which are already substantial are

further complicated by the presence of the very low-lying $^2\Sigma$ (LiO, NaO, etc.) or $^2\Pi$ (RbO, CsO, etc.) state. In order to characterize the $^2\Sigma$ and $^2\Pi$ states, it may be appropriate to search for higher-lying electronic states; however, predissociative effects will soon plague this search. There is indication that the chemiluminescent reactions $M+N_2O$, $M+O_3 \rightarrow MO^*+...$ may lead to some elucidation of the molecular parameters for the alkali oxides, however, this data is only in a preliminary state.[62]

B. "Bonding in the Triatomic Alkali Oxides and Sulfides M_2O and M_2S"

Yet another interesting group of compounds whose characterization will represent a significant contribution are the alkali oxides, M_2O. There have been several quantum chemical calculations performed on Li_2O[63] and infrared fundamentals (ν_3) have been reported for Li_2O,[56] K_2O,[57] Rb_2O,[57] and Cs_2O;[57] however, thus far, there appears to be no definitive gas phase data on these compounds and no data whatsoever on Na_2O.

"Laser Spectroscopy on Na_2O - A Preliminary Study"

In order to efficiently excite fluorescence from Na_2O, Crumley et. al.[64] have constructed the device depicted in Figure 7. Figures 7(a) and 7(b) indicate the overall layout of the cell used in these experiments. Figure 7(c) indicates the window design which is frequently necessary when working with refractory species, the gas flow system being designed to provide a uniform circulation of gas over the windows. In order to carefully control the vaporization of Na_2O in a very localized region, the device depicted in Figures

7(d) and 7(e) is used. It consists of a crucible which is suspended on a 1/8" stainless steel tube such that once the overall device is connected to the cell sidearm, the crucible is centrally located to the viewing port. The positioning control whose diameter is the same as the window shown in Figure 7(c) is held in place in precisely the same fashion as the window. When connected to the overall cell, the crucible holder is rotated 90° with respect to its depiction in the Figure. When the cell is in operation, a laser beam traverses the path indicated in Figures 7(b) and 7(d). Na_2O is directly vaporized through a thin slit into the path of the laser beam. The slit and the laser beam are parallel and the laser induced fluorescence is viewed at 90°.[65]

Using the cell described above and various pumping schemes, Crumley et. al.[64] have carried out experiments at both 100 μ (primarily background argon) and 10^{-6} torr. This range of background pressure allows one not only to do spectroscopy but also to observe quenching effects which appear to be quite significant for Na_2O. Thus far, experiments have been conducted primarily with an argon ion laser; however, some excitation has been accomplished with a rhodamine dye laser. Examples of the spectra tentatively assigned to Na_2O are shown in Figure 8. They correspond to excitation at 5145 and 4880Å. It appears that one can excite laser induced fluorescence with several of the available argon ion laser lines (4579, 4880, 4965, 5017, 5145Å) and that the fluorescence spectra can be interconnected (significant overlap) in a rather substantial Deslandres Table. Much of the analysis of the observed spectra has depended on relating the Na_2O studies to available information on Li_2O. These

data come primarily from matrix isolation spectroscopy[56] and recent quantum chemical calculations.[63] Briefly, the data has been used to (1) attempt to estimate the normal frequencies of vibration for Na_2O based on a reasonable extrapolation from Li_2O and (2) determine the most likely electronic transition which should be excited in the visible using an argon ion laser.

Using a notation common to several quantum chemical descriptions of linear $D_{\infty h}$ Li_2O, the valence orbital configuration for the ground state is

$$\ldots(3\sigma_g)^2(2\sigma_u)^2(1\pi_u)^4 \qquad {}^1\Sigma_g^+ \qquad (4)$$

where the valence orbitals are constructed primarily from 2s and 2p electrons on lithium and oxygen. The lowest Li_2O excited states correspond to the promoted configurations

$$\ldots(3\sigma_g)^2(2\sigma_u)^2(1\pi_u)^3(4\sigma_g)^1 \qquad {}^{1,3}\Pi_u \qquad (5)$$

$$\ldots(3\sigma_g)^2(2\sigma_u)^2(1\pi_u)^3(3\sigma_u)^1 \qquad {}^{1,3}\Pi_g \qquad (6)$$

and Grow and Pitzer[63b] have shown that these states are very low lying ($\Delta E_{excitation} \leq 1.3$ eV); therefore it is unlikely that even the strongly allowed ${}^1\Pi_u - {}^1\Sigma_g$ transition corresponds to the fluorescence observed upon single photon pumping with an argon ion laser. A further promotion which will result in a strongly allowed transition, most likely in the visible region, leads to the configuration

$$\ldots(3\sigma_g)^2(2\sigma_u)^1(1\pi_u)^4(4\sigma_g)^1 \qquad {}^{1,3}\Sigma_u^+ \qquad (7)$$

One anticipates that the visible transition in Na_2O which is pumped by the argon ion laser corresponds to a $^1\Sigma_u^+ \leftarrow {}^1\Sigma_g^+$ excitation involving the analog of configurations (4) and (7). In pumping this transition one removes an electron from an orbital which is both Na-O and Na-Na antibonding and promotes this electron to an orbital which is both Na-O and Na-Na bonding. Hence, one expects that both the excited state stretching and bending frequencies should exceed that of the ground electronic state of Na_2O.

The ground state frequencies for Li_2O are (matrix isolation spectroscopy) $\nu_1 \simeq 760\ cm^{-1}$, $\nu_2 \simeq 112\ cm^{-1}$, and $\nu_3 \simeq 990\ cm^{-1}$. Formulating a normal coordinate analysis based on the Li_2O measurements, one estimates a vibrational frequency of between 540 and 585 cm^{-1} for the symmetric stretch (ν_1) and 74 cm^{-1} for the bending mode of Na_2O. This is not unreasonable when comparisons are made with NaO where the vibrational frequency appears to be ~519 cm^{-1}[61] (recall that Na_2O is thought to be a linear molecule).

Although absolute quantum level numberings have not been assigned, extensive Deslandres Tables for the pumped transitions indicate an upper state vibrational frequency of ~650 cm^{-1} and a lower state (ground state) frequency of ~550 cm^{-1} consistent with the predictions outlined above. In addition, a closer view (Figure 9) of a region of the 5145Å spectrum in Figure 8 reveals what appear to be ~70 cm^{-1} separations expected for the ground state bending mode of Na_2O. Tentatively, it appears that the spectra correspond to progressions in the symmetric stretching and bending modes of the ground and excited state in a $^1\Sigma_u^+ \leftarrow {}^1\Sigma_g^+$ transition.

These studies hold the promise of providing information which is extremely useful for the understanding of fundamental dynamic processes such as the reaction of sodium dimers and oxygen atoms and they also establish a foothold for analyzing kinetic processes in which Na_2O plays a significant role. Because Na_2O represents an important constituent in energy generating systems, one desires a means to carefully monitor its behavior. It should also be noted that in addition to their use for the characterization of reaction kinetics, such studies, while still in their early phases, may well allow the determination of parameters useful in thermodynamic evaluations. Before the advent of the laser, the study of these elevated temperature free radicals rested primarily within the province of the matrix isolation spectroscopist. The versatility introduced by the laser should allow the future comparison of molecular behavior in gas phase and matrix environments.

FURTHER CONSIDERATIONS

We have attempted to indicate the nature of several important and yet sparsely characterized systems whose study will greatly aid the understanding of the gas phase chemistry associated with energy generating systems. While our discussion has focused primarily on bond energies and molecular parameterization, kinetics and energy transfer must also play an important role in the realistic description of a system. The correct modeling of energy generating systems is the subject of some controversy. Strong evidence is emerging which indicates that the modeling of an energy system assuming thermodynamic equilibrium and applying "free energy minimization" may not be entirely or even partially appropriate. In the vast majority of the systems

where thermodynamics and kinetics both play a role, observed phenomena are in large part controlled by the rates of various processes. Hence current modeling efforts are incorporating kinetic parameters.[40] In carrying out chemiluminescent studies across a wide pressure range (10^{-6}-10^{2} torr), we have observed and characterized ultrafast intramolecular energy transfer routes among the electronically and vibrationally excited states of several high temperature molecules. Thus far, these studies have indicated that energy transfer can occur at rates which may approach 1000 times the calculated gas kinetic rates. These surprising results demonstrate that vibrationally and/or electronically excited high temperature molecules act as if they were "large" or "diffuse" entities capable of strong interaction at very long range. This rapid energy transfer is a general phenomenon and effects have been observed in several molecules including SiO and KOH. The observation of such rapid energy transfer may have significant implications for the modeling of energy generating systems and the characterization of heat flow in these systems.

Acknowledgements

It is a pleasure to acknowledge partial support of some of the work described here by the U. S. Department of Energy. Professor W. H. Eberhardt read the first draft of this manuscript and provided many helpful suggestions.

References

1. D.M. Lindsay and J.L. Gole, J. Chem. Phys. 66, 3886 (1977).

M.J. Sayers and J.L. Gole, J. Chem. Phys. 67, 5442 (1977).

J.L. Gole and S.A. Pace, J. Chem. Phys. 73, 836 (1980).

A.W. Hanner and J.L. Gole, J. Chem. Phys. 73, 5025 (1980).

2. R.J. Ross, "Magnetohydrodynamic Energy Conversion," McGraw-Hill, New York, 1968

3. S.A. Medin, V.A. Ovcharenko and E.E. Shpil'rain, High Temp. U.S.S.R. 10, 390 (1972).

4. H.C. Hottel and J.B. Howard, "New Energy Technology - Some Facts and Assessments," M.I.T. Press, Cambridge, MA (1971).

L.P. Harris and G.E. Moore, IEEE Trans. Power App. Syst. 90, 2030 (1972).

5. "Open Cycle Magnetohydrodynamic Power Generation," J.B. Heywood and G.J. Womack, eds., Pergamon, Oxford, 1969.

6. F.E. Spencer, Jr., J.C. Hendrie and D. Bienstock, Symp. Eng. Aspects Magnetohydrodynam., 13th, Stanford Univ., p. VII.4.1; VII.4.6.

7. "Joint Army Navy Air Force Thermochemical Tables, 2nd ed., NSRDS-NBS37. U.S. Govt. Printing Office, Washington, D.C.

8. W.B. England, J. Chem. Phys. 68, 4896 (1978)

9. Sulfur impurities are also important. See for example, R.K. Sinha and P.L. Walker, Jr., Fuel 51, 329 (1972); F.S. Karn, R.A. Friedel and A.G. Sharkey, Jr., Fuel 51, 113 (1972).

10. J. Marlin Smith, L.D. Nichols and G.R. Seikel, NASA Lewis H_2-O_2 MHD Program, Int. Symp. Eng. Aspects of Magnetohydrodynamics, 14th April, 1974, Tullahoma, TN, p. III.7.1.

11.

12. Session on High Pressure Sampling, 10th Materials Research Symposium on Characterization of High Temperature Vapors and Gases, National Bureau of Standards, Gaithersburg, MD. September 18-22, 1978.

13. I. Fells, in Combustion and Propulsion, AGARD Colloq. 6th, Energy Sources and Energy Conversion, H.M. DeGroff, R.F. Hogland, J. Fabri, T.F. Nagey and M.E. Rumbaugh, Jr., eds., Gordon and Breach, New York, 1967, p. 477.

14. See, for example, J.W. Hastie, "High Temperature Vapors, Science and Technology," Academic Press, New York, 1975.

See also; O. Glemser and H.G. Wendlandt, Advan. Inorg. Chem. Radiochem. 5, 215 (1963).

F.T. Greene, S.P. Randall and J.L. Margrave, in "Thermodynamic and Transport Properties of Gases, Liquids and Solids," Am. Soc. Mech. Eng., New York (1959), p. 222.

D.D. Jackson, Thermodynamics of Gaseous Hydroxides, UCRL - 51137 (1971).

15. Laboratory data on the hydroxides when extrapolated may well be related to practical problems such as the nature of solid deposition in steam turbines.

16. B. Cardelino, W. Crumley and J. L. Gole, work in progress

17. A. W. Hanner and J. L. Gole, unpublished data

18. W.D. Winefordner et.al. to be published - see also references 45 and 47.

19. F.E. Stafford and J. Berkowitz, J. Chem. Phys. 40, 2963 (1964).

20. R. Kelly and P.J. Padley, Trans. Faraday Soc. 67, 740 (1971); H. Smith and T.M. Sugden, Proc. R. Soc. A 219, 304 (1953); D.H. Cotton and D.R. Jenkins, Trans. Faraday Soc. 65, 1537 (1970); D.E. Jensen and P.J. Padley, Trans. Faraday Soc. 62, 2132 (1966).

21. L.N. Gorokhov, A.V. Gausarov and I.G. Panchenkov, Russ. J. Phys. Chem. 44, 150 (1970).

22. See Table II reference c,d,e.

23. N. Acquista, S. Abramowitz and D.R. Lide, J. Chem. Phys. 49, 780 (1968).

24. N. Acquista and S. Abramowitz, J. Chem. Phys. 51, 2911 (1969).

25. A.A. Belyaeva, M.I. Dvorkin, and L.D. Sheherba, Opt. and Spectrosc. 31, 210 (1971).

26. D.R. Lide and R.L. Kuczkowski, J. Chem. Phys. 46, 4768 (1967).

27. C. Matsumura and D. R. Lide, J. Chem. Phys. 50, 71 (1969).

D.R. Lide and C. Matsumura, J. Chem. Phys. 50, 3080 (1969).

28. E.F. Pearson and M.B. Trueblood; J. Chem. Phys. 58, 826 (1973), Astrophys. Journal 174, L145 (1973)

29. E.F. Pearson, B.P. Winnewisser and M.B. Trueblood, Z. Naturforsch 31a, 1259 (1976).

30. P. Kuijpers, T. Törring and A. Dymanus, Chem. Phys. 15, 457 (1976); Z. Naturforsch, 31a, 1256 (1975).

31. P. Kuijpers, T. Törring and A. Dymanus, Z. Naturforsch 32a, 930 (1977).

32. D.E. Jensen, J. Phys. Chem. 74, 207 (1970).

33. J.L. Gole, The Characterization of High Temperature Vapors of Impart to Combustion and Gasification Processes in the Energy Technologies:

34. For a discussion of single collision conditions see, J.L. Gole, Ann. Rev. Phys. Chem. 27, 525 (1976).

For the alkali halides see, R.C. Oldenborg, J.L. Gole and R.N. Zare, J. Chem. Phys. 60, 4032 (1974).

35. See reference 1 and G.J. Green and J.L. Gole, Chem. Phys. 46, 67 (1980).

36. A. Tewarson, "Studies of Chemiluminescent Emission in Selected Low-Pressure Diffusion Flames," Ph.D. Thesis, Penn State University, 1969.

The long wavelength limit of the diffusion flame spectrum is 4654Å vs. 5708Å for the single collision spectrum. Hence the entire KCl spectrum is shifted to the blue ~1200Å when experimental conditions are changed from the single collision to the diffusion flame environment.

37. Taken from Oldenborg et. al. reference 34. Based on the study by K.J. Kaufmann, J.L. Kinsey, H.B. Palmer and A. Tewarson, J. Chem. Phys. 60, 4023 (1974).

38. Of course it is not completely correct to speak of an isolated K-O stretch in the KOH molecule. In reality there will be some coupling with the O-H stretch and the bending mode of the triatomic.

39. This is a stringent lower bound and more refined diffusion flame studies should yield an even higher value. Based upon the probable dissociation products for the ground and excited states of KOH, it is likely that the upper excited state potential may be significantly bound with respect to the dissociation assymptote of the ground electronic state. The much smaller change in the diffusion flame vs. single collision spectrum for KOH versus that for KCl indicates that this is probably the case. We anticipate that the emitting excited state of KOH may be bound by as much as 10 kcal/mole relative to the dissociation assymptote of the ground state.

40. J. Wormhoudt, V. Yousefian, M.H. Weinberg, C.E. Kolb and M.M. Slugter, "A Review of Plasma Chemical Considerations in MHD Generator Design," Seventh International Conference on MHD Electrical Power Generation, Cambridge Mass. 1980, pg. 530.

41. J. Wormhoudt and C.E. Kolb, "Mass Spectrometric Determination of Negative and Positive Ion Concentrations in Coal-Fired MHD Plasmas," 10th Materials Research Symposium, NBS Special Publication 561, Volume 2.

42. W.B. England, J. Chem. Phys. 68, 4896 (1978).

43. J. Brom and W. Weltner, J. Chem. Phys. 64, 3894 (1976).

44. J. Brom and W. Weltner, J. Chem. Phys. 58, 5322 (1973).

45. S.J. Weeks, H. Haraguchi and J.D. Winefordner, J. Quant. Spectrosc. Radiat. Trans. 19, 633 (1978).

46. S.R. Koirtyohann and E.E. Pickett, Anal. Chem. 38, 585 (1966) M. Yoshimura et. al. unpublished

47. H.G.C. Human and P.J. Th. Zeegers. Spectrochim. Acta, 30B, 203 (1975) M.B. Blackburn, J.M. Mermet and J.D. Winefordner, Spectrochim. Acta. 34A, 847 (1977).

48. H. Haraguchi, S.J. Weeks and J.D. Winefordner, Spectrochim. Acta 35A, 391 (1979).

49. See references 46-48.

50. See references 46-48.

51. A.W. Hanner and J.L. Gole, unpublished

52. D.H. Cotton and D.R. Jenkins, Trans. Faraday Soc. 64, 2988 (1968).

53. P.J. Kalff and C.T.J. Alkemade, Combust. Flame 19, 257 (1972).

54. R.R. Herm and D.R. Herschbach, J. Chem. Phys. 52, 5783 (1970).

55. D.L. Hildenbrand and E. Murad, J. Chem. Phys. 53, 3403 (1970).

56. a. R.C. Spiker, Jr. and Lester Andrews, J. Chem. Phys. 58, 702 (1973).

b. D. White, K.S. Seshardri, D.F. Dever, D.E. Mann and M.J. Linevsky, J. Chem. Phys. 39, 2463 (1963).

c. K.S. Seshardri, D. White and D.E. Mann, J. Chem. Phys. 45, 4697 (1966).

57. R.C. Spiker and L. Andrews, J. Chem. Phys. 58, 713 (1973).

58. S.M. Freund, E. Herbst, R.P. Mariella, Jr. and W. Klemperer, J. Chem. Phys. 56, 1467 (1972).

59. M. Yoshimine, J. Chem. Phys. 57, 1108 (1972); B. Liu and M. Yoshimine, J. Chem. Phys. 60, 1427 (1974). For further work see also M.J. Clugston and R.G. Gordon, J. Chem. Phys. 66, 244 (1977)

60. D.M. Lindsay, D.R. Herschbach and A.L. Kwiram, Mol. Phys. 32, 1199 (1976).

61. For a discussion of the "inner shell valence scheme" see: J.R. Morton and W.E. Falconer, J. Chem. Phys. 39, 427 (1963); W.E. Falconer, J.R. Morton and A.G. Streng, ibid 41, 902 (1964); R.C. Eachus and M.C.R. Symons, J. Chem Soc. A304 (1971)

For a further comment on alkali oxide bonding considering a ground $^2\Sigma^+$ state for KO see S.P. So. and W.G. Richards, Chem. Phys. Lett. 32, 227 (1975).

62. W. Crumley, B. Cardelino and J.L. Gole, work in progress.

63. a. R.J. Buenker and S.D. Peyerimhoff, J. Chem. Phys. 45, 3682 (1966).

b. D.T. Grow and R.M. Pitzer, J. Chem. Phys. 67, 4019 (1977).

c. E.L. Wagner, Theoret. Chim. Acta 32, 310 (1974).

d. T.K. Lin and D.D. Ebbing, Int. J. Quant. Chem. 6, 297 (1972).

64. W. Crumley, J. Appling and J.L. Gole, work in progress

65. It should be noted that extensive baffling is used in the system to avoid problems with scattered laser light.

66. The notation in Figure 8 is designed to give a relative numbering. Because v' and v", the absolute quantum numbers for the upper and lower states are not known, we use the notation v' + n', v" + n" where the indices in the figure denote the values of n' and n". In this case it is likely that the value of v" will exceed that for the level from which laser pumping occurs.

TABLE I

Observations of the Metal Monohydroxides

Species	Nature of the Detection Method and Comments
AlOH	Mass spectrometric analysis of lean H_2-O_2 flames containing aluminum.[a] Controversial results.
Alkali Hydroxides	
LiOH	Inferred from optical spectroscopic study of free atom depletion in H_2-O_2-N_2 [b] and H_2-O_2-CO_2 [c] flames.
NaOH	Inferred from optical spectroscopic study of free atom depletion in H_2-O_2-N_2 [b] and H_2-O_2-CO_2 [c] flames.
KOH	Inferred from optical spectroscopic study of free atom depletion in H_2-O_2-N_2 [b] and H_2-O_2-CO_2 [c] flames.
RbOH	Inferred from optical spectroscopic study of free atom depletion in H_2-O_2-N_2 [b] and H_2-O_2-CO_2 [c] flames.
CsOH	Inferred from optical spectroscopic study of free atom depletion in H_2-O_2-N_2 [b] and H_2-O_2-CO_2 [c] flames.
Alkaline Earth Hydroxides	
CaOH	Molecular emission observed in post-flame gases of H_2-O_2-N_2 flames.[d] Presence also inferred from optical spectroscopic study of free atom depletion[e] -dissociation energy from depletion studies.[e] Also observed in acetylene-air or O_2 flames.[f]
SrOH	Molecular emission observed in acetylene-air flames.[d,f] Presence also inferred from optical spectroscopic study of free atom depletion-dissociation energy from depletion studies.[e]
BaOH	Emission in post-flame gases of H_2-O_2-N_2 flames.[d,e] Presence also inferred from spectroscopic study of free atom depletion-dissociation energy from depletion studies[e] and mass spectrometry.[g]
CuOH	Some emission band spectra observed in acetylene-air flame.[f,h]
FeOH	Emission band spectra observed in acetylene-air, H_2-O_2-N_2 and low pressure lean flames.[i] Presence also inferred from optical spectroscopic study of free atom depletion.[j]
MnOH	Emission band spectra observed in acetylene-air post-flame gases.[d,k]
InOH	Presence inferred from optical spectroscopic study of free atom depletion.[c,l]

TABLE I (continued)

Species	Nature of the Detection Method and Comments
GaOH	Presence inferred from optical spectroscopic study of free atom depletion.[c,l,m]

[a]M. Farber, R.D. Srivastava, M.A. Frisch and S.P. Harris, Faraday Symposium 8, High Temperature Studies in Chemistry, London, 1973.

[b]D.E. Jensen and P.J. Padley, Trans. Faraday Society 62, 2132 (1966).

[c]R. Kelly and P.J. Padley, Trans. Faraday Society 67, 740 (1971).

[d]R.W. Reid and T.M. Sugden, Disc. Faraday Soc. 33, 213 (1962); L.V. Gurvich, V.G. Ryabova and A.N. Khitrov, in "High Temperature Studies in Chemistry", Faraday Symp. No. 8, Paper 8, Chem. Soc. London (1973); J. Van der Hurk, J. Hollander and C.T.J. Alkemade, J. Quant. Spectrosc. Radiat. Transf. 13, 273 (1973).

[e]D.H. Cotton and D.R. Jenkins, Trans. Faraday Society 64, 2988 (1968).

[f]Cited in "Flame Spectroscopy" by R. Maurodiveanu and H. Boiteux, Wiley, New York (1965).

[g]F.E. Stafford and J. Berkowitz, J. Chem. Phys. 40, 2963 (1964).

[h]L.M. Bulewicz and T.M. Sugden, Trans. Faraday Society 52, 1481 (1956).

[i]M.J. Linevsky, Metal Oxide Studies; Iron Oxidation. Tech. Rep. RADC-TR-71-259.

[j]D.E. Jensen and G.A. Jones, J. Chem. Soc. Faraday Trans. I 69, 1448 (1973).

[k]P.J. Padley and T.M. Sugden, Trans. Faraday Society 55, 2054 (1959).

[l]E.M. Bulewicz and T.M. Sugden, Trans. Faraday Society 54, 830 (1958); 54, 1855 (1958).

[m]L.V. Gurvich and V.G. Ryabova, High Temp. USSR 2, 486 (1964).

TABLE II

Dissociation Energies of Metal Monohydroxides

Species	D_o(M-OH) kcals/mole	Comments
LiOH	103 ± 2[a]	H_2-O_2-CO_2 flames 2nd law determination
NaOH	79 ± 2[a]	H_2-O_2-CO_2 flames 2nd law determination
KOH	84 ± 2.5[a]	H_2-O_2-CO_2 flames 2nd law determination
KOH	80 ± 3[b]	Mass spectrometry
RbOH	86 ± 3[a]	H_2-O_2-CO_2 flames 2nd law determination
CaOH	96[c]	Rich hydrogen-air flames
	94 ± 3[d]	Rich hydrogen-air flames
	103.7[e]	
	103[f]	Quoted uncertainty $\leq$ 2.5 kcals mole
SrOH	95[e]	See text for discussion
	103[e]	
	102[f]	Quoted uncertainty $\leq$ 2.5 kcals/mole
BaOH	111[c]	See text for discussion
	114.3[e]	See text for discussion
	113[f]	Quoted uncertainty $\leq$ 2.5 kcals/mole
	107[g]	Mass spectroscopy
	109 ± 3[d]	See text for discussion
InOH	90 ± 2[a]	H_2-O_2-CO_2 flame 2nd law determination
	86 ± 7[h]	H_2-O_2-N_2 flames 2nd and 3rd law determination
GaOH	102 ± 5[h]	H_2-O_2-N_2 flames 2nd and 3rd determination
TlOH	<72[a]	H_2-O_2-CO_2 flame 2nd law determination
FeOH	100 ± 3[i]	Low pressure H_2-O_2-N_2 flames

TABLE II (cont.)

Species	D_o(M-OH) kcals/mole	Comments
SnOH	$<85 \pm 9$[j]	Low pressure H_2-O_2-N_2 flames
AlOH	130[k]	Thermochemistry and reactions in hydrogen oxygen flames

TABLE II (cont.)

[a]R. Kelly and P.J. Padley, Trans. Faraday Society 67, 740 (1971).

[b]L.N. Gorokhov, A.V. Gusarov and I.G. Panchenkov, Russ. J. Phys. Chem. 44, 150 (1970).

[c]L.V. Gurvich, V.G. Ryabova and A.N. Khitrov, in "High Temperature Studies in Chemistry," Faraday Symposium No. 8, Paper 8, Chem. Soc. London (1973).

[d]V.G. Ryabova, A.N. Khitrov, and L.V. Gurvich, High Temperature 10, 669 (1973).

[e]D.H. Cotton and D.R. Jenkins, Trans. Faraday Society 64, 2988 (1968); also K. Schofield and T.M. Sugden, Symp. (Int.) Combust. 10th, p. 589, Combust. Inst., Pittsburgh, PA.

[f]P.J. Kalff and C.T.J. Alkemade, Combust. Flame 19, 257 (1972).

[g]F.E. Stafford and J. Berkowitz, J. Chem. Phys. 40, 2963 (1964).

[h]E.M. Bulewicz and T.M. Sugden, Trans. Faraday Society 54, 830, 1855 (1958).

[i]M.J. Linevsky, Metal Oxide Studies; Iron Oxidation. Tech. Rep. RADC-TR-71-259.

[j]E.M. Bulewicz and P.J. Padley, Trans. Faraday Soc. 67, 2337 (1971).

[k]D.L. Jackson, Thermodynamics of Gaseous Hydroxides, UCRL 51137, L.V. Gurvich and I.V. Veits, Dokl. Akad. Nauk. SSSR 108, 659 (1956). Note also M. Farber and R.D. Srivastave, "Thermochemical Reactions of aluminum and fluorine in hydrogen-oxygen flames, Combust. Flame 27, 99 (1976).

Table III

Infrared Data for the Alkali Hydroxides

Molecules	ν_1 (cm^{-1})	ν_2 (cm^{-1})
CsOH[a]	335.6	309.8
		302.4
CsOD[a]	330.5	226
RbOH[b]	354.4	309.0
RbOD[b]	345±3	229±3
KOH[c]	408	300
KOD[c]	399	264
NaOH[b]	431	337
NaOD[b]	422±3	250

a. Ref. 23

b. Ref. 24

c. Ref. 25

Table IV

Comparison of Thermochemical Data for the Alkali Fluorides, Chlorides, and Hydroxides

Molecules	D_o^o(M-X)	Comments
KF	117[a]	Thermochemical
KCl	102.6±2[b]	Thermochemical and Photofragment
KOH	84±2.5[c]	H_2-O_2-CO_2 flames 2nd law determination
	80±3[d]	Mass spectrometry
	85.4±3	(JANAF tables estimate)
NaF	123	NaOH 79±2[c] (flame--2nd Law)
NaCl	97.6±2[b]	
RbF	115[e]	RbOH 86±3[c] (flame--2nd law)
RbCl	101.3±2[b]	

a. E.M. Bulewicz, C.G. James, T.M. Sugden, Trans. Faraday Soc. 37, 921 (1961); A.G. Gaydon, "Dissociation Energies and Spectra of Diatomic Molecules," 3rd Edition, Chapman and Hall, 1968.

b. T-M.R. Su and S.J. Riley, J. Chem. Phys. 72, 6632 (1980).

c. R. Kelly and P.J. Padley, Trans. Faraday Society, 67, 740 (1971) also the average of three other flame studies by Smith and Sugden Proc. Roy. Soc. A219, 304 (1953) [86±1]; Jensen and Padley, Trans. Fara. Soc. 62, 2132 (1966) [82±2]; Cotton and Jenkins, Trans. Fara. Soc. 65, 1537 (1969) [86±2].

d. L.N. Gorokhov, A.V. Gusarov and I.G. Panchenkov, Russ. J. Phys. Chem. 44, 150 (1970).

e. See reference a and A. D. Caunt and R. F. Barrow, Nature, 164, 753 (1949).

Figure Captions

Figure 1: Chemiluminescent spectra of (a) KCl, (b) RbCl, (c) CsCl, with a resolution of 5Å or better. Also present in each trace are atomic (alkali) lines, some of which are off scale. (taken from reference 34.) See text for discussion.

Figure 2: Potential energy curves for an alkali halide molecule (drawn for KBr) showing the "zeroth order crossing" of the ionic and covalent states. Note the shallow excited electronic states close to the ground state dissociation asymptote.

Figure 3: Effective excited state potential curves for KI constructed from the rotationless potential of Kauffman, Kinsey, Palmer, and Tewarson (reference 37) assuming a dissociation asymptote of 27000 cm^{-1} (see reference 34).

Figure 4: Chemiluminescent spectrum obtained for KOH* formed in a diffusion flame environment. See text for discussion.

Figure 5: Molecular orbital scheme for the alkali monoxides (taken from the work of Lindsay, Kwiram and Herschbach - Reference 60) See text for discussion.

Figure 6: Potential curves based on extensive configuration interaction calculations on the $X^2\Pi$ and $A^2\Sigma^+$ states of LiO.

Figure 7: Schematic diagram of apparatus for laser fluorescence studies of Na_2O. See text for discussion.

Figure 8: Laser induced photoluminescence spectra tentatively correlated with Na_2O taken at a resolution of 1Å and using the 5145 and 4880Å argon ion laser lines for excitation. See text for discussion.

Figure 9: Close-up of laser induced photoluminescence spectrum tentatively correlated with Na_2O taken at a resolution of 0.5Å and using the 5145Å argon ion laser line for excitation. See text for discussion.

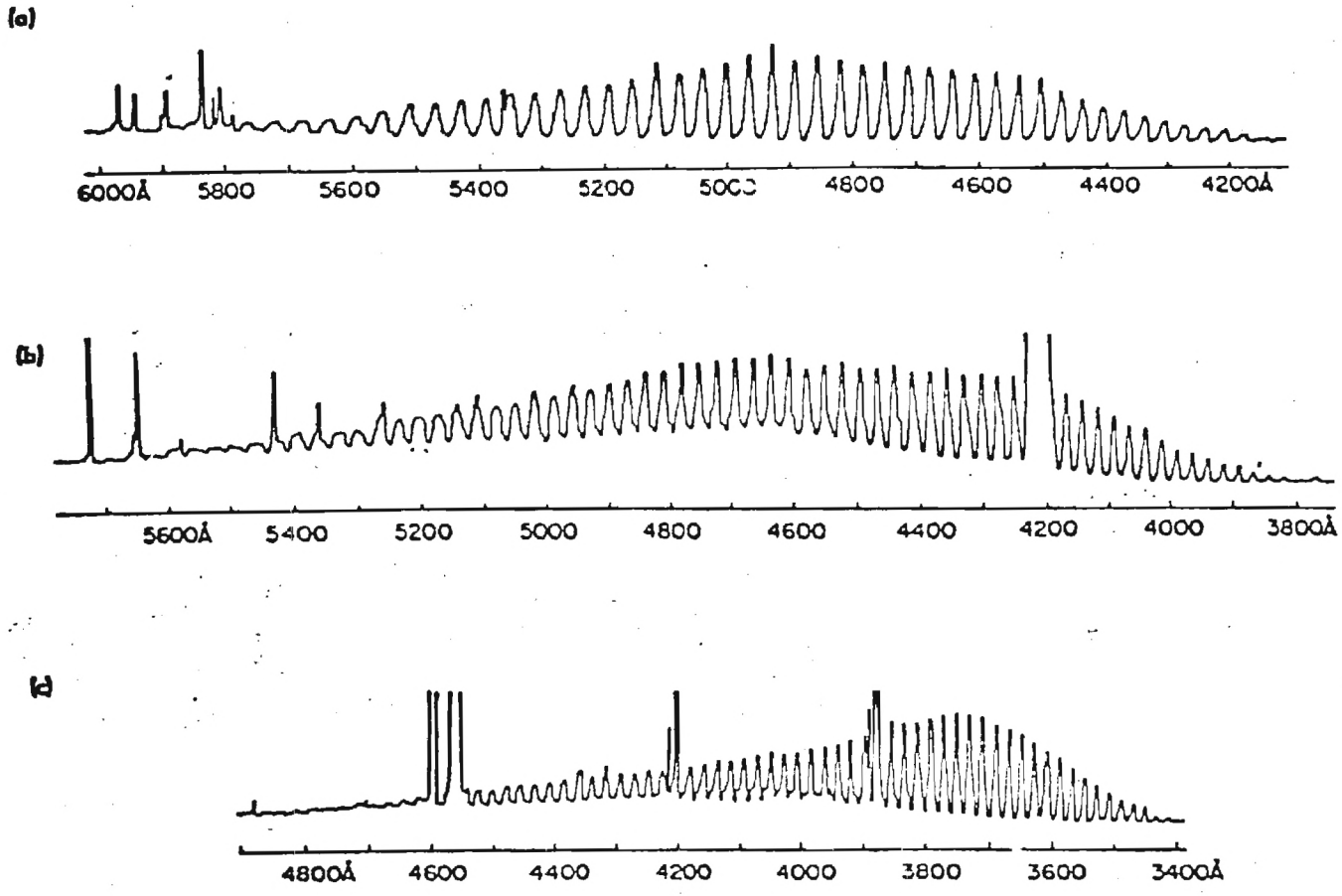
(a)
6000Å 5800 5600 5400 5200 5000 4800 4600 4400 4200Å
(b)
5600Å 5400 5200 5000 4800 4600 4400 4200 4000 3800Å
(c)
4800Å 4600 4400 4200 4000 3800 3600 3400Å

Figure 1

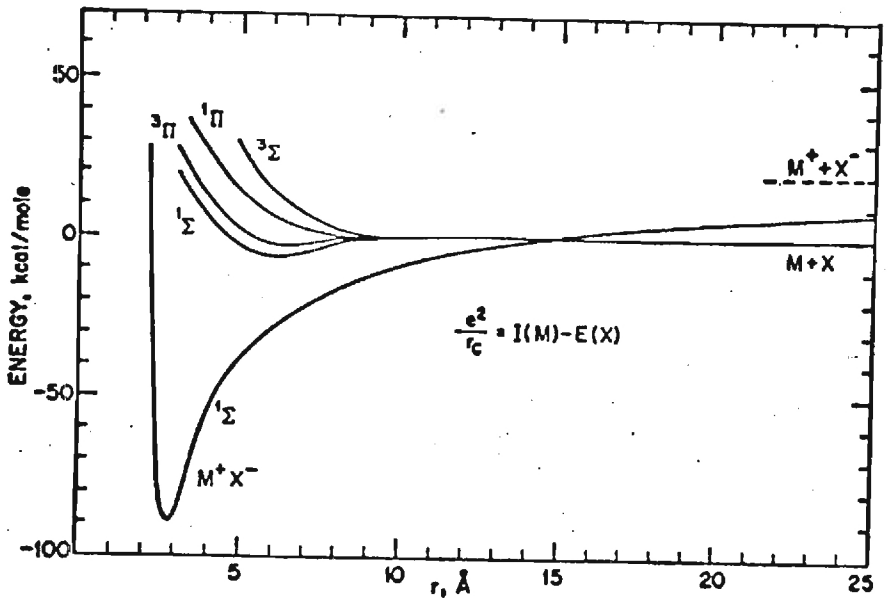
50
0
-50
-100
ENERGY, kcal/mole
5
10
15
20
25
r, Å
$^3\Pi$
$^1\Pi$
$^3\Sigma$
$^1\Sigma$
M^+X^-
$M^+ + X^-$
M+X
$\frac{e^2}{r_c} = I(M) - E(X)$

Figure 2

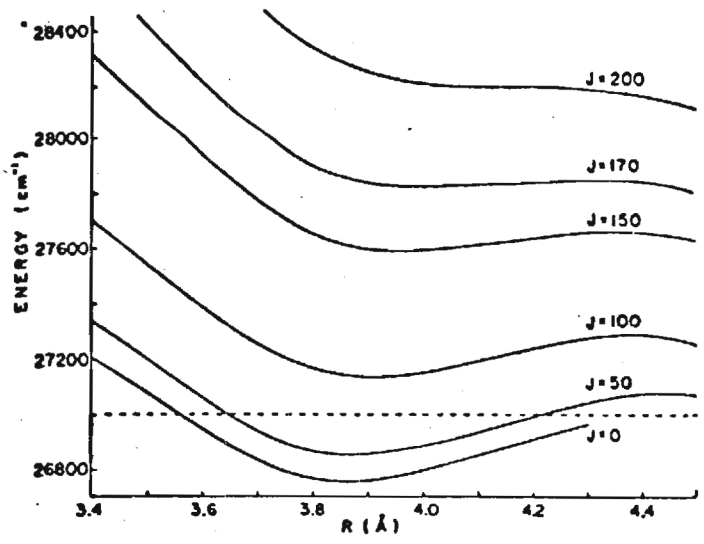
28400
28000
27600
27200
26800
ENERGY (cm⁻¹)
3.4
3.6
3.8
4.0
4.2
4.4
R (Å)
J=200
J=170
J=150
J=100
J=50
J=0

Figure 3

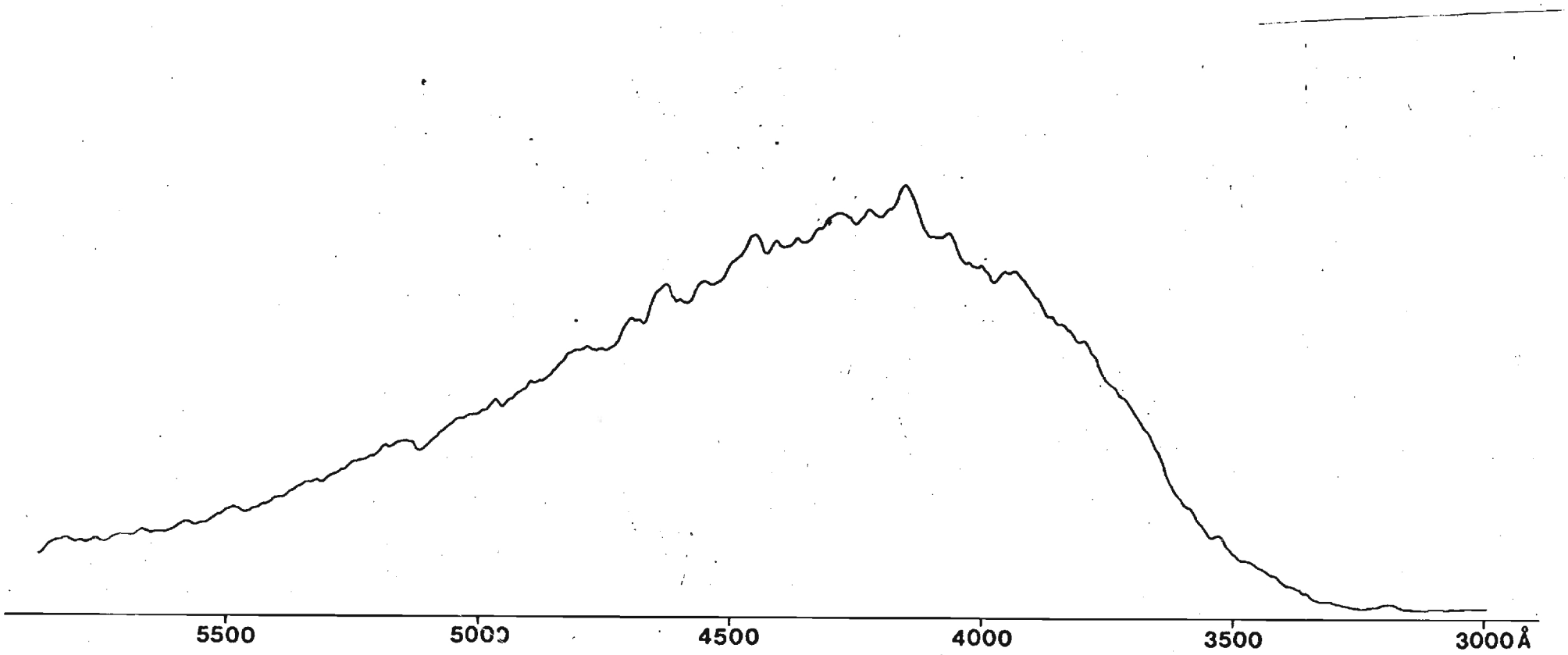

Figure 4

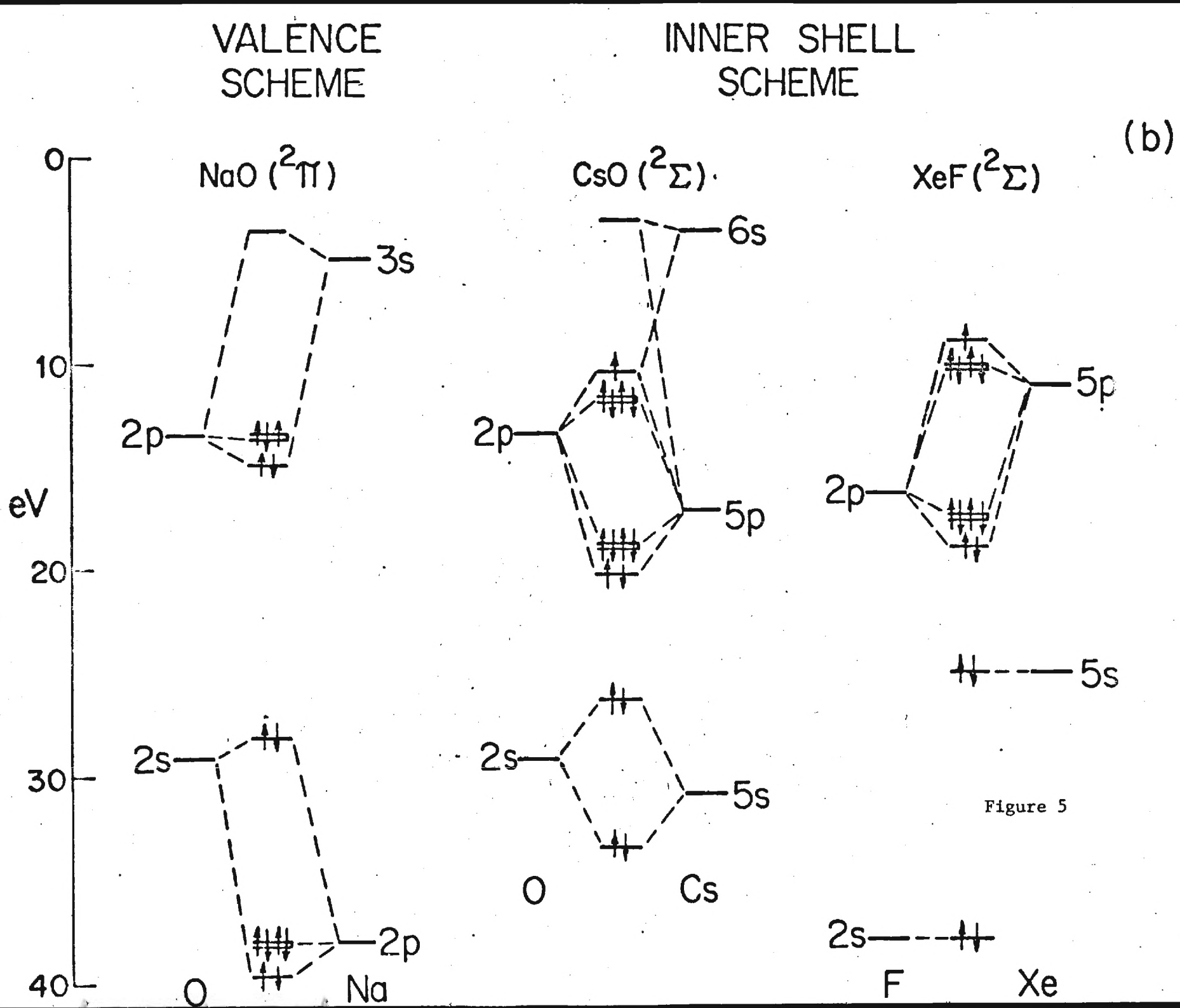
VALENCE SCHEME
INNER SHELL SCHEME
(b)
0
10
20
30
40
eV
NaO ($^2\Pi$)
CsO ($^2\Sigma$)
XeF ($^2\Sigma$)
3s
2p
6s
5p
2p
5p
2p
5s
2s
5s
2s
2p
O
Na
O
Cs
2s
F
Xe

Figure 5

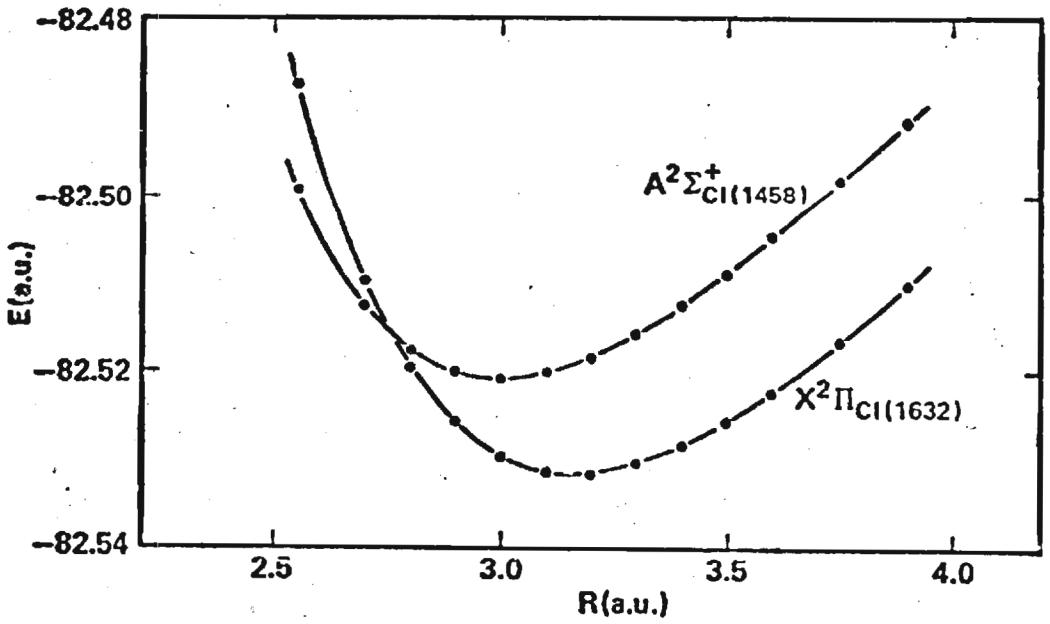
-82.48
-82.50
-82.52
-82.54
E(a.u.)
2.5
3.0
3.5
4.0
R(a.u.)
$A^2\Sigma^+_{CI(1458)}$
$X^2\Pi_{CI(1632)}$

Figure 6

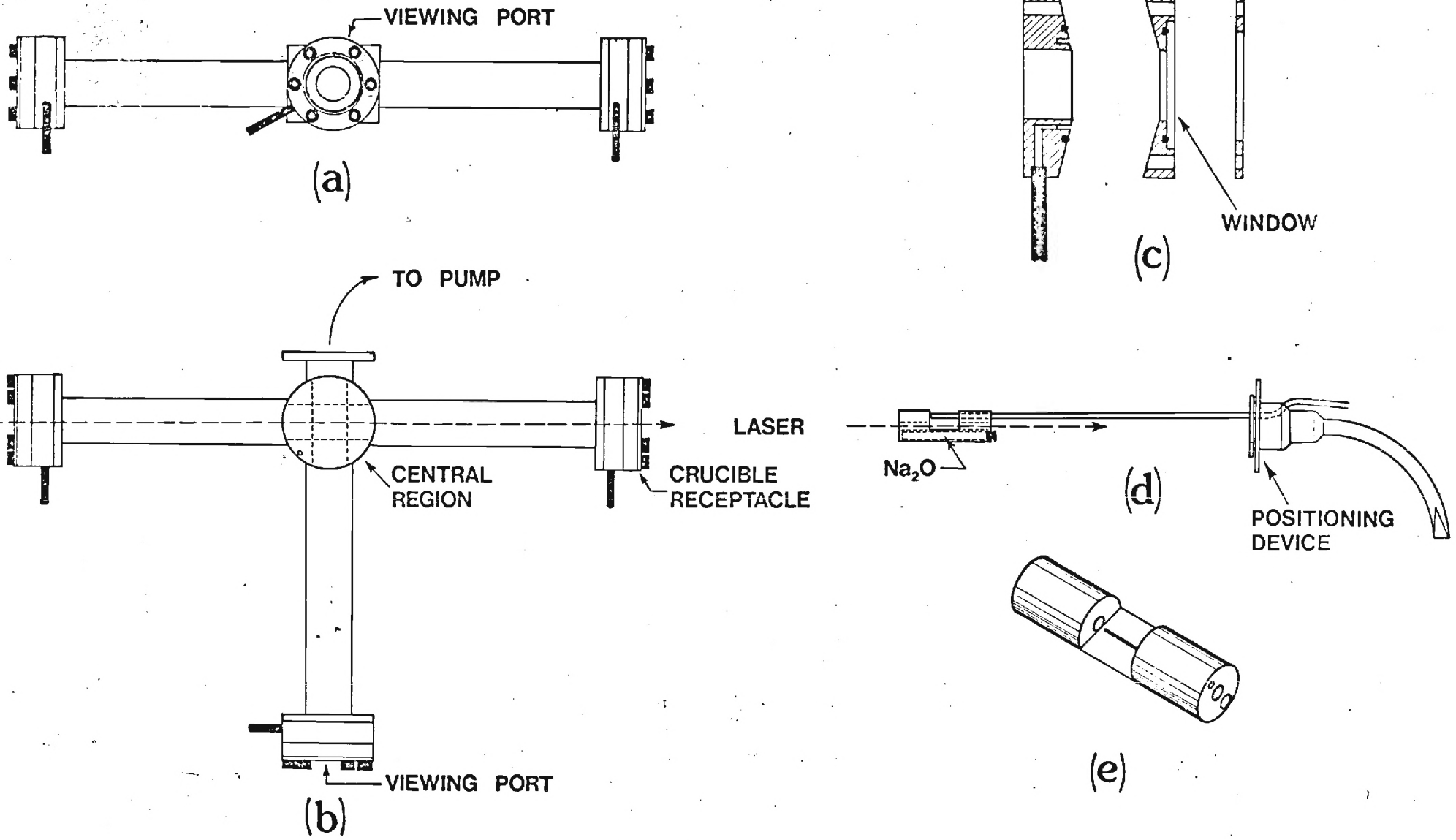
VIEWING PORT
(a)
TO PUMP
LASER
CENTRAL REGION
CRUCIBLE RECEPTACLE
VIEWING PORT
(b)
WINDOW
(c)
Na_2O
(d)
POSITIONING DEVICE
(e)

Figure 7

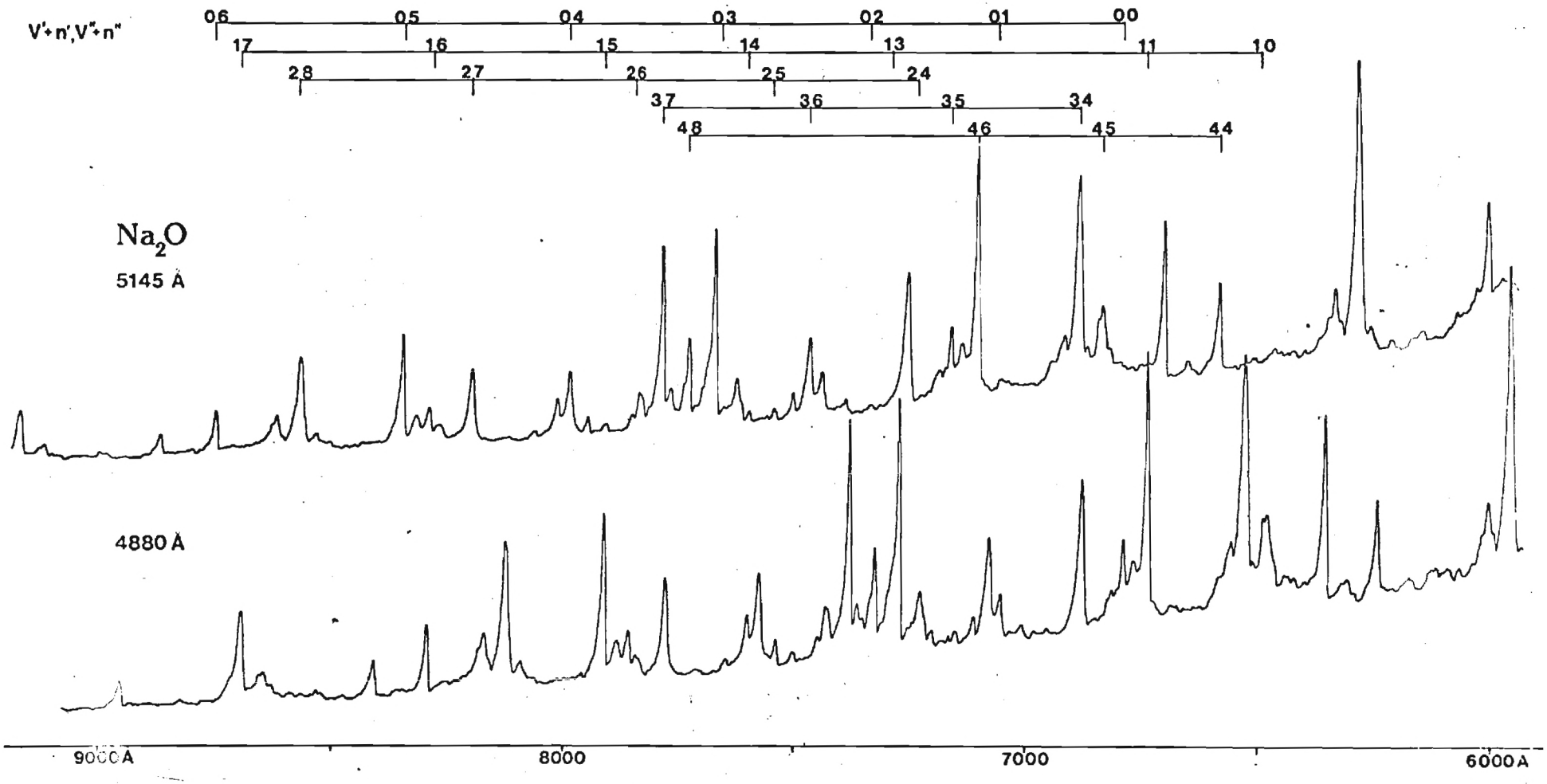
V'+n',V"+n"
06
05
04
03
02
01
00
17
16
15
14
13
11
10
28
27
26
25
24
37
36
35
34
48
46
45
44
Na_2O
5145 Å
4880 Å
9000 Å
8000
7000
6000 Å

Figure 8

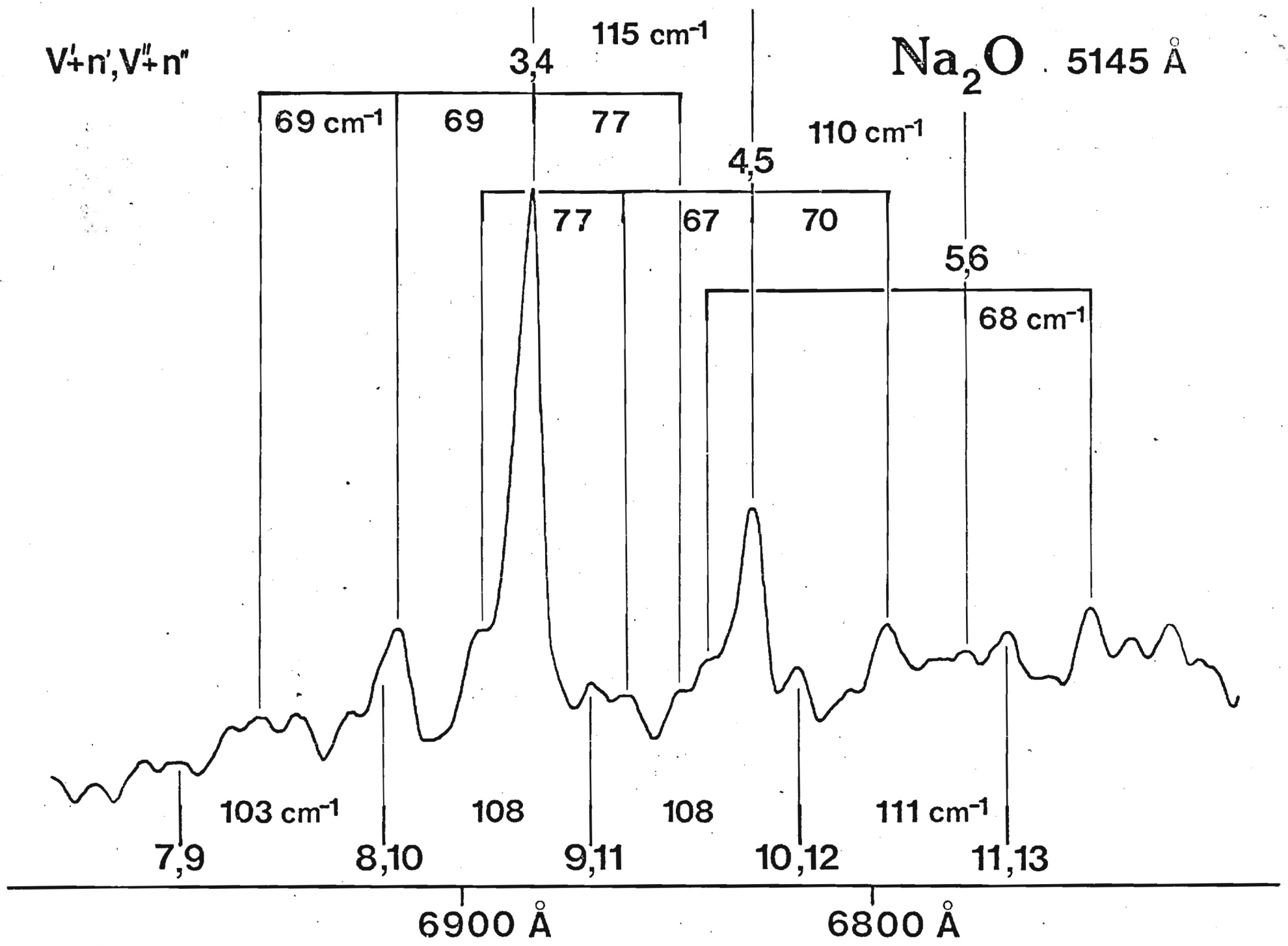
V'+n',V''+n''
3,4
115 cm-1
Na2O . 5145 Å
69 cm-1
69
77
110 cm-1
4,5
77
67
70
5,6
68 cm-1
103 cm-1
108
108
111 cm-1
7,9
8,10
9,11
10,12
11,13
6900 Å
6800 Å

Figure 9

A P P E N D I X F

LASER FLUORESCENCE STUDIES OF REFRACTORY COMPOUNDS

(Reprinted from Electro-Optics/Laser 80)

LASER FLUORESCENCE STUDIES OF REFRACTORY COMPOUNDS

by

James L. Gole
Georgia Institute of Technology
Atlanta, Georgia

As should be apparent from the wide diversity of topics discussed throughout the technical sessions associated with Electro-Optics Laser 80, lasers are finding increased use in a wide diversity of areas. In this discussion, we are concerned with a subset of these applications, namely, the characterization of refractory compounds using laser fluorescence techniques. In these few pages we hope to provide some feeling for the manner in which lasers can be combined with high vacuum and high temperature technology in order to elucidate the molecular electronic structure of high temperature molecules.

The chemistry and spectroscopy of high temperature molecules are complicated because of (1) the substantial density of states and (2) the diversity of populated levels at the typical temperatures necessary to produce sufficient gas phase concentrations for study. It is also difficult to maintain substantial concentrations because of the extremely reactive nature of most high temperature molecules. With the advent of the laser and its combination with modern sampling techniques, many of these problems are being obviated. Here, we will exemplify a portion of this work by considering the laser induced fluorescence of (1) Na_2O and Li_2O, two compounds of significant import to the energy technologies and (2) refractory species cooled in supersonic expansion. This latter topic will include a discussion of the characterization of hydrodynamically expanded sodium and copper vapor.

Laser Spectroscopy of Na_2O and Li_2O

In order to efficiently excite fluorescence from Na_2O and Li_2O we have constructed the device depicted in Fig. 1. Figs. 1(a) and 1(b) indicate the overall layout of the cell used in these experiments. Fig. 1(c) indicates the window design which is frequently necessary when working with refractory species, the gas flow system being designed to provide a uniform circulation of gas over the windows. In order to carefully control the vaporization of Na_2O in a very localized region, the device depicted in Figs. 1(d) and 1(e) is used. It consists of a crucible which is suspended on a 1/8" stainless steel tube such that once the overall device is connected to the cell sidearm the crucible is centrally located to the viewing port. The positioning control whose diameter is the same as the window shown in Fig. 1(c) is held in place in precisely the same fashion as the window. When connected to the overall cell, the crucible holder is rotated 90° with respect to its depiction in the Figure. When the cell is in operation, a laser beam traverses the path indicated in Figs. 1(b) and 1(d). Na_2O is directly vaporized through a thin slit into the path of the laser beam. The slit and the laser beam are parallel and the laser induced fluorescence is viewed at 90°.[1]

Using the cell described above and various pumping schemes, we have carried out experiments at both 100 μ (primarily background argon) and 10^{-6} torr. This range of background pressure allows us not only to do spectroscopy but also to observe quenching effects which are quite significant for both Na_2O and Li_2O. Thus far, experiments have been conducted primarily with an argon ion laser; however, some excitation has been accomplished with a rhodamine dye laser. Examples of the spectra obtained for Na_2O are shown in Fig. 2. They correspond to excitation at 5145 and 4880 Å. It appears that we can excite laser induced fluorescence with several of the available argon ion laser lines (4579, 4765, 4880, 4965, 5017, 5145 Å) and that the fluorescence spectra can be interconnected (significant overlap) in a rather substantial Deslandres Table. Much of our analysis of the observed spectra has depended on relating our Na_2O studies to available information on Li_2O. This data comes primarily from matrix isolation spectroscopy[2] and recent quantum chemical calculations.[3] Briefly, this data has been used to (1) attempt to estimate the normal frequencies of vibration for Na_2O based on a reasonable extrapolation from Li_2O and (2) determine the most likely electronic transition which should be excited in the visible using an argon ion laser.

Using a notation common to several quantum chemical descriptions of linear $D_{\infty h}$ Li_2O, the valence

orbital configuration for the ground state is

$$\ldots(3\sigma_g)^2(2\sigma_u)^2(1\pi_u)^4 \qquad {}^1\Sigma_g^+ \tag{1}$$

where the valence orbitals are constructed primarily from 2s and 2p electrons on lithium and oxygen. The lowest Li_2O excited states correspond to the promoted configurations

$$\ldots(3\sigma_g)^2(2\sigma_u)^2(1\pi_u)^3(4\sigma_g)^1 \qquad {}^{1,3}\pi_u \tag{2}$$

$$\ldots(3\sigma_g)^2(2\sigma_u)^2(1\pi_u)^3(3\pi_u)^1 \qquad {}^{1,3}\pi_g \tag{3}$$

and Grow and Pitzer[3b] have shown that these states are very low lying ($\Delta E_{excitation} \leq 1.3$ eV); therefore it is unlikely that even the allowed ${}^1\pi_u - {}^1\Sigma_g^+$ transition corresponds to the fluorescence observed upon single photon pumping with an argon ion laser. A further promotion which will result in a strongly allowed transition, most likely in the visible region, leads to the configuration

$$\ldots(3\sigma_g)^2(2\sigma_u)^1(1\pi_u)^4(4\sigma_g)^1 \qquad {}^{1,3}\Sigma_u^+ \tag{4}$$

We anticipate that the visible transition in Na_2O which is pumped by the argon ion laser corresponds to a ${}^1\Sigma_u^+ \leftarrow {}^1\Sigma_g^+$ excitation involving the analog of configurations (1) and (4). In pumping this transition one removes an electron from an orbital which is both Na-O and Na-Na antibonding and promotes this electron to an orbital which is both Na-O and Na-Na bonding. Hence, we expect that both the excited state stretching and bending frequencies should exceed that of the ground electronic state of Na_2O.

The ground state frequencies for Li_2O are (matrix isolation spectroscopy) $\nu_1 \simeq 760$ cm^{-1}, $\nu_2 \simeq 112$ cm^{-1}, and $\nu_3 \simeq 990$ cm^{-1}. Formulating a normal coordinate analysis based on the Li_2O measurements, we estimate a vibrational frequency of between 540 and 585 cm^{-1} for the symmetric stretch (ν_1) and 74 cm^{-1} for the bending mode of Na_2O. This is not unreasonable when comparisons are made with NaO where the vibrational frequency appears to be ~526 cm^{-1} (recall that Na_2O appears to be a linear molecule).

Although absolute quantum level numberings have not been assigned,[4] our extensive Deslandres Tables for the pumped transition indicate an upper state vibrational frequency of ~650 cm^{-1} and a lower state (ground state) frequency of ~550 cm^{-1} consistent with the predictions outlined above. In addition, a closer view (Fig. 3) of a region of the 5145 Å spectrum in Fig. 2 reveals what appear to be ~70 cm^{-1} separations expected for the ground state bending mode of Na_2O. Tentatively, it appears that the spectra correspond to progressions in the symmetric stretching and bending modes of the ground and excited state in a ${}^1\Sigma_u^+ \leftarrow {}^1\Sigma_g^+$ transition.

These studies not only provide information which is extremely useful for the understanding of fundamental dynamic processes such as the reaction of sodium dimers and oxygen atoms but also they establish a foothold for analyzing kinetic processes in which Na_2O plays a significant role. Because Na_2O represents an important constituent in energy generating systems, we desire a means to carefully monitor its behavior. It should also be noted that in addition to their use for the characterization of reaction kinetics, the current studies allow the independent determination of thermodynamic parameters which are extremely useful in the modeling of energy systems. Before the advent of the laser, the study of these elevated temperature free radicals rested primarily within the province of the matrix isolation spectroscopist. The versatility introduced with the laser should allow the future comparison of molecular behavior in gas phase and matrix environments.

Laser Spectroscopy of Supersonically Expanded Sodium and Copper

A recently developed technique involving the spectroscopic characterization of molecules produced in the supersonic expansion of molecular beams promises to alleviate several of the significant high temperature problems outlined in the introduction. Supersonic expansions, already well established for room temperature gas phase species,[5] offer a means of significantly cooling the internal degrees of

freedom and hence simplifying the spectroscopic analysis of those compounds of interest. A supersonic expansion of a gas from high pressure into vacuum can be engineered with either the pure compound or the compound seeded into an inert monatomic carrier gas (He, Ar). In the course of such a supersonic expansion, the translational temperature of the "carrier" gas[5] falls to an extremely low value which may approach a small fraction of a degree. [illegible]s which are effectively seeded into the expanding gas communicate with the low temperature "translational" bath provided by monatomic and/or higher cooled "clusters"[7] via two body collisions. In this way, the rotational degrees of freedom of the molecules can cool to temperatures comparable to that for translation. Vibrational cooling, although less complete than rotational cooling, can also be quite extensive.[5]

In our laboratory, supersonic expansions of refractory metals are being characterized using a combination of laser induced fluorescence and mass spectroscopy. The object of these studies is not only the attainment of cooled refractory species[8] but also the desire to use the expansion to induce the formation of small metal clusters M_n $(2 \leq n \leq 4)$. Here, we are concerned with the characterization of what is essentially the "middle ground" between the molecular electronic structure of small inorganic species and the metallic phase. In order to outline progress thus far, we will consider supersonic expansions of sodium and copper vapor.

The apparatus used in these studies is outlined schematically in Fig. 4. The details of the apparatus are discussed elsewhere.[9,10] Briefly, the output of an argon ion pumped dye laser is brought into a suitably equipped vacuum chamber where the laser beam intersects a supersonically expanded metal beam produced through use of an appropriate oven system. The oven depicted in the figure is similar to that used for the supersonic expansion of pure copper vapor.[9] The fluorescence zone is viewed at 90°, on one side by a blank phototube and on the opposite side by an appropriate focusing system and spectrometer. These devices are located in the back and front of the apparatus depicted in Fig. 4. Two types of spectral analysis are used. Total fluorescence is collected by the blank phototube as the frequency of the incoming dye laser is scanned. This is referred to as an "excitation" spectrum. With the dye laser tuned to one frequency, the light from the fluorescence zone can be dispersed by the spectrometer yielding a "photoluminescence" spectrum. Coincidental with the spectroscopic analysis of laser induced fluorescence is the analysis of the mass distribution of the supersonic beam. This is accomplished either with electron impact or photoionization (intense light source focused through sapphire window) mass spectroscopy.[10]

Sodium Expansions

The dramatic cooling which occurs as the result of a free jet expansion can be seen through comparison of the "excitation" spectra depicted in Fig. 5. Fig. 5(a) corresponds to the fluorescence signal from sodium vapor in thermal equilibrium with liquid sodium at 750 K. A stainless steel cross (concentric heat pipe[11]) similar in design to the device shown in Fig. 1 was used to contain the heated sodium and a 50 torr argon background pressure was maintained in order to prevent the sodium vapor from depositing on the windows. The stabilized output (5 mW) of a rhodamine 6G dye laser was used to excite fluorescence monitored by a 1P28 phototube. With the 0.5 cm^{-1} (FWHM) line width of the laser, the excitation spectrum was unresolved, showing no discernible features. For comparison, Fig. 5(b) is a computer simulation of an excitation spectrum for the vapor at 750 K. Although a precise one-to-one correlation cannot be made between the "peaks" in the experimental trace and those in the simulation, the absence of any discernible bands is consistent with both spectra.

Fig. 5(c) corresponds to the excitation spectrum for diatomic sodium produced in a rather mild "supersonic" beam using a double oven system (Fig. 4) with the main chamber of the oven at 820 ± 10 K (vap. pressure 10 torr) and a frontal "nozzle" chamber at 920 ± 10 K. The resolution and tuning range for the dye laser were identical to those for the thermal vapor spectrum (Fig. 5(a)). The spectrum taken in the molecular beam is dominated by the $v'' = 0$ progression (excitation from the lowest vibrational level of the ground electronic state of Na_2). Fig. 5(d) corresponds to a computer simulation of this experimental spectrum. The simulation represents a vibrational temperature of 100 K and a rotational temperature of 80 K. An uncertainty of ±20 K in the fit to the vibrational temperature and ±10 K to the rotational temperature is estimated from attempts to correlate the general appearance of the experimental spectrum with other simulated temperatures. There are some difficulties in obtaining uniform conditions throughout an experimental run with the backing pressures used for the mild expansion; however, further cooling and more uniform behavior is attained through operation at higher backing pressures where well controlled supersonic conditions are readily achieved. Fig. 6 corresponds to

a portion of the experimental excitation spectrum obtained using a rhodamine 6G dye laser with a main oven operated at 1000 K (sodium vapor pressure 140 torr) and a frontal nozzle operated at 1100 K. From a computer simulation, we find that the internal excitation of ≥99.75% of those species formed in the expansion corresponds to a [illegible] temperature of 30 K and a rotational temperature of 30 K.

From the examples given thus far, it should be apparent that supersonic refractory expansions offer great potential for simplifying the spectroscopic analysis of high temperature species. The spectra of the molecules formed in these sources are not only cleaner but also there is a significantly greater abundance per populated level. In order to take advantage of these possibilities to the fullest extent, one must be concerned with the development of suitable sources with which to achieve the high temperature hydrodynamic expansion.[12] With the goal of extending our work to these higher temperatures, we have recently been concerned with the supersonic expansion of pure copper vapor over the temperature range 2400-2800°K. The products of expansion have been characterized using laser induced excitation and photoluminescence spectroscopy covering a spectral range 4200-6600 Å. An example of the spectra obtained is shown in Figure 7(a). This excitation spectrum taken with a stilbene dye laser at 0.5 cm^{-1} FWHM corresponds primarily to fluorescence from the Cu_2 $B\ ^1\Sigma_u^+ - X^1\Sigma_g^+$ band system. The spectrum is simulated in Figure 7(b). Analysis based on this spectral simulation indicates two significant results.[9] We find that substantial cooling of the internal degrees of freedom has occurred; a rotational temperature ≤750 K and a vibrational temperature ≤900 K are found for the Cu_2 formed in expansion at oven temperatures ranging from 2600-2800 K. In addition, new features extending from 21843 to 21750 cm^{-1} are observed in the experimental spectrum. These spectral features must be attributed to a new state of Cu_2 or to polymeric Cu_3.[9] In the continuing pursuit of this problem in our laboratory, we are attempting to further cool the products of expansion through seeding of the pure copper beam with a monatomic gas such as helium or argon. Efforts thus far have been marginally successful and vibrational and rotational temperatures approaching 400 K have been obtained; however, it has still not been possible to achieve the requisite stability needed for a long range experimental scan. Indeed, it is by no means a straightforward task to obtain the needed stability in either a pure[9] or seeded copper expansion. It is significant that we find that the new spectral features grow at the expense of the Cu_2 B-X system indicating the distinct possibility that they result from polymeric copper. This result is quite encouraging in view of our desire to characterize small polymeric metallic clusters. In addition to efforts to further cool the beam, current studies are being extended to much higher resolution through use of a cw ring dye laser.[13]

Previous discussion has focused on the cooling of diatomic sodium and copper; however, the primary concern of our efforts is the use of hydrodynamic expansions to produce and characterize small metal clusters through laser photoluminescence or excitation spectroscopy. With this focus, we have attempted to excite fluorescence from polymeric sodium clusters in the spectral range 4200-6600 Å.[14] Although fluorescence from bound-bound excitations has not been observed,[15] a technique has been developed whereby bound-free transitions can be characterized through use of laser induced atomic fluorescence. Here we study the photodissociation of polymeric sodium trimers by pumping from discrete levels of the ground electronic state to a repulsive state[16] which dissociates to an excited sodium atom. Atomic fluorescence can be obtained under a variety of conditions.[17] An example of the spectra obtained under conditions discussed at length elsewhere[10] is indicated in Fig. 8. We find that D-line emission accompanies laser pumping upon cluster (M_n, $n \geq 3$) formation. The atomic emission onsets when the laser is operative ~400 cm^{-1} to the blue of the Na D-line components ($^2P_{1/2}$ 16955 cm^{-1}, $^2P_{3/2}$ 16973 cm^{-1}) and continues as the laser is tuned to higher frequency. The intensity of the atomic fluorescence varies as the frequency of the dye laser is scanned, producing a series of fluctuation bands. The structured atomic fluorescence features emanate primarily from the $^2P_{3/2}$ component (Fig. 8(b)) of the Na D-line with a considerably smaller component of fluorescence from $^2P_{1/2}$ (Fig. 8(c)). Mass spectrometric studies demonstrate that the structured atomic fluorescence corresponding to $^2P_{3/2}$ emission may be correlated with Na_3. The spectrum in Fig. 8(b) results from the photodecomposition of Na_3 via excitation from a shallow low-lying excited state or the ground electronic state.[16] Much higher resolution spectra than those shown in Fig. 8[17] (Fig. 8 rhodamine 110 dye laser, 0.5 cm^{-1} FWHM) demonstrate that the peaks observed in the fluctuation spectrum are correlated with discrete lower states and repulsive excited states. The present results for bound-free transition combined with recent two-photon ionization studies of bound-bound transitions in sodium trimer[15] are closely correlated with recent theoretical studies of the trimer.[18] Work on this system continues in our laboratory.

References

1. It should be noted that extensive baffling is used in the system to avoid problems with scattered laser light.

2. a. R. C. Spiker, Jr. and Lester Andrews, J. Chem. Phys. *58*, 702 (1973).

   b. D. White, K. S. Seshadri, D. F. Dever, D. E. Mann and M. J. Linevsky, J. Chem. Phys. *39*, 2463 (1963).

   c. K. S. Seshadri, D. White, and D. E. Mann, J. Chem. Phys. *45*, 4697 (1966).

3. a. R. J. Buenker and S. D. Peyerimhoff, J. Chem. Phys. *45*, 3682 (1966).

   b. D. T. Grow and R. M. Pitzer, J. Chem. Phys. *67*, 4019 (1977).

   c. E. L. Wagner, Theoret. Chim. Acta *32*, 310 (1974).

   d. T. K. Lin and D. D. Ebbing, Int. J. Quant. Chem. *6*, 297 (1972).

4. The notation in Fig. 1 is designed to give a relative numbering. Because v' and v'', the absolute quantum numbers for the upper and lower states are not known, we use the notation $v' + n'$, $v'' + n''$ where the indices in the figure denote the values of n' and n''. In this case it is likely that the value of v'' will exceed that for the level from which laser pumping occurs.

5. For recent studies of molecular (monomeric) species see R. E. Smalley, D. H. Levy, and L. Wharton, Laser Focus, November (1975); Acc. Chem. Res. *10*, 139 (1977); D. H. Levy, L. Wharton, and R. E. Smalley, in *Chemical and Biochemical Applications of Lasers*, Vol. II, edited by C. B. Moore (Academic, New York, 1977), p. 1; L. Wharton, D. Auerbach, D. Levy, and R. Smalley, in *Advances in Laser Chemistry*, Springer Series in Chemical Physics, edited by A. H. Zewail (Springer, New York, 1978). For recent studies of van der Waal's complexes see, for example, W. Klemperer, Ber. Bunsenges. Phys. Chem. *78*, 128 (1972); J. Chem. Soc. Faraday Discuss. *62*, 179 (1977) and references therein. See also Benjamin J. Blaney and George E. Ewing, "van der Waal's Molecules," Ann. Rev. Phys. Chem. *27*, 553 (1976) and references therein.

   NO_2 work: R. E. Smalley, B. L. Ramakrishna, D. H. Levy, and L. Wharton, J. Chem. Phys. *61*, 4363 (1974); *ibid.* *63*, 4977 (1975). *S*-tetrazine work: R. E. Smalley, L. Wharton, D. Levy, and D. W. Chandler, J. Mol. Spectrosc. *66*, 375 (1977); J. Chem. Phys. *68*, 2487 (1978).

6. Here the word "carrier" gas could refer to collisions with a helium or argon bath in large excess or collisions with monomeric components of the material of interest in a pure expansion.

7. In this way very large clusters may also be formed in a gradual building process. Clusters as large as Na_{16} have been observed in supersonic expansions of sodium. For very recent work see A. Herman, E. Schümacher, and L. Wöste, J. Chem. Phys. *68*, 2327 (1978).

8. For the initial demonstration of cooling using laser fluorescence, see M. P. Sinha, A. Schultz, and R. N. Zare, J. Chem. Phys. *50*, 549 (1973). There have been some recent elegant studies of sodium expansions at temperatures ranging from 1000 to 1200°K. Schümacher and co-workers have elegantly confirmed the study of Sinha et al. for sodium and potassium dimers and have begun the characterization of trimeric sodium (A. Herrmann, M. Hofmann, S. Leutwyler, E. Schümacher, and L. Wöste, Chem. Phys. Lett. *62*, 216 (1979)). These studies employ a combination of optical excitation and photoionization mass spectroscopy, clusters being ionized and detected (mass spectrometrically) in a two-photon process. In addition, ionization potentials have been determined for a wide range of sodium clusters up to and including Na_{16}. These studies extend and refine the earlier work of Robbins, Leckenby and Willis, Adv. Phys. *16*, 739 (1967) and Foster, Leckenby, and Robbins, J. Phys. B *2*, 478 (1969).

9. D. R. Preuss, S. A. Pace, and J. L. Gole, J. Chem. Phys. *71*, 3553 (1979).

10. a. J. L. Gole, G. J. Green, S. A. Pace, and D. R. Preuss, "Evidence for Photodissociation of

Polymeric Sodium Obtained in Supersonic Expansion--Observation of Trimer Fluctuation Bands," J. Chem. Phys., submitted for publication.

b. J. L. Gole, S. A. Pace, and D. R. [illegible], Rev. Sci. Instru., to be submitted.

11. See for example C. R. Vidal and J. Cooper, J. Appl. Phys. *40*, 3370 (1969).

12. Careful cognizance must be taken of the corrosive nature of many metals when placed in a high temperature environment. In addition, once this problem is solved, one must be concerned with the careful control of vaporization kinetics. See, for example, reference 9.

13. The bandwidth of the cw ring dye laser is 0.00015 cm^{-1}.

14. A. Herrmann, M. Hofmann, S. Leutwyler, E. Schümacher, and L. Wöste, Chem. Phys. Lett. *62*, 216 (1979). See also comments in reference 7.

15. It is also possible that one is pumping to the repulsive wall of an excited state possessing only a few bound levels.

16. These conditions are varied depending on the nature of the internal excitation characterizing the ground electronic state or very low-lying discrete electronic states formed in the beam and the repulsive character of the excited state to which optical pumping occurs. The laser induced atomic fluorescence shown in Figure 8 shows no increase in structure when scans at 0.03 cm^{-1} (FWHM) are made indicating that the possible observation of predissociative structure is unlikely.

17. The resolution used was 0.03 cm^{-1}.

18. R. L. Martin and E. R. Davidson, Mol. Phys. *35*, 1713 (1978).

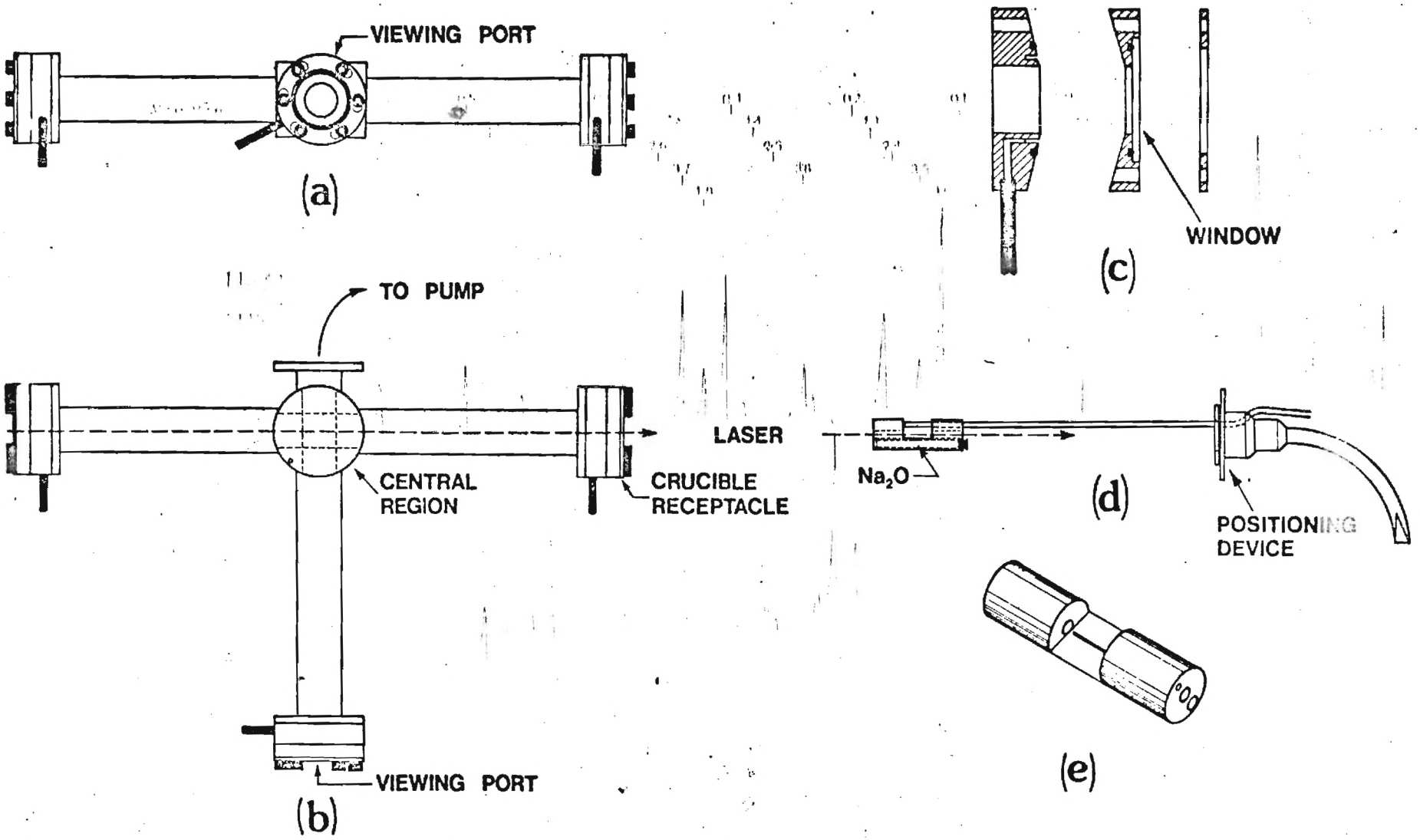

Figure 1: Schematic diagram of apparatus for laser fluorescence studies of Na_2O and Li_2O.

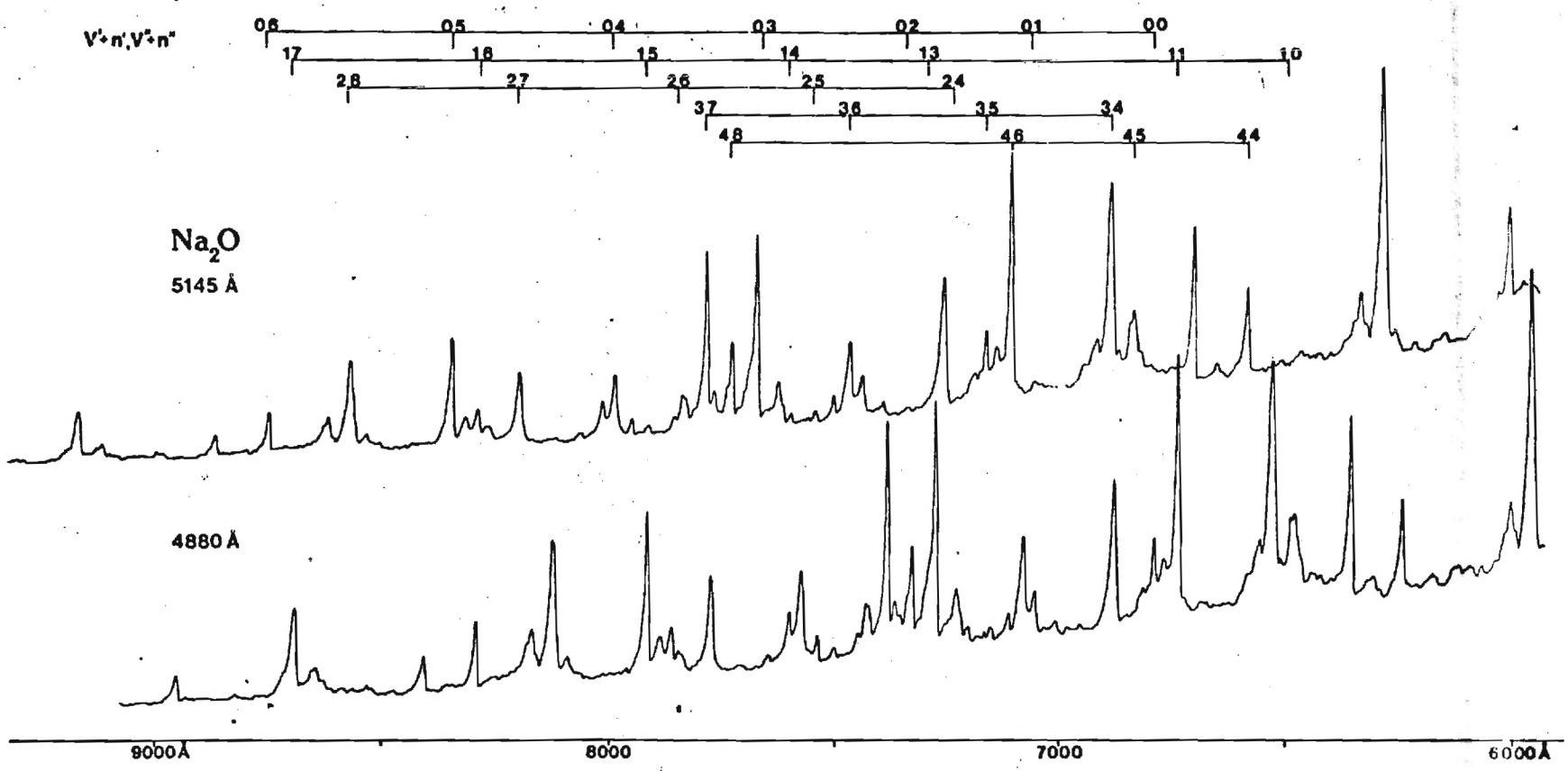

Figure 2: Laser induced photoluminescence spectra of Na_2O taken at a resolution of 1 Å and using the 5145 and 4880 Å argon ion laser lines for excitation. See text for discussion.

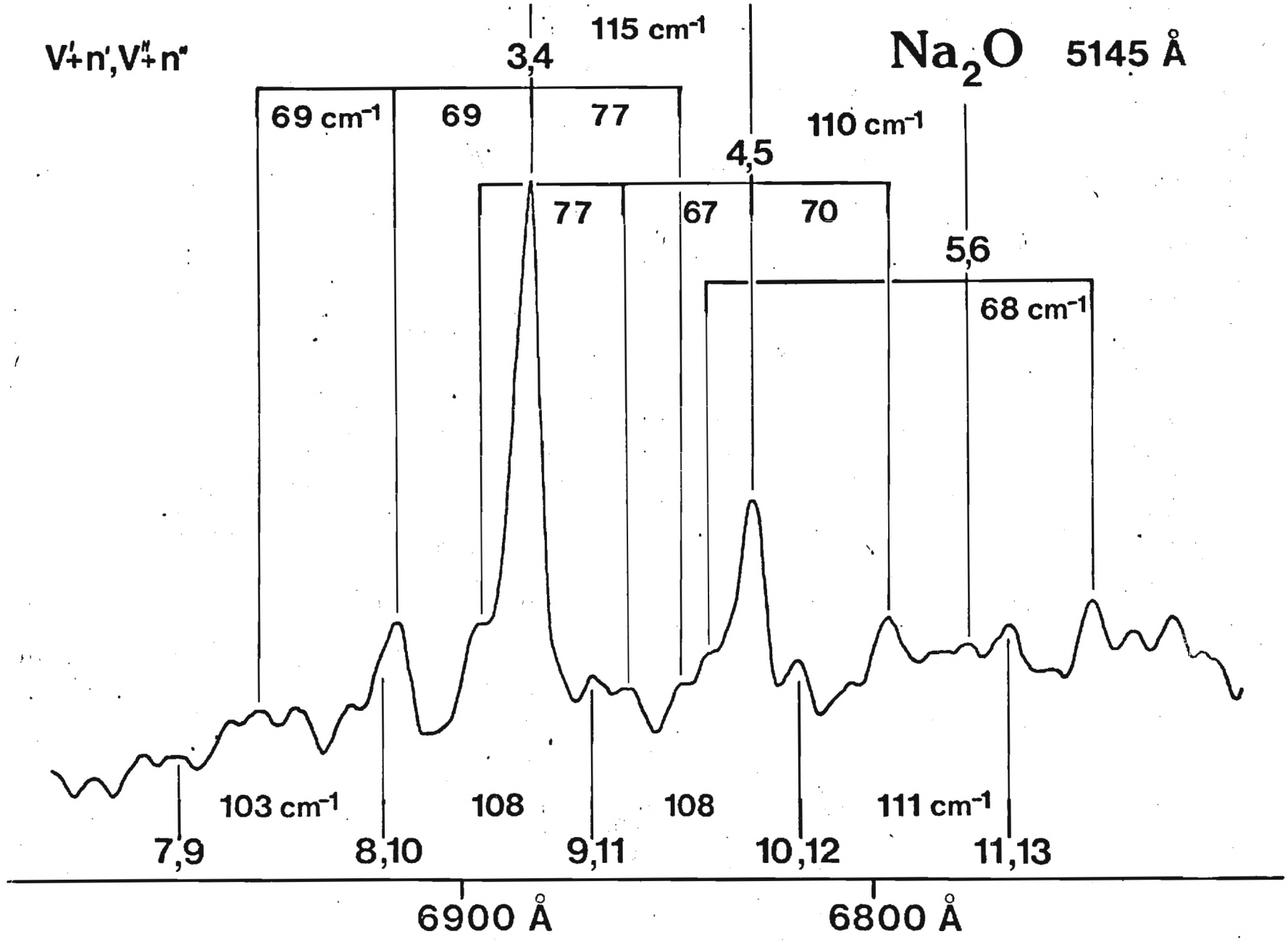

Figure 3: Closeup of laser induced photoluminescence spectrum of Na_2O taken at a resolution of 0.5 Å and using the 5145 Å argon ion laser line for excitation. See text for discussion.

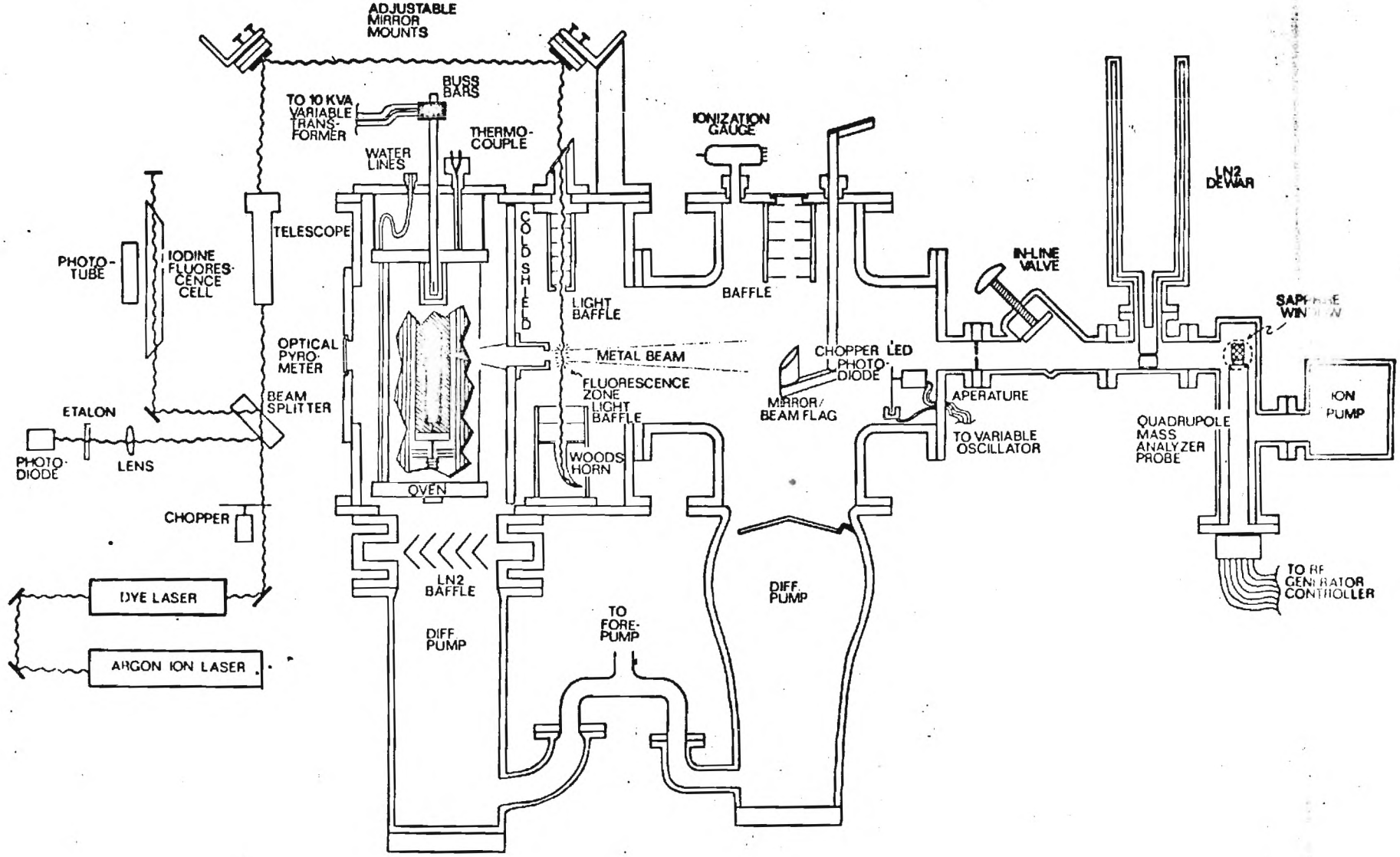

Figure 4: Schematic diagram of apparatus for supersonic expansion of refractory metals. See text for discussion.

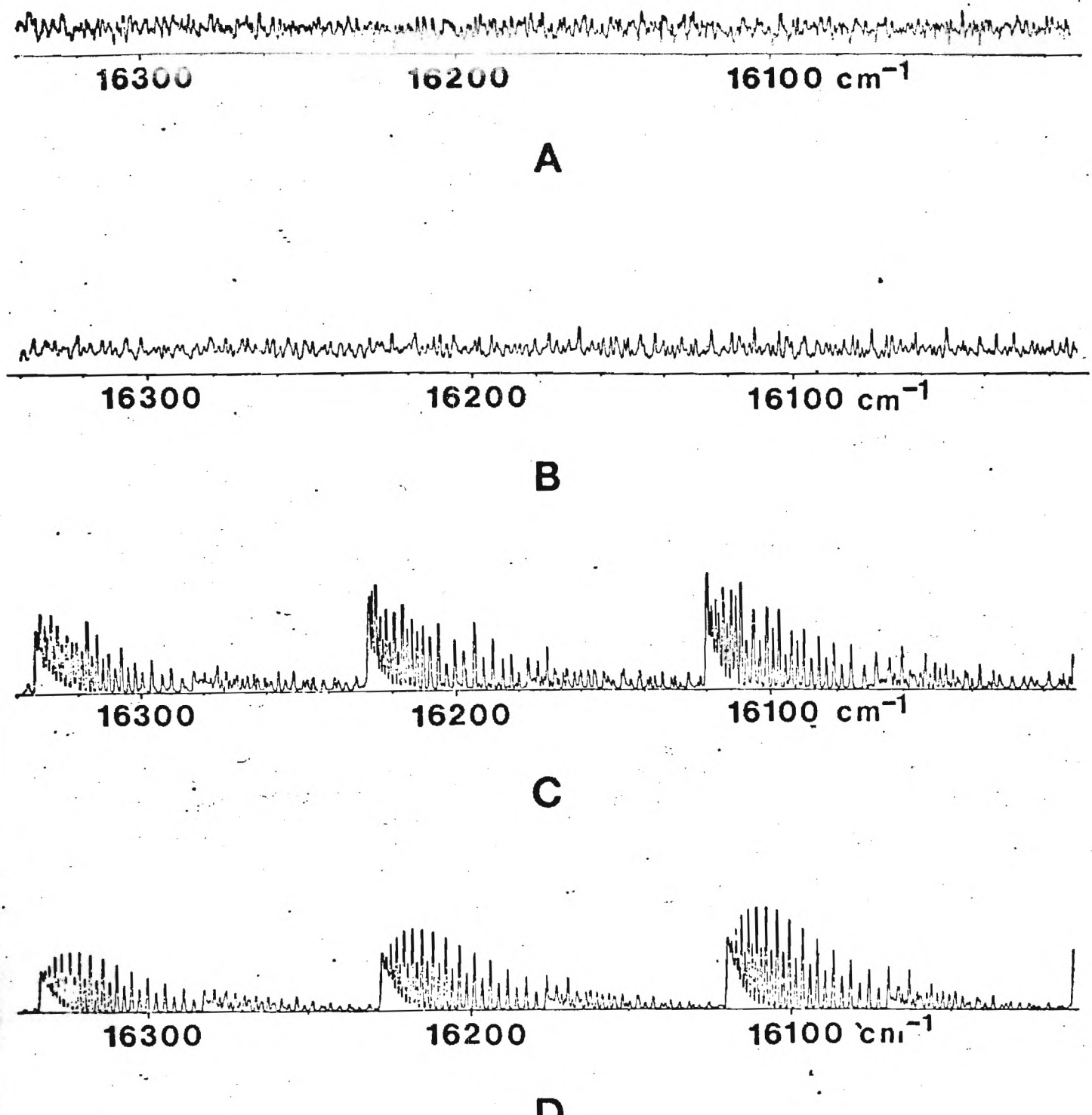

Figure 5: (a) Sodium dimer excitation spectrum obtained for the equilibrium vapor at 750 K. (b) Computer simulation of sodium dimer excitation spectrum for a vapor temperature of 750 K. (c) Sodium dimer excitation spectrum obtained in a mild supersonic expansion with an oven temperature of 820 K corresponding to a vapor pressure of 10 torr and nozzle temperature of 920 K. (d) Computer simulation of supersonic beam for T_{vib} = 100 K, T_{rot} = 80 K. See text for discussion.

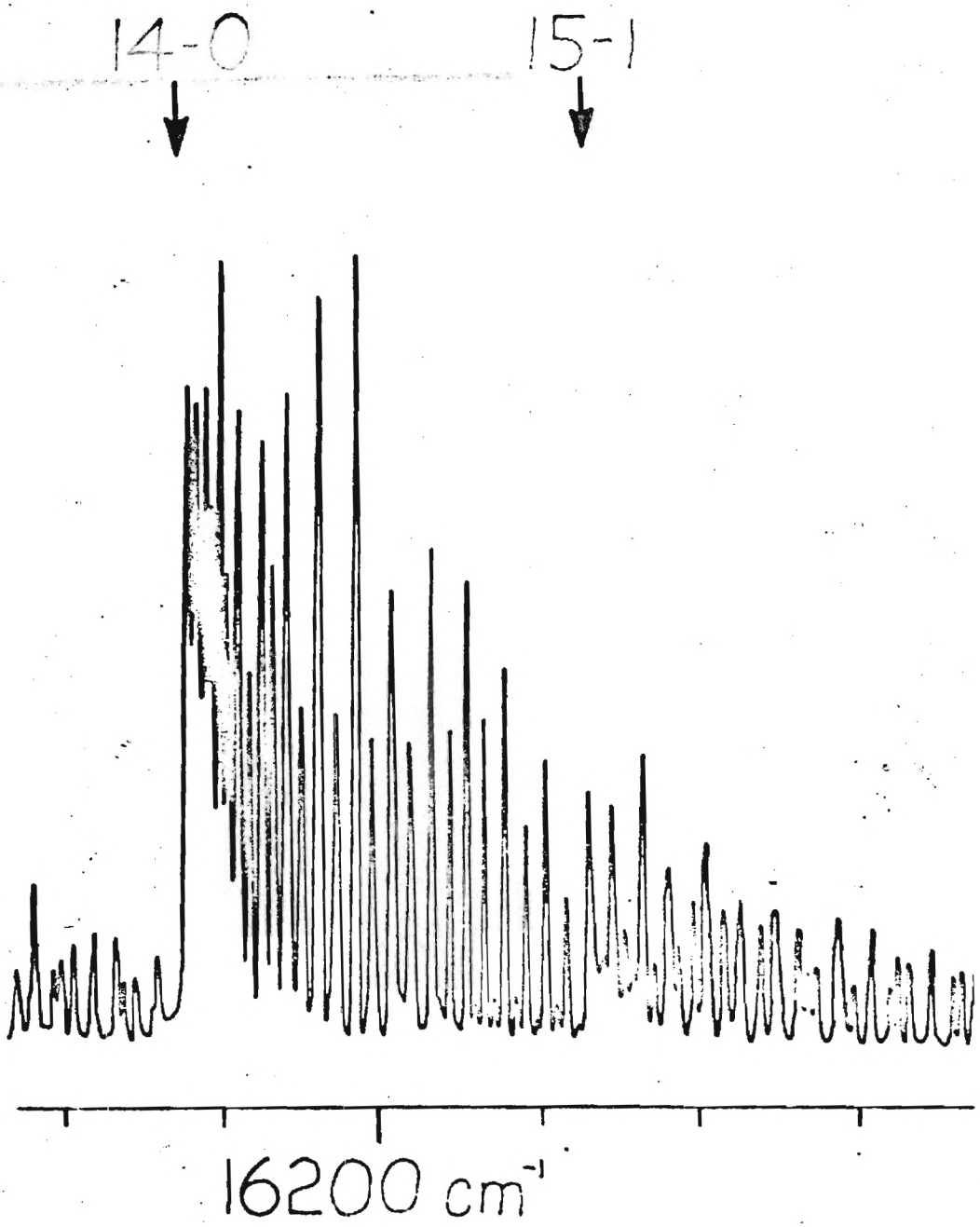

Figure 6: Sodium dimer excitation spectrum obtained with a supersonic expansion under conditions T_{oven} = 1000 K corresponding to a vapor pressure of 140 torr and T_{nozzle} = 1100 K. A computer simulation of this spectrum indicates T_{vib} = 50 K, T_{rot} = 30 K. See text for discussion.

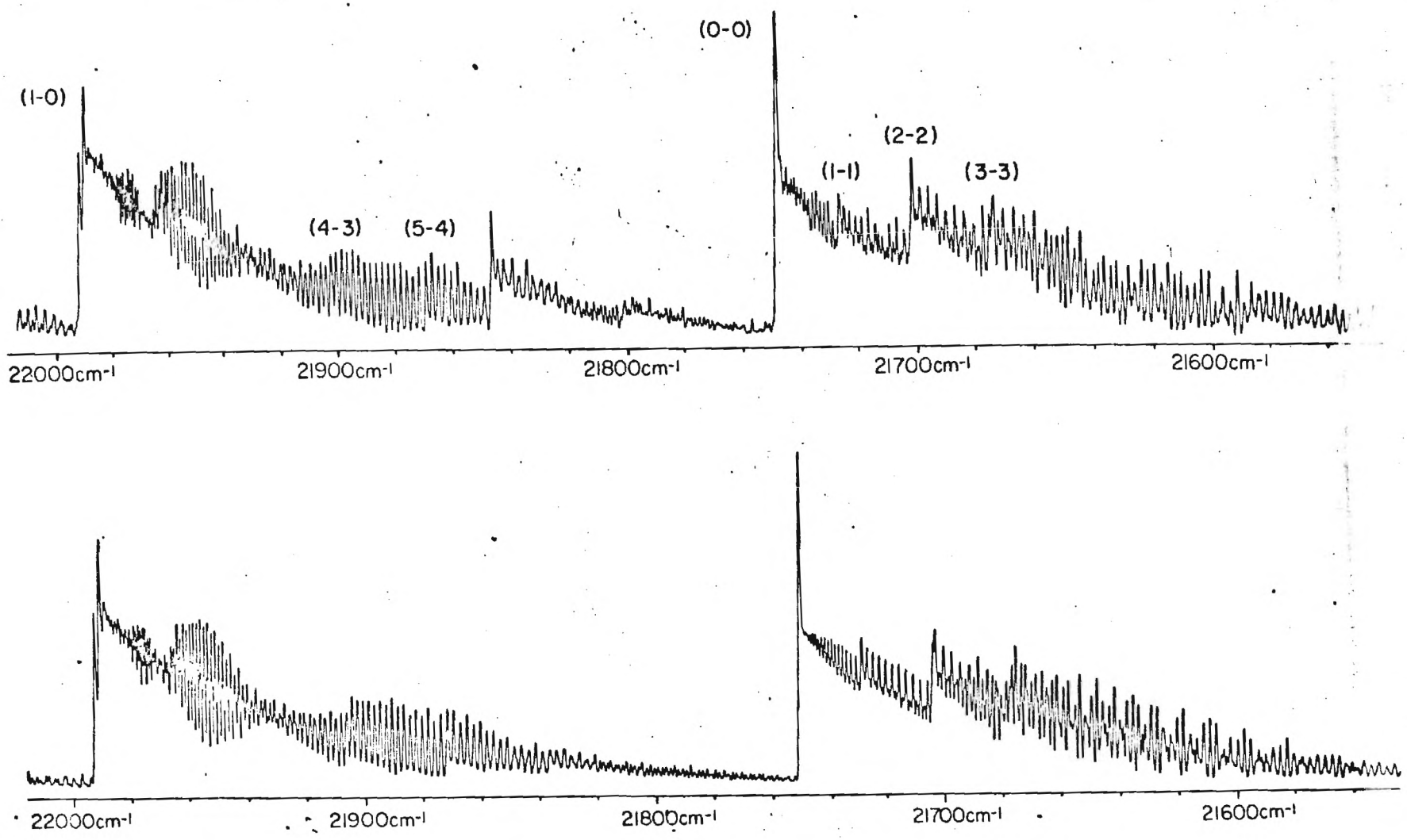

Figure 7: Excitation spectrum for supersonically expanded copper (top) excited with the output of a stilbene cw dye laser and computer simulation (bottom) of (1,0) and (0,0) sequences for Cu_2 $B^2\Sigma_u^+$ - $X^2\Sigma_g^+$ band system. The experimental spectrum is characterized by both the Cu_2 B-X system and a new copper fluorescence system (21750 - 21843 cm^{-1}). See text for discussion.

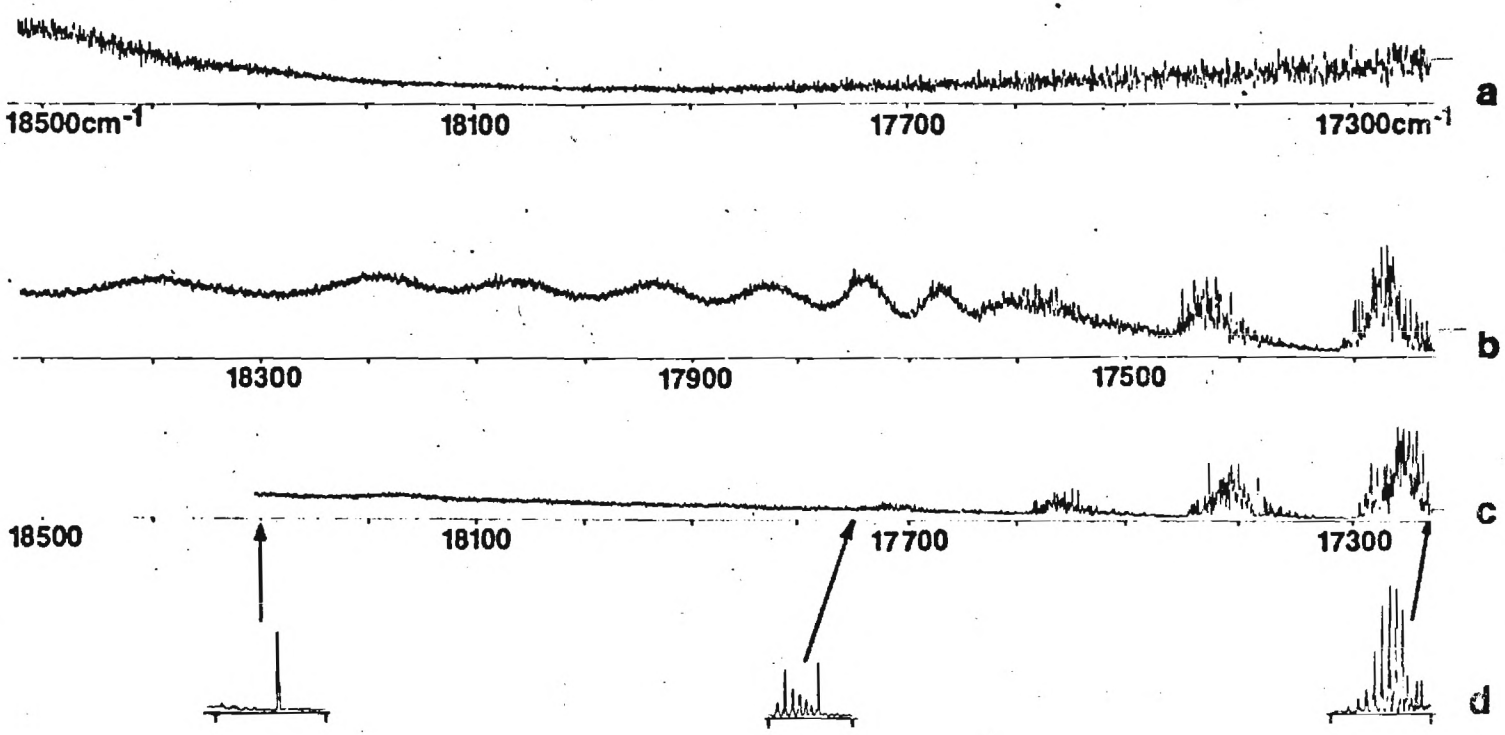

Figure 8: Spectra, as a function of dye laser excitation frequency, of supersonically expanded sodium including (a) an excitation spectrum showing the onset of Na_2 $B^1\Sigma_u^+ - X^1\Sigma_g^+$ (18000 cm^{-1}) fluorescence and the tail of Na_2 $A^1\pi_u - X^1\Sigma_g^+$ total fluorescence (b) laser induced atomic fluorescence from $^2P_{3/2}$ Na^* including fluctuation bands at ν(laser) > 17500 cm^{-1}, (c) minimal laser induced atomic fluorescence from $^2P_{1/2}$ Na^* and (d) fast photoluminescence scans indicating relative magnitudes of Na D-line and Na_2 A-X resonance fluorescence (tick marks indicate ν = 16000 and 18000 cm^{-1}). The lower frequency features appearing in scans (b) and (c) (ν_{laser} < 17600 cm^{-1}) correspond to Na_2 fluorescence coincidental with the D-line components.

APPENDIX G

(i) NONEQUILIBRIUM PRODUCT DISTRIBUTIONS OBSERVED IN THE MULTIPLE COLLISION CHEMILUMINESCENT REACTION OF Sc WITH NO_2. PERTURBATIONS, RAPID ENERGY TRANSFER ROUTES AND EVIDENCE FOR A LOW-LYING RESERVOIR STATE (J. Chem. Phys. *73*, 836 (1980)) (i)

(ii) EVIDENCE FOR ULTRAFAST V-E TRANSFER IN BORON OXIDE (BO) (J. Chem. Phys. *73*, 5025 (1980)) (ii)

Nonequilibrium product distributions observed in the multiple collision chemiluminescent reaction of Sc with NO_2. Perturbations, rapid energy transfer routes and evidence for a low-lying reservoir state

J. L. Gole and S. A. Pace

Department of Chemistry, Georgia Institute of Technology, Atlanta, Georgia 30332
(Received 5 March 1980; accepted 7 April 1980)

Nitrogen dioxide reacts with scandium to yield the $B\,^2\Sigma^+$–$X\,^2\Sigma^+$ spectrum of ScO. This reaction has been characterized from 10^{-5} to 1 Torr in order to study relaxation and rapid intramolecular E–E transfer among ScO excited states. At the lowest pressures, a ground state metal atom interacts with a tenuous atmosphere of oxidant gas (beam-gas configuration). These "single collision" studies are extended in a controlled manner to higher pressure by entraining the metal atoms in argon and subsequently carrying out the oxidation of this mixture. At all pressures, the measured $B\,^2\Sigma^+$ vibrational populations follow a markedly non-Boltzmann distribution. At the lowest pressures, the formation of ScO $B\,^2\Sigma^+$ results directly from the reaction $Sc + NO_2 \rightarrow ScO^* + NO$. At higher pressures, the $B\,^2\Sigma^+$ state is also populated via rapid intramolecular energy transfer from long-lived, weakly emitting "reservoir" states via the sequence $Sc + NO_2 + Ar \rightarrow ScO(res) + NO + Ar$ and $ScO(res) + Ar \rightarrow ScO(B\,^2\Sigma^+) + Ar$. Spin orbit and Coriolis interactions in ScO connect rovibronic levels of $B\,^2\Sigma^+$ and low-lying $^4\Pi_r$ or $^2\Pi_i$ reservoir states resulting in the observation of substantial perturbations in $B\,^2\Sigma^+$. Collisional energy transfer is particularly efficient for the most strongly perturbed levels of the $B\,^2\Sigma^+$ state. This energy transfer is manifest by the appearance of "extra" band heads representing normally forbidden (small electronic transition moment or Franck–Condon factor) "reservoir state"– ground state transitions which become allowed because of a small admixture of $B\,^2\Sigma^+$ character. The relative intensities of the extra and "main" $B\,^2\Sigma^+$–$X\,^2\Sigma^+$ transitions are strongly dependent on argon buffer gas pressure. A quantitative description of this dependence gives an estimate for the amount of mixing between the reservoir state and $B\,^2\Sigma^+$ and for the rate of energy transfer between these two states. *Collisional transfer to* ScO $B\,^2\Sigma^+$ $v' = 3$–9 *is found to proceed at rates which for certain levels approach 100 times gas kinetic*. The effects observed in ScO demonstrate that the excited states of this molecule interact in the presence of a collision partner as if they were large diffuse entities. These effects are not pathological. This behavior may have important implications for the modeling of energy systems as well as the ability to create population inversions requisite for the construction of visible chemical laser systems.

INTRODUCTION

Recently,[1,2] we have been concerned with the analysis of rapid intramolecular energy transfer routes among the excited states of molecules important at high temperatures. The energy transfer with which we are concerned is particularly efficient for the most strongly interacting excited state levels and hence the most strongly perturbed levels of each state. The magnitude of the perturbations which we observe in diatomic high temperature molecules can be comparable to that normally associated with polyatomics. While the analysis of these effects may, at first, seem impracticable, it is possible to employ the strength of the perturbations to advantage in order to obtain information at lower resolution which normally is obtained only in an exhaustive high resolution perturbation analysis.

In order to characterize rapid energy transfer in high temperature systems, we focus on highly exothermic chemiluminescent reactions involving the oxidation of refractory metals over the pressure range 10^{-6} to $\approx 10^2$ Torr. At the lowest pressures a metal atom intersects and interacts with a tenuous atmosphere of oxidant gas (beam-gas configuration)[3] forming product molecules in both ground and excited electronic states. Those excited states which are connected via an allowed transition to the ground electronic state usually emit a photon before undergoing subsequent collisions. Longer-lived "reservoir" states may also be formed in the reaction. These states may not be connected to the ground state via an allowed transition. They will emit photons at a much slower rate and may easily undergo collision before the emission of a photon. It is primarily these states with which we are concerned as we extend "single collision" studies in a controlled manner to higher pressure by entraining the metal atoms in the noble gases argon or helium and subsequently carrying out the oxidation of this mixture.

In two previous studies,[1,2] we have investigated the pressure dependence of the chemiluminescent emission from the aluminum–ozone reaction. The observed chemiluminescent spectrum is characterized by emission from both the $B^2\Sigma^+$ and $A^2\Pi$ states of AlO. At pressures in excess of 1 Torr (primarily argon buffer gas pressure) where collisional deactivation might be expected to lead to significant thermalization of nascent vibrational and rotational distributions, the measured AlO $B^2\Sigma^+$ vibrational populations follow a markedly non-Boltzmann distribution, exhibiting local maxima at vibrational level $v' = 6$, 8, 12, and 14. This behavior can be attributed to an initial chemical reaction $Al + O_3 \rightarrow AlO(A^2\Pi) + O_2$ followed by the collision induced rearrangement $AlO(A^2\Pi) + Ar \rightarrow AlO(B^2\Sigma^+) + Ar$. Spin–orbit

 0021-9606/80/140836-15$01.00

interactions in AlO connect rovibronic levels of the $A^2\Pi$ and $B^2\Sigma^+$ states and collisional energy transfer is particularly efficient for the most strongly perturbed levels of the $B^2\Sigma^+$ state. Consistent with the proposed mechanism for AlO $B^2\Sigma^+$ formation is the appearance of "extra" satellite band heads representing normally "Franck–Condon forbidden" $A-X$ transitions which become allowed because of a small admixture of $B^2\Sigma^+$ character. These features are observed concurrently with the main $B^2\Sigma^+-X^2\Sigma^+$ emission bands. In contrast to perturbations which affect only a few rotational levels in a given vibrational band or can lead to the appearance of certain extra rotational transitions,[4] the satellite bands arise from much larger perturbations which affect a range of rotational levels in the vicinity of the $B-X$ R branch heads. These observed features in AlO have now been found to be characteristic of several high temperature systems where collisional transfer analogous to that from the AlO $A^2\Pi$ state is observed and appears to emanate from long-lived reservoir states. Here we focus on the analysis of these effects in scandium oxide. More specifically, we investiga e the pressure dependence of the chemiluminescent emission from the ScO $B^2\Sigma^+$ state. Formation of this state occurs directly[5,6] via the chemical reaction

$$\mathrm{Sc}(^2D)+\mathrm{NO}_2(^2B_1)\rightarrow \mathrm{ScO}(A'^2\Delta,\ A^2\Pi,\ \underline{B^2\Sigma^+},\ C^2\Pi\cdots + \cdot\ \text{reservoir})+\mathrm{NO}(^2\Pi)$$

or as a result of rapid $E-E$ transfer from long-lived reservoir states which may be connected to the $B^2\Sigma^+$ state via a spin–orbit $A(\hat{L}\cdot\hat{S})$ or coriolis $B(\hat{L}\cdot\hat{J})$ interaction. In the present study the Sc–NO_2 reaction has been investigated over the pressure range 10^{-5} to 1 Torr. At the higher pressures an argon buffer gas was used.

As in AlO, extra satellite features are found to accompany the main ScO $B^2\Sigma^+-X^2\Sigma^+$ emission bands. In both AlO and ScO the relative intensities of the satellite and main transitions are strongly pressure dependent (argon buffer gas). The dependence may be expressed by a set of rate equations. For AlO a quantitative description of this dependence gives an estimate of the amount of mixing between the $A^2\Pi$ and $B^2\Sigma^+$ states and the rate of energy transfer between these two states. The measured rate constant (K_{AB}) for the collisional energy transfer $\mathrm{AlO}(A^2\Pi,\ v=53)+\mathrm{Ar}\rightarrow \mathrm{AlO}(B^2\Sigma^+,\ v=14)+\mathrm{Ar}$ is found to be $\sim 7\times10^6$ Torr^{-1} sec^{-1} comparable with a rate constant 9×10^6 Torr^{-1} sec^{-1} estimated for "hard sphere" collisions between Ar ($T\sim300$ °K) and AlO ($T\sim3000$ °K). This indicates that energy transfer occurs at every "hard sphere" collision on a time scale, K_{AB}^{-1} $\sim 2\times10^{-10}$ sec at 1 atm, similar to that generally associated with rotational relaxation ($R-R$ process). In the present study, we will examine much more pronounced effects observed in ScO. In contrast to AlO where pressure dependent effects are observed from 1 to 5 Torr, they are observed in ScO from 10 to 400 μm. Collisional transfer to ScO $B^2\Sigma^+$, $v'=3$–9 from long-lived reservoir states is observed to proceed at rates which for certain levels ($v'=6$, 8) approach 100 times gas kinetic, the time scale K_{RB}^{-1} being 3×10^{-12} sec at 1 atm for the most perturbed levels.

The effects which we have observed and analyzed in ScO are significant since they demonstrate that the excited states of this molecule interact in the presence of a collision partner as if they were large diffuse entities. Effectively one deals with "pseudomacromolecules" which display many of the characteristics of Rydberg states. This behavior may have important implications for the modeling of energy systems as well as the ability to create population inversions requisite for the construction of chemical laser systems. Based upon preliminary studies of potassium hydroxide as well as yttrium, lanthanum, and boron oxide formation, the effects we observe in ScO are not pathological but rather are indicative of a broad class of compounds.

EXPERIMENTAL

The burner systems used in these experiments are similar in design to those described previously.[6–8] The single collision experimental studies have been described in detail.[6] For multiple collision work, scandium metal (Alfa products 99.98%) is evaporated in a vacuum chamber from a resistively heated vapor deposited tungsten crucible (Ultramet, Pacoima, Calif.). The metal vapor is collimated by an argon or helium carrier gas (Matheson 99.9995%) and transported to the reaction zone where mixing with the oxidant gas occurs. The scandium is oxidized with NO_2 as supplied by Matheson Corp. (99.5% minimum purity). Typical operating pressures ranged from 2 to 20 μm of oxidant and from 10 to 1000 μm of argon or helium. Pressures were measured with a capacitance manometer (MKS Baratron Type 170). The sampling orifice to the manometer input head was made mobile so that pressure gradients in the chamber could be readily determined. In all cases the gas concentration in the multiple collision studies is dominated by the argon or helium carrier. For experiments run at the higher buffer gas pressures, flames were conical in shape with a base diameter of approximately 12 mm and heights ranging from 1 to 3 cm. At lower buffer gas pressures ($P_{ox}\sim2$–5 μm, $P_{argon}\sim10$–50 μm) flame definition decreased and a more diffuse glow was observed.

Fortunately scandium is one of the less corrosive and reactive high temperature metals. We have found that vapor deposited tungsten crucibles are ideally suited for long term experimental studies. These crucibles are placed in a machined carbon (Micromechanisms—99.95%) sheath which fits inside a commercial basket heater (R. D. Mathis, Long Beach, Calif.), the entire assembly being wrapped with several layers of zirconia (ZrO_2) cloth (Zircar Products, Florida, N. Y.). The zirconia insulation significantly reduces heat loss due to black-body radiative processes and, at the higher pressures, gas conduction[8]; its use permitted an upper operating temperature close to 1800 °C. The entire assembly was surrounded by a water cooled brass shield which was placed inside the vacuum chamber. This arrangement also provided an effective "light" baffle against black-body radiation from the crucible and heater. Under typical operating conditions (80 A at 12 V giving ~1600 °C), this crucible system continues to last indefinitely.

The chemiluminescent flame was focused onto the slit of a Spex 1 m monochromator, equipped with an RCA 4840 photomultiplier tube. The photomultiplier signal was detected with a Keithley 417 high sensitivity picoammeter whose output signal (partially damped) drove a Leeds and Northrop strip chart recorder. The spectrometer was periodically calibrated with a mercury resonance lamp. The entire optical system was calibrated for relative spectral response employing a quartz iodine standard lamp (EG and G #B 115 A).

ANALYSIS OF PERTURBATIONS AND RAPID TRANSFER ROUTES

In the following discussions, we focus on the nature of strong interactions between the $B\,^2\Sigma^+$ state of ScO and either previously unobserved long-lived electronic "reservoir" states or the high vibrational levels of known lower-lying electronic states from which transition may be "forbidden" primarily by virtue of the Franck–Condon principle. The reservoir states to which we refer are characterized by very small electronic transition moments connecting these states and the ground electronic state. Traditionally, emission from these states is seldom observed and, when detected, most frequently involves the lower energy state of an emission band system.

The $Sc–NO_2$ reaction is known to produce the $X\,^2\Sigma^+$, $A\,^2\Pi$, and $B\,^2\Sigma^+$ states of ScO.[9] Very weak emission may be observed from the $A'^2\Delta$ (Ref. 10) and $C^2\Pi$ states,[11] the emission from $A'^2\Delta$ being over an order of magnitude weaker than that from $A\,^2\Pi$. In the present study, we are concerned with the sequence which involves the initial reaction step

$$Sc(^2D) + NO_2(^2B_1) \rightarrow ScO(X\,^2\Sigma^+,\ A\,^2\Pi,\ B\,^2\Sigma^+\ A'^2\Delta,\ C\,^2\Pi,\ \text{Reservoir States}) + NO \qquad (1)$$

followed by collision induced transition to the $B\,^2\Sigma^+$ state:

$$ScO(\text{initial}) + Ar \rightarrow ScO(B\,^2\Sigma^+) + Ar\ . \qquad (2)$$

The nature of expected reservoir states will be discussed in a following section.

In the presence of intramolecular perturbations, neither the $B\,^2\Sigma^+$ state nor the states from which energy transfer occurs may be considered as pure states. Rovibronic levels of these initially populated states contain a small admixture of $B\,^2\Sigma^+$ character. Hence transitions from these reservoir levels, which are forbidden or very weak in the absence of perturbations, may "borrow intensity" from the $B–X$ spectrum and become allowed.[12] These features appear as satellite bands slightly shifted from the observed $B–X$ transitions. Figure 1(b) exemplifies one of these satellite features in the ScO $B\,^2\Sigma^+–X\,^2\Sigma^+$ spectrum taken at a pressure of 400 μm. Here we find a dominant (8, 5) band with a satellite observed ~ 50 cm^{-1} to the red. As we will demonstrate shortly, the energy separation ($\Delta\nu$) between the main and satellite bands is dependent on the vibrational level v' in $B\,^2\Sigma^+$ and is invariant (within experimental error) to v'', the vibrational quantum number in the ground (lower) state.

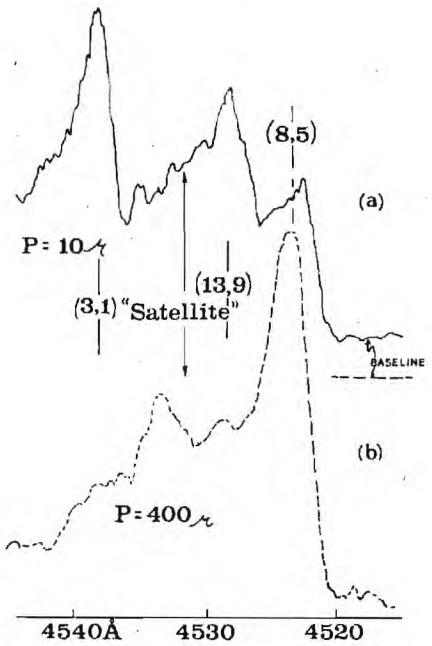

FIG. 1. Scan over portion of ScO $B\,^2\Sigma^+–X\,^2\Sigma^+$ emission spectrum (res = 1.5 Å) resulting from the $Sc + NO_2$ reaction. Band heads are denoted (v', v''). The upper trace was taken at a total pressure $P_{tot} = 10$ μm; the lower trace corresponds to $P_{tot} = 400$ μm $P_{NO_2} = 4$ μm for both traces, the remaining pressure corresponding to argon. As the argon pressure is raised an extra satellite feature becomes apparent to the red of the main $(v', v'') = (8, 5)$ band.

The magnitude of $\Delta\nu$ depends upon the "strength" of the perturbation (w) which usually involves a spin–orbit or coriolis interaction and the energy separation of the unperturbed states (δ). The eigenfunctions (Ψ) and eigenvalues (E) of the perturbed levels are[12]

$$\Psi_+ = c\Psi_1 - d\Psi_2, \quad \Psi_- = d\Psi_1 + c\Psi_2\ , \qquad (3)$$

where

$$c^2/d^2 = (\Delta\nu + \delta)/(\Delta\nu - \delta) \qquad (4)$$

and

$$(E_+ - E_-) = \Delta\nu = (4w^2 + \delta^2)^{1/2}\ . \qquad (5)$$

The subscripts 1, 2, and ± pertain to unperturbed and perturbed levels, respectively. An independent evaluation of both w and $\delta = E_1 - E_2$ is not possible from a measure of $\Delta\nu$ alone; however, sufficient additional information may be obtained from the pressure dependence of the relative intensities for the main (Ψ_+) and satellite (Ψ_-) transitions. In Fig. 2, we depict two mutually perturbed levels in the $B\,^2\Sigma^+$ state and that state formed initially via Reaction (1) which interacts strongly with $B\,^2\Sigma^+$ and from which energy transfer occurs. The initial chemical Reaction (1) with rate constant k populates a range of levels in a given reservoir state or Franck–Condon "forbidden" levels of a known electronic state. The vibrational dependence of this rate, even if known, is not required for the description given here. Strongly perturbed levels may be depopulated by spontaneous emission to the ground $X\,^2\Sigma^+$ state giving rise to the satellite feature observed in Fig. 1 or by nonradiative collisional transfer to the $B\,^2\Sigma^+$ state. The rate of this latter pro-

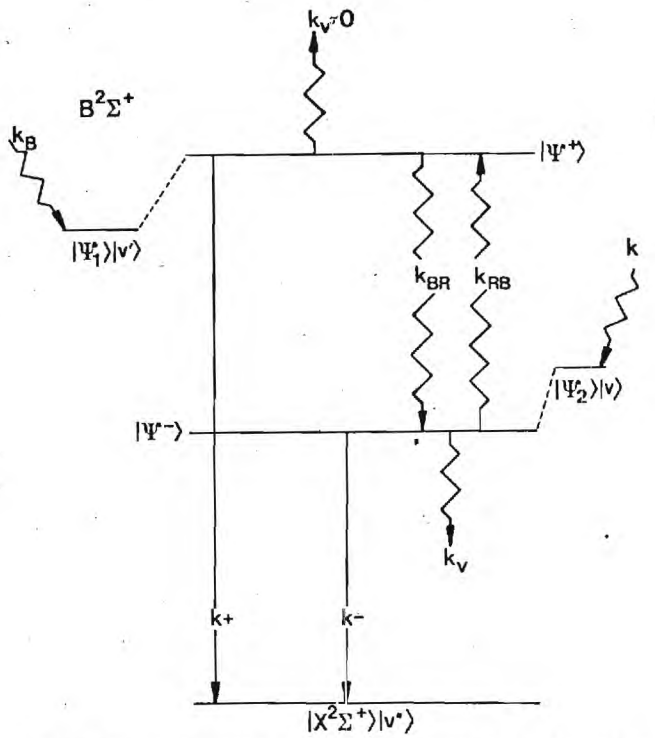

FIG. 2. Schematic representation of the competing transfer and depopulation processes, collisional redistribution (k_{RB}) from "reservoir state" levels and radiative emission (k_+ and k_-) from $B\,^2\Sigma^+$ and reservoir states. The vibrational relaxation rates are denoted by $k_{v'}$ and k_v. Transfer follows initial formation (k) of the reservoir state.

cess, intramolecular energy transfer which we denote by k_{RB}, is dependent on collisions between Ar and ScO and is therefore proportional to the argon pressure [Ar]. As a result of microscopic reversibility, there is a near equal probability of collisional transfer out of $B\,^2\Sigma^+$, i.e., $k_{BR} = k_{RB}$. k_B, the rate constant for *direct* ScO $B\,^2\Sigma^+$ formation [Reaction (1)] can be compared to the rate k_{RB}(Ar) for *collisional population* of the $B\,^2\Sigma^+$ state [Reaction (2)] by evaluating the Sc–NO_2 reaction from 10^{-5} Torr, where emission results from nascent product formation, through the pressure range where collisional transfer increases in importance and begins to dominate. The radiative rate constants k_- for Ψ_- and k_+ for Ψ_+ pertain to transitions from a single vibrational level in the upper state to all vibrational levels v'' of $X\,^2\Sigma^+$. k_+ and k_- are primarily dependent upon the upper state quantum number and to a much lesser extent on v''. The collisional rate constant is a function of both $v'(B\,^2\Sigma^+)$ and v(reservoir). k_{RB} and $k_\pm$ are purely phenomenological. They contain an implicit vibrational dependence which will be considered in a later section. k_v and $k_{v'}$ correspond to rate constants for radiative or nonradiative processes leading to vibrational relaxation in the reservoir or $B\,^2\Sigma^+$ states. As we will demonstrate in a following section, vibrational relaxation effects in either the $B\,^2\Sigma^+$ or reservoir states may safely be ignored.[13]

With the provisos indicated above, the elementary steps described in Fig. 2 which are pertinent to collisional transfer may be represented by a set of rate equations describing the time-dependent population of the $B\,^2\Sigma^+$ levels,

$$\frac{d}{dt[N_+]} = k_{RB}[N_-][\mathrm{Ar}] - k_{RB}[N_+][\mathrm{Ar}] - k_+[N_+] \ , \qquad (6)$$

where $[N_+]$ and $[N_-]$ are the population densities for the levels Ψ_+ and Ψ_-, respectively. The steady state solution[14] for Eq. (6) yields

$$[N_+]/[N_-] = k_{RB}[\mathrm{Ar}]/(k_{RB}[\mathrm{Ar}] + k_+) \qquad (7)$$

The two limiting cases can be envisioned:

$$\lim_{[\mathrm{Ar}]\to 0} \frac{[N_+]}{[N_-]} = 0 \ , \quad \lim_{[\mathrm{Ar}]\to\infty} \frac{[N_+]}{[N_-]} = 1 \ . \qquad (8)$$

The first corresponds to a low pressure extremum where the dominant population resides in those levels corresponding to Ψ_- and emission from perturbed levels of the reservoir state may dominate the observed emission spectrum[2] (given a sufficiently large transition moment). The second correspond to a high pressure limit in which the populations of Ψ_+ and Ψ_- become equal (saturation) and further increases in pressure have no effect on the relative intensities of the main and satellite features. The pressure at which the saturation point is reached is a function of the balance between the efficiency of collisional transfer (collisional transfer rate) and the radiative lifetime of the $B\,^2\Sigma^+$ state.[15]

The intensities of the main and extra transitions, $I^+(v', v'')$ and $I_-(v', v'')$, respectively, are related to the excited state populations $[N_\pm]$ by

$$I_\pm(v', v'') \propto A_\pm(v', v'')[N_\pm] \ , \qquad (9)$$

where $A_\pm(v', v'')$ represents the electronic and vibrational transition probability for emission from $\Psi_\pm$. Since the pertinent transitions are nearly coincident in frequency, phototube and frequency corrections are of minimal importance when considering relative intensities and we combine Eqs. (7) and (9) to yield

$$\frac{I_-(v', v'')}{I_+(v', v'')} = \frac{A_-(v', v'')}{A_+(v', v'')}\left(1 + \frac{k_+}{k_{RB}[\mathrm{Ar}]}\right) \ . \qquad (10)$$

A plot of relative intensity versus reciprocal pressure will be a straight line with an intercept $A_-(v', v'')/A_+(v', v'')$ and a slope which is a measure of k_+/k_{RB}. In a later section we will consider more specifically the analysis of the terms in Eq. (10) and its application to the solution of Eqs. (4) and (5).

RESULTS

We will demonstrate in this section that collisional transfer to the $B\,^2\Sigma^+$ state of ScO occurs much more efficiently than previously observed in AlO. In order to characterize this energy transfer, the strong interactions from which it results, and its effect on the relative population distribution in the $B\,^2\Sigma^+$ state, we have analyzed the B–X emission spectrum from 10^{-5} to 1 Torr.

A. Vibrational populations in $B\,^2\Sigma^+$

Figures 3, 4, and 5 depict representative scans of the ScO $B\,^2\Sigma^+$–$X\,^2\Sigma^+$ emission spectrum taken at 10^{-5}, 10^{-2}, and 1 Torr, respectively. Each spectrum is comprised of red-degraded bands falling into the sequence groupings

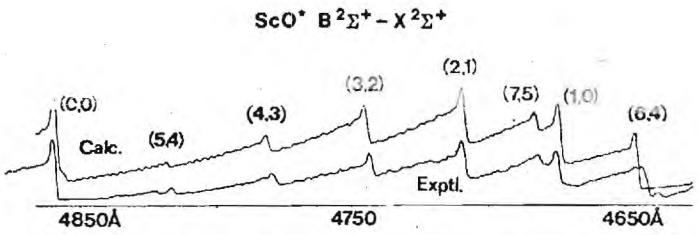

FIG. 3. Chemiluminescent spectrum obtained under single collision conditions from the reaction $Sc + NO_2 \rightarrow ScO^* + NO$. Bandheads in the ScO $B\,^2\Sigma^+$–$X\,^2\Sigma^+$ band system are denoted (v', v''). The lower trace corresponds to the experimental spectrum, while the upper trace is a computer simulation. Perturbations are apparent for levels with $v' = 3$–7. Spectral resolution is 1.5 Å. See text for discussion.

$0 \leq \Delta v \leq 2$. (The notation $\Delta v = v' - v''$ pertains to the transitions connecting vibrational levels v' of $B\,^2\Sigma^+$ and v'' of $X\,^2\Sigma^+$.) The experimental spectra were taken at a resolution of 1.5 Å and a scan speed of 0.2 Å/sec. The spectra were assigned by comparison with previously reported data.[6] All spectra were calibrated using mercury and neon resonance lamps.

In each figure, the experimental spectra are compared to computer synthesized spectra calculated with the aid of Franck–Condon factors[16] and RKR curves[17] generated using available high resolution data.[18] The computer simulation assumes no level perturbations. The comparison of experimental and calculated spectra allows the rapid assessment of strong perturbations in the $B\,^2\Sigma^+$ state. Upon analysis of the spectra, it became apparent that the $v' = 3$–9 vibrational levels of the $B\,^2\Sigma^+$ state were all significantly perturbed, and that some modification of previous wavelength assignments[9,15] was necessary. These revised level positions are listed in Table I where the error estimate (± 0.2 Å) represents one standard deviation in the wavelength calibration.

Taking into account the maximum temperature of the scandium metal undergoing reaction[19] and all other factors in addition to reaction exoergicity which contribute to the available energy for formation of ScO product, the $Sc–NO_2$ reaction can result in the population of 16 vibrational levels in the $B\,^2\Sigma^+$ state.

The relative intensities $I_{v',v''}$ of vibronic transition (v', v'') in emission are related to the excited state

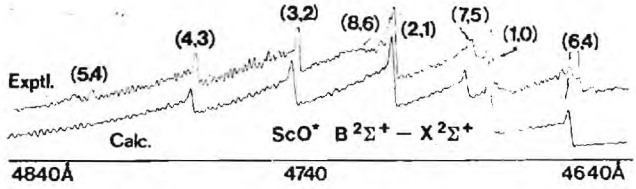

FIG. 4. Chemiluminescent spectrum obtained at $P_{tot} = 14$ μm for the process $Sc + NO_2$ ($P \approx 4$ μm) + Ar ($P \approx 10^3$ μm) → ScO* + NO + Ar. Bandheads in the ScO $B\,^2\Sigma^+$–$X\,^2\Sigma^+$ band system are denoted (v', v''). The upper trace corresponds to the experimental spectrum; the lower trace is a computer simulation. Perturbations are apparent for levels with $v' = 3$–7. A dual satellite structure accompanies the (6,4) band. Spectral resolution is 1.5 Å. See text for discussion.

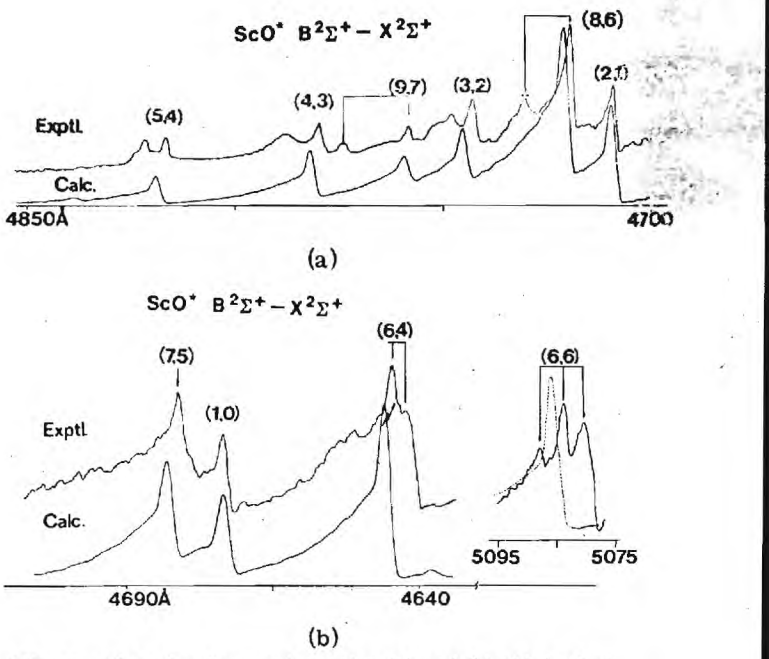

FIG. 5. Chemiluminescent spectra (a) and (b) obtained at $P_{tot} \approx 1000$ μm for the process $Sc + NO_2$ ($P \approx 30$ μm) + Ar ($P \approx 1000$ μm) → ScO* + NO + Ar. Bandheads in the ScO $B\,^2\Sigma^+$–$X\,^2\Sigma^+$ band system are denoted (v', v''). The upper traces correspond to the experimental spectrum; the lower traces are computer simulations. Perturbations and satellite structure are apparent for levels $v' = 3$–9. The computed spectrum corresponding to the (6,6) inset in (b) (dashed line) merely indicates the expected location of the (6,6) band and does not correspond to any attempted intensity match. Spectral resolution is 1.5 Å. See text for discussion.

populations $N_{v'}$ by

$$I_{v',v''} = \xi(\nu)\,\nu^4 q_{v',v''} R_e^2(\bar{r}_{v',v''}) \tag{11}$$

where $\xi(\nu)$ is a proportionality constant defined to include the variation of instrumental (spectrometer and

TABLE I. Modified parametrization for ScO $B\,^2\Sigma^+$–$X\,^2\Sigma^+$ transitions—bands observed in Figs. 3, 4, and 5.[a]

Band (v', v'')	λ (Å)[b]	Observed frequency	Calculated frequency[c]	Δ (cm^{-1}) (obs–calc)
(0,0)	4859.3	20 573	20 573	...
(1,0)	4674.0	21 389	21 389	...
(2,1)	4709.1	21 230	21 228	2
(3,2)	4743.4	21 076	21 068	8
(4,3)	4780.0	20 914	20 907	7
(5,4)	4817.5	20 752	20 746	6
(6,4)	4644.6	21 525	21 518	7
(7,5)	4681.7	21 354	21 346	8
(8,6)	4719.1	21 185	21 176	9
(9,7)	4759.2	21 006	21 002	4

[a]Bands listed are representative of $v' = 0$–9 $B\,^2\Sigma^+$ perturbations. From analysis of several transitions to $v'' = 0$ → 7, no measurable perturbations of these ground state levels are found.
[b]Only (0,0), (1,0), and (2,1) bands agree with calculated bandhead positions. All other levels are shifted.
[c]Calculated from $T_e(B\,^2\Sigma^+–X\,^2\Sigma^+) = 20640.2$, $w_e' = 825.47$, $w_e x_e' = 4.21$, $w_e'' = 964.95$, $w_e x_e'' = 3.95$. See A. Adams, W. Klemperer, and T. M. Dunn, Can. J. Phys. 46, 2213 (1968); L. Akerlind, Ark. Fys. 22, 41 (1962); and Refs. 9 and 15.

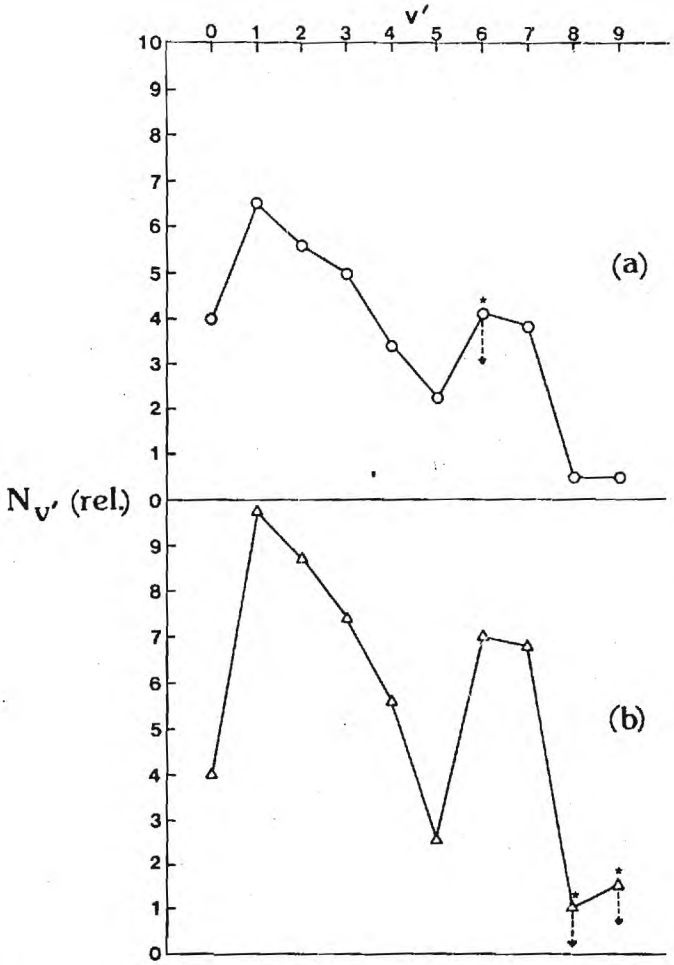

FIG. 6. $B\,^2\Sigma^+$ vibrational populations ($N_{v'}$) for (a) single collision conditions—Fig. 3; and (b) $P_{tot} = 14$ μm—Fig. 4. Relative populations are determined on the basis of the computer simulations in Figs. 3 and 4 for $v' = 0$–9. Populations denoted with an asterisk represent upper bound estimates.

photomultiplier tube) response with frequency; $q_{v',v''}$ and $\bar{r}_{v',v''}$ are, respectively, the Franck–Condon factor and r centroid for the (v', v'') transition. The electronic transition moment $R_e(\bar{r}_{v',v''})$ is written as an explicit function of the r centroid in accordance with the Fraser approximation.[20] This information is incorporated into the computer program to calculate the spectrum corresponding to a $^2\Sigma^+$–$^2\Sigma^+$ transition. Once a fit is made to a given spectrum as in Figs. 3, 4, and 5, a rotational temperature is determined for each individual vibrational band and relative vibrational level populations are evaluated. For those spectra obtained at the lowest pressures where only nascent product formation is monitored, the rotational temperature of each vibrational band can differ[21]; however, at higher pressures rotational distributions are found to equilibrate rapidly and the entire spectrum is characterized by one rotational temperature.[22]

In Figs. 6 and 7 we compare $B\,^2\Sigma^+$ vibrational populations determined for 10^{-5}, 10^{-1}, and 1 Torr chemiluminescent flames. Only those vibrational levels ($v' = 0$–9) which play a dominant role in the spectra presented in Figs. 3, 4, and 5 are considered; however, emission is also observed corresponding to those transitions from $v' = 10$–13 having the largest Franck–Condon overlap with the ground electronic state.

The single collision spectrum (Fig. 3) is characterized closely by a single rotational temperature, $T_{rot} \sim 6000\,^\circ$K. This result is consistent with a previous analysis of rotational structure in the (0, 0) band and with temperature dependence studies which demonstrate that the Sc–NO_2 reaction to form ScO $B\,^2\Sigma^+$ proceeds with a substantial activation energy.[22] Not surprisingly, the vibrational distribution observed under single collision conditions is non-Boltzmann.

The population distribution observed at $P_{total} = 14$ μm ($P_{NO_2} = 4$ μm) is presented in Fig. 6(b). Within experimental error the vibrational distribution for levels $v' = 0$–5 has changed only slightly. If present, vibrational relaxation is minimal. There is a notable change in the relative populations for vibrational levels $v' = 6$, 7. Two choices can be envisioned to explain this phenomenon: (i) the population in vibrational levels $v' = 6$ and 7 results in part from collisional transfer via an initially formed long-lived reservoir state or (ii) there is rapid vibrational relaxation in levels $v' = 8$–15, a bottleneck being encountered for levels $v' = 6$, 7. Based upon observations over the pressure range 10–1000 μm and comparison with previous studies,[23] the former mechanism is

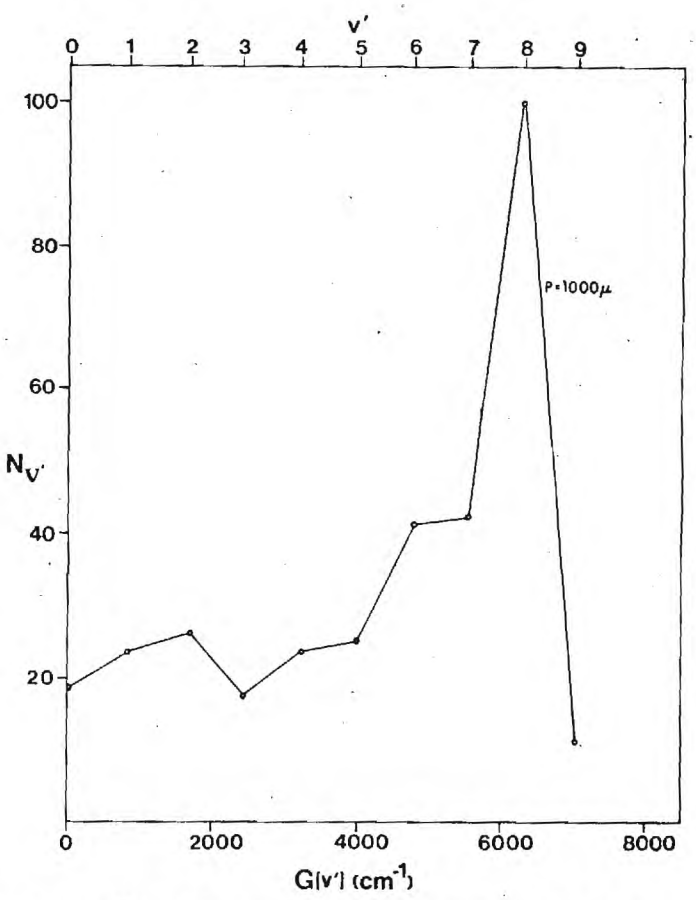

FIG. 7. $B\,^2\Sigma^+$ vibrational population ($N_{v'}$) as a function of the vibrational energy term $G(v')$ for vibrational levels $v' = 0$–9. Relative populations for $P_{tot} = 1000$ μm are determined on the basis of the computer simulations in Figs. 5(a) and 5(b).

by far the more likely possibility. For a selection of confirming evidence, we focus on the spectra in Fig. 1. At a pressure of 10 μm, it is apparent that there is substantial population in $v'=13$ relative to $v'=8$ or 9 [the FC factor for the (13, 9) transition exceeds those for all other transitions from $v'=13$ $B\,^2\Sigma^+$ but does not greatly exceed those for the (8, 5) and (3, 1) transitions]. In addition, a fit of the 400 μm data taking into account overlap with the (8, 5) and satellite bands indicates that $v'=13$ is not drastically diminished with respect to $v'=3$, as one would expect if unusually rapid vibrational relaxation were present. As a further demonstration of the presence of a collisional transfer process at 10 μm (Fig. 4) we observe the first clear indication of satellite structure. The (6, 4) band is accompanied by both long and short wavelength satellite features. As we will demonstrate shortly, collisional transfer is most efficient for the $v'=6$ level.

The vibrational bands observed at 10 μm are well fit by a rotational temperatu $T_{rot}=4500\,^\circ$K. Although some rotational relaxation has taken place relative to the single collision spectrum, $R-R$ transfer is not yet pronounced at 10 μm. This result also casts doubt on the possibility of significant $V-V$ transfer for levels $v'=0-13$ since this process is expected to proceed on a time scale two orders of magnitude slower than $R-R$ relaxation.[24]

At $P_{total}=100$ μm [Figs. 5(a) and 5(b)], we find significant spectral changes as well as a substantial modification of the population distribution observed at lower pressures. In Fig. 5(a), satellite bands are apparent for the transitions emanating from $v'=3$, 4, 5, 8, and 9 ($B\,^2\Sigma^+$). In Fig. 5(b), the dual satellite features encompassing the main $v'=6$ emission feature are emphasized. Because the $v'=6$ and 8 levels and their satellites are the most amenable to characterization over a wide pressure range, we will focus on the pressure dependence of these satellite and main features in a following section. Figure 7 depicts the population distribution at 1000 μm (1 Torr). This distribution is virtually identical to that observed at 400 μm. The observed population distribution which peaks strongly at $v'=8$ provides definitive evidence for efficient collisional transfer and casts strong doubt on the possibility of a bottleneck for vibrational relaxation at $v'=6$, 7.

The bands observed at $P=1$ Torr are well fit by a rotational temperature, $T_{rot}=800\,^\circ$K. Not surprisingly, significant rotational relaxation has occurred at this pressure. The observation of pronounced rotational relaxation focuses attention on the possibility of significant vibrational relaxation. While there are substantial changes in the observed population distribution, these changes do not indicate pronounced vibrational relaxation concomitant with the buildup of emission intensity for the lower ($v'=0-3$) vibrational levels. Rather, one observes a shift in population to higher v' levels indicative of rapid collisional transfer from initially populated states to the $B\,^2\Sigma^+$ state. More specifically, we observe pronounced transfer for $v'=6$, 7, 8 and somewhat lesser effects for $v'=4$, 5, 9. Note that while the population in $v'=9$ is substantially less than that in $v'=8$, the relative population of this level has increased significantly relative to levels $v'\leq 4$. The observed population distribution is clearly non-Boltzmann. There is also a clear trend away from a Boltzmann distribution as pressure increases. Vibrational relaxation cannot play a significant role in any explanation of the pressure dependent effects observed in this study.

TABLE II. Main and extra transitions (v', v'') in the $B\,^2\Sigma^+-X\,^2\Sigma^+$ spectrum of ScO.

Assignment	Wavelength in air (Å)		Vacuum wave numbers		Separation
	Main	Extra	Main	Extra	$\Delta\nu$ (cm^{-1})
(8, 9)	5416.9	5432.4	18455	18403	52
(8, 8)	5164.6	5178.8	19357	19304	53
(8, 7)	4932.8	4945.9	20267	20213	54
(8, 6)	4719.1	4730.8	21185	21132	53
(8, 5)	4521.7	4532.7	22109	22056	53
(8, 4)	4338.4	4348.3	23043	22991	52
(8, 3)	4167.9	4177.2	23986	23933	53
(6, 6)	5084.0	5080.6	19664	19677	13
	5084.0	5088.1	19664	19648	16
(6, 4)	4644.6	4641.9	21525	21537	12
	4644.6	4647.9	21525	21509	16
(6, 3)	4450.1	4447.3	22465	22479	14
	4450.1	4453.1	22465	22450	15

As we will discuss in a later section, the peaking in the $B\,^2\Sigma^+$ population distribution at $P=1000$ μm results primarily from the inherent population of that level which feeds $v'=8$ upon collisional transfer. The peaking is *not* related to any bottlenecks in the $B\,^2\Sigma^+$ state but can result in part from any process including vibrational relaxation which populates the "feeder" level of the reservoir state from which transfer occurs.

B. Perturbations and satellite structure

In the previous section we have considered the non-Boltzmann distribution induced in the ScO $B^2\Sigma^+$ state as a result of collisional transfer. In a future section we will consider the possible states from which this transfer can occur. Here, we focus primarily on those bands corresponding to transitions which originate in the $v'=6$ and 8 levels of the ScO $B\,^2\Sigma^+$ state. Because these bands and their satellites are the most amenable to study, they have been the most extensively investigated.

The satellite structure which accompanies the intense emission from $v'=8$ $B\,^2\Sigma^+$ is evident in Figs. 1(b) and 5(a) where we depict the (8, 5) and (8, 6) emission bands at 400 and 1000 μm, respectively. In both cases, adjacent to each of these strongest features is a weaker and red shifted satellite band. A similar but somewhat more complicated satellite structure is observed for $v'=6$ transitions in Figs. 4 and 5(b). Here the (6, 4) and (6, 6) bands are accompanied by both a blue and red shifted satellite. As indicated in Table II, several other transitions involving the $v'=6$ and 8 bands have been observed throughout the visible region. A scan of the data in Table II indicates that the energy separation ($\Delta\nu$) between the main and satellite bands depends on the vibrational

level v' in $B\,^2\Sigma^+$ and is invariant (within experimental error) to v'', the vibrational quantum number of the lower state. The average separations are (Table II) $\Delta\nu = 53 \pm 1.6$ cm^{-1} for $v' = 8$ and $\Delta\nu = 16 \pm 1.4$ cm^{-1} (red feature) and 13 ± 1.2 cm^{-1} (blue feature) for $v' = 6$. Here the uncertainties represent one standard deviation in the mean.

It is the $v' = 6$, 8 satellite features which have been the focus of our pressure dependent studies; however, further satellite features are clearly apparent at $P_{tot} = 1000$ μm in Fig. 5(a). A weak satellite is associated with the (9, 7) band, its separation being 58 ± 2 cm^{-1}. As we will demonstrate, the location of this satellite can be predicted on the basis of $v' = 6$, 8 perturbations. The red shifted satellite features which accompany the (5,4), (4,3), and (3,2) bands appear to emanate from a band system differing from that which perturbs the $v' = 6$–9 levels. The satellite and main features are separated by 25 ± 2, 22 ± 2, and 20 ± 2 cm^{-1} for $v' = 5, 4, 3$, respectively. The nature of these satellites will be considered further in the following sections.

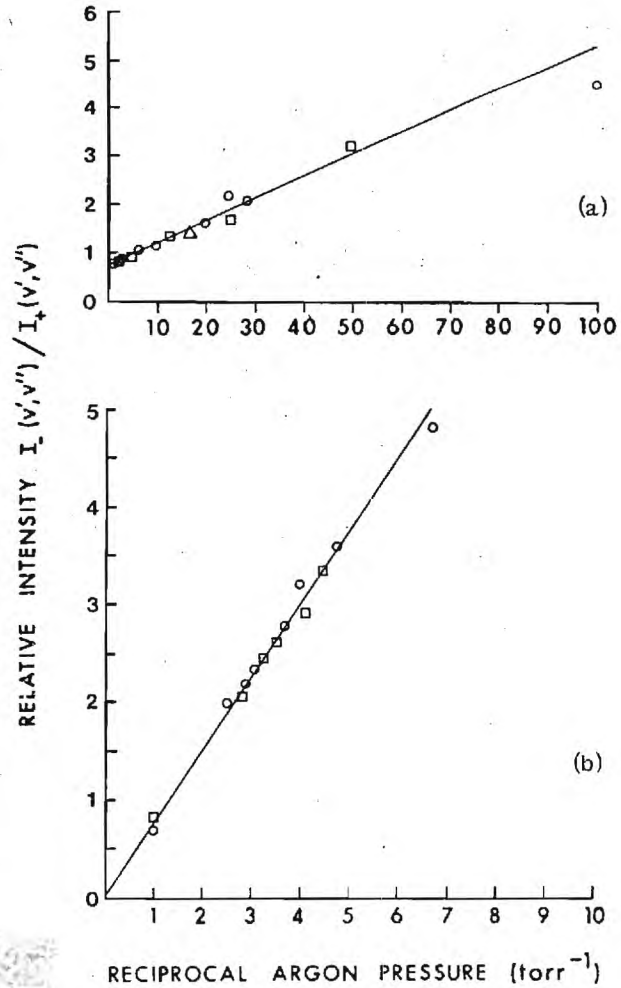

FIG. 8. (a) Variation of relative intensity of main (I_+) and satellite (I_-) bands with reciprocal argon pressure for red shifted satellite associated with $v' = 6$ ScO $B\,^2\Sigma^+$. The full line represents a linear least-squares fit to all data points [(○) (6, 6); (□) (6, 4); (△) (6, 3) band—see Table II]. (b) Similar plot for $v' = 6$ blue satellite (see Table II).

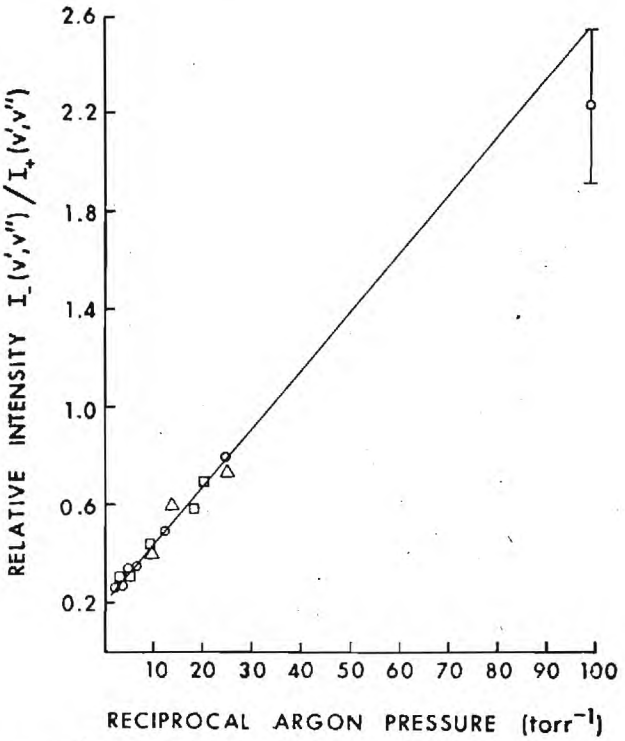

FIG. 9. Variation of relative intensity for main (I_+) and satellite (I_-) bands with reciprocal argon pressure for red shifted satellite associated with $v' = 8$ ScO $B\,^2\Sigma^+$. The full line represents a linear least-squares fit to all data points [(○) (8, 5); (□) (8, 6); (△) (8, 7) band—see Table II].

C. Pressure dependence of relative intensities

In Figs. 8 and 9, we plot the intensity ratio $I_-(v', v'')/I_+(v', v'')$ versus reciprocal argon pressure $[\mathrm{Ar}]^{-1}$ for the dual satellites associated with $v' = 6$ ScO $B\,^2\Sigma^+$ and the single satellite associated with $v' = 8$ ScO $B\,^2\Sigma^+$. Total argon pressures were measured with a calibrated capacitance manometer and are judged accurate to ±10%. Relative band intensities were measured using both peak heights and peak areas (spectra taken at a resolution of 0.8 Å and scan speed of 0.1 Å/sec), the majority of data involving peak area measurement; however, the comparative variations obtained for a given datum point in all cases were less than 20%. The data points in Figs. 8 and 9 were taken for a series of bands corresponding to transitions originating in $v' = 6$, 8 $B\,^2\Sigma^+$ and terminating in several vibrational levels v'' of the ground state. The full lines in Figs. 8 and 9 depict least squares fits in accord with the predictions of Eq. (10). Table III lists the corresponding least squares parameters $A_-(v', v'')/A_+(v', v'')$ from the intercept and k_+/k_{RB} from the slope. The error estimates result from one standard deviation uncertainty in the measured slope and intercept. The data points taken at lower pressure all display a negative deviation from the least squares fit. As we will discuss shortly, this is not surprising since the collisional transfer process and the corresponding interaction potential may be strongly influenced by significant dipole–dipole forces [ScO(res) + ScO → ScO($B\,^2\Sigma^+$) + ScO] versus the very much more prevalent dipole-induced dipole interaction [ScO + Ar → ScO($B\,^2\Sigma^+$) + Ar] at higher pressures.

TABLE III. Kinetic and spectroscopic parameters (defined in text) for vibrational levels v' = 6, 7, 8, 9 of the ScO $B\,^2\Sigma^+$ state. Estimated errors arise from one standard deviation uncertainty in the experimentally determined parameters.

v'	$\Delta\nu$ (cm^{-1})	k_+/k_{RB} (Torr)	A_-/A_+	d^2	δ (cm^{-1})	w (cm^{-1})	$k_{AB}\times10^{-6}$ ($Torr^{-1}\,sec^{-1}$)
6[a]	16±1.4[b]	0.05	0.78	0.44	2±0.6	15.9±2.5	500
	16±1.4	0.04	0.77	0.44	2±0.6	15.9±2.5	600
	13±1.2[b]	29.75	0.040	0.038	12±1.8	2.5±1.2	0.84
	13±1.2	31.25	0.037	0.036	13±1.8	2.6±1.2	0.80
7[c]	34.9±2.4	···	0.297	0.23	18.9±2.6	14.7±4	···
8[a]	53±1.6	0.12	0.20	0.17	35.8±2.4	19.5±2.4	210
	53	0.11	0.19	0.16	35.8	19.5±2.4	230
9	58±2[d]	···	(0.086)[e]	0.08	(48.8±3.2)[f]	14.4±2.8	···
	56.7±1.2[g]	···	0.076	0.08	48.7±3.2	14.5±2.8	···

[a]The first value represents the results of pressure dependence plots (Figs. 8 and 9) while the second corresponds to data obtained upon measurement of level shifts relative to unperturbed levels.
[b]The feature separated by 16 cm^{-1} appears at longer wavelength while the feature separated by 13 cm^{-1} appears at shorter wavelength.
[c]Calculated through analysis of $v'=6, 8$ perturbations.
[d]Measured perturbed level separation [Fig. 5(a)].
[e]Estimated from ratio I^-/I^+ (see text for discussion).
[f]Lower bound based on measured ratio I^-/I^+ (see text for discussion).
[g]Calculated through analysis of $v'-6, 8$ perturbations, and measurement of level shifts relative to unperturbed levels (see text for discussion).

The application of the data obtained from Figs. 8 and 9 to the solution of the perturbation relation (4) and (5) necessitates several approximations in the microscopic interpretation of $A_\pm(v', v'')$. For electric dipole radiation,

$$A_\pm(v', v'') = \left| \langle \Psi_\pm | \tilde{M}_e(r_e) | \Psi'' \rangle \right|^2 , \quad (12)$$

where the $\Psi_\pm$ are the same as in Eq. (3) and Fig. 2 and $M_e(r_e)$ is the electric dipole moment operator dependent upon the electronic coordinates r_e.[12] The wave function Ψ'' represents the $X\,^2\Sigma^+$ ground state. The wave functions for the ground state and the pure $B\,^2\Sigma^+$ and reservoir states may be written as the product of an electronic and vibronic term. Following the notation of Eqs. (3)–(5) and Fig. 2,

$$|\Psi''\rangle = |X\,^2\Sigma^+\rangle\,|v''\rangle, \quad \Psi_1 = |B\,^2\Sigma^+\rangle\,|v'\rangle, \quad \Psi_2 = |\text{res}\rangle\,|v\rangle . \quad (13)$$

Substituting for $\Psi_\pm$ and Ψ'' in Eq. (12),

$$A_+(v', v'') = \left| c\langle B\,^2\Sigma^+ | \tilde{M}_e(r_e) | X\,^2\Sigma^+\rangle\langle v' | v''\rangle - d\langle \text{res} | \tilde{M}_e(r_e) | X\,^2\Sigma^+\rangle\langle v | v''\rangle \right|^2 , \quad (14)$$

$$A_-(v', v'') = \left| d\langle B\,^2\Sigma^+ | \tilde{M}_e(r_e) | X\,^2\Sigma^+\rangle\langle v' | v''\rangle + c\langle \text{res} | \tilde{M}_e(r_e) | X\,^2\Sigma^+\rangle\langle v | v''\rangle \right|^2 . \quad (15)$$

Here "res" denotes a reservoir state or Franck–Condon forbidden high vibrational levels of a known electronic state. Because we have only a small amount of information on the source states from which collisional transfer occurs, it is difficult to estimate the magnitude of the vibrational overlap factors $\langle v | v''\rangle$ which appear in Eqs. (14) and (15). Since intensity measurements are limited to the strongest B–X features, it is reasonable to expect $\langle v | v''\rangle \lesssim \langle v' | v''\rangle$. Using $c \geq d$, we have, to good approximation,

$$A_+(v', v'') \sim c^2 \left| \langle B\,^2\Sigma^+ | \tilde{M}_e(r_e) | X\,^2\Sigma^+\rangle \right|^2 \left| \langle v' | v''\rangle \right|^2 \quad (16)$$

A similar approximation for $A_-(v', v'')$ is less satisfactory since the smaller coefficient multiplies the larger transition moment and vice versa. The cross interference term obtained upon expanding expression (15) is the most troublesome since it is proportional to $\langle v | v''\rangle$ and $\langle v' | v''\rangle$ and should therefore produce a v'' dependence in the measured intercepts. Since this effect is not observed experimentally, we feel confident that such terms may be ignored and that we are justified in the approximation

$$A_-(v', v'') \sim d^2 \left| \langle B\,^2\Sigma^+ | \tilde{M}_e(r_e) | X\,^2\Sigma^+\rangle \right|^2 \left| \langle v' | v''\rangle \right|^2 , \quad (17)$$

so that

$$A_-(v', v'')/A_+(v', v'') \simeq d^2/c^2 . \quad (18)$$

Figures 8(a) and 8(b) comprise intensity measurements for transitions $(v', v'') = (6, 4)$, $(6, 6)$, and $(6, 3)$. Since all three sets of data points fall very close to a straight line plot, these measurements indicate no v'' dependence in the parameter $A_-(v', v'')/A_+(v', v'')$. Similar results are obtained for transitions $(v', v'') = (8, 5)$, $(8, 6)$, and $(8, 7)$ in Fig. 9. Consequently, the fractional admixture of "reservoir" state character (column 5 of Table III) may be estimated from Eq. (18) and the normalization condition $c^2 + d^2 = 1$. The data in columns 6 and 7 give [from Eqs. (4) and (5)] the energy separation between unperturbed levels (δ) and the perturbation matrix elements (w), which will be dealt with more thoroughly in a later section.

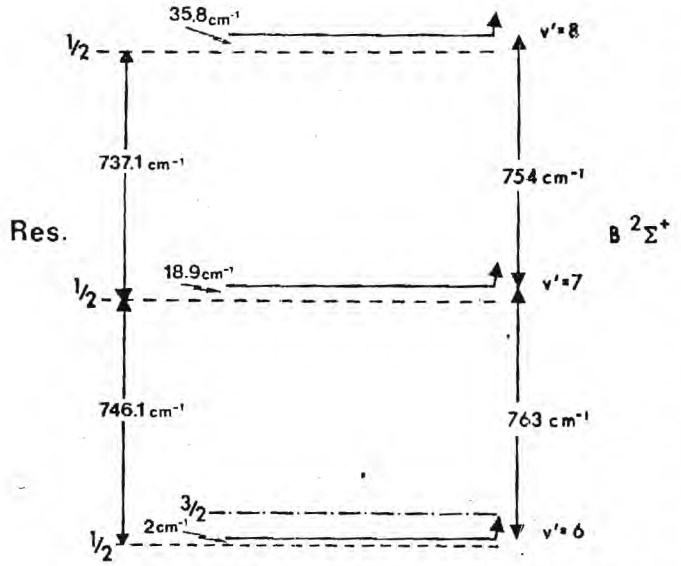

FIG. 10. Comparison of $B\,^2\Sigma^+$ and deperturbed "reservoir state" vibrational energy level spacing on the basis of the perturbation parameters given in Table III. The energy level spacings determined for the unperturbed reservoir state are indicated at the left-hand side. The location of the ScO $A'\,^2\Delta_{3/2}$ level is also indicated ($\frac{3}{2}$) in the figure. It would appear that the vibrational spacings for the reservoir state are slightly smaller than those for $B\,^2\Sigma^+$, indicating the possible interaction with a low-lying $^2\Pi_i$ state corresponding to configuration (29) in the text.

The rate constant k_+ (Table III, column 3) pertains to emission from a single vibrational level v' in $B\,^2\Sigma^+$ to all vibrational levels v'' in $X\,^2\Sigma^+$. The reciprocal of this parameter may be approximated by the radiative lifetime of the level v'. The last column in Table III gives values for k_{RB} estimated from $k_+^{-1} \sim 4\times10^{-8}$ sec, the radiative lifetime for the first four vibrational levels of $B\,^2\Sigma^+$.[25] Intramolecular energy transfer is most efficient for those $B\,^2\Sigma^+$ levels which contain the largest admixture of "reservoir" state character. For $v'=6$, an analysis of the long-wavelength satellite indicates $k_{RB} \sim 5\times10^8$ Torr^{-1} sec^{-1}, which corresponds to a time period $\tau \sim 3\times10^{-12}$ sec at 1 atm pressure. A second comparable value ($k_{RB} \sim 6\times10^8$ Torr^{-1} sec^{-1}) is obtained by noting the frequency shift of the $v'=8$ level relative to its frequency in the computer synthesized spectrum and combining this data with the I^-/I^+ ratio at a given pressure. A similar analysis has been carried out for $v'=8$ using both the data analysis from Fig. 9 and level shifts measured from Figs. 1 and 5(a). The time scale which characterizes the energy transfer is considerably shorter than the typical rotational relaxation time for R–R transfer processes.

The data obtained for the $v'=6, 8$ levels of the ScO $B\,^2\Sigma^+$ state indicates extremely strong mixing with an initially populated diffuse reservoir state (see also following sections). The observed transfer rates should be contrasted to that for the $v'=6$ short-wavelength satellite, where $k_{RB} \sim 8\times10^5$ Torr^{-1} sec^{-1} corresponds to $\tau \sim 5\times10^{-9}$ sec at 1 atm pressure. Unfortunately, the regions of $v'=7$ emission are substantially overlapped prohibiting a quantitative pressure dependence analysis (Figs. 8 and 9) at present. It does appear that transfer into $v'=7$ is comparable to that into $v'=6$ and 8 (Figs. 6 and 7); however, two overlapping levels involving more than one reservoir state appear to be involved (see following sections). Despite these problems, we were able to obtain some information on the $v'=7$ level using the results for $v'=6$ and 8. Assuming that the same reservoir state leads to the rapid transfer into $v'=6$ and 8 and using the deperturbed level separations (δ), we can estimate the vibrational level spacing in the perturbing reservoir state and the separation of the $v'=7$ level from its corresponding perturbing level. The results of this analysis are indicated in Fig. 10. Having obtained the deperturbed level separation $\delta = 18.9 \pm 2.6$ cm^{-1} we measure the shift of the $v'=7$ level from its calculated position (~ 8 cm^{-1}) to deduce $\Delta\nu \sim 34.9 \pm 2.6$ cm^{-1}. A similar calculation for $v'=9$ (shift ~ 4 cm^{-1}) yields the data given in the second column of Table III. The agreement between predicted (56.7 ± 1.2) and observed (58 ± 2) $\Delta\nu$ values is excellent lending credence to the validity of our approach for $v'=7$. The values of (A_-/A_+) for the two measurements involving $v'=9$ are not in strong agreement; however, the first value corresponds to the measured ratio I_-/I_+ and therefore represents an upper bound to (A_-/A_+). Given the determination of δ and $\Delta\nu$, it is possible to determine w (Table III, column 7) from relation (5).

We have not carried out extensive pressure dependent studies for the $v'=3, 4, 5$ levels of the $B\,^2\Sigma^+$ state. We can, however, obtain some estimate of the parameters for these levels and the states by which they are perturbed. Again, the level shifts for the main spectral features from their positions in the computer synthesized spectrum are determined. These shifts when combined with measured satellite–main feature separations ($\Delta\nu$) yield the data given in Table IV. From $\Delta\nu$ and δ a value of d^2/c^2 was estimated from Eq. (5). The determined δ values indicate that the perturbing levels must be correlated with a different perturbing reservoir state and do not correspond to an extension of those levels interacting with $v'=6$–9. The emission characterizing the $v'=3, 4$ satellites is quite broad and therefore it is difficult to estimate $\Delta\nu$ and to determine readily the relative intensities of satellite and main features. The $v'=5$ satellite is more defined and, using intensity data from Fig. 5(a), $I_-(v', v'')/I_+(v', v'')$ was deduced and combined with d^2/c^2 and the known radiative lifetimes [Eq. (10)] to estimate the transfer rate given in the last column of Table IV. It appears that collisional transfer to $v'=5$ is approximately an order of magnitude less efficient than that to $v'=6, 8$.

In summary, our pressure dependence studies indicate that there must be at least one-low-lying long-lived reservoir state interacting strongly with the $B\,^2\Sigma^+$ state. In the following section, we focus on the nature of those possible metastable states which one might correlate with the satellite levels. The number of candidates appears to be quite limited.

D. Perturbation matrix elements—possible interacting excited states

In order to assess the possible reservoir states which interact strongly with ScO $B\,^2\Sigma^+$, we consider the molecular orbital configurations associated with the low-lying

TABLE IV. Spectroscopic and kinetic parameters for vibrational levels $v'=3,4,5$ of the ScO $B\,^2\Sigma^+$ state.[a] Uncertainties correspond to one standard deviation in the mean.

v'	$\Delta\nu$ (cm^{-1})	v' Level shift (cm^{-1})	δ (cm^{-1})	d^2/c^2	d^2	w (cm^{-1})	I_-/I_+	$K_{RB}\times10^{-6}$ ($Torr^{-1}\,sec^{-1}$)
3	20 ± 2[b]	8 ± 1	4 ± 3[c]	0.67 ± 0.17[c]	0.4 ± 0.07[c]	9.8 ± 2.2[c]	>0.54[d]	···
4	22 ± 2[b]	7 ± 1	8 ± 3[c]	0.47 ± 0.15[c]	0.32 ± 0.07	10.3 ± 2.2[c]	>0.44[d]	···
5	25 ± 2	6 ± 1	12 ± 3	0.35 ± 0.12	0.26 ± 0.06	11 ± 2	0.75 ± 0.06	55 ± 40

[a]Parameters quoted in this table obtained from spectrum taken at $P_{tot}=1000$ μm [Fig. 5(a)].
[b]Band is broad and $\Delta\nu$ value must represent a lower bound to the appropriate value—see text for discussion.
[c]Lower bound due to $\Delta\nu$ measurement—see text for discussion.
[d]Obtained from peak height measurements. Broad nature of band makes quantitative measurement prohibitive—see text for discussion.

electronic states of ScO and the possibility of their spin–orbit or Coriolis interaction with the $B\,^2\Sigma^+$ state.

To date the only *ab initio* calculations carried out on any of the Group III*b* metal monoxides are those by Carlosn, Ludena, and Moser.[26] Their calculations correctly predicted the ground state to be $^2\Sigma^+$. In addition, they predicted the first excited state to be $^2\Delta_r$ with an energy of 2.0 ± 0.5 eV. Their work has since been verified experimentally.[5] The ground state configuration used in these calculations is

$$1\sigma^2\,2\sigma^2\,3\sigma^2\,1\pi^4\,4\sigma^2\,5\sigma^2\,6\sigma^2\,2\pi^4\,7\sigma^2\,8\sigma^2\,3\pi^4\,9,\ X\,^2\Sigma^+ . \quad (19)$$

The low-lying $^2\Delta_r$ state arises from the configuration

$$\cdots\,8\sigma^2\,3\pi^4\,1\delta,\ ^2\Delta_r . \quad (20)$$

The $A\,^2\Pi$ state arises predominantly from

$$\cdots\,8\sigma^2\,3\pi^4\,4\pi,\ A\,^2\Pi , \quad (21)$$

while the $B\,^2\Sigma^+$ state arises from the configuration

$$\cdots\,8\sigma\,3\pi^4\,9\sigma^2,\ B\,^2\Sigma^+ . \quad (22)$$

The predominant terms in the 9σ, 1δ, and 4π LCAO–MO's are $4s\sigma$(Sc), $3d\delta$(Sc), and $4p\,\pi$(Sc), respectively. There is also significant $np\sigma$(Sc) contribution to the 9σ orbital. The 8σ orbital is predominantly $2p\sigma$ on oxygen. The four configurations (19)–(22) represent first order descriptions of the lowest lying states from which emission has been observed in ScO.

In order to assess possible interactions with the $B\,^2\Sigma^+$ state we adopt a simplified microscopic form of the spin–orbit operator commonly used in semiempirical calculations

$$H_{SO}=\sum_{i,k,\alpha}\xi_k(r_{ki})\,l_{ik}^{\alpha}S_i^{\alpha} , \quad (23)$$

where the sum is over electrons i and nuclei k, l_{ik}^{α}, and S_i^{α} are the $\alpha=x$, y, or z components of the orbital and electron spin angular momentum, respectively, and $\xi_k(r_{ki})$ is the spin–orbit constant, proportional to the inverse cube distance r_{ki}^{-3} between electron i and nucleus k. Coriolis operators expressed in terms of one- and two-electron operators are

$$-B(J_+L_-+J_-L_+)=-\left(\frac{\hbar}{4\pi c\mu r^2}\right)\left[J_+\left(\sum_i l_{i-}\right)+J_-\left(\sum_i l_{i+}\right)\right] , \quad (24)$$

$$B(L_+S_-+L_-S_+)=\left(\frac{\hbar}{4\pi c\mu r^2}\right)\left[\left(\sum_i l_{i+}\right)\cdot\left(\sum_j s_{j-}\right)+\left(\sum_i l_{i-}\right)\cdot\left(\sum_j s_{j+}\right)\right] . \quad (25)$$

Matrix elements of these operators between several low-lying configurations and the $B\,^2\Sigma^+$ state have been evaluated to determine the extent of the possible interactions which can lead to the previously discussed satellite structure. In these calculations, we have assumed that each electronic state arises from a different single configuration, each of which is analogous to those used by Carlson *et al.* for ScO. The following low-lying configurations can couple with the $B\,^2\Sigma^+$ state

$$\cdots\,(8\sigma)(3\pi)^4(9\sigma)(10\sigma)^2\Sigma^+,\ ^4\Sigma^+ , \quad (26)$$

$$\cdots\,(8\sigma)(3\pi)^4(9\sigma)(4\pi)^2\Pi_r',\ ^4\Pi_r , \quad (27)$$

$$\cdots\,(8\sigma)(3\pi)^4(9\sigma)(\pi')^2\Pi_r',\ ^4\Pi_r , \quad (28)$$

$$\cdots\,(8\sigma)^2(3\pi)^3(9\sigma)^2,\ ^2\Pi_i , \quad (29)$$

where the 10σ and π' LCAO–MO's are $(4s+4p)\sigma$ and $3d\pi$ on scandium, respectively. There are also a small number of additional low-lying configurations which involve promotions among the $n\sigma$ ($n=8$–10) and $n\pi$ ($n=3,4$) orbitals; however, these configurations will not couple (within the approximations used here[27]) with the $B\,^2\Sigma^+$ state.

In constructing appropriate wavefunctions, we recall that parity represents a good quantum number. Therefore, the wave functions corresponding to configurations (19)–(22) and (26)–(28) are written in a parity basis. Linear combinations which transform as eigenfunctions of the parity operator are given in Table V. Methods for evaluating these matrix elements have been described elsewhere.[5,28]

The evaluation of nonzero matrix elements for the spin–orbit and Coriolis operators leads to a surprisingly simple result. Only matrix elements connecting the $B\,^2\Sigma^+$ state with the $^2\Pi_i$ configuration (29) and one component of the $^4\Pi_r$ states, specifically $^4\Pi_{r-1/2}$, are nonzero. The $^2\Pi_i$ components interact through both spin–orbit and coriolis coupling whereas $^4\Pi_{r-1/2}$ interacts only through spin–orbit coupling. All other matrix elements connecting the $B\,^2\Sigma^+$ state to those states arising from the configurations (26), (27), and (28) vanish. Because spin–orbit coupling strongly dominates the coriolis in-

TABLE V. Determinantal wave functions.

$|X\,^2\Sigma^{+\pm}, v\rangle = (1/\sqrt{2})\,[\,|\Lambda=0,\ S=\tfrac{1}{2},\ \Sigma=\tfrac{1}{2}\rangle\,|\Omega=\tfrac{1}{2},\ J\rangle \pm (-1)^{J-1/2}\,|\Lambda=0,\ S=\tfrac{1}{2},\ \Sigma=-\tfrac{1}{2}\rangle\,|\Omega=-\tfrac{1}{2},\ J\rangle\,]\,|v\rangle$[a]

$|A'\,^2\Delta^{\pm}_{3/2}, v\rangle = (1/\sqrt{2})\,[\,|2\,\tfrac{1}{2}-\tfrac{1}{2}\rangle\,|\tfrac{3}{2}\,J\rangle \mp (-1)^{J-3/2}\,|-2\,\tfrac{1}{2}\,\tfrac{1}{2}\rangle\,|-\tfrac{3}{2}\,J\rangle\,]\,|v\rangle$

$|A'\,^2\Delta^{\pm}_{5/2}, v\rangle = (1/\sqrt{2})\,[\,|2\,\tfrac{1}{2}\,\tfrac{1}{2}\rangle\,|\tfrac{5}{2}\,J\rangle \pm (-1)^{J-5/2}\,|-2\,\tfrac{1}{2}-\tfrac{1}{2}\rangle\,|-\tfrac{5}{2}\,J\rangle\,]\,|v\rangle$

$|A\,^2\Pi^{\pm}_{1/2}, v\rangle = (1/\sqrt{2})\,[\,|1\,\tfrac{1}{2}-\tfrac{1}{2}\rangle\,|\tfrac{1}{2}\,J\rangle \pm (-1)^{J-1/2}\,|-1\,\tfrac{1}{2}\,\tfrac{1}{2}\rangle\,|-\tfrac{1}{2}\,J\rangle\,]\,|v\rangle$[a]

$|A\,^2\Pi^{\pm}_{3/2}, v\rangle = (1/\sqrt{2})\,[\,|1\,\tfrac{1}{2}\,\tfrac{1}{2}\rangle\,|\tfrac{3}{2}\,J\rangle \mp (-1)^{J-3/2}\,|-1\,\tfrac{1}{2}-\tfrac{1}{2}\rangle\,|-\tfrac{3}{2}\,J\rangle\,]\,|v\rangle$[a]

$|^4\Sigma^{+\pm}_{3/2}, v\rangle = (1/\sqrt{2})\,[\,|0\,\tfrac{3}{2}\,\tfrac{3}{2}\rangle\,|\tfrac{3}{2}\,J\rangle \pm (-1)^{J-3/2}\,|0\,\tfrac{3}{2}-\tfrac{3}{2}\rangle\,|-\tfrac{3}{2}\,J\rangle\,]\,|v\rangle$

$|^4\Sigma^{+\pm}_{1/2}, v\rangle = (1/\sqrt{6})\,[\,|a\rangle + |b\rangle + |c\rangle \pm (-1)^{J-1/2}\,(|a^-\rangle + |b^-\rangle + |c^-\rangle)\,]\,|v\rangle$[b,c]

$|^4\Pi^{\pm}_{5/2}, v\rangle = (1/\sqrt{2})\,[\,|1\,\tfrac{3}{2}\,\tfrac{3}{2}\rangle\,|\tfrac{5}{2}\,J\rangle \pm (-1)^{J-5/2}\,|-1\,\tfrac{3}{2}-\tfrac{3}{2}\rangle\,|-\tfrac{5}{2}\,J\rangle\,]\,|v\rangle$[d]

$|^4\Pi^{\pm}_{3/2}, v\rangle = (1/\sqrt{6})\,[\,|d\rangle + |e\rangle + |f\rangle \pm (-1)^{J-3/2}\,(|d^-\rangle + |e^-\rangle + |f^-\rangle)\,]\,|v\rangle$[b,c,d]

$|^4\Pi_{1/2}, v\rangle = (1/\sqrt{6})\,[\,|g\rangle + |h\rangle + |i\rangle \pm (-1)^{J-1/2}\,(|g^-\rangle + |h^-\rangle + |i^-\rangle)\,]\,|v\rangle$[b,c]

$|^4\Pi_{-1/2}, v\rangle = (1/\sqrt{2})\,[\,|1\,\tfrac{3}{2}-\tfrac{3}{2}\rangle\,|-\tfrac{1}{2}\,J\rangle \pm (-1)^{J+1/2}\,|-1\,\tfrac{3}{2}\,\tfrac{3}{2}\rangle\,|\tfrac{1}{2}\,J\rangle\,]\,|v\rangle$

$|^2\Pi^{\pm\pm}_{r\,1/2}, v\rangle = (1/\sqrt{6})\,[\,|j\rangle + |k\rangle + |l\rangle \pm (-1)^{J-1/2}\,(|j^-\rangle + |k^-\rangle + |l^-\rangle)\,]|v\rangle$

$|^2\Pi^{\pm\pm}_{r\,3/2}, v\rangle = (1/\sqrt{6})\,[\,|m\rangle + |n\rangle + |o\rangle \quad (-1)^{J-3/2}\,(|m^-\rangle + |n^-\rangle + |o^-\rangle)\,]|v\rangle$

$|a\rangle,\ |b\rangle,\ |c\rangle;\ |\Lambda=0,\ S=\tfrac{3}{2},\ \Sigma=\tfrac{1}{2}\rangle$[c]

$|a^-\rangle,\ |b^-\rangle,\ |c^-\rangle;\ |\Lambda=0,\ S=\tfrac{3}{2},\ \Sigma=-\tfrac{1}{2}\rangle$[c]

$|d\rangle,\ |e\rangle,\ |f\rangle;\ |\Lambda=1,\ S=\tfrac{3}{2},\ \Sigma=\tfrac{1}{2}\rangle$[c]

$|d^-\rangle,\ |e^-\rangle,\ |f^-\rangle;\ |\Lambda=-1,\ S=\tfrac{3}{2},\ \Sigma=-\tfrac{1}{2}\rangle$[c]

$|g\rangle,\ |h\rangle,\ |i\rangle;\ |\Lambda=1,\ S=\tfrac{1}{2},\ \Sigma=-\tfrac{1}{2}\rangle$[c]

$|g^-\rangle,\ |h^-\rangle,\ |i^-\rangle;\ |\Lambda=-1,\ S=\tfrac{3}{2},\ \Sigma=\tfrac{1}{2}\rangle$[c]

$|j\rangle,\ |k\rangle,\ |l\rangle;\ |\Lambda=1,\ s=\tfrac{1}{2},\ \Sigma=-\tfrac{1}{2}\rangle$

$|j^-\rangle,\ |k^-\rangle,\ |l^-\rangle;\ |\Lambda=-1,\ s=\tfrac{1}{2},\ \Sigma=\tfrac{1}{2}\rangle$

$|m\rangle,\ |n\rangle,\ |o\rangle;\ |\Lambda=1,\ s=\tfrac{1}{2},\ \Sigma=\tfrac{1}{2}\rangle$

$|m^-\rangle,\ |n^-\rangle,\ |o^-\rangle;\ |\Lambda=-1,\ s=\tfrac{1}{2},\ \Sigma=-\tfrac{1}{2}\rangle$

[a] The determinantal wave function for ScO $B\,^2\Sigma^+$ is virtually identical to that for $X\,^2\Sigma^+$; however, the electron configurations for the $X\,^2\Sigma^+$ and $B\,^2\Sigma^+$ states differ. The $^2\Pi_i$ configuration (29) is represented by a determinantal wave function virtually identical to that for $A\,^2\Pi$; however, the configurations differ. See text for discussion.

[b] Slater determinants are symbolized by $|\Lambda S\Sigma\rangle$ when only one Slater determinant can be constructed with the specified values of Λ, S, Σ. Otherwise, letters are used as labels.

[c] Specific determinants are defined with respect to the configurations given in the text for $^4\Sigma^+$ and $^4\Pi_r$.

teraction we will consider only matrix elements of the spin–orbit operator. Using the determinantal wavefunctions in Table V, the matrix element connecting $^4\Pi_{r-1/2}$ and $B\,^2\Sigma^+$ is of the form

$$\begin{aligned} w &= \langle v,\ ^4\Pi^{\pm}_{r-1/2}\,|\,H_{SO}\,|\,B\,^2\Sigma^+_{1/2},\ v'\rangle \\ &= \tfrac{1}{4}\,\langle v|\,v'\rangle\{\pm[(-1)^{J+1/2}\,\langle -1\,\tfrac{3}{2}\,\tfrac{3}{2}|\,H_{SO}\,|\,0\,\tfrac{1}{2}\,\tfrac{1}{2}\rangle \\ &\quad + (-1)^{J-1/2}\,\langle 1\,\tfrac{3}{2}-\tfrac{3}{2}\,|\,H_{SO}\,|\,0\,\tfrac{1}{2}-\tfrac{1}{2}\rangle]\}\ , \end{aligned} \tag{30}$$

where the notation is that used in Table V, $|v\rangle$ and $|v'\rangle$ represent, respectively, vibrational wave functions for the $^4\Pi_r$ and $B\,^2\Sigma^+$ states and we have noted that

$$\langle 1\,\tfrac{3}{2}-\tfrac{3}{2}\,|\,H_{SO}\,|\,0\,\tfrac{1}{2}\,\tfrac{1}{2}\rangle = \langle -1\,\tfrac{3}{2}\,\tfrac{3}{2}\,|\,H_{SO}\,|\,0\,\tfrac{1}{2}-\tfrac{1}{2}\rangle = 0\ .$$

Expression (30) can be simplified by re-expressing the basis functions $|\Lambda S\Sigma\rangle$ in terms of antisymmetrized products of one electron molecular orbitals.[1,2] Considering the interaction between the $^4\Pi_r$ [Eq. (27)] and $B\,^2\Sigma^+$ states and omitting the 3π orbital which remains fully occupied in both $B\,^2\Sigma^+$ and $^4\Pi_r$ [Eq. (27)],

$$\begin{aligned} |\,-1\,\tfrac{3}{2}\,\tfrac{3}{2}\rangle &= |\,A(\cdots -1^+_4\,0^+_8\,0^+_9\rangle\ , \\ |\,0\,\tfrac{1}{2}\,\tfrac{1}{2}\rangle &= |\,A(\cdots 0^+_8\,0^+_9\,0^-_9\rangle\ , \end{aligned} \tag{31}$$

where numerals 0 and ± 1 identify the z component of the orbital angular momenta l_i, and superscripts $\pm$ specify the corresponding projection of s_i. A is the antisymmetrizing operator and the subscripts 4, 8, and 9 pertain to molecular orbitals 4π, 8σ, and 9σ, respectively. Expressions similar to Eq. (30) may be written for $|1\,\tfrac{3}{2}-\tfrac{3}{2}\rangle$ and $|0\,\tfrac{1}{2}-\tfrac{1}{2}\rangle$. The many-electron integrals which appear in Eq. (30) may now be reduced to tractable sums over one electron integrals noting

$$\langle -1\,\tfrac{3}{2}\,\tfrac{3}{2}|\,H_{SO}\,|\,0\,\tfrac{1}{2}\,\tfrac{1}{2}\rangle = -\langle 1\,\tfrac{3}{2}-\tfrac{3}{2}\,|\,H_{SO}\,|\,0\,\tfrac{1}{2}-\tfrac{1}{2}\rangle\ ,$$

we have

$$w = \pm\,(\tfrac{1}{2}\,\langle v|\,v'\rangle\,(-1)^{J+1/2}\,\langle -1_4|\sum_k \zeta_k(r_k)\,l^-_k|\,0_9\rangle\ . \tag{32a}$$

Through a very similar approach to that already applied to the treatment of $B\,^2\Sigma^+_{1/2}$–$A\,^2\Pi_{1/2}$ interactions in

AlO,[1] the appropriate matrix element for $^2\Pi_{i_{1/2}} - B\,^2\Sigma^+$ spin–orbit coupling is

$$\omega = \tfrac{1}{2}\langle v' | v\rangle \langle -1_3 | \sum_k \epsilon_k(r_k) l_k^- | 0_8\rangle \ . \tag{32b}$$

The presence of $\epsilon_k(r_k) \sim r_k^{-3}$ assures that only one center integrals will make a significant contribution to the Eqs. (32). A complete evaluation of the matrix elements ω requires knowledge of the molecular orbitals $|-1_4\rangle = 4\pi$, $|-1_3\rangle = 3\pi$, $|0_8\rangle = 2p\sigma$, and $|0_9\rangle = 9\sigma$. In order to evaluate the matrix elements (32), we note that the $^4\Pi_r$, $^2\Pi_i$, $B\,^2\Sigma^+$, and $A\,^2\Pi$ states can be represented to reasonable approximation by the charge distribution Sc^+O^-.[26]

To evaluate the $^4\Pi_{-1/2} - B\,^2\Sigma^+$ interaction, we represent the 4π orbital as an atomic p orbital centered on scandium and take into account the (Sc) $p\sigma$ orbital character of the 9σ orbital (using the population analysis given in Ref. 26) to determine

$$w \cong \pm 0.25/\sqrt{2}(-1)^{J+1/2} a_0 \langle v | v'\rangle \ ,$$

where we have taken advantage of the transformation property[29] $l_0^+ | P_0\rangle = \sqrt{2}\,| P_+\rangle$. The radial integral

$$a_0 = \langle p\Pi | \epsilon_0(r_0) | p\Pi\rangle$$

may be evaluated by considering the spin–orbit splitting of the ScO $A\,^2\Pi$ state which is 120 cm^{-1} (Ref. 30) giving

$$w \approx 20 \langle v | v'\rangle \, cm^{-1} \ . \tag{33}$$

A matrix element of similar magnitude can be estimated for the interaction between $B\,^2\Sigma^+$ and the $^4\Pi_r$ state corresponding to configuration (28).

The evaluation of the $^2\Pi_i - B\,^2\Sigma^+$ interaction follows from previous studies[1] in which we represent the molecular orbitals as atomic p orbitals

$$|-1_3\rangle \sim P_-(O^-) \quad \text{and} \quad |0_8\rangle \sim P_0(O^-)$$

centered on the oxygen ion (O^-). Again using the appropriate transformation properties

$$\omega \sim (1/\sqrt{2})\, a_0 \langle v' | v\rangle \ ,$$

where the radial integral

$$a_0 = \langle P(O^-) | \epsilon_0(r_0) | P(O^-)\rangle \sim 121 \ cm^{-1}$$

(Ref. 31). We arrive at the final result

$$\omega \sim 86 \langle v' | v\rangle \ . \tag{34}$$

Equalities (33) and (34) are clearly not exact because approximate representations have been used for the 3π, 4π, 8σ, and 9σ orbitals, respectively. In addition the spin–orbit coupling constant $a_0 \sim 121$ cm^{-1} is strictly appropriate to O^- and not Sc^+O^-.

It would appear that the significant energy transfer observed for the $v' = 6, 8$ levels of the ScO $B\,^2\Sigma^+$ state is related to the presence of $^4\Pi_r$ or $^2\Pi_i$ reservoir states and more specifically to the location of levels with substantial $^4\Pi_{r-1/2}$ or $^2\Pi_{i_{1/2}}$ character is close proximity to $v' = 6, 8$. There is also the possibility of second-order coupling effects associated either with $^4\Pi_{r-1/2}$ mixing (small admixture of $^4\Pi_{r-1/2}$) with other components of the $^4\Pi_r$ state or other low-lying configurations which do not couple directly with $B\,^2\Sigma^+$. Similar comments apply to $^2\Pi_i$. The representation of the ScO electronic states through more appropriate multiconfigurational descriptions will introduce further weak couplings. If we consider the long-range interactions (following section) which should characterize the weakly interacting $v' = 6$ satellite and those satellites associated with $v' = 3, 4, 5$, second order coupling effects and higher order descriptions of the interacting states may play a significant role. A similar comment applies to the multiple complicated spectral features associated with $v' = 7$ [Fig. 5(b)]. The relatively strong interactions associated with $v' = 3, 4, 5$ (Table IV) appear to emanate from a different source than $v' = 6, 8$. In view of the magnitude of the matrix elements (33) and (34) and the data in Tables III and IV, we favor an interaction with levels which are primarily $^2\Pi_{i_{1/2}}$ for $v' = 6$–9 $B\,^2\Sigma^+$ and levels which are primarily $^4\Pi_{r-1/2}$ for $v' = 3, 4, 5$. The confirmation of the exact nature of the interacting levels awaits further analysis. It is somewhat surprising that strong emission from the $^2\Pi_i$ state [configuration (29)] has not been observed; however, no information has been obtained for this state. Similarly surprising effects have been noted in ICl.[32] Finally, we should note that there appears to be a close correlation between the location of the weakly interacting $v' = 6$ satellite level and the $v = 14$ level of the ScO $A'\,^2\Delta_{3/2}$ state. This correlation is drawn on the basis of our analysis of the $A'\,^2\Delta_{3/2}$ state for which we find $T_0 = 14\,966$ cm^{-1}, $w_e = 843.6$ cm^{-1}, $w_e x_e = 4.8$ cm^{-1}. The agreement between calculated and observed level positions (3 cm^{-1}) is quite enticing. If the weak satellite is associated with $^2\Delta_{3/2}$, this interaction must result from secondary coupling effects.

SUMMARY AND DISCUSSION

The primary emphasis of the current study has been the analysis of rapid energy transfer routes connecting certain long-lived electronically excited reservoir states in ScO with ScO $B\,^2\Sigma^+$. As Table III demonstrates, the observed energy transfer rates from levels which would appear to possess substantial $^4\Pi_{r-1/2}$ and $^2\Pi_{i_{1/2}}$ character (Sec. IV D) are unusually fast for the most highly perturbed and hence most strongly interacting levels of the $B\,^2\Sigma^+$ state. Intramolecular energy transfer is most efficient for those levels of $B\,^2\Sigma^+$ which contain the largest admixture of "reservoir state" character. For both $v' = 6$ and $v' = 8$ $B\,^2\Sigma^+$, the observed bimolecular transfer rate constant is significantly larger than 10^8 Torr $\times$ sec^{-1} corresponding to a time period of 10^{-12} sec at 1 atm pressure. This is approximately two orders of magnitude faster than a typical relaxation time for rotation–rotation energy transfer.[24]

It is instructive to compare the rates observed in this study with appropriate rate constants for "hard sphere" collisions between Ar and ScO. In order to make this comparison, we assume that the ScO translational temperature will equilibrate more rapidly than the rotational temperature.[24,33] Therefore, based on previously computed rotational temperatures (Sec. IV A), we consider hard sphere collisions between Ar (300 °K) and ScO (1000 °K),[34] and compute a bimolecular rate constant $k \sim (5$–$6) \times 10^6$ $Torr^{-1}\,sec^{-1}$. Hence, the transfer

rates to $v'=8$ ScO $B\,^2\Sigma^+$ approach 50 and 100 times gas kinetic. This is not surprising for we expect long range forces to be the most efficient in causing the observed transitions. Collisions with argon[35] may be viewed as time dependent perturbations which cause transitions between states (mixing via spin–orbit coupling)

$$|+\rangle = c|B\,^2\Sigma^+\rangle\,|v'\rangle\,|J'\rangle - d|\text{res}\rangle\,|v\rangle\,|J'\rangle$$

and (35)

$$|-\rangle = d|B\,^2\Sigma^+\rangle\,|v'\rangle\,|J\rangle + c|\text{res}\rangle\,|v\rangle\,|J\rangle$$

of ScO. The selection rule[36] dictates that the two components of $|+\rangle$ and $|-\rangle$ contain the same rotational basis functions $|J\rangle$ and $|J'\rangle$. The perturbing Hamiltonian is the the time dependent intermolecular potential between Ar and ScO. For a particular trajectory, the rate constant k_{RB} is proportional to the squared matrix elements of the amplitude V of this interaction

$$k_{RB} \propto |\langle +|V|-\rangle|^2 \,. \tag{36}$$

Here, the interaction V arises primarily from the dipole–induced dipole and dispersion forces between the approaching atom and diatomic; however, at the lowest pressures characterizing the current experiments dipole–dipole interactions between ScO molecules as well as inelastic collisions with NO_2 may play a significant role.[37] The long or short range nature of the interaction causing transitions depends upon the time scale of the collision versus the frequency of the transition (arguments analogous to radiation–adsorption process). If V acts over a "range" L, energy transfer will be most efficient for those collisions having a relative velocity v such that

$$v/L \sim c\Delta\nu \,. \tag{37}$$

For a typical root-mean-square velocity of 5×10^4 cm/sec, L corresponds to 3.1 Å for the perturbed $v'=8$ level and 10.3 Å for the red shifted and most strongly interacting $v'=6$ satellite. Indeed, this simple model agrees reasonably with the relative magnitude of observed transfer rates to the $v'=6$ and 8 levels. Because the $v'=6$ transitions are expected to occur at much longer range, it is not surprising that they proceed at a faster rate. This result indicates that the observation of a population maximum at $v'=8$ at $P_{\text{total}}=1000$ μm (Fig. 7) must result primarily from the nature of the relative populations in those feeder levels associated with the transferring reservoir state. The value of L associated with the weakly interacting shorter wavelength $v'=6$ satellite is 12.6 Å. Therefore, even this weakly interacting level would be expected to exhibit observable interactions and manifest itself readily in the observed emission spectra.

If we substitute Eq. (35) into (36), we have

$$\begin{aligned} k_{RB}^{1/2} \propto\; & c^2\langle J'|\langle v'|\langle B\,^2\Sigma^+|V|\text{res}\rangle|v\rangle|J\rangle \\ & - d^2\langle J'|\langle v|\langle\text{res}|V|B\,^2\Sigma^+\rangle|v'\rangle|J\rangle \\ & + cd\{\langle J'|\langle v'|\langle B\,^2\Sigma^+|V|B\,^2\Sigma^+\rangle|v'\rangle|J\rangle \\ & - \langle J'|\langle v|\langle\text{res}|V|\text{res}\rangle|v\rangle|J\rangle\}^1 \,, \end{aligned} \tag{38}$$

where the terms in brackets are off diagonal in J alone and correspond to $R\rightarrow R$ processes within the manifolds $|B\,^2\Sigma^+\rangle\,|v'\rangle$ and $|\text{res}\rangle\,|v\rangle$. The remaining matrix elements (off diagonal in three variables) correspond to electronic quenching processes, all of which are expected to proceed at a relatively slow rate. The nature of relationship (38) indicates that we have observed the equivalent of an unusually fast $R\rightarrow R$ process. The magnitude of the effects which characterize these systems may not be surprising. In retrospect our observation may be intimately connected with the large dipole moments which characterize the ground and excited states of most refractory high temperature molecules. There may, however, be other more subtle factors operative.

The enhanced transfer cross sections observed in the present study are reminiscent of the large cross sections now being associated with energy transfer involving highly excited Rydberg states.[38] One may view a highly excited Rydberg state as an electron circulating in wide orbit about a positive ionic core.[39] If we consider collisions with a neutral molecule, the interaction potential for this Rydberg state is dominated by the electron–neutral interaction, the ionic core–neutral interaction contributing much less to the cross section. This result leads one to believe that effects observed in the present study might be correlated with an increasingly diffuse electron density associated with molecular excitation (electronically excited states or high vibrational levels of the ground electronic state); however, it is not clear what the extent of long range electron density must be in order to facilitate the observed energy transfer. In other words, the observed energy transfer may require only a small "tickle" as opposed to substantial electron density.

Effects similar to those described here for ScO have now been observed in YO and LaO where E–E energy transfer is even more pronounced. In a related study V–E energy transfer has been observed in BO at pressures as low as 10^{-5} Torr.

As more data are collected it should be possible to ascertain interesting correlations regarding the nature of these "time dependent" collisional transfers and the intermolecular potentials which characterize the processes leading to efficient transfer. We are now investigating the effects of polarizability variation in the collisional partner versus Ar using He, N_2, CO, and CO_2. There appear to be several distinct playoffs between level separation, range of interaction, and mean free path at a given pressure.

In the current studies, we have utilized the strong perturbations among the excited electronic states of high temperature molecules. Although a complete perturbation analysis of the emission spectra (all rotational levels) may be prohibitive if not impossible,[40] the appearance of the satellite features allows us to achieve a good quantitative description of those "super highways" connecting various electronic states. If one wishes to understand efficient energy deposition processes, this is a valuable tool.

ACKNOWLEDGMENTS

It is a pleasure to acknowledge the probing commentary of Professor W. H. Eberhardt on the first draft of

this manuscript and the helpful suggestions of D. M. Lindsay, G. Rosenblatt, C. Chalek, and A. Hanner. Thanks also go to Professor M. R. Flannery for helpful discussions.

[1]D. M. Lindsay and J. L. Gole, J. Chem. Phys. 66, 3886 (1977).
[2]M. J. Sayers and J. L. Gole, J. Chem. Phys. 67, 5442 (1977).
[3]J. L. Gole, D. R. Preuss, and C. L. Chalek, J. Chem. Phys. 66, 548 (1977); J. L. Gole and C. L. Chalek, *ibid.* 65, 4384 (1976); L. H. Dubois and J. L. Gole, *ibid.* 66, 779 (1977); D. R. Preuss and J. L. Gole, *ibid.* 66, 880, 2994 (1977); J. L. Gole and D. R. Preuss, *ibid.* 66, 3000 (1977), and following references.
[4]H. E. Radford and H. P. Broida, J. Chem. Phys. 38, 664 (1963).
[5]C. L. Chalek and James L. Gole, J. Chem. Phys. 65, 2845 (1976).
[6]C. L. Chalek and J. L. Gole, Chem. Phys. 19, 59 (1977).
[7]C. R. Jones and H. P. Broida, J. Chem. Phys. 60, 4369 (1974).
[8]J. B. West, R. S. Bradford, J. D. Eversole, and C. R. Jones, Rev. Sci. Instrum. 46, 164 (1975).
[9]Single collision, Ref. 6; Multiple collision, J. L. Gole and S. A. Pace (unpublished).
[10]C. L. Chalek and J. L. Gole (unpublished); see also Sec. IV. D of text.
[11]J. L. Gole and C. L. Chalek (unpublished); see also Ref. 6.
[12]G. Herzberg, *Spectra of Diatomic Molecules* (Van Nostrand-Reinhold, New York, 1950).
[13]Both vibration–vibration ($V \rightarrow V$) and vibration–translation ($V \rightarrow T$) energy transfer might contribute to an equilibration of the $B\,^2\Sigma^+$ vibrational manifold. Typical pressure (P) dependent relaxation times (τ) are $P\tau \sim 10^{-3}$ atm sec and $P\tau \sim 10^{-4}$ atm sec for $V \rightarrow V$ and $V \rightarrow T$ processes, respectively [W. H. Flygare, Acc. Chem. Res. 1, 121 (1968)]. For pressures $P_{NO_2} \sim 10$–50 μm and $P \sim 1000$ μm argon, $V \rightarrow V$ relaxation requires a time $\tau \sim 10^{-3}$ sec, whereas for $V \rightarrow T$ processes $\tau \sim 10^{-2}$ sec. Both time scales are considerably longer than the radiative lifetime of the $B\,^2\Sigma^+$ state ($\sim 4 \times 10^{-8}$ sec).
[14]H. S. Johnston, *Gas Phase Reaction Rate Theory* (Ronald, New York, 1966).
[15]An extremely fast collisional transfer rate can dominate the radiative emission rate.
[16]The programs used for these computations were written by Dr. Brian B. Wicke.
[17]R. N. Zare, J. Chem. Phys. 40, 1934 (1964), and references therein.
[18]A. Adams, W. Klemperer, and T. M. Dunn, Can. J. Phys. 46, 2213 (1968); L. Akerlind, Ark. Fys. 22, 41 (1962).
[19]Considering an appropriate determination of the most probable energy for an effusive scandium beam (Ref. 6, and references therein) under single collision conditions. Under multiple collision conditions the scandium may be thermalized and therefore will have a smaller energy contribution [see, for example, G. J. Green and J. L. Gole, Chem. Phys. 46, 67 (1980).
[20]P. A. Fraser, Can. J. Phys. 32, 515 (1954).
[21]A. Hanner and J. L. Gole (unpublished).
[22]For the high temperature systems studied thus far, rotational equilibration has been observed at pressures in excess of 0.5 Torr.
[23]J. L. Gole, S. A. Pace, A. Hanner, and J. A. Appling (unpublished work on YO, LaO, and Cu_2O; also G. J. Green and J. L. Gole, Chem. Phys. (Ref. 19); and G. J. Green, A. Hanner, and J. L. Gole (unpublished).
[24]W. H. Flygare, Acc. Chem. Res. 1, 121 (1968).
[25]K. Liu and J. M. Parson, J. Chem. Phys. 67, 1814 (1977); J. M. Parson (private communication).
[26]K. D. Carlsen, E. Ludena, and C. Moser, J. Chem. Phys. 43, 2408 (1965).
[27]If we consider higher order multiconfiguration wave functions some additional small couplings will come into play; however, they will not drastically alter the conclusions reached in the present discussion.
[28]R. W. Field, R. A. Gottscho, and E. Miescher, J. Mol. Spectrosc. 58, 394 (1975).
[29]E. U. Condon and G. H. Shortley, *The Theory of Atomic Spectra* (Cambridge, U. P., London, 1964).
[30]G. Herzberg and K. P. Huber, *Constants of Diatomic Molecules* (Van Nostrand–Reinhold, New York, 1979).
[31]H. Hotop, T. A. Patterson, and W. C. Lineberger, Phys. Rev. A 8, 762 (1973).
[32]J. I. Steinfeld, Chem. Phys. Lett. 12, 431 (1971).
[33]R. D. Levine and R. B. Bernstein, *Molecular Reaction Dynamics* (Oxford, New York, 1974).
[34]An estimate for ScO based upon the lowest rotational temperature, 800 °K, at $P_{Ar} = 1000$ μm, and the close matchup of $P = 400$ μm and 1000 μm data.
[35]A similar approach pertains to collision induced predissociation by van der Waals perturbations: J. E. Selwyn and J. I. Steinfeld, Chem. Phys. Lett. 4, 217 (1969).
[36]J. T. Hougen, Natl. Bur. Stand. Monograph 115 (1970).
[37]Dipole–dipole interactions are in general considerably stronger than dipole–induced–dipole interactions (Ref. 33). There may well be a contribution to the inelastic collisional transfer processes at the lowest pressures where the effective pressures of primarily NO_2 and possibly ScO may be sufficient so as to induce transfer.
[38]M. F. Flannery (private discussions).
[39]R. S. Mulliken, J. Am. Chem. Soc. 86, 3183 (1964); C. Jungen, J. Chem. Phys. 53, 4168 (1970), and references therein; A. B. F. Duncan, *Rydberg Series in Atom and Molecules* (Academic, New York, 1971).
[40]The analysis of multiple perturbations involving several rotational levels of a given vibrational band may prove prohibitive unless pattern recognition is relatively straightforward.

Evidence for ultrafast V–E transfer in boron oxide (BO)

A. W. Hanner and J. L. Gole

Department of Chemistry, Georgia Institute of Technology, Atlanta, Georgia 30332
(Received 29 May 1980; accepted 14 July 1980)

Boron atoms react with oxygen (O_2) and nitrous oxide (N_2O) to yield the $A\,^2\Pi$–$X\,^2\Sigma^+$ spectrum of BO. These reactions have been characterized from 10^{-5} to 10^{-3} Torr and at $P_{total} \sim 1$ Torr in order to study relaxation and the rapid intramolecular V–E transfer $BO(X\,^2\Sigma^+, v'' = 17) + X \rightarrow BO(A\,^2\Pi_{1/2}, v' = 4) + X$ where $X = O_2$, N_2O, or a combination of these oxidants with argon. At the lowest pressures, a ground state boron atom interacts with a tenuous atmosphere of oxidant gas (beam–gas configuration). These "single collision" studies are extended in a controlled manner to higher pressure by entraining the metal atoms in argon and subsequently carrying out the oxidation of this mixture. At all pressures the measured $A\,^2\Pi$ vibrational populations follow a markedly non-Boltzmann distribution. At pressures as low as 6×10^{-5} Torr, the formation of BO $A\,^2\Pi_{1/2}$, $v' = 4$ results from both the direct reaction B + RO → BO* + R and the collisional transfer $BO(X\,^2\Sigma^+) + RO \rightarrow BO(A\,^2\Pi) + RO$. The spin orbit interaction in BO connects rovibronic levels of $X\,^2\Sigma^+$ and $A\,^2\Pi_{1/2}$ facilitating a route for rapid intramolecular energy transfer. This energy transfer leads to the observation of sharp features in the neighborhood of the BO $A\,^2\Pi$–$X\,^2\Sigma^+$ (4,0) band which may be correlated with the $J' = 18.5$–21.5 perturbed rotational levels of $BO(A\,^2\Pi_{1/2})$. We characterize this phenomenon determining population distributions, rotational temperatures, and the temperature dependence (boron source) of the chemiluminescence emission. The effects observed in BO demonstrate that a highly vibrationally excited ground state species interacts in the presence of a collision partner with a cross section substantially in excess of that expected for "gas kinetic" interaction. This behavior may have important implications for the modeling of energy systems as well as the ability to create population inversions requisite for the construction of visible chemical lasers.

INTRODUCTION

Recently, it has been determined that intramolecular energy transfer among the excited states of molecules important at high temperatures proceeds at a rate comparable to or much greater than the gas kinetic collision rate.[1] This energy transfer is particularly efficient for the most strongly interacting excited state levels and hence the most strongly perturbed levels of each state. While previous studies have concentrated on rapid E–E transfer, the present study focuses in large part on rapid V–E transfer involving the high vibrational levels of ground state $BO(X\,^2\Sigma^+)$ and levels of a low-lying $A\,^2\Pi$ state. The V–E transfer in boron oxide is observed over a much lower pressure range ($\sim 10^{-4}$ to 10^{-2} Torr) than that characterizing previously observed E–E transfers.

Elemental boron represents an elusive yet ever-present component of several systems characterized by high temperature materials conversion. The nature of the products of its oxidation is of fundamental importance to the understanding of energy dispersal in the combustion environments created by metallized rocket fuels[2] and may play a significant role in the advancement of laser technology.[3] While several studies have focused on Group IIIA metal oxidation involving aluminum,[4] gallium,[5] and indium,[6] the characterization of metatheses involving boron has been limited. From the standpoint of molecular electronic structure and the detailed understanding of molecular reaction dynamics, the diatomic and triatomic compounds of boron would seem to lend themselves more readily to study; however, little effort has focused on boron oxidation since it has been extremely difficult to obtain substantial boron atom or dimer concentrations in the gas phase. Not only is boron a highly refractory compound, but also it is extremely corrosive at elevated temperatures.

In the present study, we will be concerned with the highly exothermic chemiluminescent reactions of boron with O_2 and N_2O producing the ground and low-lying $A\,^2\Pi$ states of boron oxide (BO). Metatheses which involve boron atom oxidation to produce chemiluminescent spectra of the boron oxides (BO, BO_2) have been reported. The boron atoms in these studies are formed using either the dissociation of other boron compounds[7,8] (in flow systems), laser evaporation techniques,[9] or electron bombardment heating of a carbon crucible containing a bulk metallic sample.[10] In pursuing this problem, we have developed an intense effusive thermal beam source in order to study the reactions of boron (^2P) atoms under both "single" and "multiple" collision conditions. Single collision beam–gas studies allow the characterization of nascent product formation.[11] Multiple collision experiments[12] allow the controlled study of relaxation and quenching phenomena as well as the study of rapid energy transfer routes among the electronic states of high temperature species.

It is noteworthy that early researchers[13] first used the boron oxide (BO) spectrum to demonstrate the isotope effect usually mixing BCl_3 vapor with a stream of flowing active nitrogen containing traces of oxygen. More recently, BO and BO_2 lifetimes have been studied by adding BCl_3 directly to microwave discharged O_2.[14] These methods, while leading to detailed and elegant spectroscopy and kinetics, in general, do not produce the product internal excitation inherent in a highly exothermic beam–gas chemiluminescent reaction.[15] The added excitation characterizing these processes brings to light several unusual features in boron oxide. In studying the BO $A\,^2\Pi$–$X\,^2\Sigma^+$ emission which results from the single collision B–O_2 and B–N_2O reactions, we find evidence for the rapid vibrational to electronic energy transfer $BO(X\,^2\Sigma^+, v'' = 17, K \approx 19$–$22) \rightarrow BO(A\,^2\Pi, v' = 4,$

 0021-9606/80/225025-15$01.00

$J \approx 18.5-21.5$). This intramolecular process is observed at pressures as low as 6×10^{-5} Torr (oxidant) and must correspond to the very long range interaction of a diffuse, highly vibrationally excited BO molecule. It appears that the interaction leading to energy transfer is made efficient because of a strong spin–orbit interaction between the $\Omega = 1/2$ component of the $A\,^2\Pi$ state and the $X\,^2\Sigma^+$ state of boron oxide. The correlation of the present study with those of previous researchers suggests that the $^2\Pi_{1/2}$–$^2\Sigma^+_{1/2}$ interaction is sufficient to affect the relative transition moments of the two $A\,^2\Pi$ components, i.e., at 2×10^{-4} Torr the fluorescence intensity of the $^2\Pi_{1/2}$ component ($A\,^2\Pi_{1/2}$–$X\,^2\Sigma^+_{1/2}$) is less by a factor of 1.2 than the more intense $^2\Pi_{3/2}$ ($A\,^2\Pi_{3/2}$–$X\,^2\Sigma^+$) emission.

In order to better understand the unusual effects observed in BO, we have carried out both single and multiple collision studies. We report product population and rotational temperature distributions comparing the nature of these distributions with previous studies. In addition, we characterize the pressure and temperature dependence of the B–O_2 and B–N_2O metatheses, focusing primarily on the spectral region associated with BO $A\,^2\Pi_{1/2}$, $v' = 4$ bands.

EXPERIMENTAL

The burner systems used in these experiments are similar in overall design to those outlined previously[16]; however, in order to develop intense boron sources, significant modifications were needed. In order to study nascent excited state product formation under single collision conditions in a beam–gas system, boron atoms were generated by resistive radiative heating of a 99.95% graphite (Micromechanisms) crucible containing elemental boron (Alfa Inorganics $\geq$ 99.7%). The 1.8 cm o.d. crucible is surrounded and heated by a 2.0 cm i.d. 99.95% beveled graphite radiator[17] to temperatures ranging from 2175 to 2675 K. Extensive and precisely fashioned heat shielding surrounds the crucible–radiator assembly (typically two to three shields of 0.12 mm tantalum). The construction and operation of the oven system is greatly facilitated if the coefficients of expansion and reactivity of the constituents are carefully considered. As a precaution against the corrosive nature of boron, the crucible wall thickness exceeds that of previous designs where wall thicknesses ranged from 1 to 1.5 mm. A typical crucible is 7.9 cm in height. A central chamber of diameter 1.0 cm extends downward 5.7 cm from the top of the crucible resulting in a crucible wall thickness of 3.5 to 4.0 mm. The lower 2.0 cm of crucible remains a solid rod, this configuration providing an excellent combination of structural integrity under high stress conditions together with ample crucible volume for containment of the boron sample to be vaporized.[17] Run times typically ranged from 3 to 6 h, a typical crucible being of use for two to three experiments.

The boron was vaporized through a crucible orifice ranging in diameter from 1 to 4 mm, the beam intersecting a reaction chamber filled with ($\sim$ 0.6 to 12) $\times10^{-4}$ Torr of oxidant. Variation of the orifice diameter or shape over the range indicated did not affect the structure of the observed chemiluminescence. The oxidant gases O_2 (Specialty Gases Division, Air Products $\geq$ 99.994%) and N_2O (Matheson $\geq$ 98%) were used without further purification although the O_2 was passed through a drying tube as an extra precaution.[18] Pressure dependence studies (oxidant) were carried out using both a capacitance manometer (MKS Baratron) and an ionization gauge (only O_2). Operating temperatures were recorded using a Leeds and Northrup optical pyrometer focused directly on the crucible orifice. Temperature dependence studies were carried out using the pyrometer in conjunction with an optical multichannel analyzer (Tracor Northern).

The current source should be contrasted with that of Brzychcy *et al.*,[10] who have used photon counting to study the single collision chemiluminescent reactions of boron with O_2 and N_2O. Whereas these authors were unable to observe emission from the B–N_2O reaction (even with the N_2O temperature elevated to 1300 K), we have been able to observe emission easily in the present system. We have obtained a much more intense signal from the B–O_2 reaction versus B–N_2O, substantiating the observations of Brzychcy *et al.*[10] A back-of-the-envelope calculation indicates that the current boron source and beam–gas configuration results in a chemiluminescent signal at least three orders of magnitude more intense than that reported by Brzychcy *et al.* Over the temperature range of the experiments the boron flux in the reaction zone varied from $\sim 10^{12}$ to 10^{15} atoms/cm^2 s.

In extending our studies to multiple collision conditions, boron was evaporated from a graphite crucible fitted into a tungsten basket heater (R. D. Mathis, Long Beach, Cal.), the entire assembly being wrapped with two layers of zirconia (ZrO_2) cloth (Zircar Products, Florida, N.Y.). This grouping is encircled with a tantalum heat shield surrounded by a 2 in. i.d., 3 in. o.d. zirconia collar. Both the top and bottom of this entire grouping were covered with zirconia cloth, leaving only a 5 mm opening for the boron beam to escape. The extensive zirconia–tantalum insulation and shielding significantly reduced heat loss due to black-body radiative processes and, at the higher pressures, gas conduction. Its use permitted an upper operating temperature of 2500 K,[17] considerably exceeding expectations for the tungsten basket heaters. In a few runs, the carbon crucibles were replaced with zirconium boride; however, the use of these crucibles provided no significant improvement over carbon. The entire oven assembly was surrounded by a water cooled brass shield, all components being placed inside a vacuum chamber.[17] The brass shield not only provided necessary chamber cooling but also furnished an effective "light" baffle against black-body radiation from the crucible and heater.[17]

The boron was entrained and collimated by argon carrier gas (Matheson 99.9995%) and transported to the reaction zone where mixing with the oxidant gas occurs. Typical operating pressures ranged from 200 to 1000 mTorr of argon and 10 to 50 mTorr of N_2O or O_2. In

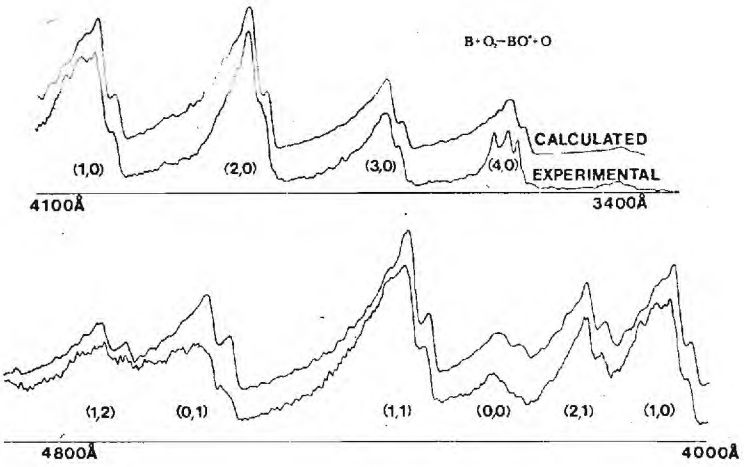

FIG. 1. Chemiluminescent spectrum obtained under single collision conditions from the reaction $B+O_2 \rightarrow BO^*+O$. Bandheads in the BO $A\,^2\Pi - X\,^2\Sigma^+$ band system are denoted (v', v''). The lower trace corresponds to the experimental spectrum while the upper trace is a computer simulation. Note the deviation in the region of the (4, 0) band. Spectral resolution is 1 Å; scan speed is 1 Å/s. See the text for discussion.

all cases the gas concentration in the multiple collision studies is dominated by the argon carrier. As a function of the argon pressure, the reaction produces a conical flame 1.2 cm at the base and from 2 to 10 cm tall. This should be contrasted with a diffuse flame observed under single collision conditions.

Both the single and multiple collision chemiluminescent flames were focused onto the slit of a Spex 1 m monochromator, equipped with an RCA 4840 photomultiplier tube. The photomultiplier was cooled using nitrogen passing through a dry-ice slush. The photomultiplier signal was detected with a Keithley 417 fast picoammeter whose output signal (partially damped) drove a Leeds and Northrup strip chart recorder. The spectrometer was calibrated with mercury and neon lamps. The entire optical system was calibrated for relative spectral response employing a quartz iodine standard lamp (EG and G #B115A).

RESULTS

Appearance of the chemiluminescent spectra

The chemiluminescence from the gas phase reactions

$$B(^2P) + O_2 \rightarrow BO^*(A\,^2\Pi) + O(^3P) \qquad (1)$$

and

$$B(^2P) + N_2O \rightarrow BO^*(A\,^2\Pi) + N_2(^1\Sigma_g^+) \qquad (2)$$

has been monitored under both single and multiple collision conditions over the wavelength range 3000–5000 Å.

Figures 1 and 2 depict representative scans of the emission which results from the boron–oxygen reaction under single and multiple collision conditions, respectively. The experimental spectrum in Fig. 1 was taken at a pressure of 2×10^{-4} Torr, while the multiple collision spectrum in Fig. 2 was taken at a total pressure (primarily argon) of 1 Torr (30 μ oxidant). Each spectrum is comprised of red-degraded bands corresponding to the BO* $A\,^2\Pi - X\,^2\Sigma^+$ system and differing sequence groupings $-1 \le \Delta v \le 5$ under single collision conditions and $-2 \le \Delta v \le 2$ under multiple collision conditions. (The notation $\Delta v = v' - v''$ pertains to transitions connecting vibrational levels v' of $A\,^2\Pi$ and v'' of $X\,^2\Sigma^+$.) Figures 3 and 4 correspond to the emission which results from the boron–nitrous oxide reaction. The experimental spectrum in Fig. 3 was taken at a pressure of 2×10^{-4} Torr, while the multiple collision spectrum in Fig. 4 was taken at a total pressure of 0.8 Torr (primarily argon with 35 μ of oxidant). The observed sequence groupings correspond to $0 \le \Delta v \le 9$ for both

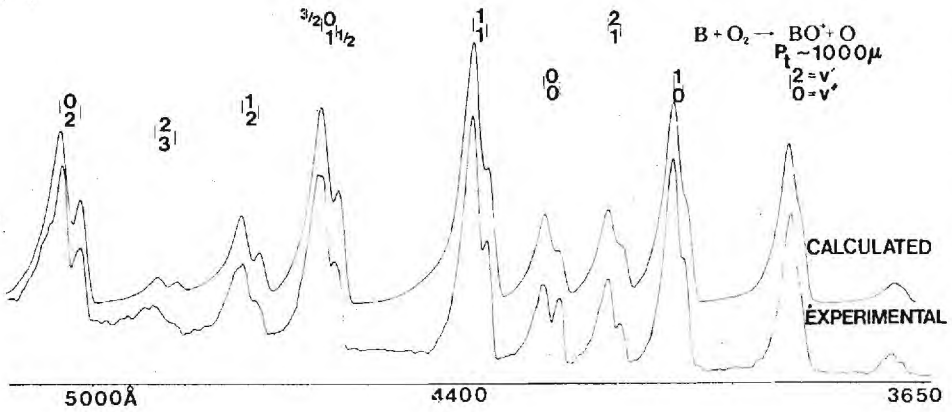

FIG. 2. Emission spectrum obtained under multiple collision conditions from the reaction $B+O_2+Ar \rightarrow BO^*+O_2+Ar$ (P_{total} = 1 Torr, $P_{Oxidant}$ = 30 μ). Bandheads in the BO $A\,^2\Pi - X\,^2\Sigma^+$ band system are denoted (v', v''). The lower trace corresponds to the experimental spectrum while the upper trace is a computer simulation. The apparent sharp increase of the $(O,O)_{1/2}$ band in the experimental spectrum is an artifact, the actual BO feature corresponding to a shoulder. Spectral resolution is 2 Å; scan speed is 2 Å/s. See the text for discussion.

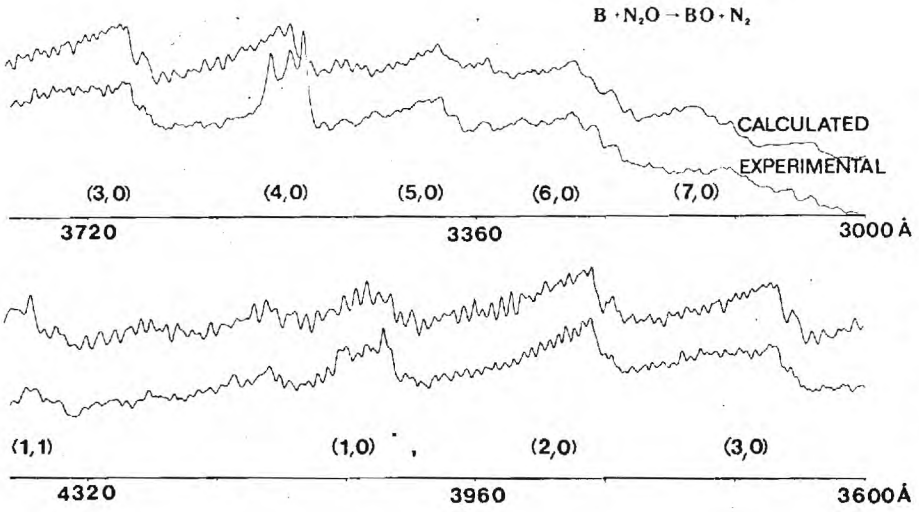

FIG. 3. Chemiluminescent spectrum obtained under single collision conditions from the reaction $B+N_2O \rightarrow BO^* + N_2$. Bandheads in the BO $A\,^2\Pi - X\,^2\Sigma^+$ band system are denoted (v', v''). The lower trace corresponds to the experimental spectrum while the upper trace is a computer simulation. Note the deviations observed in the neighborhood of the (4, 0) and (1, 0) bands. The deviation in the vicinity of the (1, 0) band is due to the (4, 2) emission band. Spectral resolution is 2 Å; scan speed is 1 Å/s. See the text for discussion.

single and multiple collision scans. The experimental spectra presented in Figs. 1–4 were taken at a resolution of 2 Å and scan speeds of 1 (Figs. 3 and 4) or 2 (Figs. 1 and 2) Å/s. The spectra were assigned by comparison with previously reported data.[13,14,19]

Vibrational populations and rotational temperatures for BO $A\,^2\Pi$

In each of the Figs. 1 to 4, the experimental spectra are compared to computer synthesized spectra calculated with the aid of Franck–Condon factors[20] and RKR curves[21] generated using available high resolution data.[13(c),19(a),(d)] The computer simulation assumes no level perturbations or excited state–ground state interactions. The comparison of experimental and calculated spectra thus allows the rapid assessment of strong $A\,^2\Pi$ perturbations. Upon analysis of the single collision spectra in Figs. 1 and 3, it became apparent that the (4, 0) band was manifest by an unusual intensity distribution not characteristic of other bands emanating from levels other than $v' = 4$. It is these sharp deviant features [three peaks superimposed on the (4, 0) band in Figs. 1 and 3] which will be the focus of the following discussion.

Taking into account the maximum temperature of the boron metal undergoing reaction (see following discussion) and all other factors in addition to reaction exoergicity which contribute to the available energy for formation of BO product, the boron–oxygen reaction would be expected to result in the population of four vibrational levels in the $A\,^2\Pi$ state. The much more exothermic $B-N_2O$ reaction could lead to the population of more than 30 vibrational levels; however, it is unlikely that emission from all these levels will be observed.

The relative intensities $I_{v',v''}$ of vibronic transitions (v', v'') in emission are related to the excited state populations $N_{v'}$ by

$$I_{v',v''} = N_{v'}\,\xi(\nu)\,\nu^4\,q_{v',v''}\,R_e^2(\bar{r}_{v',v''})\,, \tag{3}$$

where $\xi(\nu)$ is a proportionality constant defined to in-

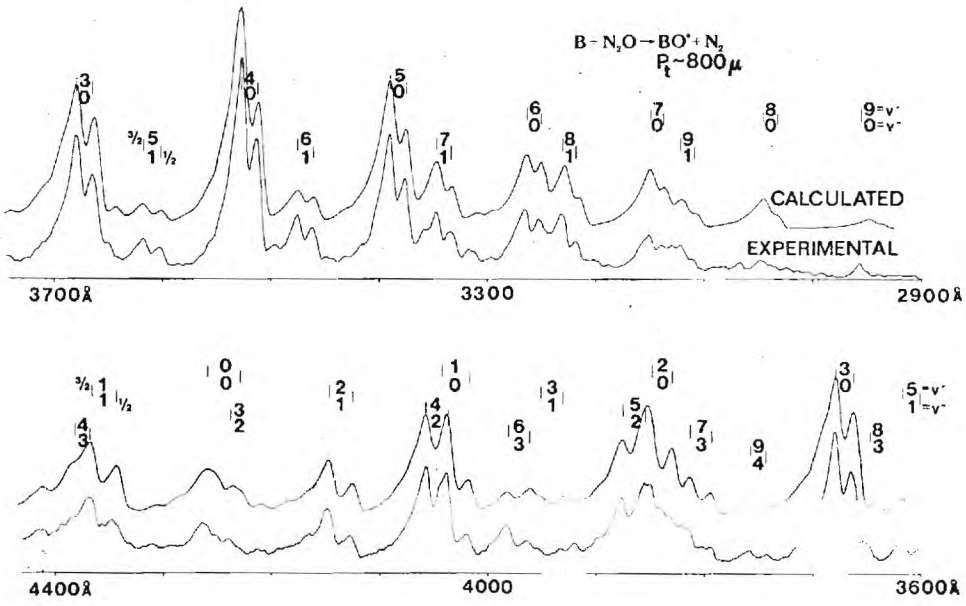

FIG. 4. Emission spectrum obtained under multiple collision conditions from the reaction $B+N_2O+Ar \rightarrow BO^* + N_2 + Ar$ ($P_{Total} = 800\ \mu$, $P_{Oxidant} = 35\ \mu$). Bandheads in the BO $A\,^2\Pi - X\,^2\Sigma^+$ band system are denoted (v', v''). The lower trace corresponds to the experimental spectrum while the upper trace is a computer simulation. Spectral resolution is 2 Å; scan speed is 1 Å/s. See the text for discussion.

clude the variation of instrumental (spectrometer and photomultiplier tube) response with frequency; $q_{v',v''}$ and $\bar{r}_{v',v''}$ are, respectively, the Franck–Condon factor and r centroid for the (v', v'') transition. The electronic transition moment $R_e(r_{v',v''})$ is written as an explicit function of the r centroid in accordance with the Fraser approximation.[22] This information is incorporated into a computer program to calculate the spectrum corresponding to a $^2\Pi(a)-{}^2\Sigma^+$ transition.[23] Once a fit is made to a given spectrum as in Figs. 1–4, a rotational temperature is determined for each individual rotational band and relative vibrational level populations are evaluated. For those spectra obtained at the lowest pressures where only nascent product formation is monitored, the rotational temperature of each vibrational band can differ[24]; however, at higher pressures rotational distributions are found to equilibrate rapidly and the entire spectrum is characterized by one rotational temperature.[1(c),12]

The computer calculation of the BO $A\,^2\Pi-X\,^2\Sigma^+$ emission spectrum at first was carried out assuming a constant electronic transition moment for all levels of $A\,^2\Pi$. In fitting the experimental spectra in Figs. 1–4, it soon became apparent that the transition moments for the $A\,^2\Pi_{1/2}-X\,^2\Sigma^+$ and $A\,^2\Pi_{3/2}-X\,^2\Sigma^+$ transitions differed, the $^2\Pi_{3/2}$ emission being more intense. Under single collision conditions (Figs. 1 and 3) the ratio $^2\Pi_{3/2}/{}^2\Pi_{1/2}$ was found to be ~1.2 whereas under multiple collision conditions (Figs. 2 and 4) the ratio $^2\Pi_{3/2}/{}^2\Pi_{1/2}$ was found to be ~1.6. The quoted ratios represent an average over the v' levels from which emission is observed.[25] The apparent behavior might result from preferential

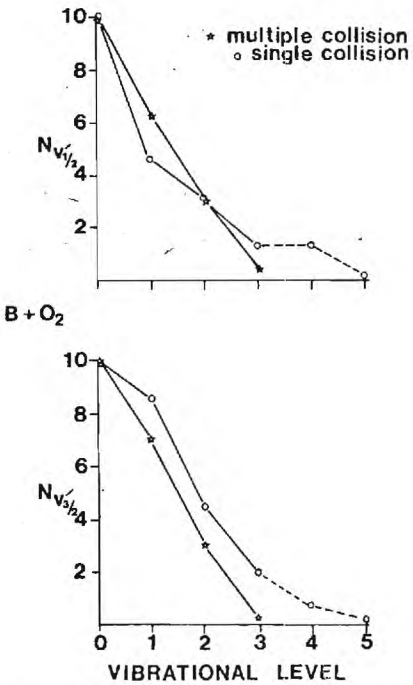

FIG. 5. BO* $A\,^2\Pi$ vibrational populations ($N_{v'}$) recorded for single (○) and multiple (*) collision conditions corresponding to the processes $B+O_2 \rightarrow BO^*+O$ and $B+O_2+Ar \rightarrow BO^*+O+Ar$, respectively. Relative populations are determined on the basis of the computer simulations in Figs. 1 and 2. See the text for discussion.

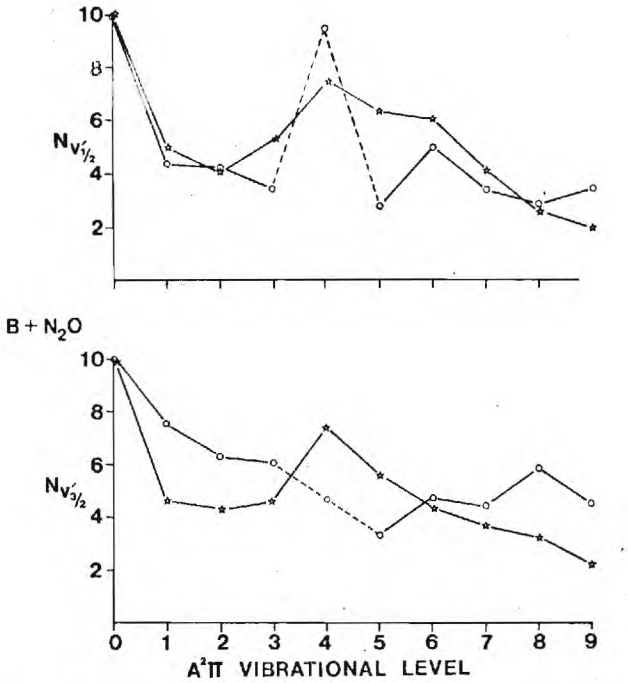

FIG. 6. BO* $A\,^2\Pi$ vibrational populations ($N_{v'}$) recorded for single (○) and multiple (*) collision conditions corresponding to the processes $B+N_2O \rightarrow BO^*+N_2$ and $B+N_2O+Ar \rightarrow BO^*+N_2+Ar$, respectively. Relative populations are determined on the basis of the computer simulations in Figs. 3 and 4. See the text for discussion.

population of $^2\Pi_{3/2}$ versus $^2\Pi_{1/2}$ levels; however, there are no symmetry constraints which would indicate this possibility for either the $B-O_2$ or $B-N_2O$ reactions. In addition, it is difficult to believe that a substantial change in preferential component population will occur as a function of the pressures considered here. Of more importance would appear to be the correlation of the present results with those of Huie *et al.*[14] Using a nitrogen pumped dye laser of bandwidth ~16 cm^{-1}, these authors investigated the pressure dependence for the radiative decay of BO($A\,^2\Pi$) at 384 and 436 nm. From Figs. 1–4 it is clear that the fluorescence excitation region corresponds to the (2, 0) and (1, 1) bands of the α system. Closer inspection reveals that the $^2\Pi_{3/2}$ component ($A\,^2\Pi_{3/2}-X\,^2\Sigma^+$ transition) should be preferentially pumped. Huie *et al.* observed "strong fluorescence which decayed much more rapidly at higher pressures." From their data (Fig. 1, Ref. 14) we predict the pressure dependence observed in our experiments for the ratio of $^2\Pi_{3/2}/{}^2\Pi_{1/2}$ emission, i.e., there appears to be a one-to-one correspondence between the component ratio and their determined change in the $^2\Pi_{3/2}$ radiative lifetime as a function of pressure. This result will be considered further in a later section.

In Figs. 5 and 6, we compare $A\,^2\Pi$ vibrational populations determined under single and multiple collision conditions from the computer simulations in Figs. 1–4. The $^2\Pi_{1/2}$ and $^2\Pi_{3/2}$ components are treated separately. The population distributions observed for both the $B-O_2$ and $B-N_2O$ metatheses are distinctly non-Boltzmann for *both* single and multiple collision studies.

The relative vibrational populations for the $^2\Pi_{3/2}$ and

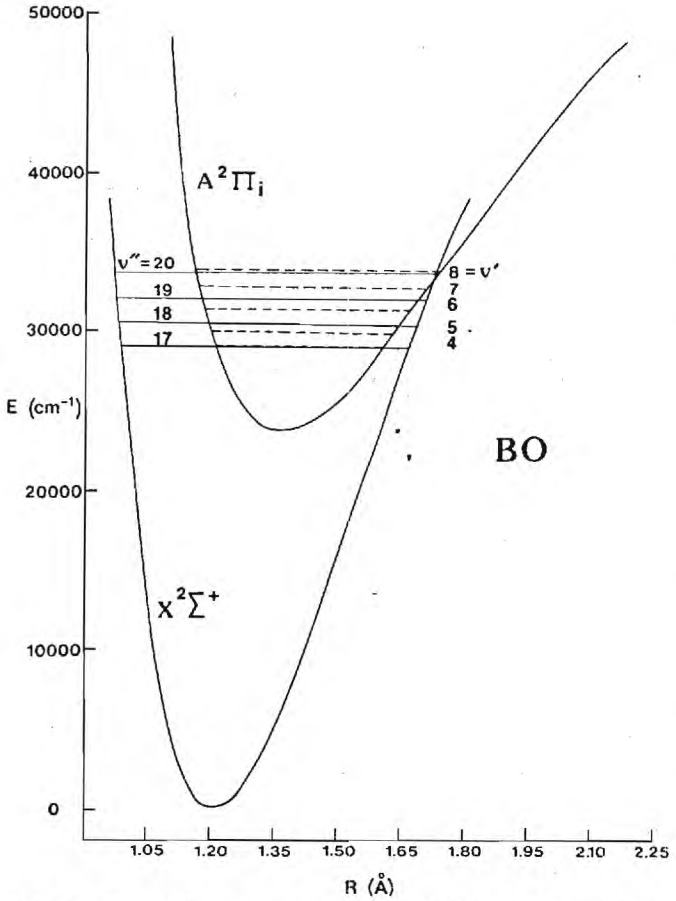

FIG. 7. Potential curves calculated for $X\,^2\Sigma^+$ and $A\,^2\Pi_i$ states using data in Table I. For the scale of this figure, the $A\,^2\Pi_{3/2}$ and $A\,^2\Pi_{1/2}$ states are virtually coincidental. Levels of $X\,^2\Sigma^+$ ($v''=17$–20) are denoted by solid lines. Levels of $A\,^2\Pi$ ($v'=4$–8) are denoted by dashed lines. See the text for discussion.

$^2\Pi_{1/2}$ components differ for both the B–O_2 and B–N_2O systems. For B–O_2 (Fig. 5), the apparent decrease in the $^2\Pi_{1/2}$ component population (versus $^2\Pi_{3/2}$) for $v'=1$ versus $v'=0$ may correspond to an effective lower transition moment resulting from significant $^2\Pi_{1/2}$–$X\,^2\Sigma^+$ mixing (see also following discussions).[25] The relative population of $v'=4$, $A\,^2\Pi_{1/2}$ definitely exceeds that for the corresponding 3/2 component, the noted population $N_{v'=3/2}(4)$ representing a stringent upper bound. Under multiple collision conditions, we observe only weak emission from $v'=3$ and no emission from $v'=4$ or 5. The differences in the single and multiple collision spectra can be accounted for if we realize that boron atom collisional thermalization, to much lower temperatures, takes place at the higher pressures corresponding to boron entrainment (see discussion). Considering the effects of boron thermalization and comparing the single and multiple collision populations for levels $v'=0$–3, it appears that vibrational relaxation is minimal under the multiple collision conditions characterizing the present B–O_2 experiments.

In Fig. 6, we depict the population distributions for the first ten ($v'=0$–9) levels of BO $A\,^2\Pi$ even though the B–N_2O reaction might populate in excess of 30 $A\,^2\Pi$ vibrational levels. We have searched for bands corresponding to higher levels, finding, at best, meager evidence for emission from $v'=10$, 11, and 12. The RKR potential curves depicted in Fig. 7 demonstrate that $A\,^2\Pi$ levels $v'>8$ may be expected to display an interesting behavior. The $v'=8$ level is at an energy correlating closely with a curve crossing at the outer turning points of the $A\,^2\Pi_{1/2,3/2}$ components and the $X\,^2\Sigma^+$ state. The nature of this curve crossing may influence the population of the $v'=8$ level and might account for the cutoff of emission after $v'=9$. The populations indicated for $v'=6$, 7, and 8 in the multiple collision scans represent average values determined by combining the various Δv transitions emanating from $v'=6$, 7, and 8. The behavior of emission from these levels appears to be slightly anomalous. A good example is obtained through comparison of the (8, 0) and (8, 1) bands in Fig. 4. A reasonable fit of the (8, 1) band requires an overestimate of the experimental intensity characterizing the (8, 0) band. This behavior would seem to indicate that Franck–Condon factors derived for the A–X transition for levels in the region of the $A\,^2\Pi$–$X\,^2\Sigma^+$ crossing may not be appropriate. The vibrational levels $v'\geq 6$ are the subject of continuing studies in our laboratory. If we compare the single and multiple collision spectra for $v'\geq 5$, there appears to be evidence for slight vibrational relaxation to $v'=5$ from vibrational levels $v'\geq 6$.

Focusing on the lower vibrational levels of the $A\,^2\Pi$ state, we find that the B–N_2O system also appears to be characterized by a decrease in the $A\,^2\Pi_{1/2}$ population for $v'=1$ versus $v'=0$ (compare to $A\,^2\Pi_{3/2}$ distribution). Hence both the B–O_2 and B–N_2O reactions may be characterized by this difference in the $^2\Pi_{3/2}$ and $^2\Pi_{1/2}$ component population distributions. The $v'=0$ and 4 levels dominate the population distributions for both $A\,^2\Pi_{1/2}$ and $A\,^2\Pi_{3/2}$ under single collision conditions. This dominance continues for the $A\,^2\Pi_{1/2}$ component under multiple collision conditions, the seemingly deviant behavior of the $v'=4$ level being most pronounced for the single collision $A\,^2\Pi_{1/2}$ populations. It is this fourth vibrational level which will be the subject of a more complete discussion in a following section.

The rotational temperature distributions which characterize the single collision B–O_2 and B–N_2O reaction are indicated in Fig. 8. The rotational temperatures as a function of vibrational level show no definite pattern. For the boron–N_2O reaction, the rotational temperature peaks at 8000 ± 300 K for $v'=3$, leveling off to a rotational temperature of 7000 ± 300 K for $v'\geq 5$. For the boron–O_2 reaction, rotational temperatures decrease almost monotonically from a maximum of 3000 ± 100 K for $v'=0$ to 1800 ± 200 K for $v'=5$. The nature of these nonequilibrium distributions will be considered in following discussion. The multiple collision B–O_2 and B–N_2O reactions are both characterized by BO product rotational temperatures $T_{rot}=600\pm 50$ K for all vibrational levels observed.

Nature of emission features observed in the region of the BO $A\,^2\Pi$–$X\,^2\Sigma^+$ (4,0) band–evidence for ultrafast V-E transfer

As we have noted in previous discussion, the single collision BO $A\,^2\Pi_{1/2}$–$X\,^2\Sigma^+$ emission spectra observed

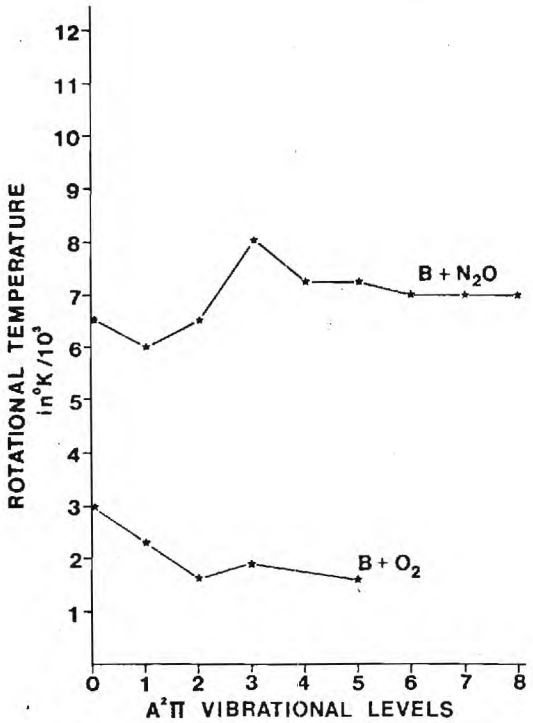

FIG. 8. BO* $A\,^2\Pi$ rotational temperatures determined for vibrational levels populated in the single collision $B+O_2 \rightarrow BO^*+O$ and $B+N_2O \rightarrow BO^*+N_2$ reactions. Rotational temperatures were deduced from the computer simulations in Figs. 1 and 3. See the text for discussion.

for the $B-O_2$ and $B-N_2O$ reactions (Figs. 1 and 3) are characterized by an unusual group of peaks in the region corresponding to the (4, 0) band. In this section, we will discuss the characterization of these features, the nature of their pressure and temperature dependence, and the evidence that they result from a rapid $V-E$ energy transfer and strong interaction among the levels $BO[X\,^2\Sigma^+,\ v''=17,\ K\approx 19-22) \rightarrow BO(A\,^2\Pi,\ v'=4,\ J\approx 18.5-21.5]$.

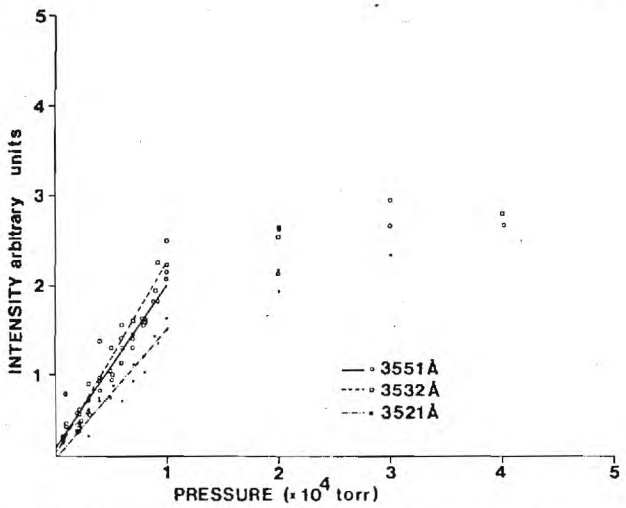

FIG. 9. Relative chemiluminescent intensity as a function of oxygen pressure for the three sharp fluorescence features observed in the region of the BO $A\,^2\Pi-X\,^2\Sigma^+$ (4, 0) band (Fig. 1). See the text for discussion.

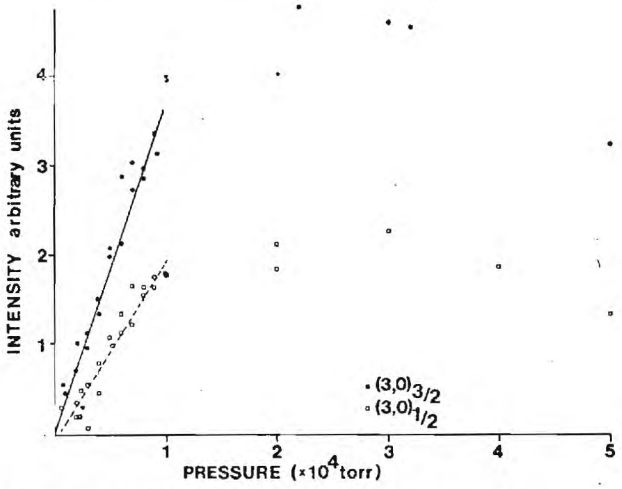

FIG. 10. Relative chemiluminescent intensity as a function of oxygen pressure for the two components of the BO $A\,^2\Pi-X\,^2\Sigma^+$ (3, 0) band (Fig. 1). See the text for discussion.

Pressure dependence of chemiluminescence spectra

Several oxidant pressure dependence scans were recorded for the BO emission spectra presented in Figs. 1 and 3. In all cases, the variation of chemiluminescent intensity with oxidant pressure was found to display the characteristics of a metathesis first order in oxidant. Examples of this behavior for the $B-O_2$ reaction are presented in Figs. 9 and 10. Here the regions corresponding to the (3, 0) and (4, 0) BO $A\,^2\Pi-X\,^2\Sigma^+$ emission bands are considered. The data points presented in Figs. 9 and 10 were taken as a function of both increasing and decreasing oxidant pressure; hence, there are approximately two data points at each of the pressures measured. The onset of the chemiluminescent intensity is linear in all cases.[26] This demonstrates that the O_2 metathesis is first order with respect to the oxidant and that the emission process is intramolecular and not collision induced.[27] At higher pressures, the data in Figs. 9 and 10 show a negative curvature. This behavior is due to the attenuation of the metal beam before it reaches the zone viewed by the spectrometer. The nature of this attenuation can be correlated with the total phenomenological cross section (elastic + inelastic + reactive) for metal beam removal.[26] In Fig. 9, the three pressure dependence plots correspond to the three sharp peaks in the neighborhood of the BO $A\,^2\Pi-X\,^2\Sigma^+$ (4, 0) emission band. The plots actually damp out the precise behavior of the pressure dependence which characterizes these sharp features. In Fig. 11, we display the nature of typical spectra (oven temp ~ 2300 K) in the region of the $A-X$ (3, 0) and (4, 0) bands taken at pressures of 0.2, 0.5, and 5×10^{-4} Torr. Inspection of this figure reveals that the ratio of intensity in the (4, 0) region increases relative to that in the (3, 0) region, the more marked change occurring in the pressure range 0.5 to 5×10^{-4} Torr. This relative increase in the region of the (4, 0) band is manifest almost entirely by the three peaks now apparent in Figs. 11(c) and 1. The effects of this increase are not apparent in Fig. 9 because metal beam attenuation is already strongly manifest at pressures in excess of 1×10^{-4} Torr.[26] Similar behavior

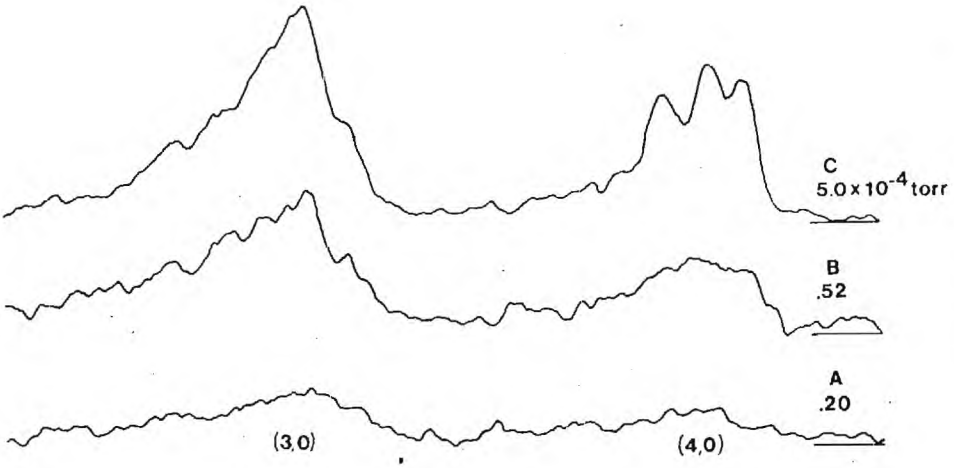

FIG. 11. Chemiluminescent spectrum for the reaction $B + O_2 \rightarrow BO^* + O$ as a function of pressure showing the onset of three peaks in the region of the BO $A\,^2\Pi - X\,^2\Sigma^+$ (4,0) band. These peaks result from the rapid $V-E$ energy transfer BO $X\,^2\Sigma^+$ ($v'' = 17$) $+ O_2 \rightarrow$ BO $A\,^2\Pi$ ($v' = 4$). See the text for discussion.

is observed in the spectrum characterizing the $B-N_2O$ reaction (Fig. 3) and in the spectrum which results from the $B-NO_2$ metathesis.[12]

Sharp features observed in the region of the (4,0) band

Because of their strong pressure dependence, the triplicate of features observed in the region of the BO $A\,^2\Pi - X\,^2\Sigma$ (4, 0) band would appear to result from a process involving collision induced energy transfer. Based upon recent experience with rapid $E-E$ transfer,[1] we investigated the possibility of collision induced intramolecular transfer to BO $A\,^2\Pi$, $v' = 4$ from a long-lived low-lying electronic state corresponding to the nascent product formed in the $B-O_2$ or $B-N_2O$ reactions. No evidence could be found[28] for a long-lived "reservoir state" which could possibly interact strongly with BO $A\,^2\Pi$, $v' = 4$; however, it soon became apparent that a near coincidence could be found between the $v'' = 17$ level of the ground $X\,^2\Sigma^+$ state and BO $A\,^2\Pi_{1/2}$, $v' = 4$. Further investigation reveals that Jenkins and McKellar[13(b)] long ago documented strong perturbations between rovibronic levels of the ground $X\,^2\Sigma^+$ state and BO $A\,^2\Pi_{1/2}$, $v' = 4$. Hence, it would appear that we are observing a rapid $V-E$ intramolecular energy transfer between strongly perturbed and interacting levels of the $A^2\Pi_{1/2}$ components and the $X^2\Sigma^+_{1/2}$ state.

Considering the nature of the potential curves in Fig. 7 and comparing to previous studies on AlO and ScO,[1] it appears that we have observed the result (Figs. 1 and 3) of a sequence which involves the initial reaction steps

$$B(^2P) + O_2(^3\Sigma_g^-) \rightarrow BO(X\,^2\Sigma^+) + O(^3P) \ , \tag{4}$$

$$B(^2P) + N_2O(^1\Sigma^+) \rightarrow BO(X\,^2\Sigma^+) + N_2(^1\Sigma_g^+) \ , \tag{5}$$

followed by collision induced transition to the $A\,^2\Pi$ state:

$$BO(X\,^2\Sigma^+,\ v'' = 17) + O_2 \rightarrow BO(A\,^2\Pi_{1/2},\ v' = 4) + O_2 \ , \tag{6}$$

$$BO(X\,^2\Sigma^+,\ v'' = 17) + N_2O \rightarrow BO(A\,^2\Pi_{1/2},\ v' = 4) + N_2O \ . \tag{7}$$

The collision induced population of BO $A\,^2\Pi_{1/2}$, $v' = 4$ must be combined with the direct Reactions (1) and (2) to produce the emission observed from BO $A\,^2\Pi$. Only in this way can the sharp differences between the simulated and observed spectra in Figs. 1 and 3 be accounted for in a reasonable manner.

The substantial rate which must characterize the energy transfer observed in the present study is not unprecedented for processes occurring among excited and strongly interacting states in high temperature molecules.[1] Although previous investigations of rapid intramolecular $E-E$ transfer revealed perturbations which were found to affect a significant range of rotational levels leading to the observance of "satellite bands," the sharp nature of the features observed in the current study indicates the interaction of only a few rotational levels in the $A\,^2\Pi_{1/2}$ and $X^2\Sigma^+_{1/2}$ states.[29] In the presence of intramolecular perturbations, neither the $A\,^2\Pi_{1/2}$ nor the $X\,^2\Sigma^+$ state from which energy transfer occurs may be considered as pure states. Rovibronic levels of the $X\,^2\Sigma^+$ state contain a small admixture of $A\,^2\Pi$ character. Transitions from these "reservoir" levels, from which emission is forbidden or very weak in the absence of perturbations, may "borrow intensity" from the $A \rightarrow X$ spectrum and become allowed.[30] Hence, we proceeded under the assumption that at least one of the triplicate of bands observed must correspond to emission from a strongly mixed $v'' = 17$ level.

Nature of $A\,^2\Pi$ perturbations

The "strength" of perturbations (w) between the $A\,^2\Pi$ and $X\,^2\Sigma^+$ states will depend on the nature of the $A-X$ interaction (typically spin orbit or Coriolis) and the energy separation of unperturbed states (δ). The eigenfunctions (ψ) of the perturbed levels are[30]

$$\psi_+ = c\psi_1 - d\psi_2 \ , \tag{8}$$

$$\psi_- = d\psi_1 + c\psi_2 \ .$$

The subscripts denoted 1, 2 and ± pertain to unperturbed and perturbed levels, respectively, ψ_+ corresponding to the perturbed A state and ψ_- to the perturbed X state. The final separation between perturbed levels can be correlated with the perturbation (w) and the original energy separation (δ) as

$$\Delta\nu = (4w^2 + \delta^2)^{1/2} \ . \tag{9}$$

In direct analogy to previous observations in AlO,[1(a),(b)] spin–orbit coupling of the $A\,^2\Pi_{1/2}$ and $X\,^2\Sigma^+$ states is expected to dominate the observed interactions. Considering the spin–orbit interaction, we must evaluate the perturbation matrix element

$$w = \langle \psi_1 | H_{so} | \psi_2 \rangle \ . \tag{10}$$

In exact analogy to AlO,[1(a),(b)] noting that the electron configurations for the $X\,^2\Sigma^+$ and $A\,^2\Pi$ states are

$$\cdots (4\sigma)^2(1\pi)^4(5\sigma)\, X\,^2\Sigma^+ \tag{11}$$

and

$$\cdots (4\sigma)^2(1\pi)^3(5\sigma)^2 A\,^2\Pi_i \ , \tag{12}$$

respectively, we arrive at a final expression of the form

$$w = \tfrac{1}{2}\langle v' | v'' \rangle \langle -1_1 | \sum_k \epsilon_k(r_k)\, l_k^- | 0_5 \rangle \ , \tag{13}$$

where the subscripts 1 and 5 pertain to one electron molecular orbitals 1π and 5σ, respectively; the numerals 0 and ± 1 identify the z component of an electron orbital angular momentum, and the sum is over nuclei k; l_k^- is an angular momentum lowering operator and $\epsilon_k(r_k)$ is the spin–orbit constant proportional to the inverse cube distance between the electron i considered and the nucleus k. In the above expression (13), $\langle v' | v'' \rangle$ corresponds to a vibrational overlap factor.

A complete evaluation of w requires some knowledge of the molecular orbitals $|-1_1\rangle = 1\pi$ and $|0_5\rangle = 5\sigma$. The presence of $\epsilon_k(r_k) \sim r_k^{-3}$ insures that only one center integrals will make a significant contribution to Eq. (13). It does not appear that extensive quantum calculations describing the $A\,^2\Pi$ state of BO are readily available. Therefore, we have compared calculations by Schamps[31] on AlO and Guest and Saunders[32] on BO in order to estimate the magnitude of the matrix element w. Considering the atomic orbital makeup of the 1π and 5σ orbitals which are centered more on boron than the corresponding 2π and 7σ orbitals in AlO[1,31,32] and the slightly increased ionic character of AlO versus BO,[1,31,32] we estimate

$$w \approx 20 \langle v' | v'' \rangle \ \text{cm}^{-1} \ . \tag{14}$$

Assignment of strongly interacting levels

Collisions with O_2 or N_2O may be viewed as time dependent perturbations which cause transitions between the spin–orbit perturbed states

$$|+\rangle = c\,|A\,^2\Pi_{1/2}\rangle\,|v'\rangle\,|J'\rangle - d\,|X\,^2\Sigma^+\rangle\,|v''\rangle\,|J'\rangle$$

and (16)

$$|-\rangle = d\,|A\,^2\Pi_{1/2}\rangle\,|v'\rangle\,|J\rangle + c\,|X\,^2\Sigma^+\rangle\,|v''\rangle\,|J\rangle$$

of BO.[33] The selection rule is $\Delta J = 0$[34] and the perturbing Hamiltonian is the time dependent (by virtue of the motion) intermolecular potential between either O_2 or N_2O and BO. For a particular trajectory, the rate constant $K_{X\to A}$ is proportional to the squared matrix elements of the amplitude V of this interaction[35]

$$K_{X\to A} \alpha |\langle + | V | - \rangle|^2 \ . \tag{17}$$

Based upon these considerations and the expected "intensity borrowing" (Sec. II) upon mixing of BO $A\,^2\Pi_{1/2}$, $v' = 4$ and BO $X\,^2\Sigma^+$, $v'' = 17$, we attempted to correlate the sharp spectral features in Figs. 1 and 3 with transfer among particular rotational levels, requiring that the $\Delta J = 0$ selection rule be satisfied.

TABLE I. Spectral parameters relating $A\,^2\Pi$ and $X\,^2\Sigma^+$ states of boron monoxide.[a]

	$B_{\text{effective}}(v' = 4) = 1.3377\ \text{cm}^{-1}$[b]
(4, 0) $A\,^2\Pi_{1/2}$–$X\,^2\Sigma^+$	$B_0''(v'' = 0) = 1.7737\ \text{cm}^{-1}$
$w_e' = 1260.70$, $w_e x_e' = 11.16$	$\nu_0 = 28466.1\ \text{cm}^{-1}$
Ground state	$B_0''(v'' = 17) = 1.4915$[c]
$w_e'' = 1885.69$, $w_e x_e'' = 11.81$	$B_0''(v'' = 0) = 1.7737$
	$\nu_0(v'' = 17 \to v'' = 0) = 28442.8\ \text{cm}^{-1}$

[a] Data used taken from Refs. 13(c), 19(a), and 19(d).
[b] $B_e' = 1.4132$, $\alpha_e = 1.96 \times 10^{-2}\ \text{cm}^{-1}$, $A = -122.36$. Evaluation of $B_{\text{effective}}$ based on Ref. 30.
[c] $B_e'' = 1.7820$ and $\alpha_e = 1.66 \times 10^{-2}\ \text{cm}^{-1}$.

We first considered the rotational branch structure for the $A\,^2\Pi - X\,^2\Sigma^+$ (4, 0) band. The separation between the $^2\Pi_{1/2}$ and $^2\Pi_{3/2}$ subbands is ~ 125 cm^{-1}, indicating that the $^2\Pi$ state follows Hund's case (a) coupling. For a $^2\Pi_i(a) - ^2\Sigma^+$ transition each subband is expected to consist of six branches, those for $^2\Pi_{1/2}$ being $P_2(J)$, $Q_2(J)$, $R_2(J)$, $P_{21}(J) \sim Q_2(J-1)$, $Q_{21}(J) \sim R_2(J-1)$, and $R_{21}(J)$.[30,36] For a molecule which closely follows Hund's case (a) coupling, the $R_{21}(J)$ branch is expected to be reasonably strong; however, as the molecule tends to case (b) (higher rotational quantum number) this satellite branch is expected to weaken considerably. Therefore, the nature of the branch structure for the $^2\Pi_{1/2}$ component dictates that a strong interaction and energy transfer involving a few rotational levels should be manifest by three dominant features for $R_2(J)$, $P_2(J)$, and $Q_2(J)$ and a weaker feature for $R_{21}(J)$.

Similar considerations can be applied to the $v'' = 17$ level of the $X\,^2\Sigma^+$ state as it borrows intensity from $A\,^2\Pi_{1/2}$ for those few rotational levels which interact strongly. The weak transition $X\,^2\Sigma^+$, $v'' = 17 \to X\,^2\Sigma^+$, $v'' = 0$ will be observed at energies corresponding to the levels of $X\,^2\Sigma^+$ which interact strongly with $A\,^2\Pi$. Because of the mixing with $A\,^2\Pi$, we expect features corresponding to P, Q, and R branches dictated by the appropriate selection rules.

In summary, the mixing and energy transfer among certain rotational levels BO $A\,^2\Pi_{1/2}$, $v' = 4$, J' and BO, $X\,^2\Sigma^+_{1/2}$, $v'' = 17$, K'' is expected to produce six relatively strong peaks and one weak feature. In our attempts to fit these peaks, we take advantage of high resolution data on the $A\,^2\Pi$ and $X\,^2\Sigma^+$ states of BO to determine the parameters given in Table I.

Clearly, the three peaks observed in Figs. 1 and 3 do not account completely for the expected structure in the region of the (4, 0) band. Slower 0.2 Å/s scans (resolution = 2 Å) of the 3510–3560 Å region are presented in Fig. 12. These spectra result from the B–O_2 reaction. We observe four pronounced peaks and one and possibly two weaker features merging to three strong features at higher temperature. These features are cataloged in Table II. Outstanding signal to noise is precluded since there is underlying structure resulting from both the $A\,^2\Pi_{3/2} - X\,^2\Sigma^+$ and $A\,^2\Pi_{1/2} - X\,^2\Sigma^+$ transitions for those

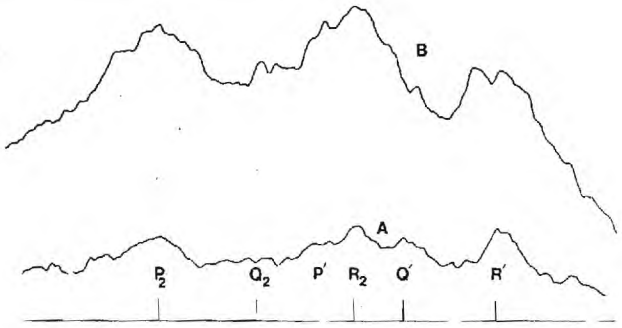

FIG. 12. Slow scan (0.2 Å/s) of features which are attributed to energy transfer effects in the region of the BO* A–X (4,0) band. The features P_2, Q_2, and R_2 are associated with BO $A\,^2\Pi_{1/2}$ $v'=4$, the labels corresponding to branches of an $A\,^2\Pi_{1/2}$–$X\,^2\Sigma^+$ transition. The features P', Q', and R' are associated with BO $X\,^2\Sigma^+$, $v''=17$, the labels corresponding to branches of a Π–Σ transition. See the text for discussion.

molecules formed directly in the $A\,^2\Pi$ state via Reaction (1). Nevertheless, an assignment of the observed spectral features is possible. Using the data in Table I, we attempted to calculate the frequencies corresponding to the maxima in Fig. 12(a) searching for both a close frequency fit and the necessary satisfaction of perturbation selection rules. Our final results are given in column 3 of Table II. These calculated frequencies correspond closely to the maxima observed for the features in Fig. 12(a). In order to obtain this close agreement, we first determined that the broad maxima for two of the more intense features $P_2(J)$ and $R_2(J)$ could be fit assuming an emission emanating from $A\,^2\Pi_{1/2}$, $v'=4$, $J'\approx 19.5$–20.5. Although more difficult to assess directly, this assignment was also consistent with a weaker feature $Q_2(J)$ which is also associated with the $A\,^2\Pi_{1/2}$–$X\,^2\Sigma^+$ (4,0) band. Note that for an inverted $A\,^2\Pi$ state, the level $J'=19.5$ corresponds to $K'=20$. Significantly, the maxima of the remaining two well developed features (P', Q') were well fit, assuming that they were associated with emission from $v''=17$, $J=19.5$. The correspondence is in striking agreement with the $\Delta J=0$ selected rule which must be satisfied for $A\,^2\Pi_{1/2}$–$X\,^2\Sigma^+$ perturbations. On this basis it appears that the sharp spectral features observed in Figs. 1, 3, and 12 should be associated with the process

$$\mathrm{BO}(X\,^2\Sigma^+,\ v''=17,\ K''\approx 19\text{–}22) \rightarrow \mathrm{BO}(A\,^2\Pi_{1/2},\ v'=4,\ J'\approx 18.5\text{–}21.5)\ . \qquad (18)$$

Further indication of the feasibility of the proposed energy transfer may be garnered from a consideration of the single (Fig. 8) and multiple collision temperatures deduced in the region of the (4,0) band. The temperatures are approximately 2000 K for B–O_2 and 7000 K for B–N_2O under single collision conditions. If we assume that these temperatures reflect the temperatures of ground state vibrational levels isoergic with the (4,0) band, using the data in Table I ($B_{v''=17}$), we consider the rotational population distribution and determine $K'_{max}\approx 21$ at 2000 K and $K''_{max}\approx 40$ at 7000 K.[30] At 600 K, the temperature characterizing the multiple collision scans K''_{max} should be approximately 12. These values of K''_{max} are consistent with both the single and multiple collision features characterizing the region of the (4,0) band. If $K''_{max}\approx 21$ for the B–O_2 system, this will facilitate ready observation of the collisional transfer which must be induced by a long range BO–O_2 interaction. The B–N_2O system, while being characterized by a much higher K''_{max}, should still possess substantial population in levels $K''\approx 19$–22.

B + N_2O–Single vs multiple collision spectra: The (4,0) band

The population of vibrational levels in excess of BO $A\,^2\Pi$, $v'=3$ taxes the exothermicity of the B–O_2 reaction whereas such levels are energetically easily accessible to the much more exothermic B–N_2O reaction. If we consider the extension of our single collision studies to multiple collision conditions, rotational relaxation is expected to quickly delete the possibility of substantial V–E collisional energy transfer in the B–O_2 system.[37] However, in extending the B–N_2O system to higher pressure, rotational relaxation can provide a source of molecules in the appropriate ground state levels (relaxation from $K''_{max}\approx 40$ to $K''\approx 21$). In this sense it is appropriate to consider the expression obtained upon substitution of the basis functions (16) into the rate expression (17):

$$K^{1/2}_{X\text{–}A} \propto c^2\langle J'|\langle v'|A\,^2\Pi|V|X\,^2\Sigma^+|v''\rangle|J\rangle - d^2\langle J'|\langle v''|X\,^2\Sigma^+|V|A\,^2\Pi|v'\rangle|J\rangle$$

TABLE II. Spectral features characterizing the rapid energy transfer BO($^2\Sigma^+$, $v''=17$) → BO($A\,^2\Pi_{1/2}$, $v'=4$).

Observed peak wavelength (Å)	Frequency at maximum (cm^{-1}, vac)	Calculated frequency (cm^{-1}) and assignment	Δ (cm^{-1})
3521	28 392.9	28 391, $R'(J=19.5)$	1.9
3529	28 328.5	28 329.9, $Q'(J=19.5)$	−1.4
3532	28 304.6	28 310.8–28 293.8, $R_2(19.5\text{–}20.5)$	−8
(3541)	(28 232.5)	28 224.8–28 236.2, $Q_2(19.5\text{–}20.5)$	~6
3546	28 194.3	28 181.3–28 203.7, $P_2(19.5\text{–}20.5)$	~9

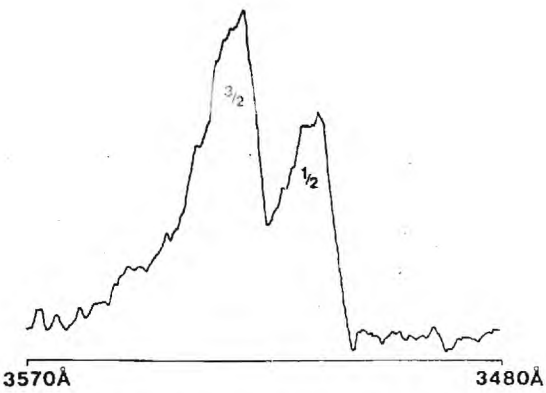

FIG. 13. Scan of emission spectrum for the multiple collision reaction $B+N_2O+Ar \rightarrow BO^*+N_2+Ar$ in the region of the BO $A\,^2\Pi$–$X\,^2\Sigma^+$ (4, 0) band. Emission from both the $A\,^2\Pi_{3/2}$ and $A\,^2\Pi_{1/2}$ components is shown. See the text for discussions.

$$+cd\langle\langle J'|\langle v'|\langle A\,^2\Pi|V|A\,^2\Pi|v'\rangle|J\rangle$$
$$-\langle J'|\langle v''|\langle X\,^2\Sigma^+|V|X\,^2\Sigma^+|v''\rangle|J\rangle\rangle\ . \qquad (19)$$

The terms in braces are off diagonal in J only and consequently represent $R \rightarrow R$ processes within the manifolds $|A\,^2\Pi\rangle|v'\rangle$ and $|X\,^2\Sigma^+\rangle|v''\rangle$. The remaining matrix elements are off diagonal in all three variables and correspond to electronic quenching processes, all of which are expected to be relatively slow.

The expression (19) demonstrates the close correlation between the V–E collisional transfer process and expected rotational relaxation in the $A\,^2\Pi$ and $X\,^2\Sigma^+$ manifolds. At low pressure, the potential V inducing relaxation will be dictated by the nature of O_2–BO or N_2O–BO interactions.[38] As the argon pressure is increased, however, a strong component of the potential should result from the dipole–induced dipole interaction between BO and argon.[39]

In Fig. 13, we depict a slow scan (0.2 Å/s) of the BO $A\,^2\Pi$–$X\,^2\Sigma^+$ (4, 0) band observed under multiple collision conditions. This spectrum, which results from the $B-N_2O$ metathesis, is not characterized by the triplet of distinct features observed under single collision conditions. Rather, we observe two sharp bands corresponding to emission from the $^2\Pi_{1/2}$ and $^2\Pi_{3/2}$ components. The (4, 0) band does, however, display an anomalous behavior when compared to the other features (Fig. 4) observed under multiple collision conditions. As noted previously, the $^2\Pi_{3/2}$ and $^2\Pi_{1/2}$ emission intensities and hence transition moments appear to differ, the ratio varying from ~1.2 to ~1.6 as the background pressure is raised from 10^{-4} to 1 Torr. Under multiple collision conditions, with one exception, the $^2\Pi_{3/2}/^2\Pi_{1/2}$ ratio is close to 1.6, varying from 1.56 to 1.63 for the $v'=0$–3, 5–9 emission features. In sharp contrast, the $^2\Pi_{3/2}/^2\Pi_{1/2}$ ratio is 1.44 for the (4, 0) band. Indeed, Fig. 6 demonstrates that the $^2\Pi_{1/2}$ population distribution goes through a maximum at $v'=4$. The most logical explanation for this deviation is again collision induced energy transfer via the process (7). The fact that t' e is no evidence for the triplicate of features observ at 10^{-4} Torr can be explained through a simple seque e invoking rotational relaxation. Consider the transfer process (7) followed by

$$BO(A\,^2\Pi,\ v'=4,\ J'=18.5\text{–}21.5)+Ar \rightarrow BO(A\,^2\Pi,\ v'=4,$$
$$J'=\text{randomized})+Ar\ . \qquad (20)$$

A collision, even at long range,[1(c)] between Ar and BO will liberate sufficient energy ($KT_{300\,K}=208\ cm^{-1}$) so as to randomize the rotational distribution resulting from the original BO $X \rightarrow A$ energy transfer.

Temperature dependence of chemilumescent emission

We have considered the temperature dependence for the chemiluminescent emission from the single collision $B-O_2$ and $B-N_2O$ reactions. The focus of these studies has been primarily the region of the (3, 0) and (4, 0) $A\,^2\Pi$ emission bands. The extensive calibration procedures used in previous studies[40,41] were not employed here since we wished only to establish reaction of ground state $B(^2P)$ atoms[42] generated via either vaporization or sublimation. Further, more refined studies will represent a future effort in our laboratory. A representative example of data from the current temperature dependent studies is presented in Fig. 14. In the figure,

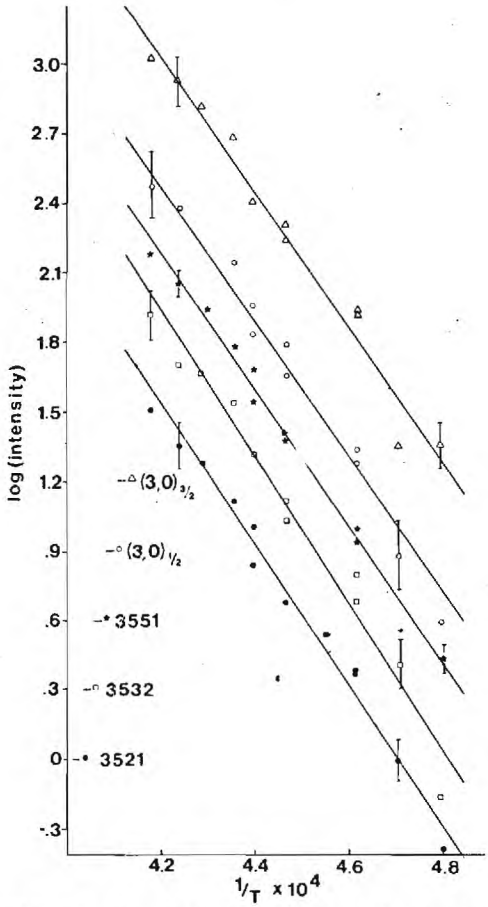

FIG. 14. Temperature dependence for the reaction $B+O_2 \rightarrow BO^*+O$. Logarithm of relative chemiluminescent intensity versus the reciprocal of the boron source temperature at the orifice of the source for several features in the region of the BO $A\,^2\Pi$–$X\,^2\Sigma^+$ (3, 0) and (4, 0) bands. The horizontal dashes preceding the label legends indicate the zero lines for the respective plots. Note the correspondence with Fig. 9 and 10. See the text for discussion.

TABLE III. Slope heats for boron atom production (Fig. 14).[a]

Feature monitored [λ(Å)]	$\Delta H_{sublimation}$ (upper bound—kcal/mol)[b]
3521 Å (4,0)[c]	143.8 ± 7.0
3532 Å (4,0)[c]	149.1 ± 7.9
3551 Å (4,0)[c]	140.4 ± 4.6
$(3,0)_{1/2}$[d]	139.4 ± 11.1
$(3,0)_{3/2}$[d]	138.3 ± 7.6

[a]Data obtained from $B + O_2 \rightarrow BO^* + O$.
[b]Rigorous upper bound to $\Delta H_{sublimation}$ determined from addition of slope heat determined from Fig. 4 added to RT_B over the temperature range of the experiment—see text for discussion.
[c]BO $A\,^2\Pi$–$X\,^2\Sigma^+$ emission feature resulting from rapid energy transfer.
[d]BO $A\,^2\Pi$–$X\,^2\Sigma^+$ emission features corresponding to $\Omega = 3/2$ and 1/2 components of $A\,^2\Pi$ state.

we plot $\log I$ versus $1/T_B$, where I is the chemiluminescent intensity and T_B is the beam (crucible) temperature. The data was collected in the region of the (3, 0) and (4, 0) bands at the wavelengths indicated in the figure. There is a direct correlation between Fig. 14 and Figs. 9 and 10. The slope and linearity of the plots in Fig. 14 indicates that the reactions are first order in boron flux. Recently, a relation between the temperature dependence of the chemiluminescent intensity and the parameters of a beam–gas experiment has been formulated.[40] It is

$$-R\,\frac{d(\ln I)}{d(1/T_B)} = \Delta H - RT_B + E_A\,\frac{d(1/T_{eff})}{d(1/T_B)}\ , \qquad (21)$$

where E_A is the Arrhenius activation energy for the formation of the product whose chemiluminescence is monitored, ΔH is the enthalpy of sublimation or vaporization for the metal atom reacting to produce the observed chemiluminescence, and

$$T_{eff} = (m_B\,T_G + m_G\,T_B)/(m_G + m_B)\ , \qquad (22)$$

where T_G is the temperature of the gas O_2 or N_2O, and m_B and m_G are the masses of the beam atoms and gas molecules, respectively. Equation (21) may take into account the effect of low-lying electronic states,[16(a)] but generally considers the reaction of only ground state metal atoms. It may also take into account the reaction of dimers. An analysis of the slopes in Fig. 14 yields the data presented in Table III. If we consider that the lowest excited state of the boron atom $B\,^4P$ lies ~ 29 000 cm^{-1} (83 kcal/mol)[42] above the ground state and that the B_2 dissociation energy is 67 kcal/mol,[43] the data in Table III indicate that we have observed the reaction of gaseous boron atoms sublimed from the solid. The heat of sublimation across the temperature range of the experiment varies from 134.8 to 134.0 kcal/mol.

DISCUSSION

Further characterization of rapid V-E transfer

Throughout our previous discussion we have contrasted spectra observed for the B–O_2 and B–N_2O reactions under single [$(0.6–12)\times10^{-4}$ Torr] and multiple (1–2 Torr) collision conditions. The term single collision is slightly misleading in the present study since we have observed rapid V–E collisional transfer at pressures as low as 6×10^{-5} Torr; however, the majority of the emission which is depicted in Figs. 1 and 3 results from the direct Reactions (1) and (2), i.e., most of the observed emission is due to excited state formation followed by emission of a photon long before subsequent collisions can occur. This becomes apparent through combination of the data obtained by Huie *et al.*[14] and our own computer simulations of the observed spectra. Huie *et al.* determined radiative lifetimes of 131 ± 15 and 103 ± 6 ns for the $v' = 1$ and 2 levels, respectively, of BO $A\,^2\Pi$. They probed levels which should be associated primarily with the $\Omega = 3/2$ component. These measured lifetimes should be compared to the mean time between collisions at 10^{-4} Torr which is on the order of milliseconds. Hence, emission of a photon occurs long before subsequent collision. This situation need not exist for molecules formed in the BO $X\,^2\Sigma^+$ ground electronic state. The boron system is similar to most chemiluminescent reactions in that the quantum yield for fluorescence corresponds to a fraction of the total product molecules formed in reaction.[10] Therefore, most product molecules are formed in the ground electronic state. The nature of vibrational transition probabilities is such that the time scale for an infrared transition can be comparable to the mean time between collisions at 10^{-4} Torr. There are two effects which must be considered: (1) A molecule in the 17th vibrational level of the ground electronic state could be expected to have a lifetime for a $\Delta v = 1$ transition an order of magnitude shorter (10^{-4}–10^{-5} s)[45] than the typical mean time between collisions. (2) A molecule in a high state of vibrational excitation presents a much larger effective target and therefore its effective collision frequency is expected to be much higher than the typical collision frequency.[1,48] If we correlate these two factors, it is not surprising that rapid intramolecular collisional transfer can be induced between strongly interacting highly excited levels in an ostensibly "diffuse" molecule.

In direct analogy to recent studies of rapid E–E transfer, the rate of collision induced V–E transfer must significantly exceed the gas kinetic collision rate. We have previously described a method for assessing the transfer rate which in the present study corresponds to $K_{X\text{-}A}$. If we study the relative intensities of those levels associated with the perturbed $A\,^2\Pi$ ($v' = 4$) and $X\,^2\Sigma^+$ ($v'' = 17$) states as a function of pressure, we may derive the expression[1(a),(c)]

$$\frac{I_-}{I_+} = \frac{A_-}{A_+}\left[1 + \frac{K_+}{K_{X\text{-}A}[P_c]}\right]\ , \qquad (23)$$

where I_- corresponds to the intensity of the perturbed $X\,^2\Sigma^+$ feature, I_+ the intensity of the perturbed $A\,^2\Pi$ feature, A denotes the electronic plus vibrational transition probability, K_+ is the radiative lifetime of the $A\,^2\Pi$ state, and P_c corresponds to the background pressure of the respective collider gas. The ratio I_-/I_+ varies with pressure and a plot of this ratio yields $K_{X\text{-}A}$ (slope) and A_-/A_+ (intercept).[47] We have begun stud-

ies of this pressure dependence for several chemiluminescent reactions including $B + O_2$, N_2O, NO_2, O_3, and ClO_2. The desire is to futher characterize the $B-O_2$ and $-N_2O$ systems and to compare observed effects in these systems with metatheses involving NO_2, ClO_2, and O_3 followed by subsequent product interaction with these collision partners. Among other factors, we are concerned with the effect of perturbed level separation, the range of interaction, and its correlation with the polarizabilities and effective dipole moments of collision partners. For example, we are currently attempting to compare the nature of energy transfer observed in the single collision $B-NO_2$ metathesis with the $B-O_2$ and $B-N_2O$ systems. These studies are complicated by extensive BO_2^* formation in the NO_2 system; however, it does appear that the collisional transfer in the $B-NO_2$ system is more pronounced. It is not surprising that NO_2 represents a more effective collision partner, for its dipole moment considerably exceeds that of N_2O (and O_2!). On the microscopic scale, one expects some dipolar–dipolar interactions between BO and NO_2 even among rapidly rotating collision partners. The dipole–dipole interaction is expected to lead to very large collision and rotational inelastic cross sections, the interaction being much stronger than the pronounced inductive effects which dominate ScO–Ar[1(c)] and AlO–Ar[1(a),(b)] collisions.

In view of the discussion in the fourth section, it will be appropriate to assess carefully the magnitude of V–E collisional transfer and its relation to rotational relaxation in the $A\,^2\Pi$ and $X\,^2\Sigma^+$ manifolds. The N_2O system will represent a good example. Here we have begun studies as a function of background pressure in a region where rotational relaxation produces a temperature less than $T_{rot} = 7000$ K (temperature observed in single collision system) but greater than 2000 K (temperature corresponding to maximum population in that ground state rotational level which transfers most efficiently). It seems apparent that these studies will also involve coincidental laser probing of the ground state.

Vibrational and rotational distribution

The BO^* $A\,^2\Pi$ vibrational distributions observed in the current studies are definitely non-Boltzmann for both the O_2 and N_2O reactions. Our assessment for the $B-O_2$ system would appear to differ from the analysis of Brzychcy *et al.*,[10] who indicate that the BO^* emission is Boltzmann at 1950 K. Employing a Boltzmann distribution at 1950 K, we have been unsuccessful in our attempts to duplicate either the experimental emission spectrum in Fig. 1 or the spectrum presented by Brzychey *et al.*[10] It does appear that our vibrational distribution can be approximated by a Boltzmann distribution at 2550 K.

The rotational temperature distributions observed in the present studies should be contrasted with those determined for ScO^* $B\,^2\Sigma^+$[1(c)] produced in the $Sc-NO_2$ reaction. Here the entire manifold of vibrational bands was well fit by a rotational temperature of 6000 K.[1(c)] The results for both studies indicate a negative correlation between the vibrational and rotational excitation[48] of the freshly formed metal oxide product. It will be interesting to characterize the nature of the rotational temperature distribution as a function of varying reactive impact parameters for product formation.[36,49] It seems apparent that the rotational distributions in many of these systems signal the presence of intriguing dynamic constraints.[11,16(b)]

Energy balance in the $B-O_2$ reaction

Under single collision conditions, the $B-O_2$ reaction leads to the population of five vibrational levels in the $A\,^2\Pi$ state of BO while only three levels are observed in the multiple collision studies. Under single collision conditions the available energy to populate BO excited states is

$$E_{Available} = [D_0^0(BO) - D_0^0(O_2)] + [E_{int}(B) + E_{int}(O_2) + E_T^i] , \quad (24)$$

where $E_{int}(B)$ and $E_{int}(O_2)$ are the internal energies of boron and O_2 evaluated in a manner previously described,[50] and E_T^i is the relative translational energy of the reactants boron and O_2 evaluated as $\frac{3}{2} kT_{eff}$ [T_{eff} defined in Eq. (22)] also as previously described. The boron beam ranges in temperature from 2175 to 2675 K and O_2 is assumed to be at room temperature. If we take the mass spectrometric value for $D_0^0(BO) = 8.3 \pm 0.05$ eV[51] and $D_0^0(O_2)$[52] $= 5.12$ eV, we find

$$E_{Available} = (25\,653 \pm 403\ cm^{-1}) + (2015-2405\ cm^{-1}) , \quad (25)$$

where the range in the second parenthesis corresponds to the temperature range of the boron source. The energy available to populate the $A\,^2\Pi$ state is

$$E_{Available}(A\,^2\Pi) = (25\,653 \pm 403 - T_0) + (2015-2405\ cm^{-1})$$
$$= (2007 \pm 403) + (2015-2405\ cm^{-1}) ,$$

where $T_0(A\,^2\Pi) = 23\,646\ cm^{-1}$.

Based upon the vibrational constants given in Table I, the available energy is sufficient to easily populate three vibrational quanta and very close to the precise energy required to populate four vibrational levels. In equating the translational energy to $\frac{3}{2} kT_{eff}$,[50] one considers an average over boron–O_2 encounters, averaging over the translational energy of the beam. In the present study it appears that emission from BO $A\,^2\Pi$, $v' = 4, 5$ results in large part from the reaction of boron atoms in the high energy tail of the translational energy distribution. Put another way, the population of BO $A\,^2\Pi$, $v' = 5$ requires the reaction of boron atoms with an effective translational temperature $T_{eff} = 3800$ K. These results are consistent with the data in Table III, which indicates that there is a significant activation energy for formation of BO $A\,^2\Pi$. Such an activation energy will force the reaction of boron atoms at higher energies.

If the boron atoms which undergo reaction are thermalized at higher pressure, the contribution to the available energy in Eq. (24) decreases by virtue of a decrease in the energy sum corresponding to the second brace. If the boron atoms are thermalized to 600 K, the energy sum $E_T^i + E_{int}(B)$ reduces to 560 cm^{-1} and there is only sufficient energy to populate two vibrational quanta in

the $A\,^2\Pi$ state. Hence, we observe strong emission from $v' = 0, 1, 2$ and only weak emission from $v' = 3$.

Varying intensities for $\Omega = 3/2$, $\Omega = 1/2$ emission

The observation of varying intensities for the $A\,^2\Pi_{3/2}$–$X\,^2\Sigma^+$ and $A\,^2\Pi_{1/2}$–$X\,^2\Sigma^+$ emission systems is striking as is the apparent correlation of their relative intensities with the pressure dependence of the $A\,^2\Pi_{3/2}$ radiative lifetime. The result may be rationalized by assuming a substantial $^2\Pi_{1/2}$–$^2\Sigma^+_{1/2}$ excited state-ground state mixing which effectively decreases the $A\,^2\Pi_{1/2}$ transition moment relative to that of the $A\,^2\Pi_{3/2}$ state. The effect would appear to be similar to that in NO_2, where excited state–ground state mixing produces anomalously long radiative lifetimes.[53] In view of the effects observed in the present experiments, we suggest the careful probing of BO $A\,^2\Pi$ lifetimes in several regions of the spectrum in order to assess directly the possible effects of $^2\Pi_{1/2}$–$^2\Sigma^+_{1/2}$ mixing on the radiative processes in this system.

Note added in proof: Clynne and Heaven (Chem. Phys., in press) have recently carried out new measurements of the BO A–X radiative lifetime. These authors determine a radiative lifetime, $T_R \sim 1.7_6 \pm 0.1_3\ \mu s$ for BO $A\,^2\Pi$, $11 \geq v' \geq 0$, in disagreement with the results of Huie *et al.* (Ref. 14). Clynne and Heaven also determine transition moments, $|R_e|^2$, for vibrational levels $v' = 0$, 4, 7, 9, 10, and 11 which, in combination with the data presented in the current study, may show significant trends. The transition moment appears to be significantly smaller for $v' = 4$ and 9 relative to $v' = 0$, 7, 10, and 11. Not only do these results correlate well with the strong A–X spin–orbit mixing ($A\,^2\Pi$, $v' = 4$ – $X\,^2\Sigma^+$, $v'' = 17$) evidenced in the study reported here, but also RKR curves generated in the present study indicate (see also Fig. 7) a crossing of the $A\,^2\Pi$ and $X\,^2\Sigma^+$ states between $v' = 8$ and $v' = 9$ (closer to $v' = 9$). It may also be significant that the transition moments for $v' = 10$ and 11 are slightly smaller than for those for $v' = 0$ and 7.

ACKNOWLEDGMENT

It is a pleasure to acknowledge the probing commentary of Professor W. H. Eberhardt on the first draft of this manuscript.

[1](a) D. M. Lindsay and J. L. Gole, J. Chem. Phys. **66**, 3886 (1977); (b) M. J. Sayers and J. L. Gole, J. Chem. Phys. **67**, 5442 (1977); (c) J. L. Gole and S. A. Pace, J. Chem. Phys. **73**, 836 (1980).

[2]See, for example, Air Force Systems Command Research Planning Guide (Research Objectives), 1 May 1978.

[3]S. P. Davis, Air Force Weapons Lab, Kirkland Air Force Base (private communication); Air Force Office of Scientific Research, Contractors Meeting—Chemical Laser Program, May 1977; H. Michels, United Technologies Inc. (private communitcation).

[4]S. B. Oblath and J. L. Gole, Combust. Flame **37**, 293 (1980) and references therein; S. Rosenwaks, R. E. Steele, and H. P. Broida, J. Chem. Phys. **63**, 1963 (1975) and references therein; J. L. Gole and R. N. Zare, J. Chem. Phys. **57**, 5331 (1972) and references therein; E. Murad and W. Swider, Geophys. Res. Lett. **6**, 929 (1979) and references therein; E. Murad, J. Geophys. Res. **83**, 5525 (1978).

[5]J. Parson (private communication).

[6]R. C. Estler and R. N. Zare, J. Am. Chem. Soc. **100**, 1323 (1978).

[7]U. C. Sridharan, T. G. Digiuseppe, D. L. McFadden, and P. Davidovits, J. Chem. Phys. **70**, 5422 (1979).

[8]U. C. Sridharan, D. L. McFadden, and P. Davidovits, J. Chem. Phys. **65**, 5373 (1976).

[9]S. P. Tang, N. G. Utterback, and J. F. Friichtenicht, J. Chem. Phys. **64**, 3833 (1976).

[10]A. Brzychcy, J. Dehaven, A. T. Pringel, and P. Davidovits, Chem. Phys. Lett. **60**, 102 (1978).

[11]See, for example, J. L. Gole, D. R. Preuss, and C. L. Chalek, J. Chem. Phys. **66**, 548 (1977); J. L. Gole and C. L. Chalek, J. Chem. Phys. **65**, 2845 (1976); W. Schwenz and J. M. Parson, J. Chem. Phys. **73**, 259 (1980). There are several references to other work in these articles and throughout following references.

[12]Gary J. Green and J. L. Gole, Chem. Phys. **46**, 67 (1980)—see also Refs. 1.

[13]See, for example, (a) R. S. Mulliken, Phys. Rev. **25**, 119 and 259 (1925); F. A. Jenkins, Proc. Natl. Acad. Sci. (U.S.A.) **13**, 496 (1927); (b) A. Elliott, Proc. Acad. Sci. Amsterdam **33**, 644 (1930); Z. Phys. **67**, 75 (1931); Proc. Acad. Sci. Amsterdam **38**, 736 (1935); Proc. Phys. Soc. London **45**, 627 (1933); (c) F. A. Jenkins and A. McKeller, Phys. Rev. **42**, 464 (1932).

[14]R. E. Huie, N. J. T. Long, and B. A. Thrush, Chem. Phys. Lett. **55**, 404 (1978).

[15]J. L. Gole, Annu. Rev. Phys. Chem. **27**, 525 (1976).

[16]Single collision: (a) L. H. Dubois and J. L. Gole, J. Chem. Phys. **66**, 779 (1977); (b) C. L. Chalek and J. L. Gole, Chem. Phys. **19**, 59 (1977). Multiple collision: (c) J. B. West, R. S. Bradford, J. D. Eversole, and C. R. Jones, Rev. Sci. Instrum. **46**, 164 (1975). (d) C. R. Jones and H. P. Broida, J. Chem. Phys. **60**, 4369 (1974).

[17]G. J. Green, A. W. Hanner, J. L. Gole, and D. M. Lindsay (in preparation).

[18]S. B. Oblath and J. L. Gole, J. Chem. Phys. **70**, 581 (1979). We have found that boron also reacts with water vapor to yield chemiluminescence, the reaction $B + H_2O \rightarrow BO + H_2$ being more exothermic than $B + O_2$.

[19](a) A. Lagerqvist, N. E. L. Nelsson, and K. Wigartz, Ark. Fys. **13**, 379 (1958); (b) A. A. Malteev, D. I. Kataev, and V. M. Tatevskii, Fiz. Probe Spectrosk. Acad. Nauk. SSSR **1**, 194 (1962); (c) A. A. Maltsev and D. I. Kataev, Vestn. Mosh. Univ. Ser. II **22**, 23 (1967); (d) T. M. Dunn and L. Hanson, Can. J. Phys. **57**, 1657 (1969).

[20]The programs used for these computations were written by Dr. Brian G. Wicke.

[21]R. N. Zare, J. Chem. Phys. **40**, 1934 (1964) and references therein.

[22]P. A. Fraser, Can. J. Phys. **32**, 515 (1954).

[23]Intensity factors were taken from L. T. Earls, Phys. Rev. **48**, 423 (1935).

[24]This phenomenon has been observed by a number of authors, the first evidence being the BaO $A\,^2\Pi$ rotational temperatures observed by C. D. Jonah, Ch. Ottinger, and R. N. Zare, **56**, 263 (1972).

[25]With the exception of $A\,^2\Pi_{1/2}$, $v' = 1, 4$ the $^2\Pi_{3/2}/^2\Pi_{1/2}$ ratio varied from 1.16 to 1.23 under single collision conditions and 1.56 to 1.63 under multiple collision conditions. Further investigations of the transition moment behavior are underway in our laboratory.

[26]Ch. Ottinger and R. N. Zare, Chem. Phys. Lett. **5**, 243 (1970); see also Ref. 24.

[27]J. L. Gole, D. R. Preuss, and C. L. Chalek, J. Chem. Phys. **66**, 548 (1977).

Data privately communicated by Dr. Harvey Michels proved invaluable. His calculated potential curves for BO demonstrate that no metastable excited states are to be found in the vicinity of the $v' = 4$ level.

[29]This behavior is reminiscent of early studies by Broida and co-workers; see N. H. Kiess and H. P. Broida, J. Mol. Spectrosc. 7, 194 (1961); H. E. Radford and H. P. Broida, J. Chem. Phys. 38, 664 (1963).
[30]G. Herzberg, *Spectra of Diatomic Molecules* (Van Nostrand-Reinhold, New York, 1950). Note that the rotational constant used here is somewhat approximate since we have not taken account of the perturbation.
[31]J. Schamps, Chem. Phys. **2**, 352 (1973).
[32]M. F. Guest and V. R. Saunders, Mol. Phys. **28**, 819 (1974).
[33]A similar approach has been taken in Refs. 1 and also pertains to collision induced predissociation by van der Waal's pertrubations. See J. E. Selwyn and J. I. Steinfeld, Chem. Phys. Lett. **4**, 217 (1969).
[34]J. T. Hougen, Natl. Bur. Stand. Monogr., 115 (1970).
[35]Equation (17) is an expression of the "Fermi golden rule." In the present context, for collisions with O_2, V arises from a combination of dipole induced dipole and dispersion forces. Because of its small dipole moment, collisions with N_2O may be characterized by a somewhat more effective V (dipole–dipole interaction).
[36]James L. Gole and C. L. Chalek, J. Chem. Phys. **65**, 4384 (1976).
[37]For a typical rotational distribution, the population in levels $J > J_{max}$ drops off rapidly as exponential factors begin to dominate. This is to be contrasted with the slow rise in rotational level population for $J \leq J_{max}$. This behavior will have a profound effect on the number of molecules available to collisional transfer as rotational relaxation lowers the rotational temperature characterizing the $v'' = 17$ band.
[38]W. H. Flygare, Acc. Chem. Res. **1**, 121 (1968).
[39]R. D. Levine and R. B. Bernstein, *Molecular Reaction Dynamics* (Oxford, New York, 1974).
[40]D. R. Pruess and J. L. Gole, J. Chem. Phys. **66**, 2994 (1977); J. L. Gole and D. R. Preuss, J. Chem. Phys. **66**, 3000 (1977).
[41]C. L. Chalek and J. L. Gole, "Beam–gas chemiluminescent reactions of group IIIB metals and halogen molecules—evidence for selective excited state emission (in preparation).
[42]C. E. Moore, Natl. Stand. Ref. Data Ser. Natl. Bur. Stand. **35** (1971).
[43]G. Verhaegen, P. E. Stafford, and J. Drowart, J. Chem. Phys. **40**, 1622 (1964).
[44]R. Hultgren, P. D. Desai, D. T. Hawkins, M. Gleiser, K. K. Kelley, and R. D. Wagman, *Selected Values of the Thermodynamic Properties of the Elements* (American Society for Metals, Metals Park, 1975).
[45]The lifetime for vibrational transitions generally decreases with decreasing vibrational level separation and should decrease as one proceeds up the vibrational manifold for the ground electronic state.
[46]See, for example, D. J. Wren and M. Menzinger, Chem. Phys. Lett. **20**, 471 (1973).
[47]The determined intercept may be related to the expressions for the wave functions ψ_+ and ψ_- [expression (8)] and the level spacings [expression (9)] to yield the perturbation parameters, See Refs. 1(a), (c).
[48]Note that this is contrary to phase-space arguments. These negative correlations have been observed in many visible and infrared chemiluminescent studies.
[49]G. J. Green and James L. Gole, Chem. Phys. Lett. **69**, 45 (1980).
[50]P. J. Dagdigian, H. W. Cruse, and R. N. Zare, J. Chem. Phys. **62**, 1824 (1975).
[51]O. M. Uy and J. Drowart, High Temp. Sci. **2**, 293 (1970).
[52]A. G. Gaydon, *Dissociation Energies and Spectra of Diatomic Molecules* (Chapman and Hall, London, 1968).
[53]There are numerous papers discussing anomalous lifetimes in NO_2; however, an explanation for the phenomenon was first proposed by A. E. Douglas, J. Chem. Phys. **45**, 1007 (1966).

A P P E N D I X H

CHEMILUMINESCENCE STUDY OF METHANE-FLUORINE COMBUSTION: OBSERVATION AND ANALYSIS OF HCF $\tilde{A}^1A'' - \tilde{X}^1A'$

(Chem. Phys. *52*, 461 (1980))

Chemical Physics 52 (1980) 385–395

CHEMILUMINESCENCE STUDY OF METHANE–FLUORINE COMBUSTION: OBSERVATION AND ANALYSIS OF HCF $\tilde{A}\,^1A''$–$\tilde{X}\,^1A'$

Rajendra I. PATEL ‡, Gerald W. STEWART #
Department of Chemistry, West Virginia University, Morgantown, WV 26506, USA
Kent CASLETON
Morgantown Energy Technology Center, United States Department of Energy, Morgantown, WV 26506, USA
James L. GOLE
Department of Chemistry, Georgia Institute of Technology, Atlanta, GA 30324. USA
and
John R. LOMBARDI
Department of Chemistry, The City College of the City University of New York, New York, NY 10031, USA

Received 9 April 1980

The chemiluminescent emission which results from excited state product formation upon the intimate mixing of CH_4 with F_2 is shown to be dominated by visible emission from $CH^*(A\,^2\Delta–X\,^2\Pi)$, $C_2^*(A\,^3\Pi_g–X\,^3\Pi_u)$, $HCF^*(\tilde{A}\,^1A''–\tilde{X}\,^1A')$ and vibrationally excited $HF^\dagger(X\,^1\Sigma^+)$. The corresponding reaction mixture $CD_4 + F_2$ produces the deutero analogs. This study represents the first observation of the HCF emission spectrum from a CH_4/F_2 flame. The observation of the HCF $\tilde{A}\,^1A''–\tilde{X}\,^1A'$ emission spectrum and the corresponding DCF system allows the unequivocal assignment of these visible transitions to a progression dominated by the excited state bending mode. Transitions $(0, v_2', 0) \rightarrow (0, 0, 0)$, $v_2' = 1–5$ for HCF and $v_2' = 2–6$ for DCF are observed. An analysis of the spectra yields the electronic and vibrational parameters $T_0 = 17274 \pm 6.8\ cm^{-1}$, $\omega_e = 1024 \pm 6.4\ cm^{-1}$, $\omega_e x_e = -7.7 \pm 1.2\ cm^{-1}$ for HCF and $T_0 = 17281 \pm 8\ cm^{-1}$, $\omega_e = 787.5 \pm 4.4\ cm^{-1}$, $\omega_e x_e = -3.86 \pm 0.5\ cm^{-1}$ for DCF. Each vibrational transition shows resolved K-type subbands characteristic of a near-symmetric rotor. Although this structure is highly perturbed for the entire HCF system, a partial rotational analysis has been obtained for two bands in the DCF spectrum. The derived rotational parameters are also consistent with the observation of the excited state bending mode.

1. Introduction

Recent studies of several hydride–halogen combustion mixtures have produced various unique or seldom studied free radicals in a high temperature combustion environment. Specific studies include gas–gas mixtures of B_5H_9 and B_2H_6 with F_2 [1], SiH_4 and Si_2H_6 with F_2, ClF and Cl_2 [2], GeH_4 with F_2 and Cl_2 [3], and N_2H_4 with F_2 and ClF [4]. These studies have led to the observation of emission spectra for the HBF, HSiCl, HGeCl, and HNF free radicals as well as several diatomic species. The observation of emission spectra for HAB radicals in the above systems has led to a reinvestigation of the methane–fluorine flame. Previous studies of the methane–fluorine flame report C_2^* and CH^* but no researchers have identified HCF^* as an emitting species [5–11]. In this paper, we report the observation of the HCF free radical and its deutero-analog in CH_4 and CD_4-fluorine flames. Several vibrational levels in the $\tilde{A}\,^1A''$ excited state of HCF and DCF have been observed. Many of these vibronic transitions show resolvable K-type subbands. A partial rotational analysis is given for two bands in DCF.

‡ Present address: Space Sciences Department, Washington University, St. Louis, MO 63130, USA.
# Center for Chemical and Environmental Physics, Aerodyne Research, Inc. Bedford, MA 01730, USA.

2. Experimental

The flame system is similar in design to that used in the study of silane–halogen chemiluminescence [2]. Reactions were carried out in a vacuum chamber at total pressures ranging from 0.5 to 5 Torr. A concentric nozzle arrangement [2] in which the effusing methane gas was bathed in excess fluorine confined the reaction zone to a few centimeters in diameter. The flow rates of the reactants and oxidants were measured by electronic mass flowmeters (Teledyne–Hasting), and the total pressure in the reaction chamber was monitored by a capacitance manometer (MKS Baratron, 0–100 Torr pressure transducer). The range of flow rates for fluorine was 10–200 sccm (standard cubic centimeters per minute at 20°C and 1 atm pressure) and that for methane was 5–50 sccm. Fluorescence from the reaction zone of the flame was focused onto the entrance slit of a 1.26 m Spex scanning monochromator (model 1269) operated in first order with an 1800 groove/mm grating blazed at 5000 Å. The aperture of the spectrometer was $f/9$ with a linear dispersion of 6.5 Å/mm. An RCA C31034 water cooled photomultiplier with a spectral response from 3000 Å to 9200 Å was attached to the exit slit of the spectrometer. The photon flux was measured using a Spex digital photometer (DPC2) in the photon counting mode and was output to a chart recorder to provide a tracing of the emission spectrum. The spectrometer was periodically calibrated with a mercury resonance lamp.

3. Results and discussion

3.1. Observed spectra

Fig. 1 shows a fast (10 Å/s) scan of the chemiluminescence in the region 4000–9000 Å which results from a $CH_4 + F_2$ mixture at a total pressure of 1.3 Torr. The principal emission features are the (0,0) band for the A–X transition of CH [12] at 4315 Å, a $\Delta v = 4$ sequence of HF vibrational–rotational transitions extending from 6500 Å to 9000 Å [13] and the $\tilde{A}(^1A'')$–$\tilde{X}(^1A')$ transition of HCF [14]. The dominant features in the HCF spectrum consist of several complex well separated bands extending from 4500 Å to beyond 7000 Å. The bands at shorter wavelength are more intense and the band contours are strongly degraded to the violet. Between 4500 Å and 5800 Å, these bands form a regular progression with a frequency interval on the order of 1000 cm^{-1}. In addi-

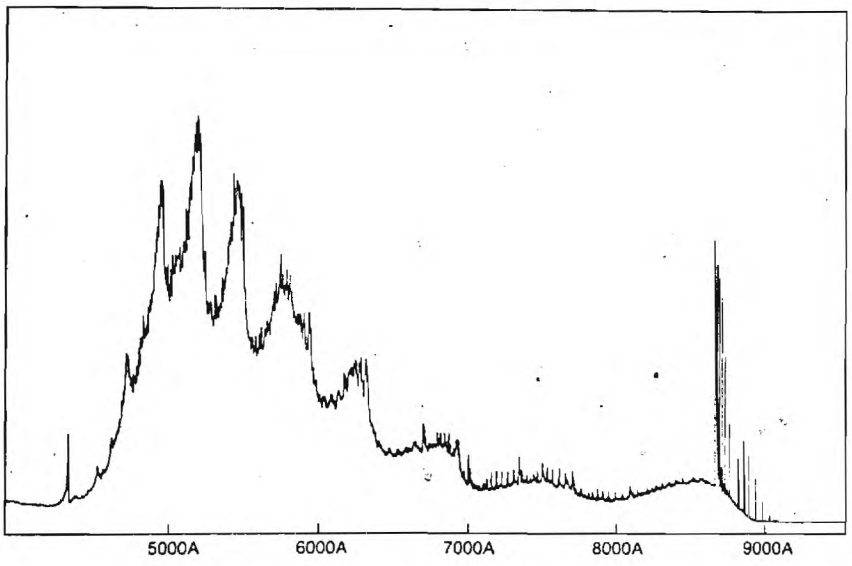

Fig. 1. Chemiluminescent spectrum observed for the methane–fluorine flame. $(F_2)/(CH_4) = 18$, $P_{total} = 1.3$ Torr. At wavelengths less than 4000 Å emission from CF_2 is observed.

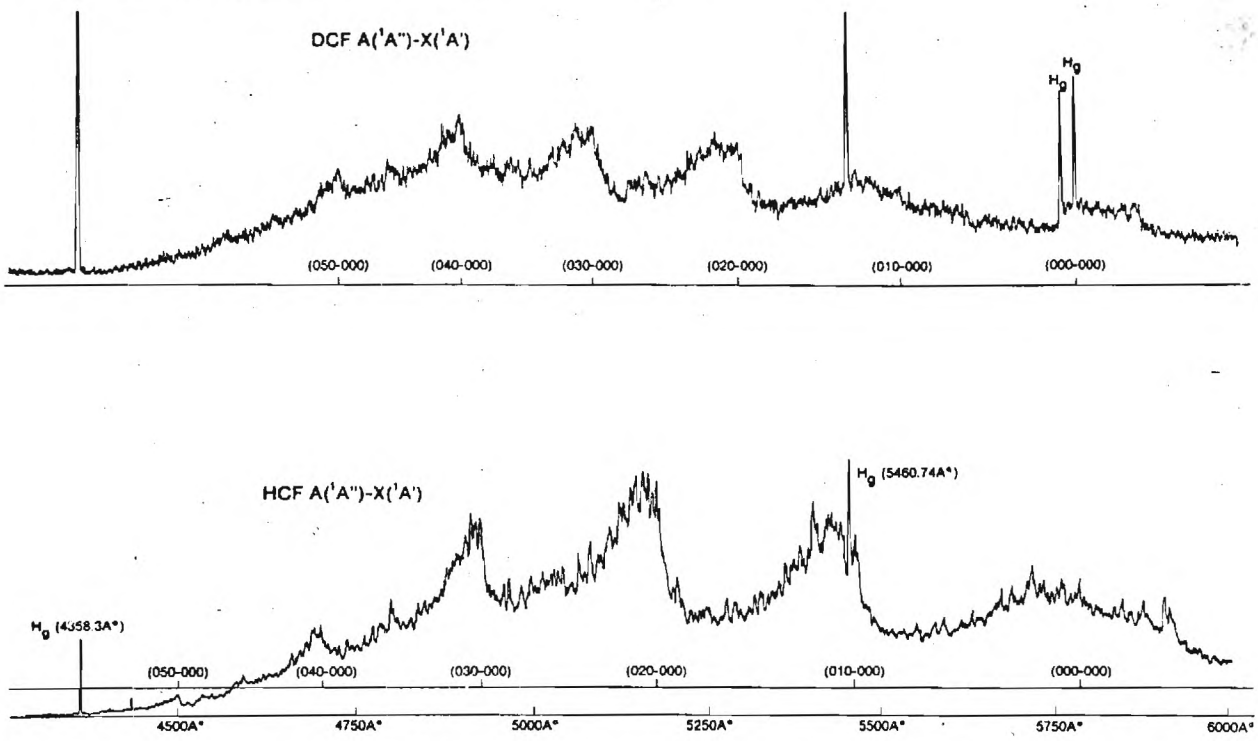

Fig. 2. HCF and DCF spectra in the region 6000–4300 A. The spectra are assigned to a progression in the excited state bending mode. See text for discussion.

tion to the bands shown in fig. 1, there is a continuum emission in the region 2200–4000 Å which correlates with the A–X transition of CF_2 [15]. The emission spectrum for HCF, which is discussed in more detail in a following section, can be correlated in part with the A–X [(0,1,0) ... (0,0,0)] band previously observed in absorption [14].

When CD_4 is used as the reactant, the resulting chemiluminescence spectrum for DCF displays the same qualitative features as that for HCF. Higher resolution spectra for HCF and DCF are shown in fig. 2. One observes a change in frequency spacing from $\approx$1000 cm^{-1} for HCF to $\approx$800 cm^{-1} for DCF.

The methane–fluorine flame emission shows considerable variation as a function of reactant flow rate and concentration. Differences can be observed when studying the change in emission as a function of both oxidant to fuel ratio and total pressure. The variation of the emission with changes in oxidant to fuel mole ratio at 2.3 Torr total pressure is shown in fig. 3. For

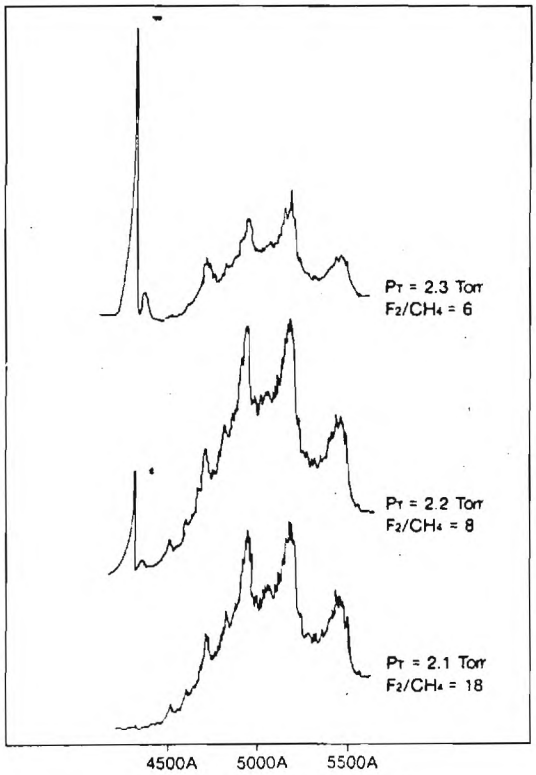

Fig. 3. The changing emission spectrum as a function of oxidant to fuel ratio. Parameters are quoted in the figure.

conditions involving large amounts of fluorine (high O/F ratio), the emission spectrum is predominantly due to HCF while the (0,0) band of the CH A–X transition (4300 Å) is barely visible. As the oxidant to fuel ratio decreases, the CH (0,0) band becomes more intense while the HCF emission is diminished. Sharp spectral features due to the C_2 Swan bands also begin to appear. The emission spectrum was also studied as a function of total pressure by holding the O/F mole ratio constant and increasing the total flow rate. For a constant O/F mole ratio, HCF emission predominates at low total pressures. In summary, HCF emission is favored by high O/F mole ratios and low total pressures whereas CH and C_2 emissions are favored by low O/F mole ratios and high total pressures.

3.2. Spectroscopy of HCF

There has been only one previous observation of the HCF spectrum. Merer and Travis [14] observed an absorption spectrum for HCF in the region 4300–6000 Å when photolyzing dibromofluoromethane. The HCF spectrum was tentatively assigned to a single progression of highly coupled and perturbed bands. A high resolution rotational analysis of the less severely perturbed bands [(0,0,0) ← (0,0,0) and (0,1,0) ← (0,0,0)] shows them to be of type-C and to involve a molecule which is nonlinear in both the upper (127°) and lower (102°) electronic states of the transition. The large change in bond angle which accompanies the transition leads to axis switching effects and the appearance of Q branches (^sQ, ^qQ, ^rQ corresponding to $\Delta K = 0, \pm 2$ subbands) in addition to those obeying the ordinary type-C selection rule ($\Delta K = \pm 1$). No isotopic labeling was reported in the Merer and Travis study.

In this work, we have observed emission spectra in both CH_4–F_2 and CD_4–F_2 flames. Observed spectral features can be assigned to the species HF, DF, CH, CD, C_2, HCF, and DCF (see also fig. 1). Since the spectra for HF, CH, and C_2 (Swan bands) have been thoroughly investigated, we concentrate here on the emission from HCF and DCF. The current study represents the first observation of emission spectra for this compound and the first isotopic study of the observed transition. Vibrational and electronic parameters for the $\tilde{A}\,^1A''$ state of both HCF and DCF are presented in tables 1 and 2. Lower resolution spectra are depicted in fig. 2. The spectra are clearly dominated by a progression which we assign to the excited state bending mode. The current data considerably extend the vibrational analysis of Merer and Travis [14]. We observe and assign the additional transitions $(0, v_2', 0) \rightarrow (0, 0, 0)$ where $v_2' = 2$ to 5 for HCF and 2 to 6 for DCF. The assignments are made on the basis of the substantial spectral shift upon deuteration, the

Table 1
Vibrational parameters for the $\tilde{A}\,^1A'$ state of HCF

Assignment	ν_{meas} (cm^{-1}) [a]	ν_{calc} (cm^{-1})	$\nu_{meas} - \nu_{calc}$ (cm^{-1})
010–000 [c]	18282 ± 2 [c]	18290.2	8.2 [c]
020–000	19300 ± 2	19292.4	−7.6
030–000	20280 ± 3	20278.3	−1.7
040–000	21243 ± 3	21248.8	+5.8
050–000	22206 ± 3	22203.8	−2.2
010–010	16915 ± 2		
000–010	15839 ± 2		
	T_0 = 17274 ± 6.8 cm^{-1}		
	ω_e = 1024 ± 6.4 cm^{-1} [a,b]		
	$\omega_e x_e$ = −7.7 ± 1.2 cm^{-1} [a,b]		

[a] Quoted errors correspond to accuracy of measurements based on 0.5 Å resolution for a typical scan.
[b] Errors estimated for ω_e and $\omega_e x_e$ correspond to one standard deviation from the mean.
[c] Also observed by Merer and Travis [14].

Table 2
Vibrational parameters for the $\tilde{A}\,^1A'$ state of DCF

Assignment	$\overline{\nu}_{meas}$ (cm^{-1}) [a]	$\overline{\nu}_{calc}$ (cm^{-1})	$\nu_{meas} - \nu_{calc}$ (cm^{-1})
020–000	18851 ± 2	18850.1	−0.9
030–000	19616 ± 2	19618.3	+2.3
040–000	20380 ± 3	20378.7	−1.3
050–000	21132 ± 3	21131.4	−0.6
060–000	21876 ± 3	21876.5	+0.5
	T_0 = 17281 ± 8 cm^{-1}		
	ω_e = 787.5 ± 4.4 cm^{-1} [a,b]		
	$\omega_e x_e$ = −3.86 ± 0.5 cm^{-1} [a,b]		

[a] Quoted errors correspond to accuracy of measurements based on 0.5 Å resolution for a typical scan.
[b] Errors estimated for ω_e and $\omega_e x_e$ correspond to one standard deviation from the mean.

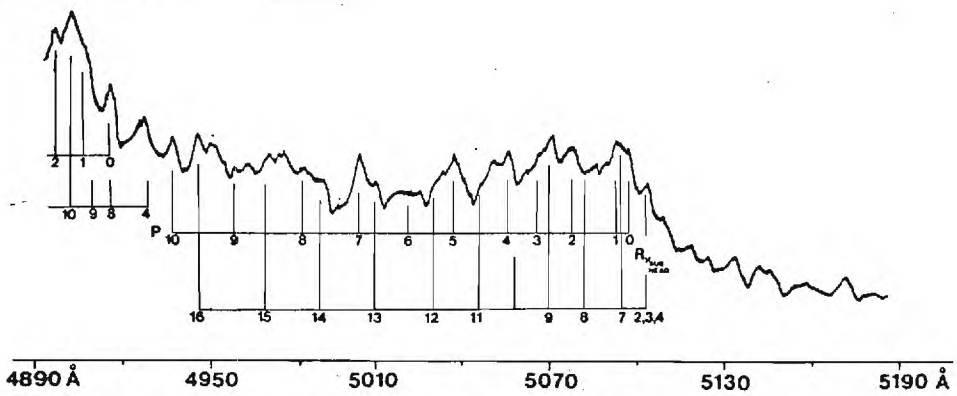

Fig. 4. Observed K structure for the (0,3,0) → (0,0,0) band of the $\tilde{A}\,^1A''$–$\tilde{X}\,^1A'$ transition in DCF. The labeled K structure is detailed in table 3. The features denoted with an asterisk represent structure which is highly perturbed or not readily reproducible (due to flame fluctuations) upon repeated scans of the spectrum. These features were not included in the analysis to obtain the parameters given in table 5.

magnitude of the frequency separation between observed bands in the progression, and the shift in the HCF frequency separations upon deuteration. The assignment to the excited state bending mode as opposed to a CF stretching mode is now unequivocal. The determined values of ω'_e and $\omega_e x'_e$ should be compared with the value of 1021.3 cm^{-1} quoted by Merer and Travis for the upper state bending frequency (based on measurements of the $v'_2 = 0,1$ frequency separation).

Merer and Travis [14] observed severe perturbations in $K \geqslant 1$ rotational levels of the higher vibrational levels ($v'_2 > 1$) of the upper $\tilde{A}\,^1A''$ state which they ascribed to interactions between the upper state and higher vibrational levels of the ground electronic state. The magnitude of the perturbations was found to be so extensive that it precluded further rotational analysis. In the present study, it has been possible to observe extensive K structure in several emission bands. However, due to higher temperatures and somewhat lower resolution, we have not been able to resolve J structure within the K-type subbands. We have carried out a partial rotational analysis of these K-type subbands for the (0,3,0) → (0,0,0) and (0,4,0) → (0,0,0) transitions in DCF where perturbations are much less severe than observed for other bands such as (0,2,0)–(0,0,0). The spectra are depicted in figs. 4 and 5. A listing of observed fre-

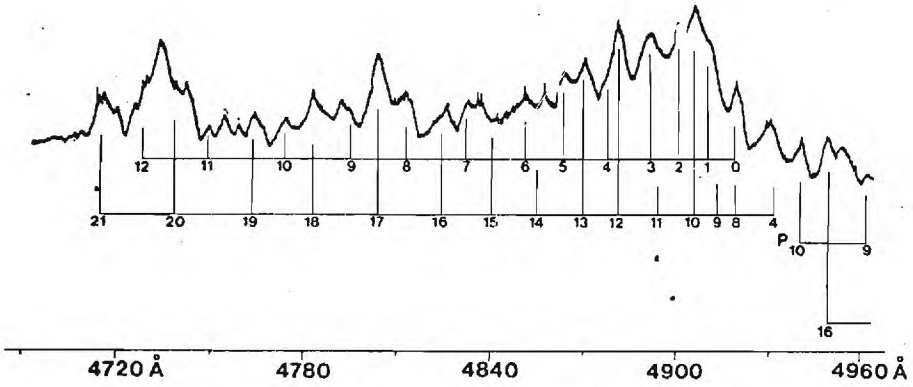

Fig. 5. Observed K structure for the (0,4,0) → (0,0,0) band of the $\tilde{A}\,^1A''$–$\tilde{X}\,^1A'$ transition in DCF. The labeled K structure is detailed in table 4. The features denoted with an asterisk represent structure which is highly perturbed or not readily reproducible (due to flame fluctuations) upon repeated scans of the spectrum. These features were not included in the analysis to obtain the parameters given in table 6.

Table 3
Assignments and wavelengths measured for subband structure in DCF 030–000

Assignment (K)	λ_{air} (Å)	$\bar{\nu}_{vac}$ (cm^{-1})	$\bar{\nu}_{calc}$ (cm^{-1})	$\nu_{mean} - \nu_{calc}$ (cm^{-1})
P_{branch}				
10	4940.2	20237	20242	−5
9	4960.9	20153	20147	+6
8	4984.3	20058	20060	−2
7	5003.8	19980	19980	0
6	a)	–	19908	–
5	5036.3	19851	19843	+8
4	5055.4	19776	19786	−10
3	5064.9	19739	19736	+3
2	5077.0	19692	19693	−1
1	5085.8	19658	19658	
0 *	5096.7 *	19615 *	19632 *	−16 *
R_{branch}				
1	–	–	–	–
2	–	–	–	–
3	5102.8	19592	19594	−2
4	–	–	–	–
5	–	–	–	–
6	–	–	–	–
7	–	–	–	–
8	–	–	–	–
9	5070.0	19719	19720	−1
10	–	–	–	–
11	–	–	–	–
12	–	–	–	–
13	5008.9	19959	19954	+5
14	4990.4	20034	20031	+3
15	4972.8	20115	20116	+1
16	4948.4	20204	20208	+4
17 *	4930.2 *	20278 *	20308 *	−30 *

* Highly perturbed – not included in fit.
a) Overlapped bands.

quencies and assignments is given in tables 3 and 4.

Relative intensitives were not reproducible from run to run due to flame instabilities. Assignments are based on several runs of the spectra in addition to those shown. There are several intense features shown which are not assigned. Some of these could not be reproduced in other runs. Several others are most likely due to overlapping of adjacent bands or perturbations. Linewidths were such that frequencies could not be determined to better than ±2 cm^{-1}. In addition, the asymmetry splitting is sufficiently small that it is not observed in these experiments and a symmetric rotor description is satisfactory. Given the accuracy of the spectral data, the nature of perturbations in these systems, and the inherent instability of the CD_4 fluorine flame, we take as our expression for the measured frequencies

$$\nu = A_0 + A_1 K + A_2 K^2,$$

where $A_0 = \nu_0 + (A' - \bar{B}')$, $A_1 = \pm 2(A' - \bar{B}')$ and $A_2 = (A' - \bar{B}') - (A'' - \bar{B}'')$. The fits were made using an iterative least-squares computer program fitting the P and R branch structure (see tables 3 and 4) for the constants A_0, A_1, and A_2. The results of our analysis for the $v_2' = 3$ and 4 bands are presented in tables 5 and 6. The estimated error for the parameters quoted in these tables corresponds to one standard deviation. It is interesting to note that the value of $A' - \bar{B}'$ increases from $v_2' = 3$ to $v_2' = 4$ also indicating the observation of a progression in the excited state bending mode. This phenomenon was also observed by Merer and Travis [14] for the $v_2' = 0$ and 1 levels in the HCF spectrum.

Table 4
Assignments and wavelengths measured for subband structure in DCF 040–000

Assignment (K)		λ_{air} (Å)	$\bar{\nu}_{vac}$ (cm^{-1})	$\bar{\nu}_{calc}$ (cm^{-1})	$\nu_{meas} - \nu_{calc}$ (cm^{-1})
P_{branch}	11	4746.3	21064	21055.2	+8.8
	10	4771.5	20953	20955.5	−2.5
	9	4797.8	20860	20862.5	−2.5
	8	4811.1	20780	20776.2	+3.8
	7	4830.8	20696	20696.8	−0.8
	6	4849.6	20615	20624.1	−9.1
	5	4862.7	20560	20558.2	+1.8
	4	(4880.8) *	(20487) *	–	–

Table 4 (continued)

Assignment (K)		λ_{air} (A)	$\bar{\nu}_{vac}$ (cm^{-1})	$\bar{\nu}_{calc}$ (cm^{-1})	$\nu_{meas} - \nu_{calc}$ (cm^{-1})
	3	4891.0	20441	20446.6	−5.6
	2	4999.8	20404	20401.0	+3.0
	1	4909.8	20362	20362.1	−0.1
	0	4919.0	20324	20330.0	−6.0
R_{branch}	1	–	–	–	–
	2	–	–	–	–
	3	–	–	–	–
	4	4930.2	20278	20269.3	8.7
	5	–	–	–	–
	6	–	–	–	–
	7	–	–	–	–
	8	–	–	–	–
	9	–	–	–	–
	10	4905.3	20381	20381.1	−0.1
	11	–	–	–	–
	12	–	–	–	–
	13	4868.8	20534	20528.4	+5.6
	14	4856.0	20588	20591.0	−3.0
	15	(4835.4) *	(20676) *	–	–
	16	–	–	–	–
	17	4802.0	20820	20819.4	+0.6
	18	4780.4	20914	20909.1	+4.9
	19	4761.2	20998	21005.6	−7.6

* Highly perturbed – not included in fit.

Table 5
Rotational parameters for 030–000 band of DCF

$A' - \bar{B}' = 11.9\ cm^{-1} \pm 0.1$
$(A' - \bar{B}') - (A'' - \bar{B}'') = 3.7\ cm^{-1} \pm 2.3$
$A'' - \bar{B}'' = 8.2\ cm^{-1} \pm 2.4$

origin
$\nu_0 = 19619\ cm^{-1}$
$A_0 = 15.9 \pm 2.1;\ A_1 = 23.7 \pm 0.2;\ A_2 = 3.7 \pm 2.3$

Table 6
Rotational parameters for 040–000 band of DCF

$A' - \bar{B}' = 14.4\ cm^{-1} \pm 0.1$
$(A' - \bar{B}') - (A'' - \bar{B}'') = 3.4\ cm^{-1} \pm 0.1$
$A'' - B'' = 11.0\ cm^{-1} \pm 0.2$

origin
$\nu_0 = 20316\ cm^{-1}$
$A_0 = 6.0 \pm 2.1;\ A_1 = 28.7 \pm 0.2;\ A_2 = 3.38 \pm 0.02$

4. Summary

In the current study, we have characterized the chemiluminescent products of the methane–fluorine flame over an extensive range of conditions. We have observed electronic emission from C_2, CH, CF_2, and HCF and vibronic mission from HF; the corresponding deutero compounds have also been observed. This study reports the first observation of the HCF chemiluminescent emission spectrum. The first observation of the HCF $\tilde{A}\,^1A''$–$\tilde{X}\,^1A'$ emission spectrum and the corresponding DCF system allows the assignment of these visible transitions to a progression dominated by the excited state bending mode. Several vibrational levels in the $\tilde{A}\,^1A''$ excited state of HCF and DCF have been observed and vibrational constants ω_e and $\omega_e x_e$ obtained. As has been noted previously [4,14], the observed emission spectrum follows a pattern expected on the basis of previous discussions of the molecular electronic structure of 12 and 13 valence electron HAB molecules. Many of

the observed vibrational transitions for both HCF and DCF show resolvable *K*-type subbands. Although this structure is highly perturbed, a partial rotational analysis has been obtained for two bands in the DCF spectrum, the results being consistent with the excited state bending modes.

Acknowledgement

R.I. Patel and G.W. Stewart wish to acknowledge support from the U.S. Department of Energy under contract number EY-77-C-21-8087, J.L. Gole wishes to acknowledge partial support from the Department of Energy, Morgantown, West Virginia and J.R. Lombardi wishes to acknowledge the American Chemical Society, PRF 9398-AC6.

References

[1] J.L. Gole, A. Hanner, unpublished data.
[2] C.P. Conner, G.W. Stewart, D.M. Lindsay and J.L. Gole, J. Am. Chem. Soc. 99 (1977) 2540.
[3] R.I. Patel and G.W. Stewart, Can. J. Phys. 55 (1977) 1518.
[4] D.M. Lindsay, J.L. Gole and J.R. Lombardi, Chem. Phys. 37 (1979) 333.
[5] R.A. Durie, Proc. Roy. Soc. A65 (1952) 125; 211; 110; 1952.
[6] R.F. Simmons and H.G. Wolfhard, Z. Elektrochem. 61 (1957) 601.
[7] M. Vanpee, K.D. Cashin and R.J. Mainiero, Comb. Flame 31 (1978) 187.
[8] G. Schatz and M. Kaufman, J. Phys. Chem. 76 (1972) 3586.
[9] G. Black, M. Luria, D.J. Eckstrom, S.A. Edelstein and S.W. Benson, J. Chem. Phys. 60 (1974) 3709.
[10] U.C. Sridharan and D.L. McFadden, J. Chem. Phys. 63 (1975) 5061.
[11] N.G. Fedotov, O.M. Sarkisov and V.I. Vedeneev, Khim. Vys. Energy 9 (1975) 17.
[12] L. Gero, Z. Physik 118 (1941) 27.
[13] D.E. Mann, B.A. Thrush, D.R. Lide, Jr., J.J. Ball and N. Acquista, J. Chem. Phys. 34 (1961) 420.
[14] A.J. Merer and D.N. Travis, Can. J. Phys. 44 (1966) 1541.
[15] J.E. Hesser and K. Dressler, J. Chem. Phys. 47 (1967) 3443.